DEVELOPMENT OF DOPE BISMUTH SULFIDE SYSTEM FOR THERMOELECTRIC APPLICATION

FITRIANI

FACULTY OF ENGINEERING
UNIVERSITY OF MALAYA
KUALA LUMPUR

2019

DEVELOPMENT OF DOPE BISMUTH SULFIDE SYSTEM FOR THERMOELECTRIC APPLICATION

FITRIANI

THESIS SUBMITTED IN FULFILMENT OF THE REQUIREMENTS FOR THE DEGREE OF DOCTOR OF PHILOSOPHY

FACULTY OF ENGINEERING
UNIVERSITY OF MALAYA
KUALA LUMPUR

2019

UNIVERSITY OF MALAYA
ORIGINAL LITERARY WORK DECLARATION

Name of Candidate: **Fitriani**

Matric No: KHA140072

Name of Degree: Doctor of Philosophy

Title of Project Paper/Research Report/Dissertation/Thesis (“this Work”):

Development of Dope Bismuth Sulfide System for Thermoelectric Application

Field of Study: **Energy**

I do solemnly and sincerely declare that:

(1) I am the sole author/writer of this Work;
(2) This Work is original;
(3) Any use of any work in which copyright exists was done by way of fair dealing and for permitted purposes and any excerpt or extract from, or reference to or reproduction of any copyright work has been disclosed expressly and sufficiently and the title of the Work and its authorship have been acknowledged in this Work;
(4) I do not have any actual knowledge nor do I ought reasonably to know that the making of this work constitutes an infringement of any copyright work;
(5) I hereby assign all and every rights in the copyright to this Work to the University of Malaya (“UM”), who henceforth shall be owner of the copyright in this Work and that any reproduction or use in any form or by any means whatsoever is prohibited without the written consent of UM having been first had and obtained;
(6) I am fully aware that if in the course of making this Work I have infringed any copyright whether intentionally or otherwise, I may be subject to legal action or any other action as may be determined by UM.

Candidate’s Signature Date:

Subscribed and solemnly declared before,

Witness’s Signature Date:

Name:

Designation:

DEVELOPMENT OF DOPE BISMUTH SULFIDE SYSTEM FOR THERMOELECTRIC APPLICATION

ABSTRACT

Bismuth sulfide (Bi_2S_3) has attracted increasing attention in thermoelectric investigations due to the availability of raw resources, lowered material and production costs, and environmental friendly compared with Bi_2Te_3-based materials. Bi_2S_3 also has a high Seebeck coefficient and low thermal conductivity at room temperature. The main obstacle for further improving its thermoelectric performance is due to its intrinsically high electrical resistivity. Therefore, the main objective of this work is to enhance the thermoelectric performance of Bi_2S_3 through several strategies. Elemental doping approach was selected to improve the carrier concentration and reduce the electrical resistivity of Bi_2S_3. Either the single doped system of $Bi_{2-x}Ni_xS_3$, $Bi_{2-x}Sn_{3x}S_3$ and Bi_2S_3+xNiO or double doped system of $Bi_{0.95}SbX_{0.05}S_3$ (X = Ni, Hf, Zn and Sn) were evaluated. Nanostructure and nano-microporous structure methods were chosen to further improve thermoelectric performance through reduction of thermal conductivity. Mechanical alloying (MA) method using high energy ball milling (BM) was applied to produce the nanoparticle powders, which will then be consolidated into bulk thermoelectric materials either through cold pressing or spark plasma sintering (SPS) process. Evidently, it is proved that all the samples exhibited predominant phase of orthorhombic Bi_2S_3. The use of Ni and Sn dopant atoms with lower valence than Bi host atom which can lead to the formation of interstitial solid solution is an effective strategy to increase the carrier concentration hence decrease the electrical resistivity of Bi_2S_3. Amongst the investigated samples, $Bi_{1.95}Ni_{0.05}S_3$ SPSed sample exhibited the lowest electrical resistivity of 8.27×10^{-4} Ω.m at 623 K, and further presented a highest dimensionless figure of merit (ZT) which is 0.38 at 623K. Addition of NiO also had significant effect to reduce the electrical resistivity of Bi_2S_3 system, which was suppressed up to ~ 98% by the addition of 0.5 mol% NiO. Moreover, all NiO added samples showed a relative monotonously constant on electrical resistivity values with increasing temperature. The changing of lattice constant due to substitution or inclusion of dopant atoms into Bi_2S_3 lattice affected the Seebeck coefficient of Bi_2S_3 system. Lattice shrinkage due to atomic substitution will increase the effective mass, m^*, thus increase the Seebeck coefficient. $Bi_{1.99}Ni_{0.01}S_3$ and $Bi_{1.99}Sn_{0.03}S_3$ which has the smallest volume cell in its system presented the highest Seebeck coefficient values in the whole measured temperature. The highest Seebeck coefficient of -766.15 μV/K at 300 K and -1170.25 μV/K at 323 K were exhibited by $Bi_{1.99}Ni_{0.01}S_3$ and $Bi_{1.99}Sn_{0.03}S_3$, respectively. In the thermal conductivity behaviors, the presence of porous structures give a significant effect on reduction of thermal conductivity, by a reduction of ~59.6% compared to a high density Bi_2S_3. In addition, the presence of Sb_2S_3 secondary phase in $Bi_{0.95}SbX_{0.05}S_3$ system contributed on enhancement of phonon scattering hence resulted in the reduction of thermal conductivity. $Bi_{0.95}SbNi_{0.05}S_3$ sample presented the lowest thermal conductivity value which is 0.21 W/mK at room temperature. Conclusively, this works have shown useful results for comprehensive understanding of Bi_2S_3 as potential material for low to middle temperature thermoelectric energy conversion.

Keywords: Bi_2S_3, elemental doping, mechanical alloying, thermoelectric.

PEMBANGUNAN SISTEM BISMUTH SULFIDE UNTUK APLIKASI TERMOELEKTRIK

ABSTRAK

Bismuth sulfide (Bi_2S_3) semakin menarik perhatian dalam penyiasatan termoelektrik disebabkan oleh ketersediaan sumber bahan mentah, kos bahan dan pengeluaran yang rendah serta mesra alam sekitar, jika dibandingkan dengan bahan-bahan berasaskan Bi_2Te_3. Bi_2S_3 juga mempunyai pekali Seebeck yang tinggi dan kekonduksian haba yang rendah pada suhu bilik. Halangan utama untuk meningkatkan lagi prestasi termoelektrik ialah kerintangan elektrik intrinsiknya yang tinggi. Oleh itu, objektif utama kerja ini adalah untuk meningkatkan prestasi termoelektrik dari Bi_2S_3 melalui beberapa strategi. Kaedah doping unsur dipilih untuk meningkatkan kepekatan pembawa dan mengurangkan kerintangan elektrik Bi_2S_3. Sama ada sistem dopan tunggal $Bi_{2-x}Ni_xS_3$, $Bi_{2-x}Sn_{3x}S_3$ dan $Bi_2S_3 + x$NiO atau sistem dopan berganda $Bi_{0.95}SbX_{0.05}S_3$ (X = Ni, Hf, Zn dan Sn) dikaji. Kaedah struktur nanostruktur dan nano-microporous dipilih untuk meningkatkan prestasi termoelektrik berikutan pengurangan kekonduksian terma. Kaedah mengaloi mekanikal (MA) dengan menggunakan pengilangan bola tenaga tinggi (BM) telah digunakan untuk menghasilkan serbuk nanopartikel, yang kemudiannya akan disatukan menjadi bahan termoelectrik pukal sama ada melalui proses tekanan sejuk atau plasma sintering (SPS). Jelas terbukti bahawa semua sampel menunjukkan fasa utama ortorombik Bi_2S_3. Penggunaan atom dopan Ni dan Sn dengan valensi yang lebih rendah daripada atom hos Bi yang boleh menyebabkan pembentukan larutan interstisial adalah strategi yang berkesan untuk meningkatkan kepekatan pembawa sehingga mengurangkan kerintangan elektrik Bi_2S_3. Antara sampel, kerintangan terendah 8.27×10^{-4} Ω.m didapati oleh sampel SPS $Bi_{1.95}Ni_{0.05}S_3$ pada suhu 623 K dan ianya mempamerkan nilai ZT tertinggi sebanyak 0.38 pada suhu 623K. Penambahan NiO juga memberi kesan yang signifikan terhadap kerintangan elektrik bagi sistem Bi_2S_3, yang ditindas sehingga ~ 98%

dengan penambahan 0.5 mol% NiO. Selain itu, kesemua larutan NiO menunjukkan suhu yang bebas daripada kerintangan elektrik. Perubahan kekisi tetap disebabkan oleh penggantian atau kemasukan atom dopan ke dalam kisi Bi_2S_3 juga menyebabkan perubahan pada pekali Seebeck bagi sistem Bi_2S_3. Pengecutan kisi kerana penggantian atom akan membawa kepada peningkatan jisim yang berkesan, m^*, justeru itu meningkatkan pekali Seebeck. $Bi_{1.99}Ni_{0.01}S_3$ dan $Bi_{1.99}Sn_{0.03}S_3$ yang mempunyai sel isipadu terkecil dalam sistemnya memberikan nilai pekali Seebeck tertinggi dalam keseluruhan suhu pengukuran. $Bi_{1.99}Ni_{0.01}S_3$ dan $Bi_{1.99}Sn_{0.03}S_3$ mempamerkan pekali Seebeck tertinggi ialah -766.15 μV/K pada 300 K dan -1170.25 μV/K pada 323 K. Dalam kelakuan konduktiviti terma, kehadiran struktur berliang memberikan kesan yang signifikan terhadap pengurangan kekonduksian terma, dengan penurunan ~ 59.6% berbanding dengan kepadatan tinggi Bi_2S_3. Di samping itu, kehadiran fasa sekunder Sb_2S_3 dalam sistem $Bi_{0.95}SbX_{0.05}S_3$ menyumbang kepada penambahan penyemburan phonon yang mengakibatkan pengurangan kekonduksian terma. Sampel $Bi_{0.95}SbNi_{0.05}S_3$ menyampaikan nilai kekonduksian terma terendah iaitu 0.21 W / mK pada suhu bilik. Secara ringkasnya, karya ini telah menunjukkan hasil yang berguna untuk pemahaman yang komprehensif tentang Bi_2S_3 sebagai bahan potensial untuk penukaran tenaga termoelektrik suhu rendah-pertengahan.

Kata kunci: Bi_2S_3, doping unsur, pengaloian mekanikal termoelektrik,

ACKNOWLEDGEMENTS

All praise is only for Allah SWT, who has bestowed me a precious and wonderful life in this world.

My sincere thanks go to my supervisor, Assoc. Prof. Ir. Dr. Suhana Mohd Said, for her guidance, inspiration, patience, and invaluable assistance during all the time of research. I would like to thank Dr. Shaifulazur bin Rozali and Dr. Bui Duc Long for the encouragement of this research. I also would like to dedicate my deepest gratitude to Prof. Tadachia Nakayama and Prof. Masatoshi Takeda for giving me the opportunity to conduct the research at Nagaoka University of Technology, Japan. The provision by Assoc. Prof. Ir. Dr. Faizul Mohd Sabri of laboratory facilities in Nano Lab, and the receipt of IGRAS scholarships, are gratefully recognized. I extend thanks to Dr. Nguyen Thanh Son and Mr. Kimoto Yuichiro, for all of their help during my period of time at Nagaoka, Ms. Shafinie for her sincere hospitality and assistance, and all the members of LCD and EM labs for their supports and friendship.

Finally I wish to my father and mother, my lovely husband: Yose Fachmi Buys, and my sons; Samy and Tsaqib, for their support and encouragement over the years.

TABLE OF CONTENTS

LIST OF FIGURES

LIST OF TABLES

LIST OF SYMBOLS AND ABBREVIATIONS

TW : Terawatt

CO_2 : Carbon dioxide

Z : Thermoelectric figure of merit

ZT : Dimensionless thermoelectric figure of merit

α : Seebeck coefficient

Π : Peltier coefficient

τ : Thomson coefficient

ΔV : Voltage difference

I : Current

T : Temperature

η : Carnot efficiency

ρ : Electrical resistivity

σ : Electrical conductivity

κ : Thermal conductivity

κ_{lat} : Lattice thermal conductivity

κ_e : Electronic thermal conductivity

PF : Power factor

mfp	:	Mean free path
TEG	:	Thermoelectric generator
TEC	:	Thermoelectric cooling
RTGs	:	Radioisotope thermoelectric generators
TAGS	:	Tellurium-Antimony-Germanium-Silver
STUs	:	Skutterudite segmented thermoelectric uni-couples
CTMS	:	Cascaded thermoelectric modules
SUV	:	Sports utility vehicle
CNG	:	Compressed natural gas
QW	:	Quantum well
TCS	:	Thermoelectric cogeneration system
EEG	:	Electroencephalography
ECG	:	Electrocardiography
CNT	:	Carbon nanotube
MEMS	:	Micro electro mechanical system
MA	:	Mechanical alloying
BM	:	Ball milling
CP	:	Cold pressing
SPS	:	Spark plasma sintering

XRD : X-ray diffraction

SEM : Scanning electron microscope

EDS : Energy dispersive X-ray spectroscopy

TEM : Transmission electron microscope

FIB : Focused ion beam

T_H : Hot-side/upper temperature

T_L : Lower temperature

R : Resistance

DC : Direct current

A : Cross sectional area

l : Distance between probe

LFA : Laser flash method

d : Density of sample

Cp : Specific heat

D : Diffusivity

$t_{1/2}$: Time required to reach one-half of the peak temperature

GHP : Guarded hot plate

HFM : Heat flow meter

TCT : Thermal conductivity tester

DSC : Differential scanning calorimetry

FHWM : Full width a half maximum

SD : Standard deviation

FESEM : Field emission scanning electron microscope

IUPAC : International union of pure and applied chemistry

$\acute{e}$: Electron charge

n : Carrier concentration

μ : Mobility

R_H : Hall coefficient

L : Lorenz number

κ_S : Thermal conductivity with porosity = 0

f : Porosity

$\dot{h}$: Hole concentration

$\mathrm{k_B}$: Boltzmann constant

h : Plank constant

$m*$: Effective mass

Eg : Energy gap

E : Electron energy

$\hbar$: Reduced Planck constant

E_F : Fermi energy

T_m : Melting temperature

CHAPTER 1: INTRODUCTION

1.1 Background

The world's energy and environment have become some of the critical issues in this 21st century. Based on projections of population growth and economic development, the rate of global energy expenditures is predicted to rise from 13.5 TW in 2001 to 27.6 TW in 2050 and expected to increase up 43 TW in 2100 (Lewis & Nocera, 2006). Even though there are oil, natural gas, and coal reserves to meet energy requirements in the future, there could be dramatic consequences to utilizing these carbon based fuels (Lewis & Nocera, 2006). Furthermore, there are also serious climate concerns about the increasing levels of CO_2 in the atmosphere. In April 2017, Mauna Loa observatory in Hawaii, USA recorded the CO_2 level in the atmosphere was about 410 ppm, which is much higher than pre-industrial levels of between 210 to 300 ppm (Kahn, 2017; Petit *et al.*, 1999; Siegenthaler *et al.*, 2005). Research suggests that a dramatic climate effects might be observed at 550 ppm and at this level the CO_2 in the atmosphere could enter a positive feedback loop (Houghton, 2001). Without serious changes in global energy strategies, atmospheric CO_2 levels are predicted to pass this tipping point and more than double within the 21st century.

Therefore, the discovery of new environmental friendly energy sources and energy optimization is important for our societies (Koumoto & Mori, 2015). Amongst the viable technologies for this purpose, thermoelectric energy converters are of increasing interest because these solid-state devices can directly convert heat given off from sources such as power plants, factories, motor vehicles, computers or even human bodies into electrical power using the Seebeck effect (Fthenakis & Kim, 2010; Liu *et al.*, 2010; Martín-González *et al.*, 2013; Saidur *et al.*, 2012; Shu *et al.*, 2013; Vélez *et al.*, 2012; Wang *et al.*, 2011). There are numerous advantages of thermoelectric energy converters including solid-state operation, the absence of toxic residuals, vast scalability, maintenance-free operation vis-à-vis the lack of moving parts or chemical reactions, and a long life span of reliable operation (Dai *et al.*, 2011; Riffat & Ma, 2003; Tie & Tan, 2013; Ullah *et al.*, 2013). Conversely, solid-state thermoelectric devices can also transform electrical energy into thermal energy for cooling or heating via Peltier effect, as shown schematically in Figure 1.1. Although compressor-based cooling has been established for a long time, thermoelectric device offers several distinct advantages over the conventional system, such as moving mechanical part-free that makes the system rugged, reliable, and quiet, no ozone-depleting chlorofluorocarbons or other materials that may require periodic replenishment, precise temperature-control (< 0.1 Celsius), as well as being extremely compact (Enescu D & Virjoghe EO, 2014; Hamid Elsheikh M *et al.*, 2014).

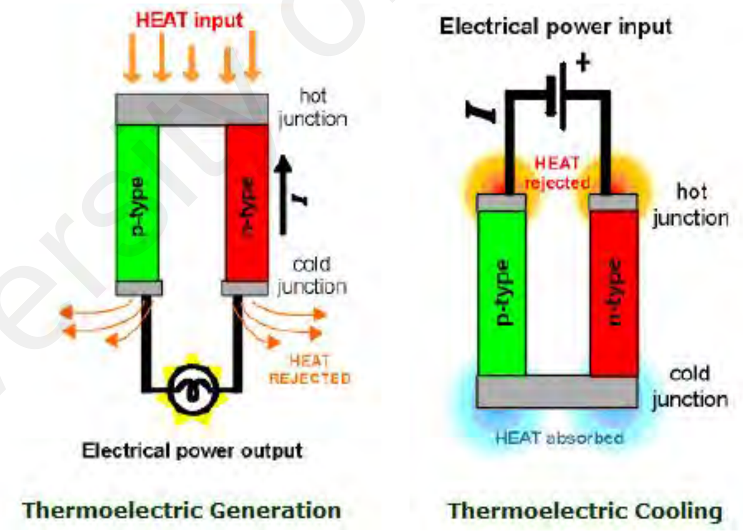

Figure 1.1: Schematic of thermoelectric module operation (Fitriani *et al.*, 2016).

Despite many advantages of thermoelectric energy converter, for many years the uses of thermoelectric were limited to space applications where its extreme reliability justified to provide electricity to the majority of probes sent into space (Voyager, Apollo, Pioneer, Curiosity, etc.) (Champier, 2017). Low efficiency and high cost have been an obstacle to thermoelectric development for more common applications. Therefore, researchers and manufacturers have tried to improve three main factors to overcome the low efficiency issue (Champier, 2017): (1) improving the dimensionless figure of merit *ZT*, (2) increasing the operating range of materials to work with higher temperature differences and, (3) searching for low-cost materials to counteract the negative effect of low efficiency. Currently, the available bulk thermoelectric materials have a maximum *ZT* ~ 1.65, which was attained by Zintl $Mg_3Sb_{1.48}Bi_{0.48}Te_{0.04}$ (Zhang *et al.*, 2017). Moreover, bismuth telluride (Bi_2Te_3) has been the only material which has been used for industrial thermoelectric modules in the last decades.

1.2 Problem statement

Semiconducting chalcogenide compounds have been receiving much attention because of their wide range of applications in various fields of science and technology (Chen *et al.*, 1997). The family of chalcogenide compounds, A_2B_3 (A= Bi, Sb, Pb; B = S, Se, Te) are considered to be the most promising for thermoelectric application (Rowe & Bhandari, 1983). In particular, $(Bi,Sb)_2Te_3$ based materials have been used extensively in room temperature thermoelectric applications for more than 30 years and significant advancements have been done in improving their thermoelectric properties. It was reported by Xie *et al.* (2010) that the maximum *ZT* of ~ 1.56 was attained of $Bi_xSb_{2-x}Te_3$ compound at 300 K. However, the key component element in this high-*ZT* material is a very rare element in the Earth's crust i.e., Te (0.001 ppm by weight) (Amatya & Ram, 2012). If thermoelectric devices are to reach mass markets in the future, cost and environmental conservation issues should be taken into consideration when choosing elements used for thermoelectric materials (Chen, 2016). Therefore, it is necessary to develop alternative materials to replace the use of tellurium. Bi_2S_3 is a promising candidate material not only because of its eco-friendly, abundance and low-cost but also demonstrates a high Seebeck coefficient and low thermal conductivity at room temperature (Snyder & Toberer, 2008). The main obstacle for further improving its thermoelectric performance is its intrinsically high electrical resistivity (about two orders of magnitude higher than that of Bi_2Te_3 compounds). Because of its high electrical resistivity, research on Bi_2S_3 as thermoelectric materials is still limited (Yu *et al.*, 2011). Thus, the scope of this work was to explore the potential of doped systems to enhance the thermoelectric performance of Bi_2S_3 using relatively simple and timeless fabrication methods. Elemental doping approach was selected to improve the carrier concentration and reduce the electrical resistivity of Bi_2S_3. Whilst, the concept of nanostructuring and and nano-microporous structure were chosen to improve thermoelectric performance through reduction of thermal conductivity.

1.3 Research objectives

The main objective of this research is to improve the thermoelectric properties of Bi_2S_3 bulk system, which subjectively can be defined as follows:

1. To formulate new Bi_2S_3 thermoelectric materials through single doped systems by addition of Ni, Sn and NiO ($Bi_{2-x}Ni_xS_3$, $Bi_{2-x}Sn_{3x}S_3$ and Bi_2S_3+xNiO) and double doped systems of $Bi_{0.95}SbX_{0.05}S_3$ (X = Ni, Hf, Zn and Sn).
2. To synthesize Ni doped Bi_2S_3 porous thermoelectric material to improve thermal transport property through a combination process of mechanical alloying and cold pressing.
3. To synthesize high-performance elementals doped Bi_2S_3 thermoelectric materials through a simple and short processes of mechanical alloying and spark plasma sintering.

4. To evaluate the influence of various dopant elements (Ni, Sn, NiO, Sb, Hf, Zn and Sn) on the microstructural properties and thermoelectric properties such as electrical resistivity, Seebeck coefficient, charge transport and thermal conductivity of the developed materials.

1.4 Thesis outline

This thesis contains five (5) chapters. The contents of each chapters have been organized as follows:

Chapter 1 presents the background knowledge including the necessity of developing thermoelectric materials and the purpose of the current study.

Chapter 2 is the literature review which will go into depth on the theoretic background behind thermoelectric, explaining basic thermoelectric principals and the applications of thermoelectric. The definition of thermoelectric figure of merit (*ZT*) is elaborated, as well as the fundamentals to achieve higher *ZT* values are also discussed. Moreover, the chapter concludes with the developments achieved in state-of-the-art of bismuth based thermoelectric materials, as well as theory behind increased thermoelectric performance of bismuth sulfide based materials and discussion on applied method of Hume - Rothery for selecting potential dopant atoms.

Chapter 3 describes the details of experimental procedures used in synthesize and characterization processes of elemental doped Bi_2S_3 bulk materials. The operation principles of experimental setup for measuring electrical resistivity, Seebeck coefficient and thermal conductivity are also discussed.

Chapter 4 discusses the results in terms of microstructure, electrical transport properties, thermal transport properties, and the resulted *ZT* value.

Chapter 5 addresses the general conclusions, remaining challenges and potential future direction for optimizing the thermoelectric performance of Bi_2S_3 system.

CHAPTER 2: LITERATURE REVIEW

2.1 Thermoelectric phenomena

Thermoelectric effect is defined as the direct conversion of temperature differences to electric voltage and vice versa. A thermoelectric device creates a voltage when there is a different temperature applied on each side. Conversely, when a voltage is applied to such a device, it creates a temperature difference. At the atomic scale, an applied temperature gradient causes the diffusion of charge carriers in the material from the hot side to the cold side, thus inducing a thermal current. This behavior is similar to a classical gas that expands when heated, leading a flux of the gas molecules. Moreover, thermoelectric devices could also efficient as temperature controllers due to the direction of heating and cooling is determined by the polarity of the applied voltage.

The basic thermoelectric circuit is shown in Figure 2.1. Its behavior depends in part on the Seebeck coefficient (α), Peltier coefficient (Π), and Thomson coefficients (τ). The details of those phenomena could be defined as follow (Nolas *et al.*, 2013):

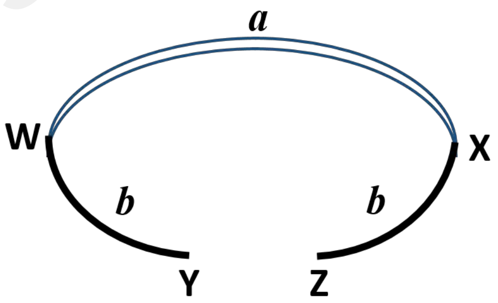

Figure 2.1: Basic thermocouple (Nolas *et al.*, 2013).

Two different conductors, *a* and *b*, have junctions at *W* and *X*. If a temperature difference is created between *W* and *X*, a voltage difference *(V)* appears between the two *b* segments. Under open circuit conditions, the Seebeck coefficient is defined as:

$$\alpha_{ab} = \frac{\mathrm{d}V}{\mathrm{d}T} \tag{2-1}$$

If W is hotter than X, a thermocouple ab that would drive a clockwise current is said to have a positive α. By contrast, if an imposed clockwise current (I) liberates heat at W and absorbs heat at X, then thermocouple ab has a negative Π. The rate of heat exchange at the junctions is:

$$Q = \Pi_{ab}\, I \tag{2-2}$$

If current is flowing and there is a temperature gradient, there is also heat generation or absorption within each segment of the thermocouple because α is temperature dependent. The gradient of the heat flux is given by:

$$\frac{\mathrm{d}Q}{\mathrm{d}s} = \tau\, I\, \frac{\mathrm{d}T}{\mathrm{d}s} \tag{2-3}$$

where s is a spatial coordinate.

It is useful that both τ and Π can be obtained from α, which is easily measured. Experiments have confirmed the relationships derived by Kelvin:

$$\tau_a - \tau_b = T\, \frac{\mathrm{d}\alpha_{ab}}{\mathrm{d}T} \tag{2-4}$$

and;

$$\Pi_{ab} = \alpha_{ab}\, T \tag{2-5}$$

The last equation provides a fundamental link between thermoelectric cooling (Π) and thermoelectric power generation (α).

Thermoelectric cooling and power generation require joining two different materials. Therefore, it is Π and α of couples that matter in practice. However, the absence of α for superconductors has made it possible to define an absolute α and Π for individual materials. The α value for Pb-~Sn couples measured up to the critical temperature of the latter gave α_{Pb}, for T < 18 K. Then, measurement of τ from 18 K to high temperatures [2.1, 2.2] yielded an absolute α for Pb, which became a reference material. The absolute thermoelectric coefficients also obey the Kelvin relationships:

$$\tau = T\,\frac{\mathrm{d}\alpha}{\mathrm{d}T} \tag{2-6}$$

and;

$$\Pi = \alpha T \tag{2-7}$$

2.2 Conversion efficiency and figure of merit

The working principle of thermoelectric module is similar to that of a heat engine, where instead of heat, electrons and/or holes are being utilized as the energy carriers. The efficiency of thermoelectric material is governed by the Carnot efficiency, η, and material figure-of-merit, *ZT,* according to the following relation:

$$\eta = \frac{W}{Q_H} = \frac{T_H - T_C}{T_H} . \frac{\sqrt{1+ZT} - 1}{\sqrt{1+ZT} + T_C/T_H} \tag{2-8}$$

where W is the electrical power output and Q_H is the thermal power supplied. T_H and T_C are the average temperature of hot side and cold side, respectively (Rowe & Bhandari, 1983). For all heat engines, the upper limit of power generation efficiency is the Carnot efficiency, $[(T_H - T_C)/T_H]$. The device would approach the Carnot efficiency if ZT could reach infinity. Therefore, maintaining a large temperature gradient and improving ZT are both effective means to increase the power generation efficiency. Figure 2.2 presented the conversion efficiency of state-of-the-art materials at different temperatures, with cold side = 300 K. It can clearly be seen that most state-of-the-art nanocomposites have a conversion efficiency, η, ranging from 8% – 16% (Biswas *et al.*, 2011; Hsu *et al.*, 2004; Joshi *et al.*, 2011; Liu *et al.*, 2011).

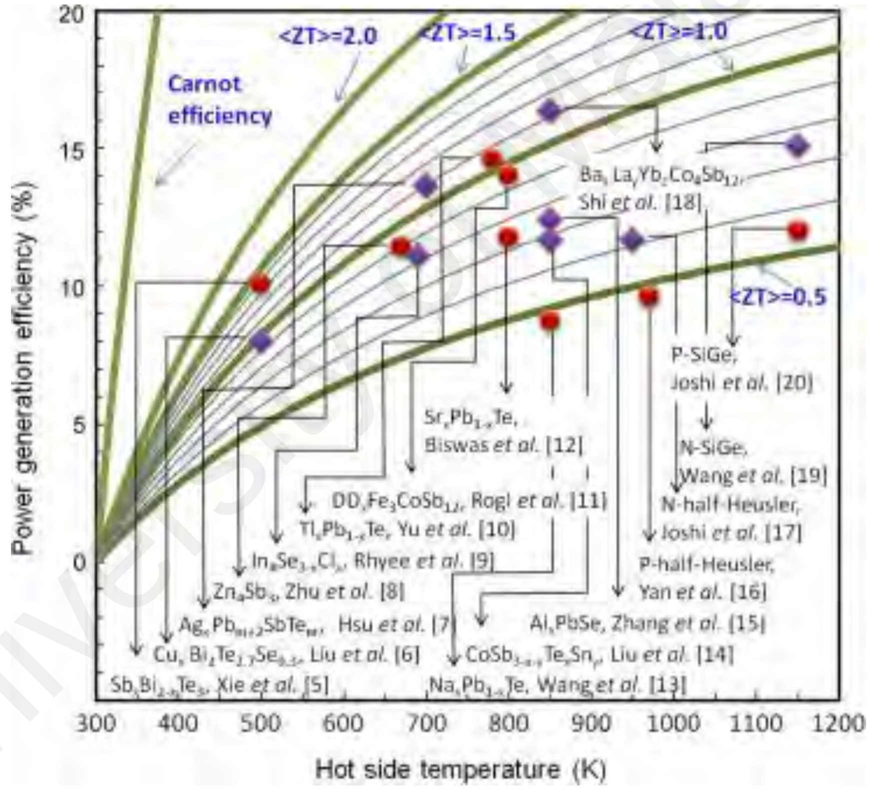

Figure 2.2: Comparison of conversion efficiency state-of-art materials (Liu *et al.*, 2012).

Generally in thermoelectric materials research, it is more convenient to evaluate the thermoelectric performance of each material singularly, rather than as a component in a device (Chen, 2016). In 1911, Altenkirch derived the thermoelectric figure of merit for a single material, which has defined as:

$$Z = \frac{\alpha^2 \sigma}{\kappa} = \frac{\alpha^2}{\rho\, \kappa} \tag{2-9}$$

$$\kappa = \kappa_e + \kappa_{lat} \tag{2-10}$$

where α is the Seebeck coefficient of materials, ρ is electrical resistivity, σ is electrical conductivity, κ is total thermal conductivity, κ_e is electronic thermal conductivity, and κ_{lat} is lattice thermal conductivity. The Z factor provides a means information of comparing for overall thermoelectric performance between materials. The units of thermoelectric figure of merit is K^{-1}, thus it is usually multiplied by the mean absolute operating temperature, T, to give the dimensionless figure of merit, ZT. Moreover, to increase ZT, expressed as $\alpha^2\sigma$ (= α^2/ρ), also known as the power factor (*PF*), needs to be increased in relation to the thermal conductivity. As shown in Figure 2.3, the power factor for semiconductors can be maximized only within a certain carrier concentration range, where the peak typically occurs at carrier concentrations between 10^{24} and 10^{27} carriers per m^3, which fall in between common metals and semiconductors, that is, the concentration must be found in heavily doped semiconductors (Snyder & Toberer, 2008).

Besides tuning carrier concentration, there are some special cases to improve the power factor $\alpha^2\sigma$, in which one quantity can be increased while the other remains constant or both quantities can be increased simultaneously (Chen, 2016). For instance, the work of Heremans *et al*. (2012) and Jaworski *et al*. (2011) had enhanced the Seebeck coefficient in Tl-doped PbTe and its alloys by introducing an impurity state in conduction band which caused distortions in density of states near Fermi level. An increase on Seebeck coefficient values were also reported by Ko *et al*. (2011) through carrier energy filtering in Pt-Sb_2Te_3 nanocomposite. Whilst, a simultaneous high Seebeck coefficient and high electrical conductivity through band convergence in Na doped $PbTe_{1-x}Se_x$ was found in the work of Pei *et al.* (2011). Although those strategies only work in very specific situations and very difficult to be commonly applied in all different materials, they showed the possibilities to further improvements in power factor and *ZT* value (Chen, 2016).

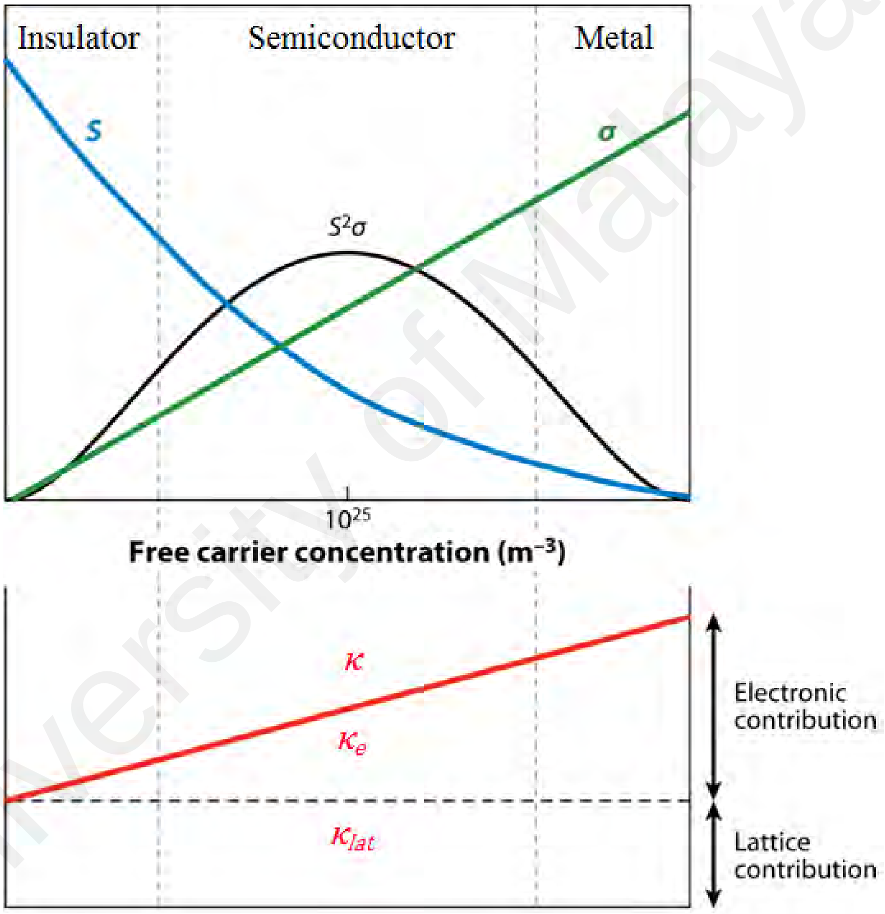

Figure 2.3: Schematic dependence of electrical conductivity (σ), Seebeck coefficient (α), power factor ($\alpha^2\sigma$), and thermal conductivity (κ) on carrier concentration. (Rowe, 1995; Shakouri, 2011).

Moreover, Figure 2.3 also has implies that the reduction of thermal conductivity especially reduction of lattice thermal conductivity is another approach to increase *ZT*. The lowest thermal conductivity in crystalline solids is often called the alloy limit due to scattering of phonons by atomic substitutions (Kim *et al.*, 2006). Historically, it has been challenging to increase *ZT* > 1 because of the difficulty of reducing thermal conductivity below the alloy limit. Recent reports have shown that *ZT* can be increased beyond unity by nanostructuring thermoelectric materials, and the key reason for increase in *ZT* was the reduction of thermal conductivity (Harman *et al.*, 2002; Hsu *et al.*, 2004; Venkatasubramanian *et al.*, 2001)

The nanostructuring concept is relatively simple. It is by: reducing the grain size to a nanoscale in order to increase phonon scattering, then it will subsequently reduce the lattice thermal conductivity, whilst still maintaining good electrical property (Martín-González *et al.*, 2013). As an example, a theoretical modeling on the contribution of phonon scattering to the lattice thermal conductivity as a function of the mean free path (*mfp*) for Si was conducted. The calculations indicated that 90% of the thermal conductivity accumulation in Si is due to phonons that have an *mfp* greater than 20 nm (Henry & Chen, 2008). Therefore, if the grain size was reduced to 20 nm, a reduction of 90% in the lattice thermal conductivity could be achieved. At the same time, the carrier mobility will not be affected. This is because the electron *mfp* in Si was calculated to be only a few nanometers (Bux *et al.*, 2009). Through nanostructuring, the improvement in thermoelectric properties can be obtained where it cannot be achieved in traditional bulk materials. The guidelines for the nanoparticle dimensions vary for different material systems, but the critical feature sizes must remain in range of the nanoscale (1 to 100 nm). Some improvements of *ZT* using the nanostructuring method are shown in Figure 2.4.

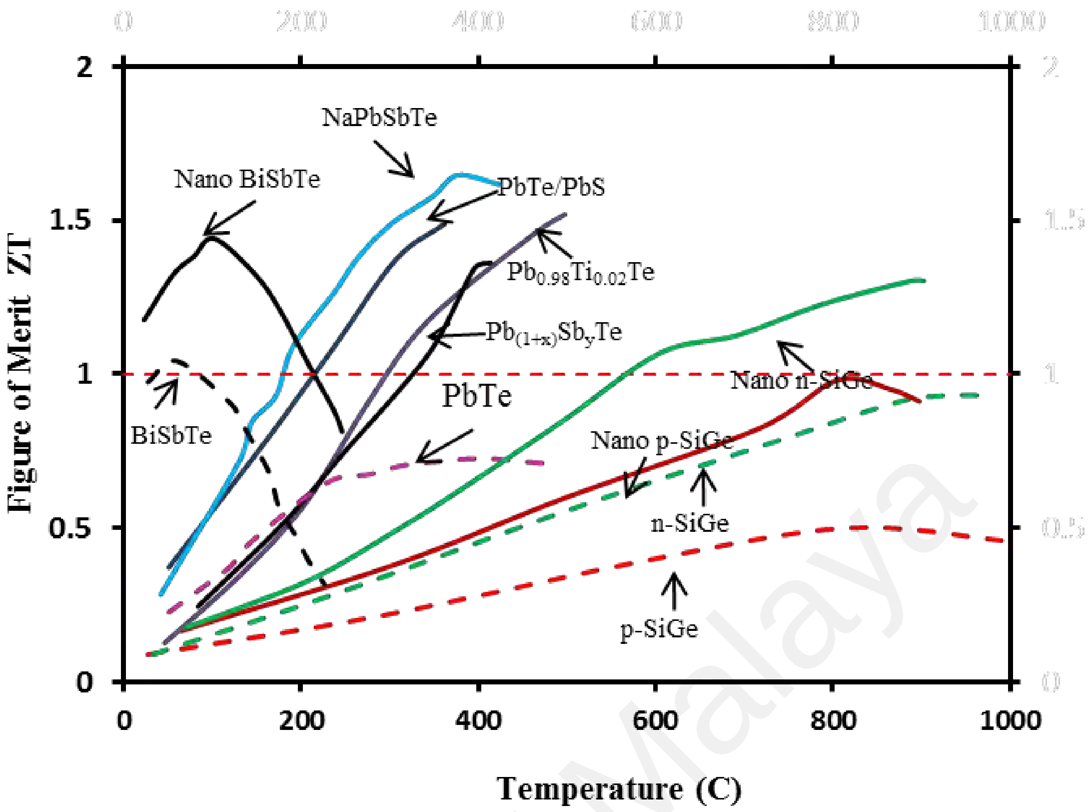

Figure 2.4: *ZT* Values of thermoelectric materials are plotted as a function of temperature. (The dashed lines show the maximum *ZT* values for bulk state of the art materials, and the solid lines show recently reported *ZT* values (Minnich AJ *et al.*, 2009).

In recent year, introducing porous structures have been reported as a new paradigm on reducing thermal conductivity (Mori, 2017). Previously, Tarkhanyan and Niarchos (2013) studied a physical model for the reduction in κ_{lat} of graded porous structures with inhomogeneous porosity. The results shown that the presence of various pore groups with different diameters of spherical hole pores leads to the significant reduction in the κ_{lat} compared not only to bulk materials with zero porosity but also to the materials with homogeneous porosity. They proposed that this type of porous materials can be regarded as potential candidates for next-generation thermoelectric materials (Tarkhanyan & Niarchos, 2013). Recently, Khan *et al*. (2017) reported a skutterudite material with porous architecture containing nano- to micrometer size irregularly shaped and randomly oriented pores, scattering a wide spectrum of phonons without employing the conventional rattling phenomenon. They found that the lattice thermal conductivity reaches the phonon glass limit and the design yields >100% enhancement in *ZT*, as compared to the pristine sample. A *ZT* of 1.6 at 500˚C was obtained for $CoSb_{2.75}Si_{0.075}Te_{0.175}$ alloy (Figure 2.5).

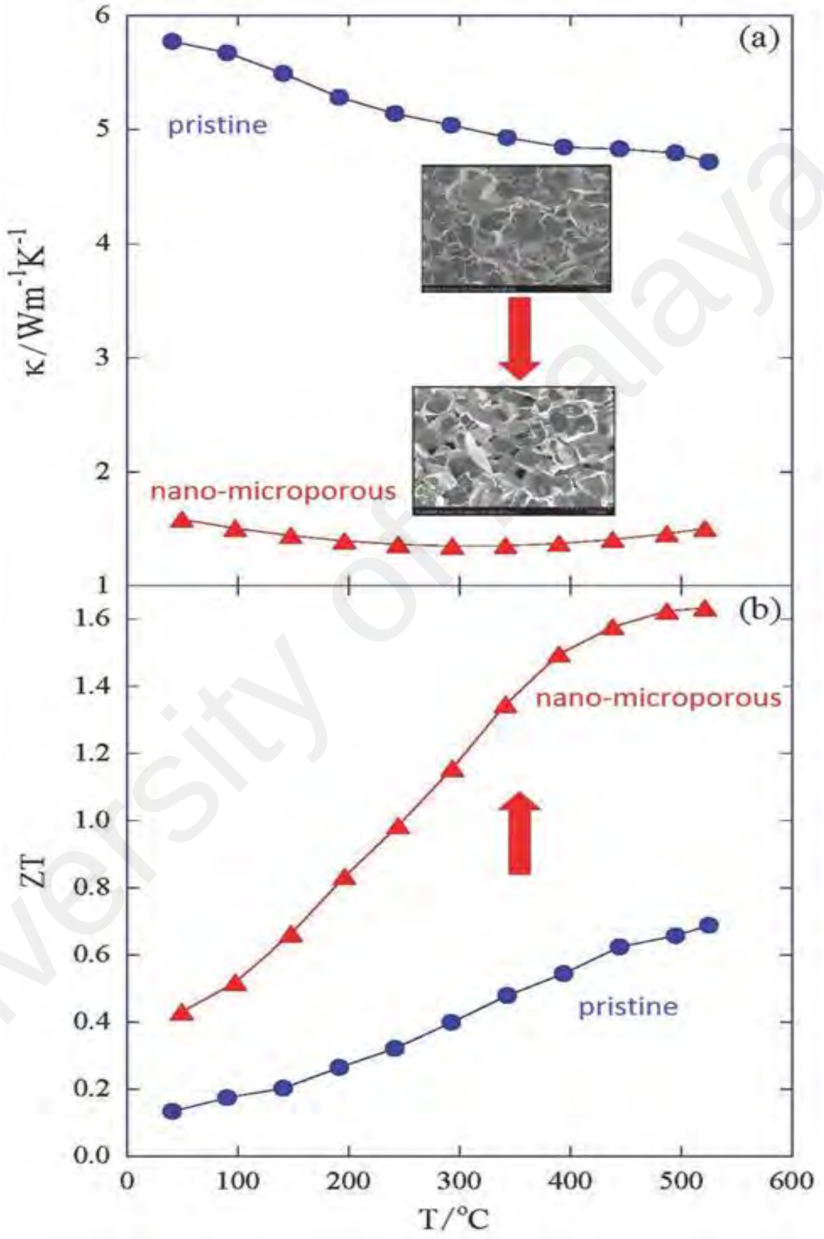

Figure 2.5: Thermal conductivity a) and *ZT* b) of $CoSb_{2.75}Si_{0.075}Te_{0.175}$ before ("pristine") and after ("nano-microporous") annealing and creation of nano-micropores (Khan *et al.*, 2017; Mori, 2017).

2.3 Applications of thermoelectric materials

Thermoelectric materials are receiving much renewed attention due to their extensive applications. As mentioned above, the thermoelectric effect can convert heat to electricity, and vice versa. Thus, the thermoelectric applications are mainly based on those two aspects by either generate electrical power from the heat energy by using thermoelectric generator (TEG) or thermal energy (in terms of heating or cooling) will be produced when the electrical power is applied (TEC).

2.3.1 Thermoelectric generator (TEG)

TEG can directly converse the heat into electricity with solid state which makes it adaptable in many areas. The heat sources for TEG could be various from solar, biomass and the earth. It should be pointed out that the temperature ranges for TEG recently are relatively low. The higher operation temperature makes the TEG less competitive.

2.3.1.1 Aerospace

For numerous planetary exploration missions, solar power is not an enabling option for producing electricity because of the progressively weaker solar brightness. It is said that the solar radiation is around 1375 W/m^2 on the Earth and falls to 1W/m^2 around Pluto. Therefore, the space industry has used TEGs since the beginning of the conquest of space in combination with thermal generators based on nuclear technology, i.e. radioisotope thermoelectric generators (RTGs). Radioisotope generators (Figure 2.6) do not use nuclear fission or fusion, but heat from the natural radioactive decay of plutonium- 238 (mainly in the form of 238PuO$_2$ plutonium dioxide) . The RTGs can operate for several years and even several decades after their launch. The Voyager I and II spacecraft, launched in 1997, also used RTGs, due to their extreme reliability, to power the on board instruments and transmission systems to the ends of the solar system. On October 2015, the probes were 19.5 billion and 16 billion km from Earth. Each spacecraft was equipped with 3 RTGs which supplied 423W in power overall from about 7000W in heat. The power decreases gradually by about 7W a year due to the decay of the plutonium and the degradation of the silicon germanium thermocouples. On September 2015, the power was about 255 W, which have sufficient electrical power to operate until 2020 ("Voyager, the interstellar mission n.d.," 2015).

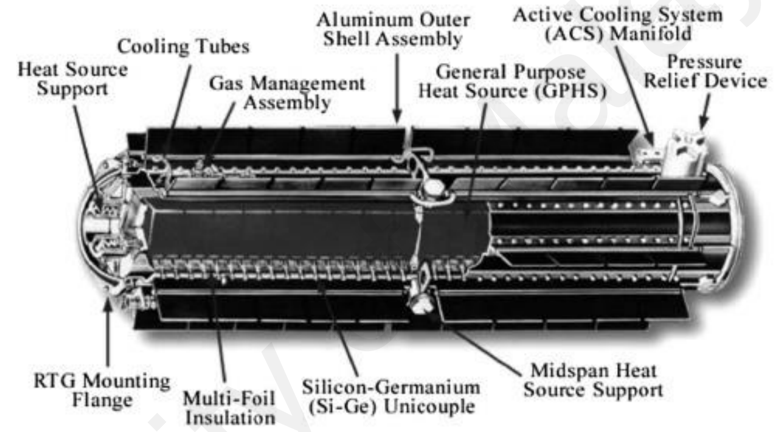

Figure 2.6: Current RTGs with 18 GPHS modules and SiGe thermoelectric unicouples for generating 280 We at beginning of life (~5.5 We/kg) (El-Genk & Saber, 2005).

The materials used for the thermocouples in RTGs are PbSnTe, TAGS-PbTe and SiGe. Current research is focusing on improving the performance of proven materials (decreasing lattice conductivity and improving electrical properties) and the study of other materials and couple assembly (Zintl, skutterudite and segmented couples) (Caillat *et al.*, 2009). El-Genk et al. (2003) have compared the performance of SiGe ($Si_{0.8}Ge_{0.2}$) and skutterudite segmented thermoelectric unicouples (STUs) which was set in the hot side temperature of 973 K and cold side temperatures of 300, 573 and 673 K. The results showed that the STU could potentially hit the peak efficiency of 7.8% and 14.7% when operated at a cold side temperature of 573 K and 300 K which are 55% and 99% higher, respectively, than for SiGe at the same temperatures. The results also indicated that for higher density of skutterudite, the electrical power densities at the peak efficiency of the STUs were 39 and 109We/kg, whilst they were 92 and 232We/kg for SiGe at cold side temperatures of 573 K and 300 K, respectively. El-Genk and Saber (2006) also have investigated the use of skutterudite unicouples in the bottom array with SiGe unicouples in the top array, which has been proposed for cascaded thermoelectric modules (CTMs) for use in radioisotope power systems (RPSs) to generate electric power of 108 W_e and to achieve a net decrease of ~43% in the required amount of $^{238}PuO_2$. However, an operational issue with skutterudite-based unicouples is the sublimation of antimony from the legs near the hot junction at ~973 K. Such sublimation could change the thermoelectric properties of the material and degrade the unicouples' performance over time (El-Genk *et al.*, 2006).

The use of TEGs in commercial aerospace vehicles, which is expected to reduce fuel consumption by 0.5%, is also being explored by Boeing Research & Technology (Huang, 2009). As a rough estimate, this fuel savings, if implemented solely in the US, would save passenger and cargo airlines more than $12 million every month and reduce global carbon emissions by 0.03% (Kousksou *et al.*, 2011).

2.3.1.2 Automobile

Typically, the energy used in gasoline combustion engines breaks down into 25% for mobility, 30% in coolant, 5% in friction and parasitic losses, and 40% in exhaust gas (Figure 2.7). For diesel light-duty trucks using 100 kW of fuel power, this represents 30 kW of heat loss in exhaust gases (Champier, 2017). Converting this lost energy into electricity, even with efficiency of 3%, could represent 900W of electricity. According to the Fiat Research Centre, 800–1000 Wel means a reduction of 12–14 g/km CO_2 (Champier, 2017). The TEG can be used to convert heat energy to electricity to improve the total efficiency.

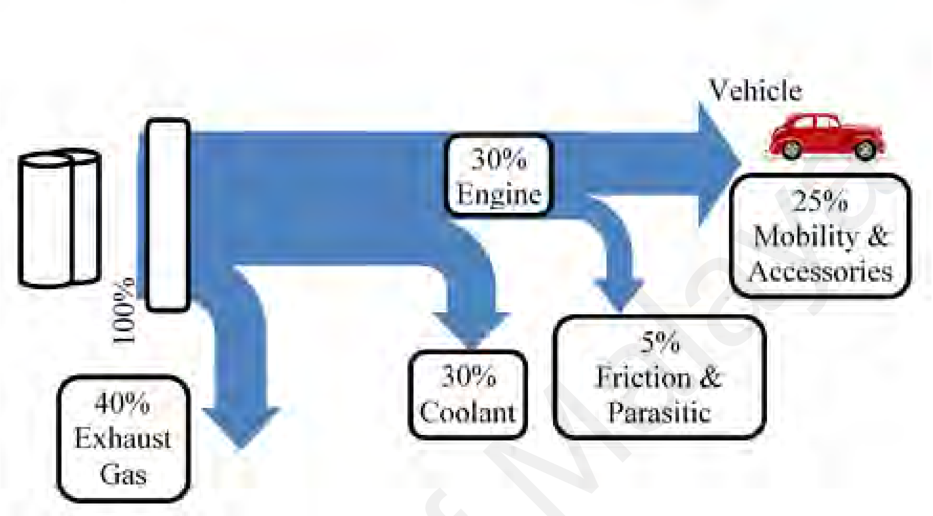

Figure 2.7: Energy flow for Vehicle with Gasoline-Fueled Internal Combustion Engines (Yang & Stabler, 2009).

The installation of a TEG on a vehicle must meet the following conditions (Champier, 2017); (i) The TEG should not change the operating point of the engine. The acceptable pressure losses are very limited (around a few tens of millibars). (ii) The maximum temperature of thermoelectric materials must be respected. In order to have a significant temperature difference, the TEG should be operated near its limits. Therefore, it is necessary to add control command including sensors and actuators to bypass part or all the hot gas. (iii) The materials must be recycled and environmentally friendly, and also the economic cost must be competitive.

Hsiao *et al*. (2010) have done the simulation of a thermoelectric module composed of thermoelectric generators and a cooling system which was purposed to enhance the efficiency of an internal combustion engine. The results showed that the maximum power of 51.13 mW/cm^2 was produced from the module at 563 K temperature difference and thermoelectric module presents better performance on the exhaust pipe than on the radiator. Karri *et al*. (2011) have investigated the power and fuel savings of a sports utility vehicle (SUV) and a stationary, compressed-natural gas-fueled engine generator set (CNG) which have the TEG in the exhaust steam for energy conversion. Two different thermoelectric materials, commercially available bismuth telluride (Bi_2Te_3) or quantum-well (QW) thermoelectric material are used. The results showed that the relative fuel savings for the SUV averaged around ~0.2% using Bi_2Te_3 and 1.25% using QW generators and for the CNG case using Bi_2Te_3 and using QW generators the fuel savings was around 0.4% and around 3%, respectively. The results also revealed that there were negative fuel gains in the SUV for parasitic losses and the dominant parasitic loss. Yu and Chau (2009) have purposed and implemented a thermoelectric waste heat energy recovery system (Figure 2.8), which uses maximum power point tracking to charge the electricity energy regulated by DC–DC C'uk converter, for internal combustion engine automobiles including gasoline vehicles and hybrid electric vehicles. The analysis and experimental results revealed that system can work well under different working conditions.

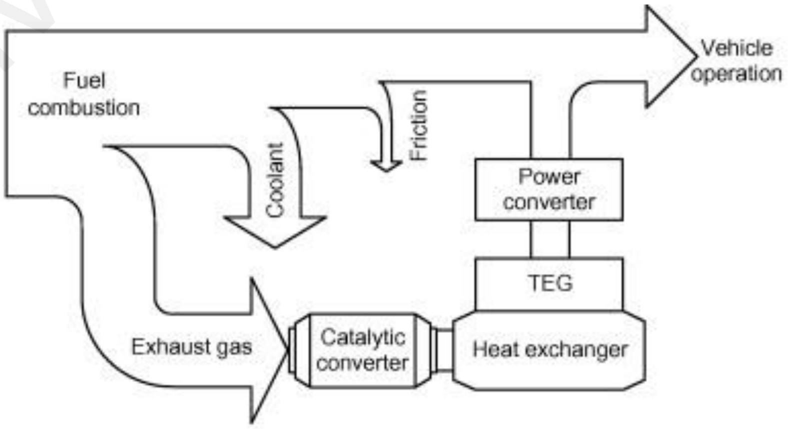

Figure 2.8: Waste heat energy recovery system for automobile (Yu & Chau, 2009).

2.3.1.3 Building

Zheng *et al*. (2014; 2013) have investigated the domestic thermoelectric cogeneration system (TCS) which can use an available heat sources in domestic environment to produce preheated water for home use and also generate electricity. The system can utilize the unconverted heat (over 95% of the total absorbed heat) to preheat feed water for domestic boiler by integrating the thermoelectric cogeneration with the existing domestic boiler using a thermal cycle. Electric, thermal, hydraulic and dynamic thermal responses have been evaluated to analyze the system performance. The results showed that the matched externally loaded electrical resistance which gave the maximum power output varies with the operating temperature due to the temperature dependent internal electrical resistance. The system can also be adopted to other sectors or areas, in which the combustion appliances are used and preheating is needed (He *et al.*, 2015).

2.3.1.4 Flexible devices

One distinct advantage of TEG is its flexibility, which makes it very effective to scavenge the low-grade waste heat to supply the electricity for small devices such as wearable electronics, wireless communication units and sensors (He *et al.*, 2015). Weber *et al*. (2006) have investigated the coiled-up thermoelectric micro power generator with the metal films sputtered on a thin polyimide foil, which intends to gain high voltages at a small generator area. Yu *et al*. (2008) have developed a kind of self-renewing photovoltaic and thermoelectric hybrid power source for sensor nodes. The whole system combined with solar cells, thermoelectric generators and heat sinks. The solar cell functioned as the heat sources for the TEG. The results showed that the photovoltaic and thermoelectric hybrid power source can refill the energy by itself. They recommended that structure is sufficient for the low-power electronics like a wrist-watch. Moreover, Wang *et al*. (2009) have evaluated a full-fledged wearable miniaturized TEG using poly-SiGe thermopile specifically engineered for human body applications. Later, Leonov *et al*. (2010) have investigated the hybrid wearable energy harvesters consisting of a thermoelectric generator and photovoltaic which were used to power two autonomous medical devices: an electroencephalography (EEG) system and an electrocardiography (ECG) system in a shirt.

Kim *et al*. (2014) have developed both *p*- and *n*-type fabric-like flexible lightweight materials by functionalizing the large surfaces and junctions in carbon nanotube (CNT) mats. The results showed that the optimized device design can independently supply the power for an electro-chromic glucose sensor without batteries or external power supplies, demonstrating self-powering capability. In the same year, Choi *et al*. (2014) have investigated the tellurium nanowire films hybridized with single-walled carbon nanotube as a flexible thermoelectric material. The results show that the excellent mechanical stability and the electrical conductivity enhance the flexibility of that material.

2.3.2 Thermoelectric cooling (TEC)

In comparison to the traditional refrigeration or heat supplying devices, TEC has many advantages such as solid-state, no vibration, simplicity and environmentally friendly. Current TEC applications can be categorized into the following application areas. Firstly as the cooling of small enclosures such as domestic and portable refrigerators, portable iceboxes, beverage can coolers and picnic baskets (David *et al.*, 2012; Min & Rowe, 2006). Secondly, medical applications (Putra *et al.*, 2010) such as laboratory and scientific equipment cooling for laser diodes or integrated circuit chips (Mansour *et al.*, 2006). Thirdly, TEC has attracted great attention for heat dissipation in electronic devices cooling and industrial temperature control (Chang *et al.*, 2009; Chein & Huang, 2004; He *et al.*, 2015; Zhu *et al.*, 2013), as well as automobile mini-refrigerators, thermoelectric cooler/heaters in car seats (Choi *et al.*, 2007; Lineykin & Ben-Yaakov, 2007) and automobile air-conditioning applications (Luo *et al.*, 2010; Miranda *et al.*, 2013). Furthermore, some researchers are in progress in making thermoelectric domestic air-conditioning systems (Cheng *et al.*, 2011; Gillott *et al.*, 2010) in hoping they can be compete with their vapor-compression counterparts. However, despite the advantages, the main disadvantages of TEC should also be considered such as its high cost and low energy efficiency (two or three times less efficient than a household refrigerator or air conditioner.). Riffat and Qiu (2004) compared performances of the thermoelectric and conventional vapor compression air-conditioners. Results showed that the actual coefficient of performance (COPs) of vapor compression and thermoelectric air-conditioners were in the range of 2.6-3.0 and 0.38-0.45, respectively. The low conversion efficiency have restricted the application of TEC in the case where the system cost and energy efficiency are less important than energy availability, system reliability and noise reduction during operation (Zhao & Tan, 2014).

2.4 Bismuth based thermoelectric materials

2.4.1 Bismuth – telluride thermoelectric materials

Bi_2Te_3 has been studied extensively since 1954 (Goldsmid & Douglas, 1954), and is one of the most widely used thermoelectric materials which is a narrow-gap semiconductor with an indirect gap of approximately 0.15 eV. Although it has been described the Bi_2Te_3 compound as a rhombohedra structure of the space group (*R3m*), it is easier to represent its structure by a hexagonal cell. The hexagonal cell is formed by the stacking of layers (Te1-Bi-Te2-Bi-Te1), stacked by van der Waals interactions along the *c*-axis in the unit cell (Figure 2.9). Bi_2Te_3 displays unique properties such as a high

Seebeck coefficient (~220 V/K), good electrical conductivity (~400 S/cm), and low thermal conductivity (~1.5 W/m K). It has a low melting temperature of 858 K and the room temperature band gap is 0.13 eV (Goldsmid, 2016). Bi_2Te_3 has gained a lot of attention due to its superior conversion efficiency near room-temperature (Du *et al.*, 2014b) and it has been proven that the Bi_2Te_3 bulk system possess $ZT = 1$.

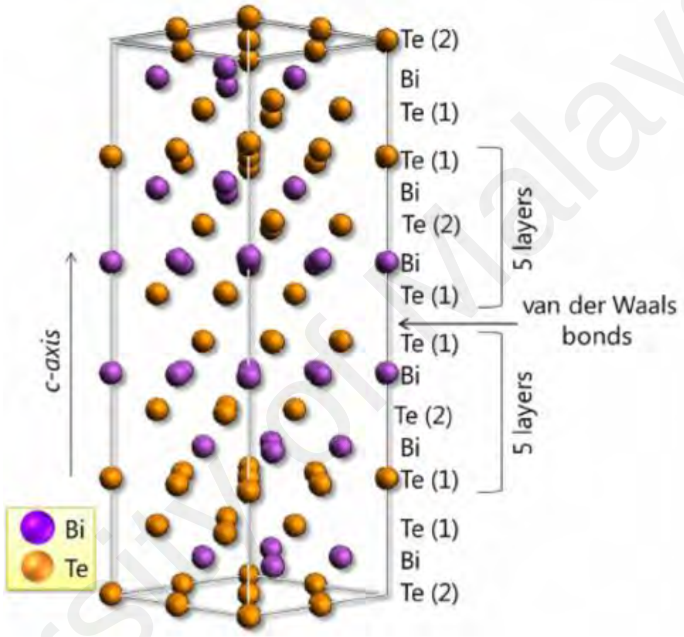

Figure 2.9: Crystal structure of bismuth telluride (Manzano *et al.*, 2016).

To date, many studies have been conducted either on Bi_2Te_3 or its compounds to improve their thermoelectric properties. The work of Tang *et al.* (2007) had prepared Bi_2Te_3 bulk material with a layered structure by melt-spinning and spark plasma sintering (SPS) processes. Under the applied synthesis method, they found an increase in electrical conductivity and a decrease in thermal conductivity when the rolling speed was increased. A maximum ZT of 1.35 was obtained at room temperature (Tang *et al.*, 2007). Cao *et al.* (2008) utilized a simple hydrothermal technique to synthesize *p*-type $(BiSb)_2Te_3$, where a $ZT \sim 1.47$ was achieved at 440 K. A nanostructuring approach was applied for synthesizing a *p*-type Bi_2Te_3 system by Xie *et al.* (2010). The nanostructuring system resulted in a low lattice thermal conductivity with no reduction in its electrical conductivity (α ~ 225 V/K, σ ~625 S/cm, and κ_{lat} ~0.5 W/m K), thus a high *ZT* of ~1.5 was obtained at 390 K (Xie *et al.*, 2010). This *ZT* value is about ~ 50% higher than the commercially available zone-melted materials (Xie *et al.*, 2010). The work of Nguyen *et al.* (2012) reported a *p*-type $Bi_{0.5}Sb_{1.5}Te_3$ bulk system containing nano grain architecture with grain size of 20–50 nm yielded a *ZT* of ~1.36 at 360 K. The presence of nano grain structure contributed to a significant reduction in thermal conductivity (~0.9 W/m K), thus resulted in those high *ZT* value.

In 2013, Puneet *et al.* (2013) studied a chemically exfoliated *n*-type Bi_2Te_3 2D sheets prepared by SPS and a *ZT* of ~0.95 was obtained at 300 K, which was higher than the ingot form (*ZT* ~0.6). The studies on Bi_2Te_3 by Yoon *et al.* (2013) have shown that *ZT* can be increased by decreasing the grain size and/or increasing the number of pores within the material. However, both can lead to a decrease in the thermal/electrical conductivity. Thus, proper control of the microstructure and relative density is needed to overcome this limitation. Moreover, the study on nanocomposites composed of ball-milled $(Bi_2Te_3)_{0.2}(Sb_2Te_3)_{0.8}$ dispersed with amorphous SiO_2 nanoparticles of ~50 nm size had been done. These materials showed a *ZT* of 1.12 and 1.27 at 303 and 363 K, respectively, which were higher than those of the undispersed $(Bi_2Te_3)_{0.2}(Sb_2Te_3)_{0.8}$ sample (Dou *et al.*, 2013). The power factor of $(Bi_2Te_3)_{0.2}(Sb_2Te_3)_{0.8}$ was increased and thermal conductivity was decreased due to the scattering of phonons at the phase boundaries and nanoparticles (Dou *et al.*, 2013).

Wu *et al*. (2014) studied the effect of doping rare earth elements, such as Ce, Y, and Sm, in $R_{0.2}Bi_{1.8}Se_{0.3}Te_{2.7}$, achieving a *ZT* of 1.21 at 413 K for $Y_{0.2}Bi_{1.8}Se_{0.3}Te_{2.7}$. The used of dopant atoms could reduce the electrical resistivity and concurrently provided the additional phonon-scattering centers for reducing the thermal conductivities (Wu *et al.*, 2014). Kim *et al*. (2015) studied the effect of dense dislocation on the thermoelectric performance of $Bi_{0.5}Sb_{1.5}Te_3$. This material exhibited a *ZT* of 1.86 at 320 K, which could be attributed to the combination effects of grain boundary, point defect, and dislocations generated in an excess of Te-rich melt-spun $Bi_{0.5}Sb_{1.5}Te_3$. The dislocations helpful in the reduction of thermal conductivity (~0.65 W/m.K) with minimizing charge-carrier scattering (Kim *et al.*, 2015).

Recently, Ge *et al.* (2018) introduced a dense dislocations by adding excess of Te into Bi_2Te_3 powder through the combination process of ball milling and SPS. During the high temperature SPS process, the excess Te spilled out of the die. The presence of dislocation enhanced the phonon scattering, thus decrease the lattice thermal conductivity. The highest *ZT* value of 0.7 at 398 K was obtained for a pure Bi_2Te_3 bulk sample which is 175% higher than that of pristine Bi_2Te_3 sample.

2.4.2 Bismuth – antimonite thermoelectric materials

Bismuth antimonite (BiSb) alloys are interesting from the physics point of view because they can exhibit semi metallic, semiconducting, or gapless characteristics, depending on the percentage of Sb, the strength of the applied magnetic field, the tension and temperature (Ibrahim & Thompson, 1985). They are also of interest from an applications point of view because the alloys with less than 20% Sb have the potential for efficient thermoelectric conversion (Ibrahim & Thompson, 1985).

Cadavid and Rodriguez (2005) studied the polycrystalline $Bi_{0.88}Sb_{0.12}$ samples grown by mechanical alloy using different milling time. They found that the enhancement of Seebeck coefficient close to −300μV/K in the samples under 45 hours of milling time.

The electrical resistivity showed a weak semiconductor behavior with the temperature and increased with milling time. The *ZT* reached values close to 0.3, which were characteristic values for single crystalline alloys. The work of Poudel *et al.* (2008) had synthesized an alloy composed of Bi and Sb and investigated the effect of alloying on its thermoelectric properties. The alloying process yields a *ZT* of ~1.4 for the Bi–Sb alloy (Poudel *et al.*, 2008).

Recently, the $Bi_{85}Sb_{15}$ samples which were prepared by mechanical alloying and hot isostatic pressing, followed by sever plastic deformation (SPD) has been studied by El-Asfoury *et al.* (2018a). SPD was applied by either equal channel angular extrusion (ECAE) or non-equal channel angular extrusion (NECAE). They found that the highest thermoelectric figure of merit (*Z*) value was achieved via NECAE at 423 K, and had a value of 0.39×10^{-3} K^{-1} at 250 K, which is 55% higher than that of the hot-pressed sample, 0.22×10^{-3} K^{-1} at 270 K. In other work of El-Asfoury *et al.* (2018b), they studied graphene (Gr) doped $Bi_{85}Sb_{15}$ system which was synthesized under ball milling and SPS. They found that the inclusion of Gr nanosheets refined the structures, and distributed throughout the grain boundaries and the matrix of the solid Bi-Sb composites. Those microstructures created more coherency, new interfaces and structural deformities in the matrix of Bi-Sb alloys. Thus, enhanced the electric conductivity simultaneously with Seebeck coefficient. The highest achieved *ZT* of 0.39 at 260 K was obtained for the sample with 0.5 wt% Gr, which was two times larger than that of the pristine sample (0.18 at 280 K).

2.4.3 Bismuth – sulfide thermoelectric materials

As the analogue of bismuth telluride, bismuth sulfide (Bi_2S_3) belongs to the same VA–VIA group compounds, possessing a similar layered structure as shown in Figure

2.10, and has an orthorhombic crystal structure (W. Hofmann, 1935). It has a direct band gap of 1.3 eV, which is much larger than that of Bi_2Te_3 (0.13 eV). Bi_2S_3 has been applied in photochemical, photo conductive, optoelectronic and MEMS (micro electro mechanical system) devices, as well as biochip and infrared detector (Killedar *et al.*, 2000; Tang *et al.*, 2010; Tang *et al.*, 2011; Ubale *et al.*, 2008). Recently, there are intensive studies on Bi_2S_3 as a potential tellurium free material for thermoelectric application as it exhibits a high Seebeck coefficient and low thermal conductivity at room temperature. The restriction for further improving its thermoelectric performance is its intrinsically high electrical resistivity (about two orders of magnitude higher than that of Bi_2Te_3 compounds).

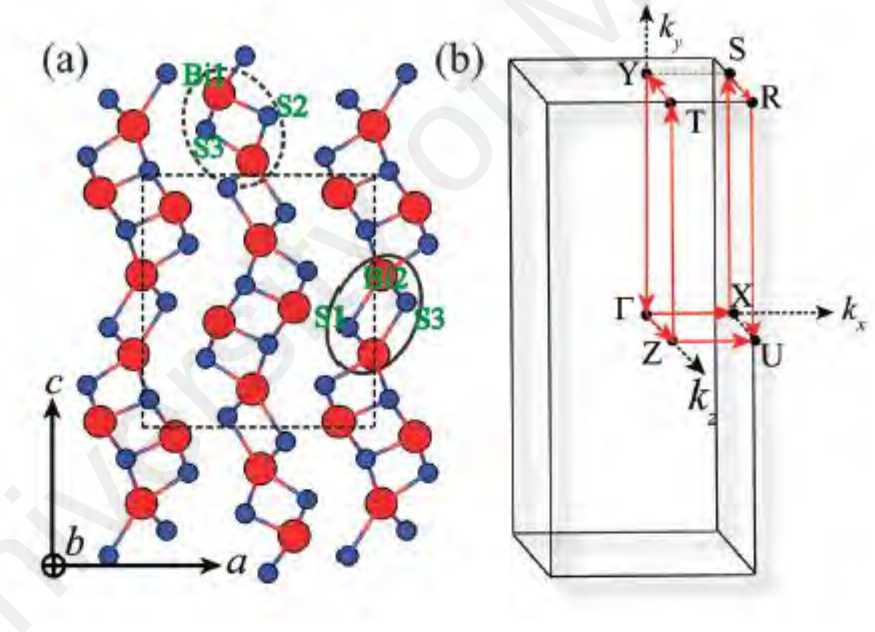

Figure 2.10: (a) crystal structure of Bi_2S_3 as viewed down the b-axis (xz plane). (b) The Brillouin zone for Bi_2S_3 unit cell (Pandey & Singh, 2016).

The studies on Bi_2S_3 was firstly done by Case (1917) which reported the photoconductivity of Bi_2S_3 in mineral samples. Later, Chen *et al.* (1997) reported the thermoelectric properties of Bi_2S_3 and they proposed that it could be a potential thermoelectric material as it shows high power factor and low thermal conductivity (<1 W/m.K). Furthermore, many studies have been conducted to improve the thermoelectric performance of Bi_2S_3, especially to decrease its electrical resistivity. These comprised different techniques, such as optimization of synthesizing process, nano-structuring, optimization of process parameters (e.g. the use of dopant atoms) and also the stoichiometry (Barma, 2016), and have been evaluated on the polycrystalline or bulk systems as well as the low dimensional system of Bi_2S_3.

The investigation on thermoelectric performance of Bi_2S_3 polycrystalline or bulks system was initiated by Mizoguchi *et al.* (1995). They successfully reduced the electrical resistivity of Bi_2S_3 crystals and bulk samples by vacuum annealing method. They found that sulfur deficiencies have significant effect on reducing the electrical resistivity of Bi_2S_3. Later, the work of Zhao *et al.* (2008) found that the electrical resistivity of Bi_2S_3 bulk could be decreased not only by fabricating a non-stoichiometric sample but also by texturing using a hot-forging method, and the textured $Bi_2S_{2.9}$ sample obtained a maximum *ZT* of 0.11. In 2011, the works of Ge *et al.* (2011b) and Yu *et al.* (2011) reported that controlling sulfur vacancies through optimization of the mechanical alloying process could improve the electrical transport properties, despite a concurrent increase in its thermal conductivity. Later, their work reported that fine tuning of the Cu content was able to reduce both the electrical resistivity and the thermal conductivity at the same time, and consequently enhance the thermoelectric performance of Bi_2S_3 (Ge *et al.*, 2012a).

Other works on elemental doped Bi_2S_3 bulk system have been also reported to improve its number of charge carriers and reduce the electrical resistivity. Elements such as silicon and germanium (Sterzel, 2006), selenium (Zhang *et al.*, 2013), antimony (Kawamoto & Iwasaki, 2014), zinc oxide (Du *et al.*, 2015), and bismuth chloride (Biswas *et al.*, 2012; Du *et al.*, 2014a) have been applied with various results. In 2015, Chmielowski *et al.*

(2015) reported a significant improvement for $BiCl_3$ doped Bi_2S_3 at a higher temperature of 700 K. The stability of $BiCl_3$-doped Bi_2S_3 against thermal stress and current stress was investigated, and it was found to be promising to be used in thermoelectric devices. They found that an optimum power factor above 500 $\mu V/m\ K^2$ at room temperature was achieved for 0.25 mol% of $BiCl_3$ doped compound and a higher *ZT* value of 0.6 at 700 K was reported (Chmielowski *et al.*, 2015). In the same year, the work of Liu *et al.* (2015) reported an enhancement on thermoelectric performance of *n*-type Bi_2S_3 by Br doping and Cu nanoparticles. The electrical conductivity was increased with Br doping and Cu intercalation. Because of the strong point defects produced by Br alloying and Cu nanoparticles, the lattice thermal conductivity of Bi_2S_3 with 1 mol. % CuBr was reduced by more than 50 %. A maximum *ZT* of 0.72 at 773 K was obtained for a 0.5 mol. % $CuBr_2$ doped sample parallel to the press direction, which is the highest *ZT* value ever reported for Bi_2S_3 system.

Recently, the relatively high power factor of 3.1 $mWcm^{-1}K^{-2}$ at 773 K was obtained for Bi_2S_3 polycrystalline sample doped with 1.0 mol% BiI_3 (Yang *et al.*, 2017). Furthermore, the thermal conductivity was also reduced moderately. As a result, a maximum *ZT* value of 0.58 was obtained, which is 4 times higher than that of pristine Bi_2S_3. The work of Guo *et al.* (2017) reported a simultaneous enhancement of electrical conductivity and Seebeck coefficient by electronic band structure engineering due to Sn doping. A single orthorhombic bulk materials were prepared by combining solvothermal method with microwave sintering. It was found that Sn^{4+} as a dopant element increased the electrical conductivity due to tuning carrier concentration (*n*) and simultaneously “stabilized” the Seebeck coefficient, which is probably ascribed to the effect of resonant level doping. The maximum *ZT* of 0.67 at 673 K was recorded for of $Bi_{1.985}Sn_{0.015}S_3$.

The initial study on low dimensional systems of Bi_2S_3 for thermoelectric application was conducted by Yang *et al.* (2013). They reported that the Bi_2S_3 nanowires with lengths up to 20 μm and high crystallization are obtained by a modified composite molten salt method. The low resistivity of the Bi_2S_3 nanowires film was a result of the high carrier concentration and high carrier mobility due to the high orientation degree and better crystallization (Yang *et al.*, 2013). Furthermore, the introduction of many interfaces from smaller size of grains, which scatter phonons more effectively than electrons, or serve to filter out the low-energy electrons at the interfacial energy barriers, allows the enhancement of Seebeck coefficient. Thus, result in a higher power factor of 63.01 $\mu W/mK^2$ for the Bi_2S_3 nanowires. Recently, the studied from Tarachand *et al.* (2016) on the nanostructured $Bi_{2-x}Cu_xS_3$ ($x = 0.1–0.4$) samples, which were successfully synthesized by a simple polyol method found that the rod-like structure of Bi_2S_3 (Figure 2.11) appeared to play a very important role in achieving a high Seebeck coefficient. The absolute value of the Seebeck coefficient decreased with increasing Cu doping. Consequently, an enhancement in the figure of merit of 34% was observed for the $Bi_{1.6}Cu_{0.4}S_3$ sample as compared to undoped Bi_2S_3 at 300 K (Tarachand *et al.*, 2016).

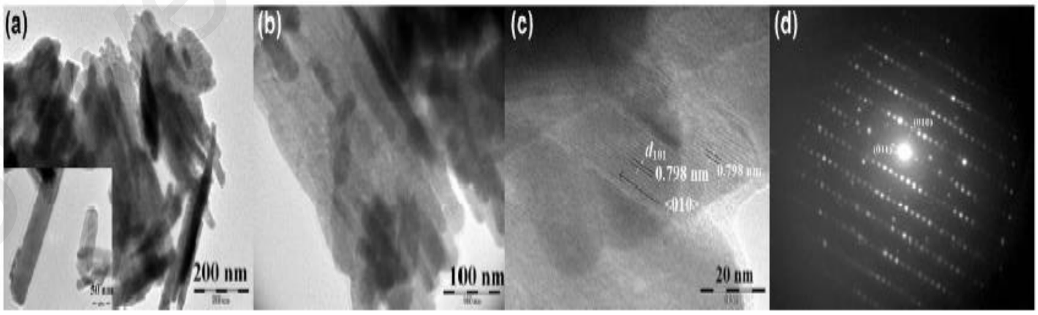

Figure 2.11: (a), (b), and inset of (a) Transmission electron microscopy images of Bi_2S_3 nanorod at different magnifications. (c) HRTEM image and (d) SAED pattern of nanorods (Tarachand *et al.*, 2016).

In summary, bismuth (Bi) based semi conducting alloys are well known for their good thermoelectric properties. Bismuth telluride (Bi_2Te_3) is efficient at room temperature and commonly used for Peltier refrigeration, but its efficiency dramatically decreases at low temperature. Bi-Sb alloys are the best thermoelectric materials for applications under 200 K. The potential of Bi-Sb single crystals for refrigeration near nitrogen liquid temperature has been largely considered. In the past several years, Bi_2S_3 has attracted extensive attention as promising thermoelectric materials owing to its low cost, abundance, and low toxicity. However, problems, such as low thermoelectric performance and stability, must be intensively studied and resolved.

2.5 Dopant selection for high performance bismuth – sulfide based thermoelectric materials

To overcome the optimization mentioned in section 2.2, a good thermoelectric material should have distinct regions serving different functions of power factor (electronic transport) and thermal conductivity. A high crystallinity or highly ordered region (electron-crystal region) is responsible for the electron transport to improve Seebeck coefficient, α, and electrical conductivity, σ, and a disorder region (phonon-glass region), normally is responsible for phonon scattering to reduce thermal conductivity, κ (Snyder & Toberer, 2008). The disorder region for phonon scattering can be achieved through interstitial sites, partial occupancies or rattling atoms.

Bi_2S_3 has a notable low intrinsic carrier concentration of which lies around $2x10^{18}$ cm^{-3}, which is two orders of magnitude below what can be achieved in Bi_2Te_3 ($10^{20}cm^{-3}$) (Chmielowski *et al.*, 2015; Rowe, 1995). The low intrinsic carrier concentration makes it necessary to extrinsically dope Bi_2S_3. The dopant atoms in Bi_2S_3 system are predicted to substitute the host atoms (Bi or S sites) in the electron-crystal region without disturbing the phonon scattering sites.

2.5.1 Hume – Rothery rules

As a set basic rules describing the conditions under which an element could dissolve in a metal to form a solid solution, the Hume-Rothery rules have earned a great reputation in the field of materials science as simple but powerful guides to be considered when designing a new alloy (Mizutani, 2016). A rules were established in the 1920s and 1930s by the efforts of Hume-Rothery (1899-1968) and his associated, as well as other crystallographers and physicists. Below are the criteria for the formation of a complete soluble substitution solid solution under Hume Rothery rules (Mizutani, 2016):

1. The percentage different in size (atomic radii) between the dopant atoms and the host atoms must be less than 15%.
2. Difference in electronegativity between the dopant atoms and the host atoms should be as small as possible.
3. For complete solubility, the valences of solute and solvent are the same.
4. Dopant atom element and host atom element should have the same crystal structure.

2.5.2 Candidate dopants

Considering the Hume-Rothery rules for the formation of substitutional solid solutions-complete solubility, the properties of potential dopants for Bi_2S_3 based thermoelectric material were listed in Table 2.1. Nickel, zinc, tin, hafnium and antimony are suitable dopants to be used on Bi site and their properties are in well agreement with the Hume Rothery rules. Less than 12 % difference in size when compared to the host atom (Bi), and the difference in electronegativity between the dopant and host atom is significantly small to avoid the formation of compound instead of solid solution. There are the differences in valence and crystal structure for the chosen dopants with host atom (Bi). However, based on the previous works on Ag- and Cu- doped Bi_2S_3 system as also inserted in Table 2.1, those differences can be acceptable.

Table 2.1: Properties of Dopants.

Dopants	Atomic size (nm)	% Different in size with host atom	Electronegativity (Pauling scale)	Valence	Crystal structure
Bismuth, Bi	0.143	-	2.02	5	Base Centered Monoclinic
Sulfur, S	0.088	-	2.58	6	Face Centered Orthorhombic
Silver, Ag	0.165	15.4	1.93	1	Face Centered Cubic (FCC)
Copper, Cu	0.145	1.4	1.90	2	Face Centered Cubic (FCC)
Chloride, Cl	0.079	-10.22*	3.16	5	Base Centered Orthorhombic
Antimony, Sb	0.133	6.99	2.05	5	Simple Trigonal
Nickel, Ni	0.149	4.2	1.91	2	Face Centered Cubic (FCC)
Zinc, Zn	0.134	- 6.29*	1.65	2	Hexagonal Close Packed (HCP)
Hafnium, Hf	0.159	11.19	1.3	4	Hexagonal Close Packed (HCP)
Tin, Sn	0.140	-2.098	1.96	2	Tetragonal Face Centered Diamond Cubic

*negative means the size of dopant atom is small than host atom.

CHAPTER 3: METHODOLOGY

3.1 Introduction

This chapter reviews in detail all the applied experimental steps including the synthesize process and materials characterization techniques used in this work in order to comprehensively study Bi_2S_3 bulk system as thermoelectric material. All processes are presented sequentially as a flow chart in Figure 3.1.

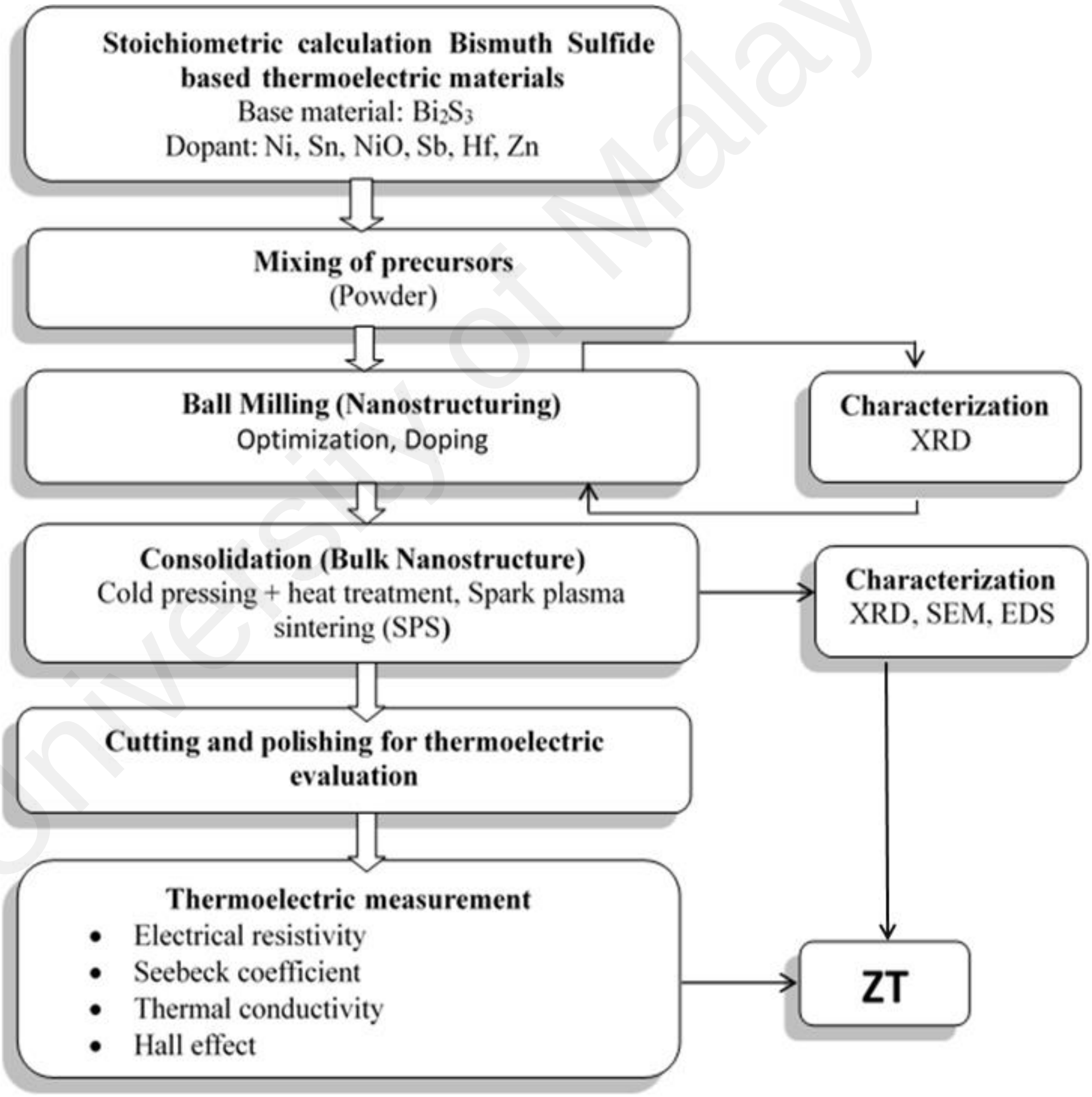

Figure 3.1: Flowchart of experimental procedures.

3.2 Synthesis of bismuth – sulfide based thermoelectric material

3.2.1 Powder materials

In this research, the commercial high purity powders of Bi (99%, -100 mesh, Sigma Aldrich), Zn (99.9%, -325 mesh, Strem Chemical), Ni (99.9%, <150 µm, Sigma Aldrich), S (99.5%, -325 mesh, Alfa Aesar) , Sn (99.5%, -325 mesh, Strem Chemical), Sb (99.7%, -100 mesh, Alfa Aesar), and Hf (>99.9 wt%, 200 mesh, Strem Chemical) were used as the starting materials. Either a single doped or double doped Bi_2S_3 systems were evaluated. The starting materials were weighed out in a stoichiometric atomic ratio of nominal composition as shown in Table 3.1. For optimization of ball milling process, Bi, Zn and S powders were used according to the stoichiometric formula of Bi_2ZnS_4. While for studying the effect of porosity samples, $Bi_{2-x}Ni_xS_3$ ($0 \leq x \leq 0.07$) powders were used as starting powders.

Table 3.1: The type of sample and compositions.

Formulation	No	Composition	Formulation	No	Composition
$Bi_{2-x}Ni_xS_3$	1.	Bi_2S_3	$Bi_2S_3 + x\ NiO$	1.	Bi_2S_3
	2.	$Bi_{1.995}Ni_{0.005}S_3$		2.	$Bi_2S_3 + 0.5\ NiO$
	3.	$Bi_{1.99}Ni_{0.01}S_3$		3.	$Bi_2S_3 + NiO$
	4.	$Bi_{1.97}Ni_{0.03}S_3$		4.	$Bi_2S_3 + 1.5\ NiO$
	5.	$Bi_{1.95}Ni_{0.05}S_3$	$Bi_{0.95}SbX_{0.05}S_3$	1.	Bi_2S_3
	6.	$Bi_{1.93}Ni_{0.07}S_3$		2.	$Bi_{0.95}SbNi_{0.05}S_3$
$Bi_{2-x}Sn_{3x}S_3$	1.	Bi_2S_3		3.	$Bi_{0.95}SbHf_{0.05}S_3$
	2.	$Bi_{1.99}Sn_{0.03}S_3$		4.	$Bi_{0.95}SbZn_{0.05}S_3$
	3.	$Bi_{1.98}Sn_{0.06}S_3$		5.	$Bi_{0.95}SbSn_{0.05}S_3$
	4.	$Bi_{1.9}Sn_{0.3}S_3$			

3.2.2 Mechanical alloying/ball milling technique

Recently, the use of mechanical alloying technique (MA), in particularly high energy ball milling (BM) has attracted much attention to synthesize nanoparticle powders as it is a simple process. In BM, elemental powders or intermetallic compounds are loaded into a milling container with balls which can be made from stainless steels, tungsten carbides and zirconia (Kurlov & Gusev, 2007). The containers are then loaded into a high energy ball milling machine. Normally, powders are milled under the argon atmosphere to prevent oxidation during the BM process. The powders will be subjected to a series of impact collisions between the ball to ball, and ball to the wall (Figure 3.2(a)). During ball milling, the powders are constantly cold-welded and fractured which will lead to the formation of nanostructured domains (Suryanarayana, 2001).

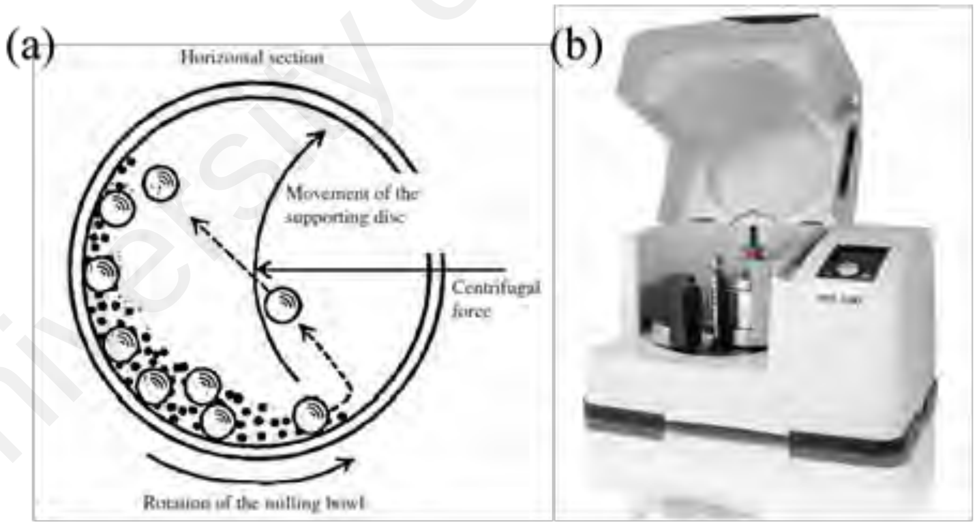

Figure 3.2: (a). A schematic illustration of the ball milling process (Suryanarayana, 2001), (b) planetary ball milling machine (PM100).

As the first step, a series of BM experiments were designed to optimize the milling duration to achieve desired Bi_2S_3 phase. Milling duration was optimized by performing from 2 to 35 hours of milling, while the other parameters fixed for each sample. After milling process completed, the sample was collected for crystal structure analysis using X-ray diffraction (XRD) technique.

For all processes, the stoichiometric powders (8 gm) where loaded into stainless steel vial (125ml) with stainless steel balls (Ø10mm) and the weight ratio of ball to powder was kept at 15:1. Loading and unloading of powders were operated in a glove-box filled with argon atmosphere to avoid the oxidization process. To create argon atmosphere in the glove box, the glove box was evacuated using a vacuum pump and filled by argon gas consecutively for three times. The vial where placed into a planetary ball mill (PM-100, Retsch, Germany, Figure 3.2(b)) with 300 rpm of speed. To avoid the cold welding, the milling process condition was fixed: running every 10 min and break for 5 min. After milling process completed, the powder were subjected to the consolidation process.

3.2.3 Consolidation process

3.2.3.1 Cold pressing following with heat treatment process

A cold-pressing method is chosen if the densification of powder materials is carried out at or very near room temperature. In this method, the synthesized powders are loaded into a die (usually stainless steel) with the application of hydrostatic pressures. After pressing, the green compacted pellet is then heated to about 70% of its theoretical melting point in order to complete the consolidation of nanopowders (Fitriani *et al.*, 2016). In this work, the MA-treated powders were cold pressed under a uniaxial stress of 375 MPa for 5 minutes in a cylindrical high strength stainless steel die with an internal diameter of 10 mm. Then, the compacted samples with dimension of Ø10mm x 2mm (approx.) subjected to the sintering process by using Mila 5000 furnace (Ulvac-Riko, Japan) to complete the consolidation of nano-powders. The sintering process was conducted in a ~ 5 Pa vacuum condition, from room temperature to various temperatures (in between 523 – 673 K) with the heating rate of 4°C/min. The variation of temperatures were done for evaluating the effect of sintering temperature in the Bi_2S_3 phase formation. The temperature was then held at the studied temperature for 1 hour, after which the sample was left to cool naturally to room temperature. Figure 3.3 shows a schematic illustration of cold-pressing followed with the sintering process.

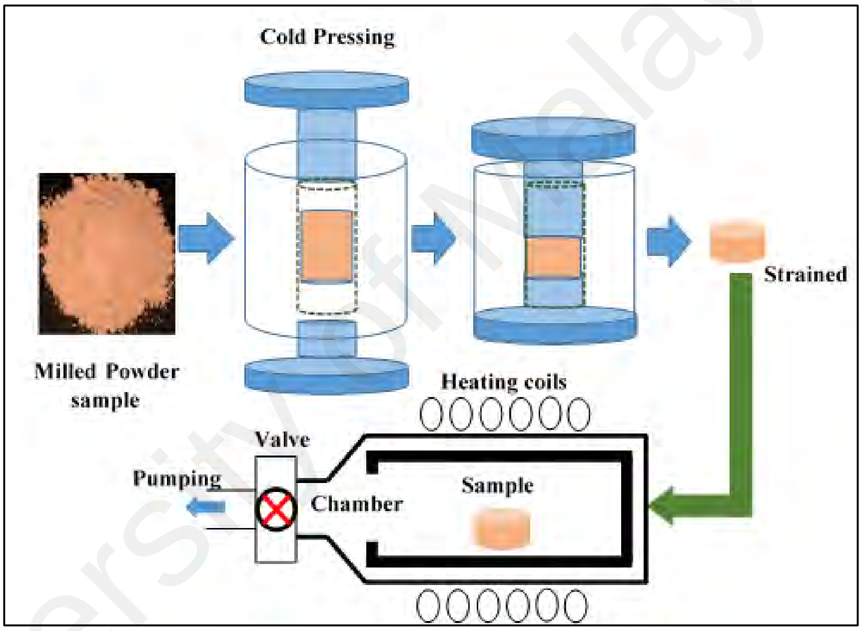

Figure 3.3: A Schematic illustration of cold-pressing followed with sintering process. This figure is adapted from Jung *et al.* (2014).

3.2.3.2 Spark plasma sintering process

The spark plasma sintering (SPS) process involves the sintering of powders under the simultaneous influence of a current and pressure (Munir *et al.*, 2006). SPS has often been considered as a good technique owing to their advantages which include: lower sintering temperature, shorter holding time, and marked comparative improvements in properties of materials consolidated (Munir *et al.*, 2006). Lower temperatures and shorter holding times have made it possible to sinter nanometric powders to near theoretical values with little grain growth (Anselmi-Tamburini *et al.*, 2004a; Anselmi-Tamburini *et al.*, 2004b; German, 2013).

In this work, the pretreated powders by MA were charged directly into an Ø 10 mm graphite die. To facilitate the release of samples from the mold, the inner of graphite die was lined with graphite sheet. Then, the powder samples were consolidated into compact bulk materials using SPS machine (Dr. Sinter 515S SPS) as shown in Figure 3.4. The SPS was conducted at 673 K for 5 min under a mechanical pressure of 50 MPa in vacuum system to obtain a higher dense material. The detail temperature profile for SPS process is presented in Figure 3.4(b).

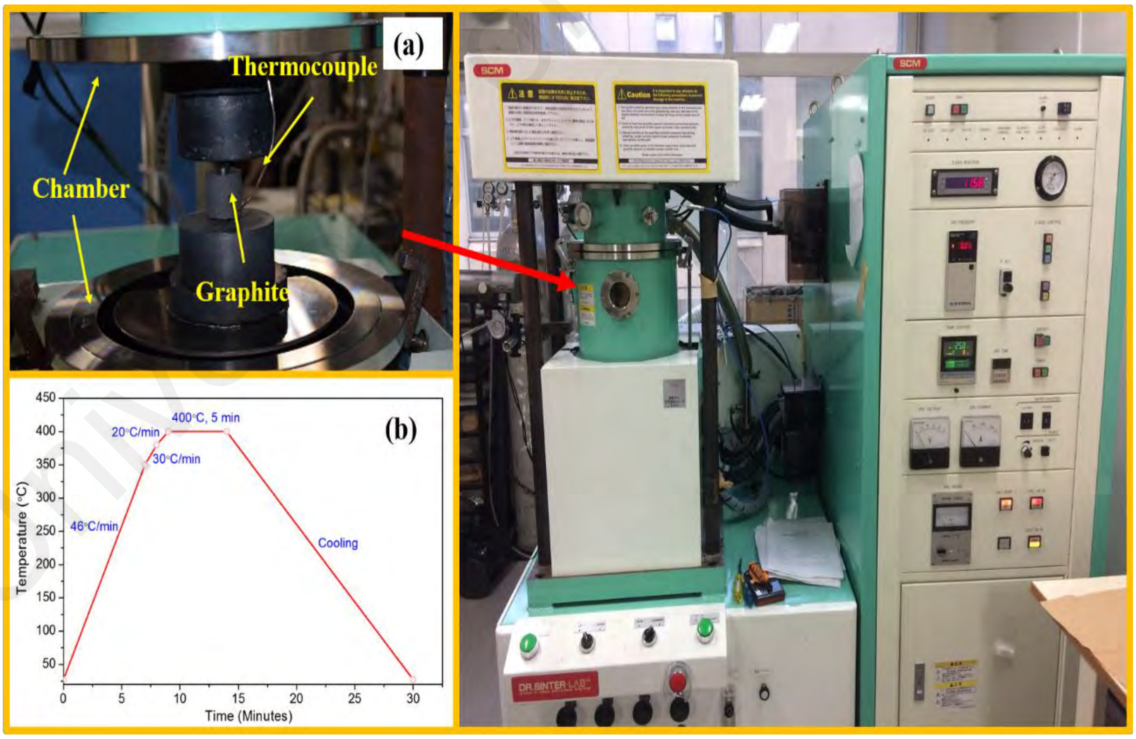

Figure 3.4: Spark plasma sintering (SPS) system; (a) graphite die inside the chamber, and (b) temperature profile for SPS process.

3.2.4 Sample preparation for thermoelectric evaluation

After consolidation process, the produced disk-shape bulk samples were cut by a low-speed diamond saw followed with manually ground into quadratic prisms with an average size of 2 mmW×2 mm D×7 mm L ~ 4 mmW×4 mm D×9 mm L mm (all surfaces pairwise parallel to each other) for electric resistivity and Seebeck coefficient measurements. Silicon carbide (SiC) sandpaper was used to grind the samples with grit size in a sequence of 800, 1200, 2400 and 4000. Whilst, the actual size of disk-shape bulk samples with high precision were maintained as this a requirement for the thermal conductivity measurement. The disk-shape bulk samples were also used for others characterization process; XRD, SEM-EDS and Hall Effect.

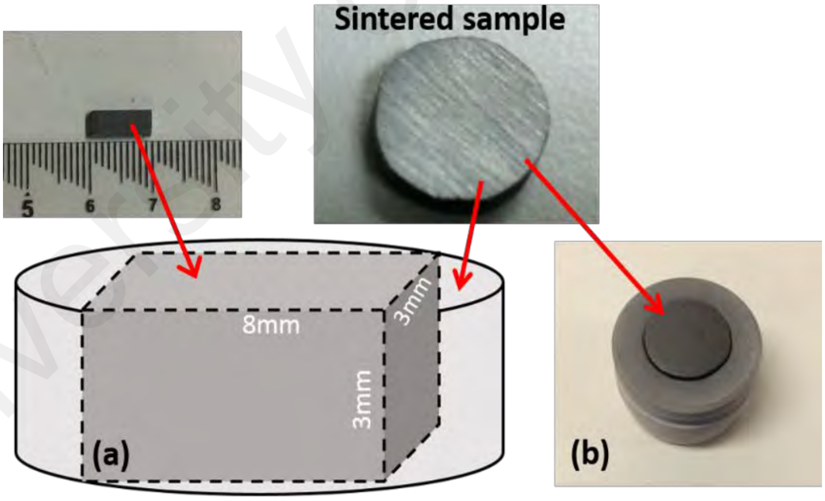

Figure 3.5: Sintered sample prepared for thermoelectric measurements; (a) rectangular bar shape for electrical resistivity and Seebeck coefficient, (b) thermal conductivity.

3.3 Microstructural analysis

3.3.1 X-ray powder diffraction (XRD)

X-ray diffraction (XRD) is a rapid analytical to obtain crystallographic information of materials. It is a non-destructive, reproducible and fast characterization technique to identify crystalline phases and orientation. It usually use to determine structural properties such as crystallite size, lattice parameters, grain size, phase composition, atomic arrangement etc. (Hossain, 2015). The interaction of the incident beams with the sample produces diffracted beams that satisfies the Bragg's law, which relates the wavelength of electromagnetic radiation (λ) to the diffraction angle (θ) and the lattice spacing in a crystalline sample (d):

$$n\lambda = 2d\sin\theta \tag{3-1}$$

As illustrated in Figure 3.6, all possible diffraction patterns of the lattice is obtained by scanning the sample through a range of 2θ angles due to the random orientation of the material. The important atomic and molecular structure of the crystal can be acquired by analyzing the position, shape and intensity of the diffraction peaks.

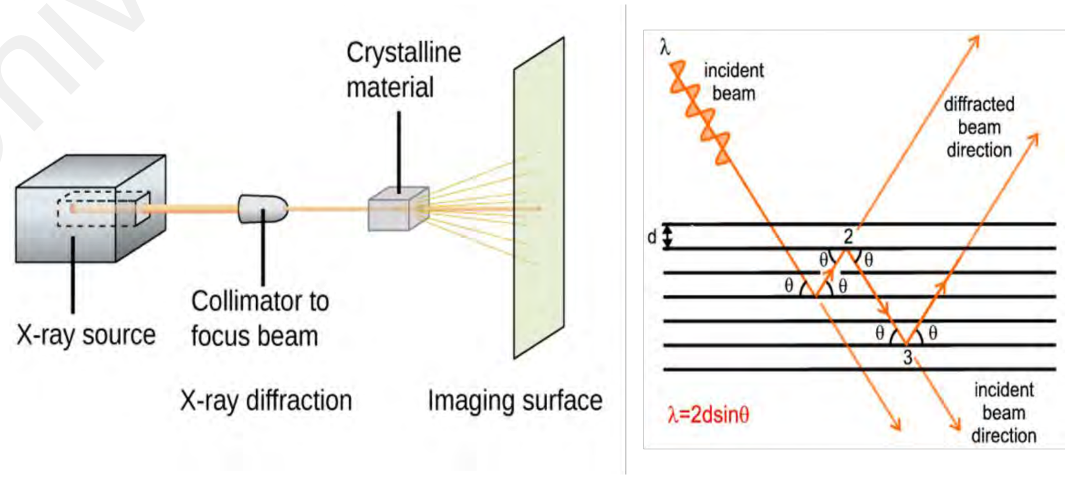

Figure 3.6: Basic working Principle of X-Ray Diffraction.

In this research, XRD measurements for milled powder and/or compacted samples were performed on a PANalytical diffractometer, a computer controlled system (EMPYREAN). The XRD system was operated in the vertical angle of θ-2θ configuration using Cu-$K\alpha$ radiation (1.54060Å) which was generated at 45 kV and 40 mA. The step increment for sample was 0.026° for counting times of 1 second. XRD was primarily used to identify the Bi_2S_3 and other phases, the lattice constant, and the crystallite size either for milled powder or bulk samples. The crystallite size was estimated by analyzing XRD patterns with the Scherrer's equation:

$$\text{Crystallite size} = \frac{0.9\,\lambda}{B\ \text{Cos}\ \theta} \tag{3-2}$$

where B is the half-height width of the reflection peak at 2θ and λ is the wavelength of the radiation.

The Rietveld refinement method using JANA 2006 program (Petříček *et al.*, 2014) was used for refining the structural parameters (lattice parameter, Bi atoms positions) and for analyzing the dopant atoms site distribution in Bi_2S_3 structure. The crystal structure plotted after refinement will clarify that dopant atoms were successfully substituted Bi site or enter other sides. The initial input parameters for elemental doped Bi_2S_3 samples were assumed to be the same as those obtained for Bi_2S_3 reference (PDF 98-015-3946) with dopant atom substituted Bi (1) position in the 4c (0.43, 0.25, 0.47) and Bi (2) position in the 4c (0.02, 0.25, 0.68). The results of the Rietveld refinement demonstrated the error range of data calculated by JANA2006 were less than 1%.

3.3.2 Scanning electron microscopy (SEM)

A scanning electron microscope (SEM) is a type of electron microscope that images a sample by scanning it with a high-energy beam of electron in a raster scan pattern. The SEM was assessed as early as 1935 by Knoll (Gilfrich, 1993), i.e. at about the same time and by the same research group as the conventional TEM. The electrons interact with the atoms that make up the sample producing signals that contain information about the surface topography, composition, and other properties. In detail, the basic working principle of SEM as follow (Hossain, 2015): a beam of incident electrons is generated by a suitable source in an electron column above the sample chamber (presented in Figure 3.7). Depending on the evaluation objectives, the energy of the incident electrons may vary from 100eV up to 30 keV. The generated electrons are focused into a small beam by a series of electromagnetic lenses in the SEM column. Scanning coils near the bottom of the column directed and positioned the focused beam onto the sample surface. The incident electrons cause electrons to be emitted from the sample due to elastic and inelastic scattering from the sample's surface and near surface material. High energy electrons that are ejected by an elastic collision of an incident electron are referred to as backscattered electrons. Back scattered imaging mode provides an image contrast as a function of elemental composition, as well as, surface topography. Emitted lower energy electrons resulting from inelastic scattering are referred as secondary electrons. The SEM column and sample chamber are maintained at a moderate vacuum to allow the electrons to travel freely from the electron beam source to the sample and then to the detectors. Imaging of non-conductive, volatile, and vacuum-sensitive samples can be performed at higher pressures.

In this work, the microstructural analysis of the investigated samples were performed on Zeiss Auriga FIB-SEM which integrated with an energy-dispersive X-ray spectroscopy (EDS). The crystallinity, composition, homogeneity and distribution of the dopant atoms and grain boundaries were studied.

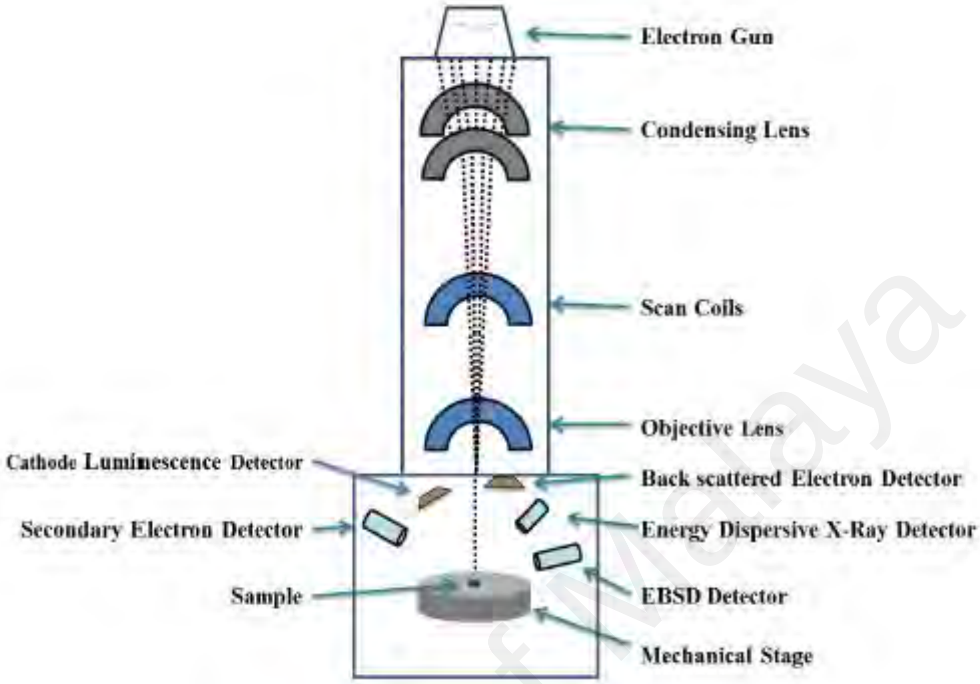

Figure 3.7: Schematic diagram of a typical Scanning Electron Microscope. (Goldstein *et al.*, 1981).

3.3.3 Energy dispersive X-ray spectroscopy (EDS)

EDS is an analytical technique used for the elemental analysis or chemical characterization of materials. Backscattered electron images in the SEM display compositional contrast that results from different atomic number elements and their distribution. EDS allows to identify what those particular elements are refer to and their relative proportions (atomic % or weight %). EDS relies upon X-ray spectrum emitted by a solid sample bombarded with a focused beam of electrons to obtain a localized chemical analysis. All elements from atomic number 4 (Beryllium, Be) to 92 (Uranium, U) can be detected, though not all instruments are equipped for 'light' elements (atomic number, Z < 10). Qualitative analysis (identification of the elements present) refers to the identification of the lines in the X-ray spectrum. Quantitative analysis (measuring the concentrations of the elements present) entails measuring line intensities for each element in the sample and for the same elements in calibration standards of known composition. By scanning the beam in a television-like raster and displaying the intensity of a selected X-ray line, element distribution images or 'maps' can be produced. Furthermore, those produced images reveal the surface topography or mean atomic number differences according to the mode selected. In this work, the elemental composition of the microstructures were obtained on polished surfaces samples (final polishing with 1µm diamond suspension).

3.4 Thermoelectric transport properties measurements

3.4.1 Simultaneous measurement of electrical resistivity (*ρ*) and Seebeck coefficient (*α*)

The electrical resistivity, ρ, and the Seebeck coefficient, α, were measured simultaneously using four-probe and differential methods respectively with commercially available high temperature ULVAC-RIKO ZEM-3 system. The schematic view of equipment is shown in Figure 3.8. The rectangular bar sample was positioned between the upper and lower block of the furnace. After the sample was heated to a certain temperature, the lower block was heated to create a temperature difference. The Seebeck coefficient was determined by measuring the upper and lower temperatures T_H and T_L with the thermocouples pressed against the side of the sample followed by measuring the voltage difference (ΔV) between those two points of contacts. The resistance, R, was determined by the DC four point method, where a constant current I was supplied to both ends of the sample. The voltage drop dV between the two probes was then measured to obtain $R = \mathrm{d}V/I$.

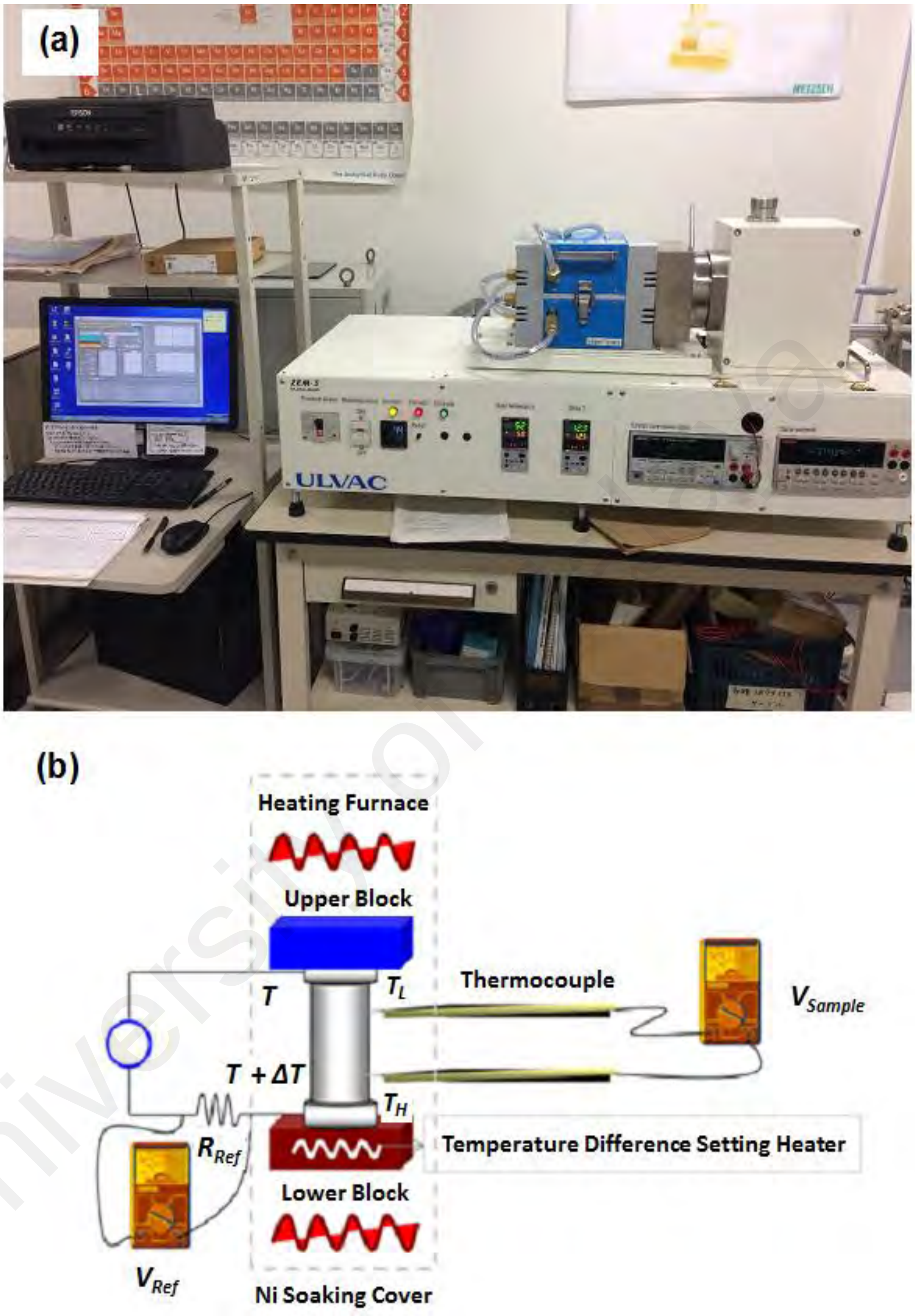

Figure 3.8: (a) Commercial ZEM-3 system device, (b) Schematic diagram of the four probe measurement in ZEM-3 system ULVAC ZEM-3 in helium atmosphere (Kim, 2013).

The Seebeck coefficient and resistivity were calculated as:

$$\alpha = \frac{\Delta V}{\Delta T} = \frac{(V_H - V_L)}{(T_H - T_L)} \tag{3-3}$$

$$\rho = R\frac{A}{l} \tag{3-4}$$

where R is the sample resistance, A is the cross sectional area of the sample, and l is the distance between the probes. The measurement temperature range was from RT to 573 K and 623 K for cold pressed and SPSed samples, respectively. Inert atmosphere was maintained inside the furnace using –0.9 MPa Helium gas during the measurement.

3.4.2 Thermal conductivity

The thermal properties of the bulk samples can be measured by laser flash method (LFA), which was introduced by Parker *et al.* (1961). The LFA investigations generally take much less time than thermal conductivity measurements by means of guarded hot plate (GHP), heat flow meter (HFM) or thermal conductivity tester (TCT). A typical apparatus of LFA is shown in Figure 3.9. The sample was heated and held at a specific temperature under N_2 flow. When the temperature reached a stable condition, the lower surface of the sample was first heated by a short energy pulse (Figure 3.9(b)). The resulting temperature change on the upper surface of the sample was then measured with an infrared detector. The typical resulted signals is presented in Figure 3.9(c) (red curve).

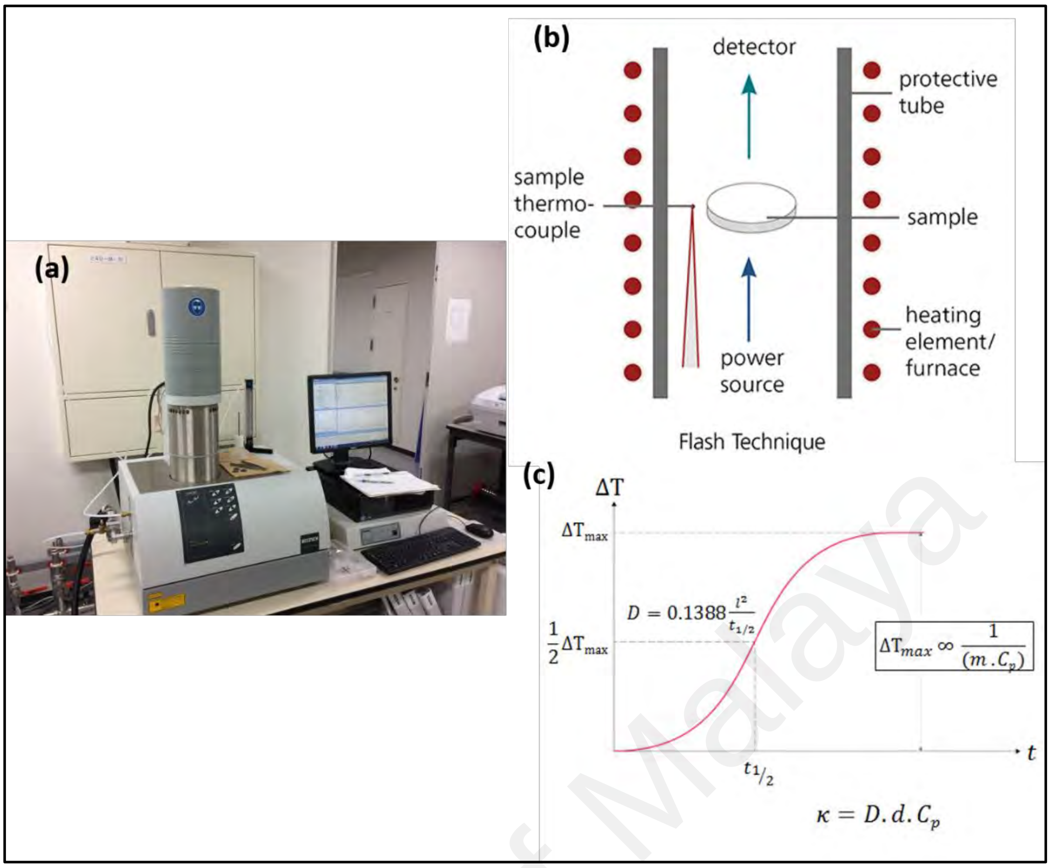

Figure 3.9: (a) LFA 457 instrument for thermal conductivity measurement, (b) and (c) schematic view of the laser flash method.

In the complete absence of heat loss from the sample, the temperature would rise monotonically to a limiting value. In a real situation, the measured temperature will peak and then return to ambient temperature. The time required to reach one-half of the peak temperature at the rear face of the specimen, $t_{\frac{1}{2}}$ can be used to determine diffusivity (*D*) according to (Rowe, 1995):

$$D = \frac{0.1388 l^2}{t_{\frac{1}{2}}} \tag{3-5}$$

The thermal diffusivity is related to the thermal conductivity as equation below:

$$\kappa = D\ d\ C_p \tag{3-6}$$

where κ is the thermal conductivity of the specimens, d is the experimental density , and C_P is the heat capacity. Furthermore, the C_P of solids can be determined using the signal height (ΔT_{max}) compared to the signal height of a reference material.

In this work, LFA 457 instrument (NETZSCH) with a cylindrical pellet sample of Ø 10 mm and the thickness of ~ 2 mm was used for the measurement. To minimize the laser reflection, both surfaces of the sample was coated by graphite spray. The D value was directly measured and Cp was indirectly derived using standard sample (pyroceram). The densities (d) of the samples were measured by Archimedes method using electronic densimeter apparatus (Alfa Mirage, MDS-3000).

3.4.3 Carrier concentration and mobility

The Van der Pauw method (Van der Pauw, 1958) is one of the most utilized measurement methods for the evaluation of electrical properties in semiconductor materials such as resistivity, carrier density, and mobility. In general, this method can be used to calculate samples of arbitrary shape, although several basic sample conditions must be satisfied to obtain accurate measurements, such as the thickness of the sample must be constant, point contacts placed at the edges of the samples must be used for the measurements, and the sample quality has to be homogeneous. In this work, the prepared bulk samples were analyzed by using Hall measurements in Van der Pauw configuration (ECOPIA HMS-3000, see Figure 3.10) at room temperature. The sample shape was cylindrical with Ø 10 mm and the thickness of ~ 2 mm, and probes were contacted on four corners of the surface of the sample through ohmic contacts. The Hall parameters such as carrier concentration, Hall mobility of the material, and Hall coefficient were determined.

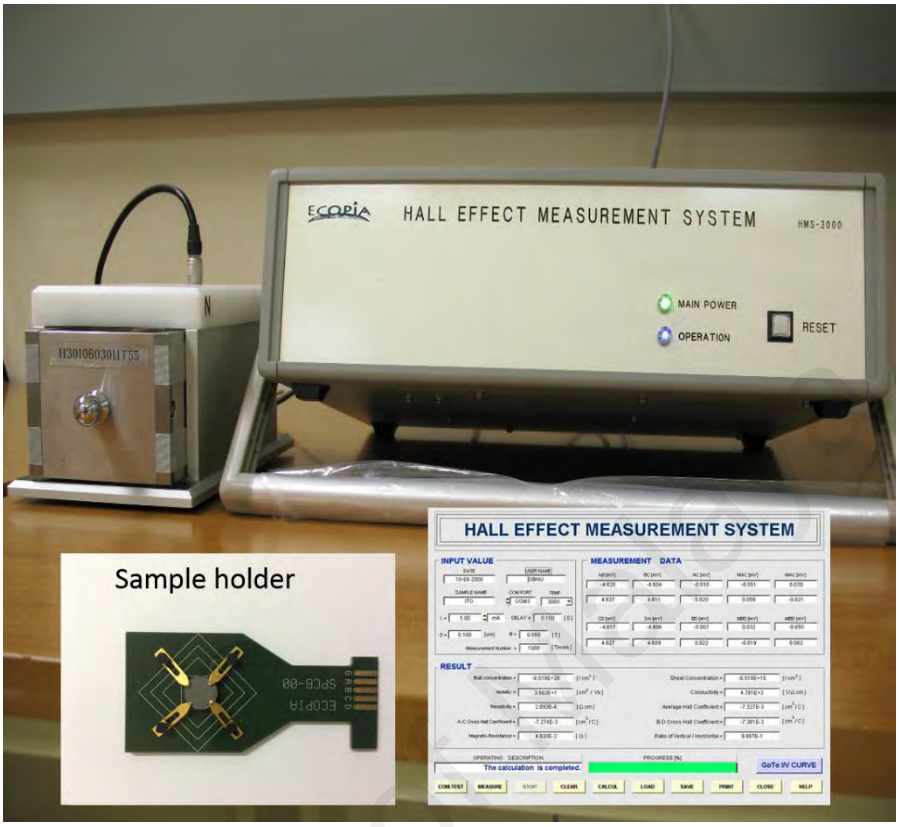

Figure 3.10: The ECOPIA HMS-3000 series instrument for Hall measurement.

CHAPTER 4: RESULTS AND DISCUSSION

In this chapter, the analysis of Ni, Sn, and NiO as a single dopant atom, as well as Sb-X (X = Ni, Hf, Zn and Sn) as double dopant atoms for Bi_2S_3 bulk system will be discussed. The details of discussion could be outlined as follows:

a) In the first sub section, the variation of milling time for synthesized Bi_2ZnS_4 compound using mechanical alloying method (MA) will be presented. Further, the optimum milling time was chosen to be applied for other MA of doped Bi_2S_3 system.

b) The effect of Ni dopant and porous bulk samples which were synthesized using the combination MA followed by cold pressing and sintering process will be discussed on the microstructural and thermoelectric behaviors in the second sub section.

c) Finally, the effect of dopant elements: Ni, Sn, NiO and Sb-X for Bi_2S_3 system which was consolidated by spark plasma sintering (SPS) process will be evaluated in the next sub sections to demonstrate the achievement of thermoelectric dimensionless figure of merit, *ZT*.

4.1 Milling duration

Figure 4.1 performed the XRD patterns of powder samples that were subjected to MA with different time which was varying from 2 hours to 35 hours for constant milling speed (300 rpm). The graphs also included the XRD pattern for mixing condition of powder sample (without MA). For the mixing sample, the resulted peaks represented all the starting elements i.e. Bi, S and Zn. The XRD peaks of powder samples started to change after the introduction of MA process for 2 hours, which is represented by the peak intensities of Zn and S become smaller. Starting from 5 hours of milling time, all the diffraction peaks of powder samples corresponded well to those of Bi_2S_3 (PDF#98-015-3946) without any detectable secondary phase(s), which suggests that a single Bi_2S_3 phase was synthesized during MA process. There was no phase changing even as the milling time was increased to 35 hours, which implied that the stable condition of Bi_2S_3 phase formation already achieved. Thus, 5 hour was chosen as the milling time for the next MA process.

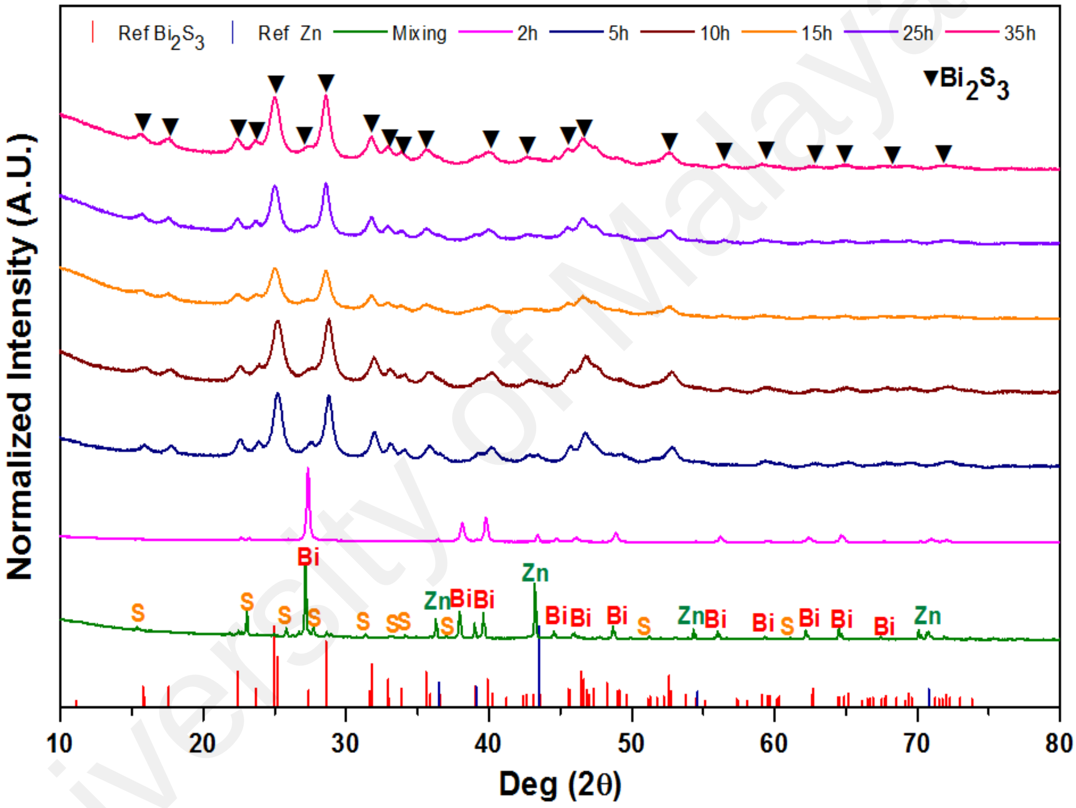

Figure 4.1: XRD patterns of Bi_2ZnS_4 samples after ball milling process. Bi_2S_3 phase was found to be stable after 2 hours of milling time.

4.2 Group A: Ni_x- added Bi_2S_3 porous system ($0 \leq x \leq 0.07$)

4.2.1 Microstructural properties

Figure 4.2 presents the XRD patterns of the $Bi_{2-x}Ni_xS_3$ samples with different Ni content after ball milling process. The diffraction peaks of all samples corresponded well to those of Bi_2S_3 (PDF#98-015-3946) without any detectable second phase (s), which indicates that a single phase of orthorhombic Bi_2S_3 was synthesized under MA method. This is consistent with previous reports (Ge *et al.*, 2012a; Yu *et al.*, 2011).

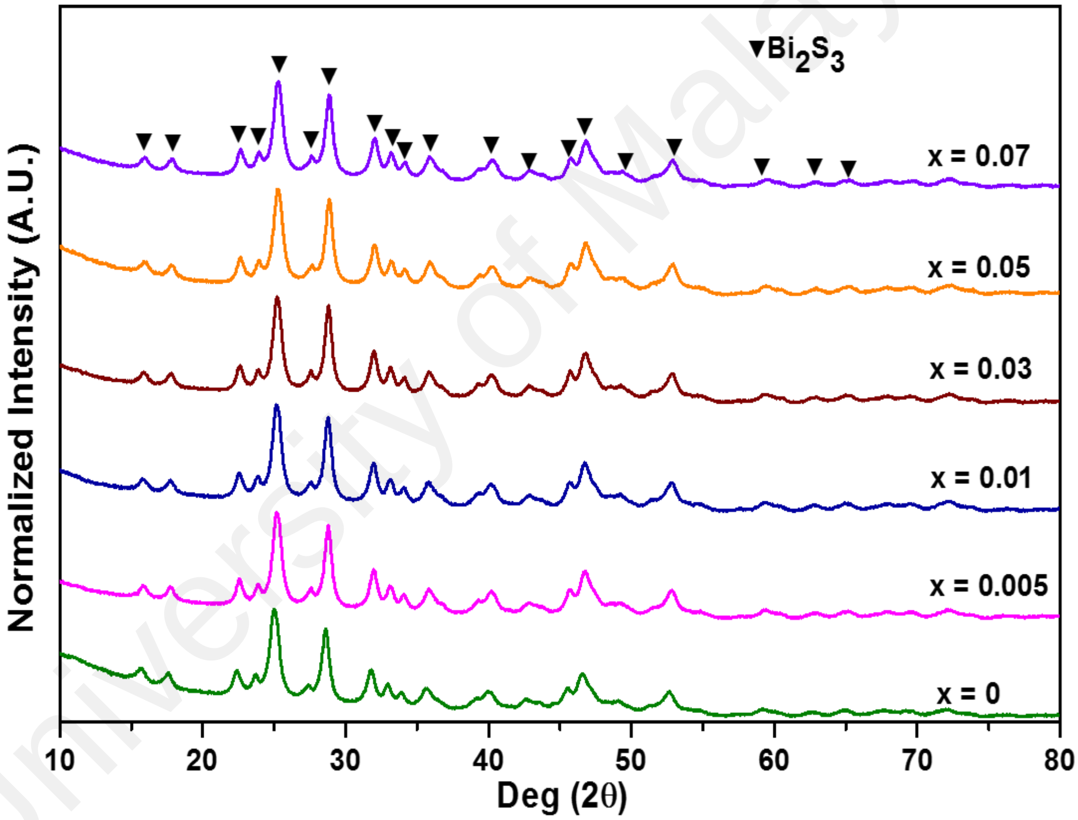

Figure 4.2: XRD patterns of $Bi_{2-x}Ni_xS_3$ samples after ball milling process.

Several sintering processes with various temperatures had been done in order to fix the sintering temperature that will be applied for post-annealing after consolidation process. The milled powder sample was compacted by cold pressing to obtain a dense sample. The chosen conditions for sintering process were adopted from the previous works related with elemental doped Bi_2S_3 system as summarized in the following Table 4.1. In this work, the 0.005 of Ni content was chosen for those purpose. All samples were heated until the appropriate temperature in Mila 5000 furnace and held for about 1 hour.

Table 4.1: Summary of previous results on elemental doped Bi_2S_3 system.

Dopant	Dopant composition with high *ZT*	Sintering temperature	References
Silver (Ag) $Bi_{2-x}Ag_xS_3$	x = 0.01	673 K	(Yu *et al.*, 2011)
Copper (Cu) $Bi_{2-x}Cu_xS_3$	x = 0.005	673 K	(Ge *et al.*, 2012a)

Figure 4.3 showed the XRD results of $Bi_{1.995}Ni_{0.005}S_3$ sample for three different sintering temperatures (523, 623, and 673 K). A small intensity of secondary phase peak appeared in sample under sintering temperature of 673 K. This may attributed to no longer stable Bi_2S_3 phase under that sintering condition. The DSC analysis result for Bi_2S_3 milled powder has confirmed that the Bi_2S_3 phase is no longer stable for temperatures higher than 673 K (Figure 4.4).

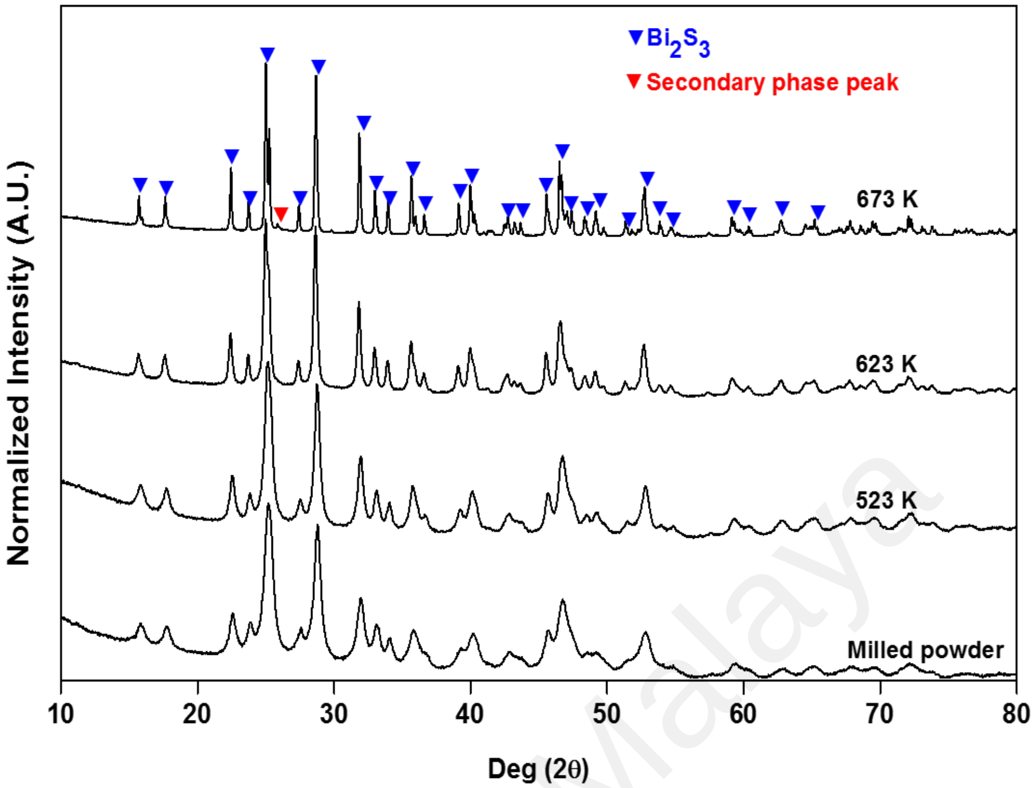

Figure 4.3: XRD patterns for sintered $Bi_{1.995}Ni_{0.005}S_3$ system at range temperatures of 523 – 673 K.

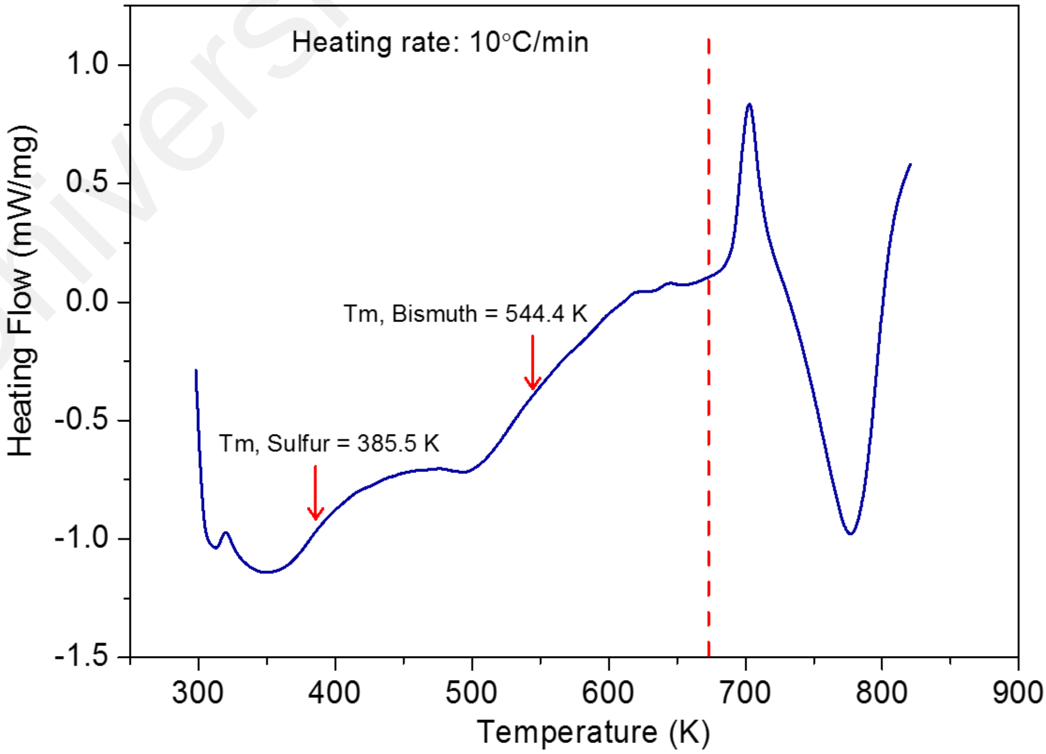

Figure 4.4: DSC result for Bi_2S_3 milled powder.

Several sintering processes were conducted in the temperature range of 623 - 673 K, in order to obtain more accurate information on the sintering temperature in which the secondary phase start to form. The XRD results for those sintered samples are presented in Figure 4.5. A small intensity of secondary phase peak already appeared in sample under sintering temperature of 663 K. It can be concluded that the highest temperature for $Bi_{1.995}Ni_{0.005}S_3$ sample in which the secondary phase did not form was 653 K. Further, this temperature was applied to other sintering processes with different Ni contents (x = 0, 0.01 and 0.05) and the related XRD results are presented in Figure 4.6. It was found that the peak of secondary phase already formed in samples with Ni content more than 0.005. Those results indicated that the applied sintering temperature should be lower than 653 K. Therefore, this work assigns the temperature of 643 K to be applied for the next sintering process.

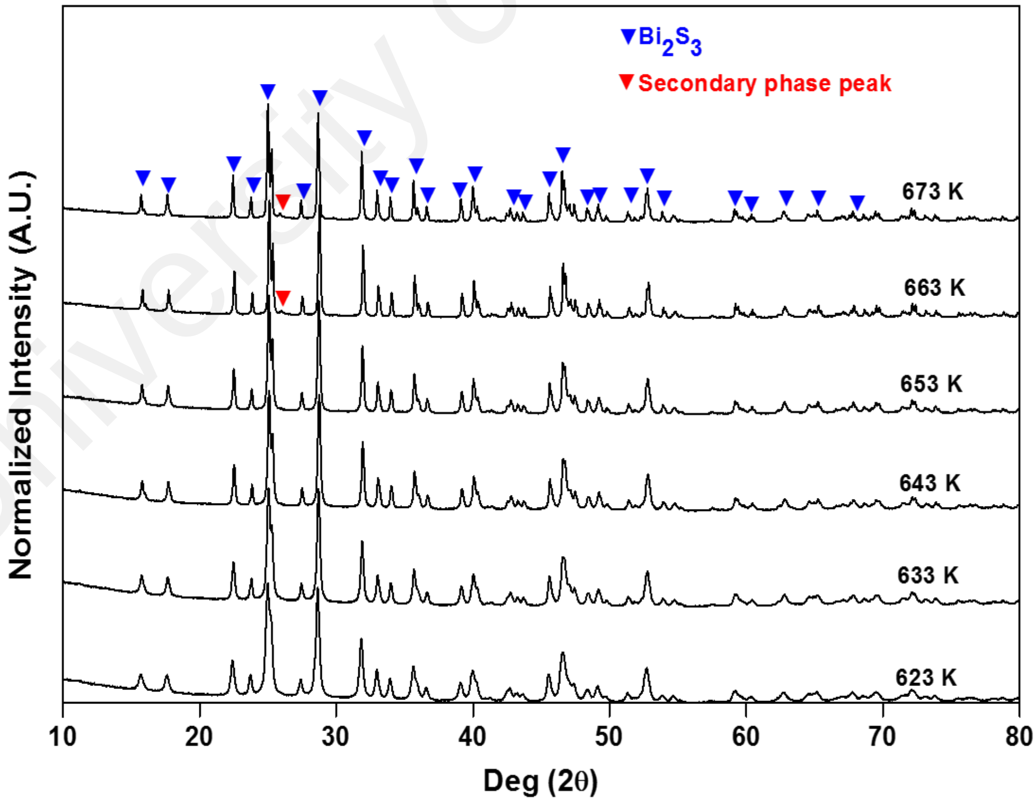

Figure 4.5: XRD patterns for sintered $Bi_{1.995}Ni_{0.005}S_3$ system at range temperatures of 623 – 673 K.

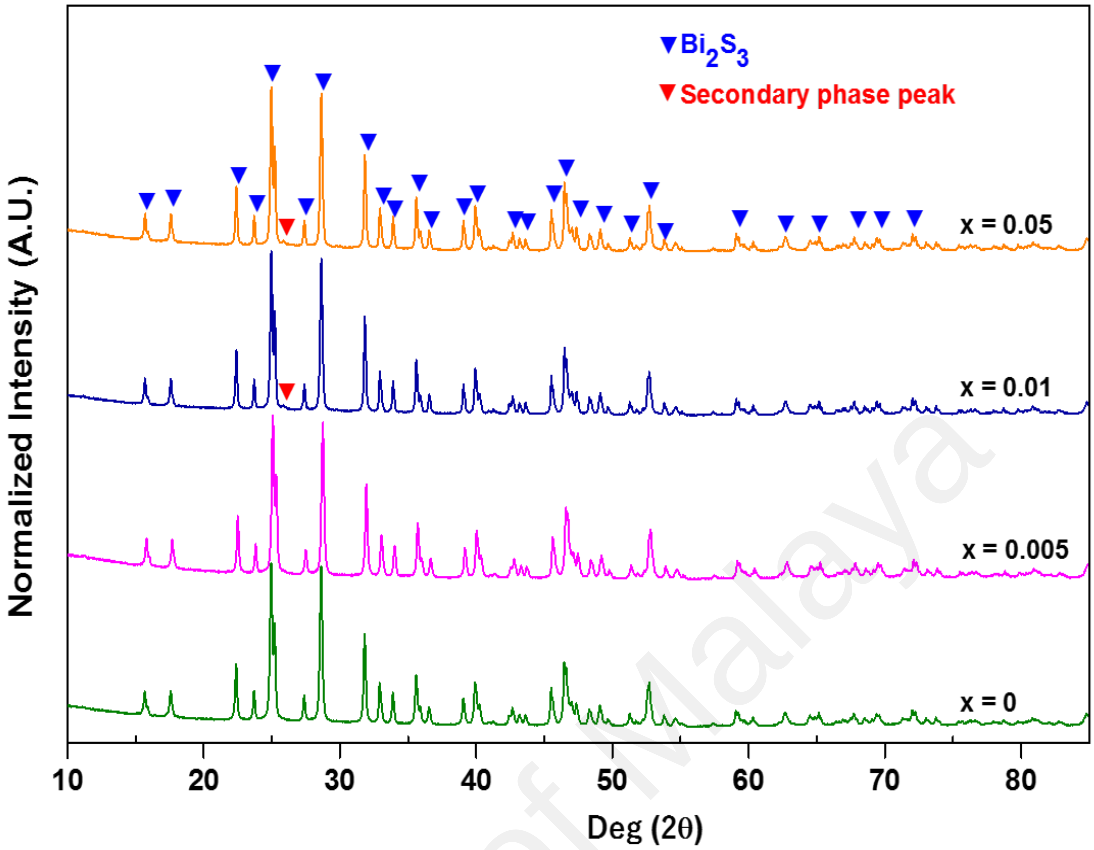

Figure 4.6: XRD patterns for sintered $Bi_{2-x}Ni_xS_3$ ($0 \leq x \leq 0.05$) system at 653 K with different Ni content.

Figure 4.7(a) reveals the XRD patterns of sintered samples of Bi_2S_3 with different Ni content after sintering process (643 K, 1 hour). It was confirmed that a single phase of Bi_2S_3 was formed and no secondary phase appeared. The intensity peaks obtained were sharp with narrowed full width at half maximum (FWHM) for sintered samples, which is a sign of grain growth and a well ordered crystalline phase compared to the powder form. The average crystallite size which was calculated by Scherrer's equation showed that the milled powder samples were in the range of 41.11 – 87.83 nm, whilst the sintered samples were in the range of 64.53 – 94.78 nm with standard deviation (SD) of 117.95 nm and 11.62 nm for milled and sintered samples, respectively (as listed in Table 4.2). The cold pressed samples followed by the sintering process showed larger crystallite size than the milled powder samples (except for x = 0.05) due to thermally activated grain growth during post processing annealing (Zhang *et al.*, 2012). As shown in Figure 4.7(b), the main diffraction of sintered samples peaks around 24.9˚ and 28.6˚ tend to shift to lower 2θ value which indicates that the size of the unit cell become enlarged.

Table 4.2: Average crystallite size, density and porosity of $Bi_{2-x}Ni_xS_3$ samples.

Samples with Ni content (x)	Density g/cm^3	Average crystallite size (nm)		Porosity (%)
		Milled powder	CP + Sintered	
0	5.21 (76.52%)	76.95	94.78	23.48
0.005	5.23 (76.77%)	52.44	94.78	23.23
0.01	5.17 (75.96%)	48.03	78.14	24.04
0.03	5.21 (76.53%)	41.11	64.53	23.47
0.05	5.10 (74.82%)	87.83	78.14	25.18
0.07	5.16 (75.73%)	60.19	78.13	24.27

The percentage value given for density is the relative density value.

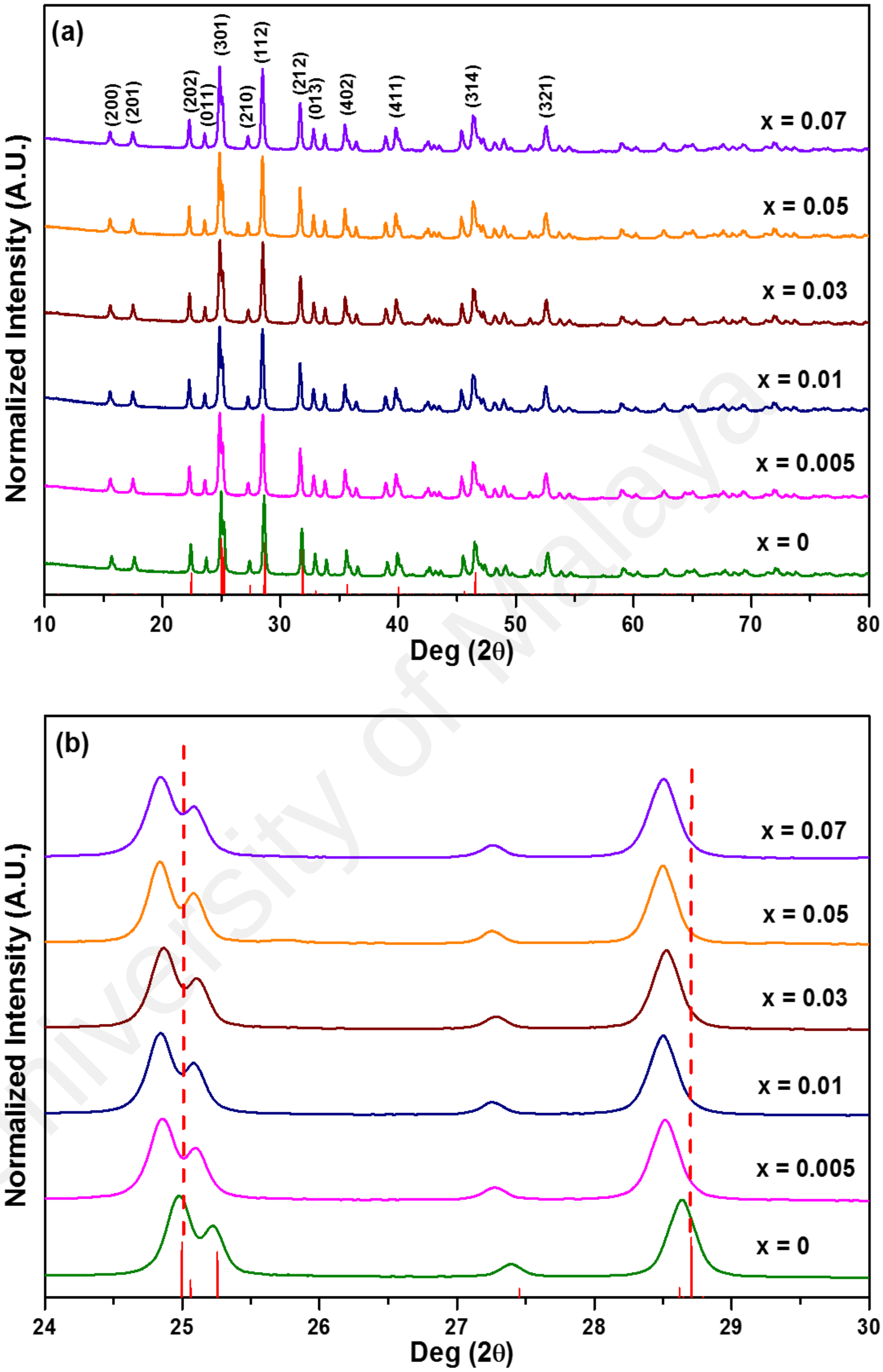

Figure 4.7: XRD patterns of $Bi_{2-x}Ni_xS_3$ cold pressed samples after sintering process at 643 K for 1 hour.

The final results of Rietveld refinement for the $Bi_{2-x}Ni_xS_3$ bulk samples have been presented in Table 4.3. It is shown that the lattice parameters *a*, *b*, and *c* of sintered samples as well as unit cell volume are larger than the reference values. If a part of Bi is substituted by Ni, it is predicted by VEGARD's law (Pearson & Bardeen, 1949; Vegard, 1921) that the host lattice should be constant or shrinking because Ni possesses a smaller effective ionic radius (0.69Å) compare to Bi (1.03Å). Therefore, the enlargement of host atom is attributed to the inclusion of Ni atom into the Bi_2S_3 lattice interstices rather than substitution for all formulation of this group, as supported from the crystal structure plotted after refinement (in Figure 4.8). Furthermore, the atomic position of Ni atoms is not fixed to a specific coordinate which means that the position is random. For Ni-free sample (Bi_2S_3), the enlargement of lattice may be caused by stress that is generated during the MA process. In the previous studies, the enlargement of the Bi_2S_3 lattice was reported as a result of the sulfur volatilization during MA and spark plasma sintering (SPS) process (Ge *et al.*, 2012b; Ge *et al.*, 2011b). Additionally, although the size of sintered samples is bigger than the reference, there is no significant difference in volume cell for each sintered sample. This may due to a low level content of Ni dopant in the synthesized samples. It can be seen that for doped samples, the volume of unit cell expanded up to $x = 0.01$, and then contracted upon further Ni doping. This can be attributed to the difficulty in inducing doping of Ni into Bi_2S_3 lattice using cold pressing as it is a relatively low energy process. The low energy of the cold pressing method is also thought to be of insufficient energy to induce substitution of Ni atom in the Bi site, resulting in the interstitial location of Ni dopant. Hence, excess Ni acts as impurities and causes electrostatic repulsion between itself and the Ni in the interstitial site.

Table 4.3: Nominal composition, actual composition from JANA, lattice parameters and volume of unit cell of as-sintered $Bi_{2-x}Ni_xS_3$ samples.

Ni content (x)	Nominal Composition	Actual Composition (JANA)	Lattice Parameters (Å)			Volume Unit Cell (Å^3)
			a	b	c	
0	Bi_2S_3 (reference)	Bi_2S_3	11.2690	3.9720	11.1290	498.14
0	Bi_2S_3	$Bi_{1.985}S_3$	11.2939	3.9816	11.1440	501.12
0.005	$Bi_{1.995}Ni_{0.005}S_3$	$Bi_{1.995}Ni_{0.005}S_3$	11.2960	3.9827	11.1458	501.43
0.01	$Bi_{1.99}Ni_{0.01}S_3$	$Bi_{1.99}Ni_{0.0094}S_3$	11.2978	3.9833	11.1475	501.67
0.03	$Bi_{1.97}Ni_{0.03}S_3$	$Bi_{1.97}Ni_{0.027}S_3$	11.2955	3.9824	11.1458	501.37
0.05	$Bi_{1.95}Ni_{0.05}S_3$	$Bi_{1.95}Ni_{0.045}S_3$	11.2955	3.9824	11.1456	501.36
0.07	$Bi_{1.93}Ni_{0.07}S_3$	$Bi_{1.93}Ni_{0.058}S_3$	11.2960	3.9822	11.1447	501.27

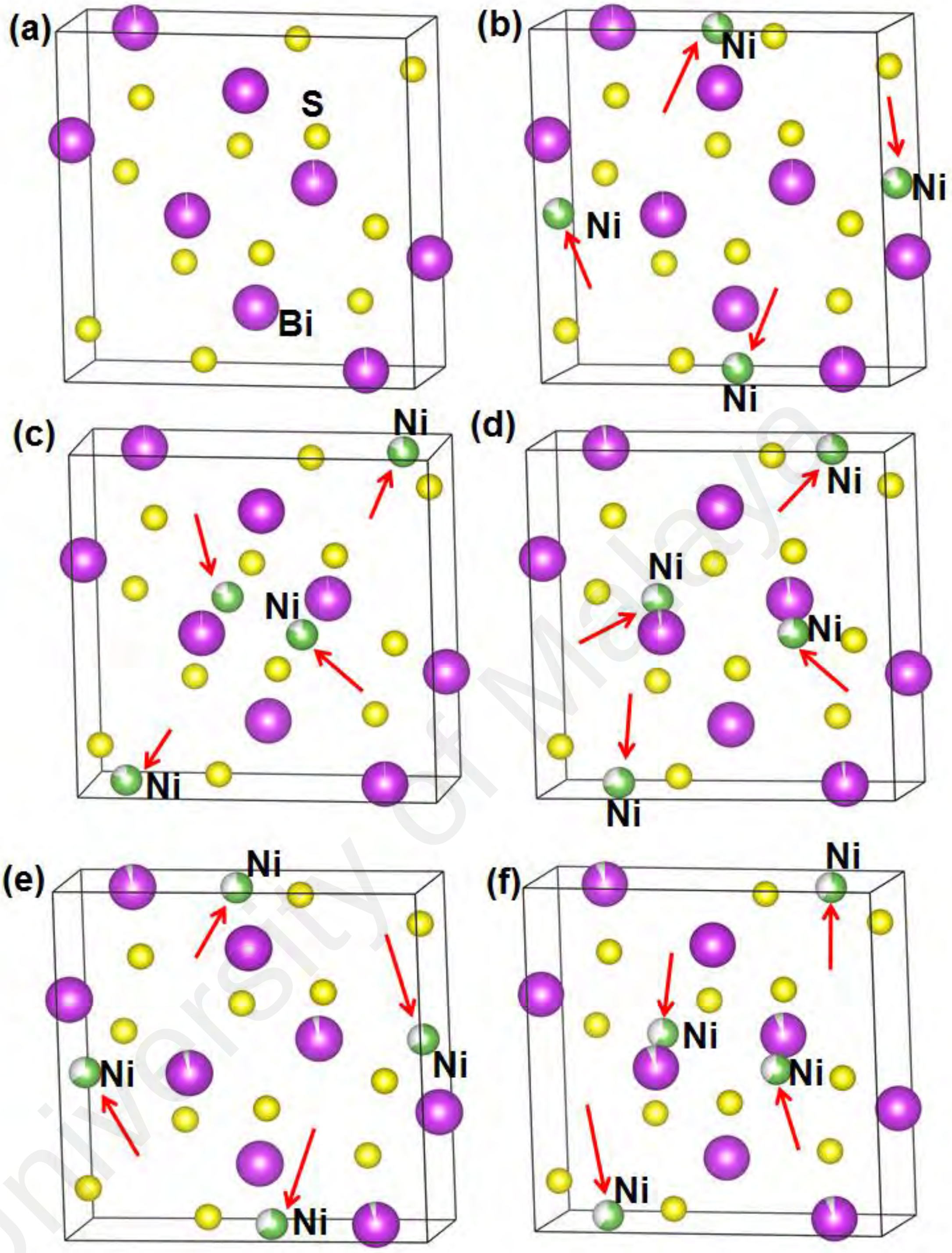

Figure 4.8: The crystal structure of sintered $Bi_{2-x}Ni_xS_3$ samples after refinement using JANA 2006; (a) x = 0, (b) x = 0.005, (c) x = 0.01, (d) x = 0.03, (e) x = 0.05 and (f) x = 0.07. The arrows denoted the interstitial location of the Ni atoms, which do not substitute the Bi site.

The FESEM images of fractured surfaces for $Bi_{2-x}Ni_xS_3$ sintered samples are presented in Figure 4.9. All the samples showed a granular structure with no obvious secondary phase could be found on the grain boundary. The fracture surface of samples indicated that the average grain size is less than 1 μm. The microstructural analysis confirmed that all the doped samples were porous, as supported by measured density values listed in Table 4.2, which generally have density less than 77%. The average pore sizes ranged from 1.15 to 5.63 nm (SD = 1.8 nm), which is classified as being micro and meso-porous under the IUPAC classification of pores.

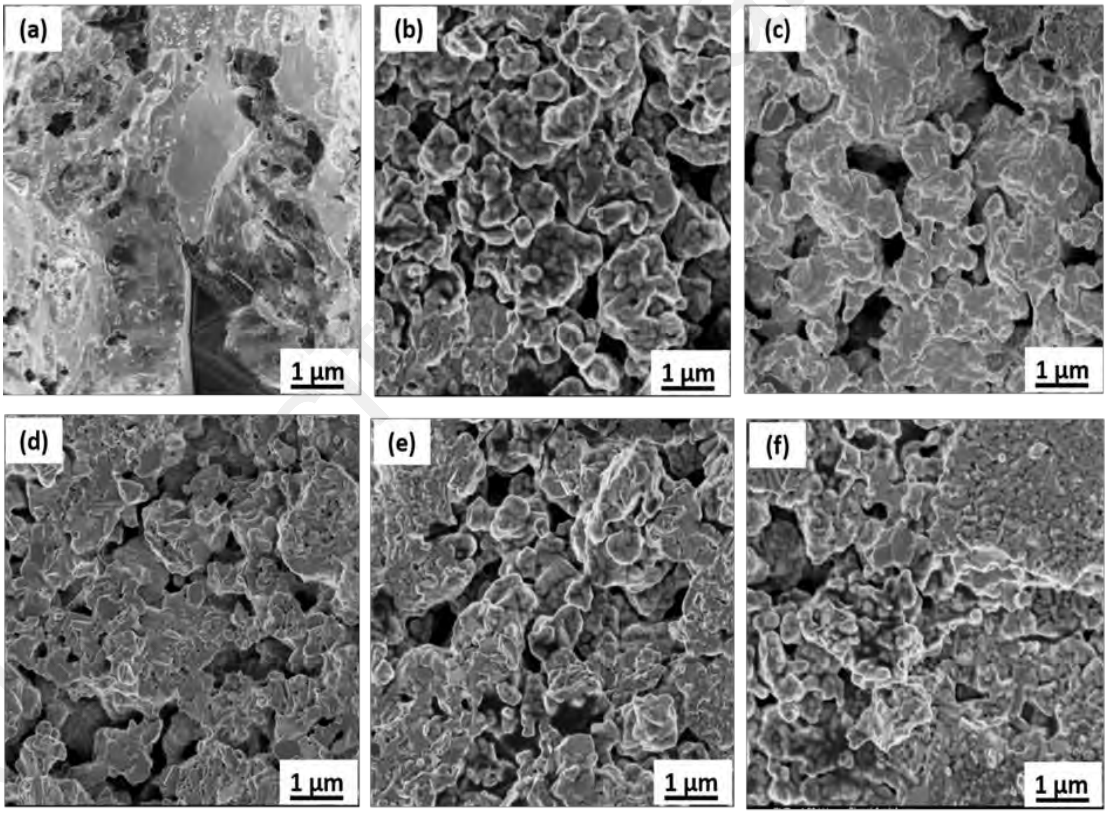

Figure 4.9: FESEM images of the fractured surface of cold pressed samples of $Bi_{2-x}Ni_xS_3$. (a) x = 0, (b) x = 0.005, (c) x = 0.01, (d) x = 0.03, (e) x = 0.05 and (f) x = 0.07.

The energy dispersive x-ray analysis (EDS) results for $Bi_{1.99}Ni_{0.01}S_3$ sample is performed in Figure 4.10. The EDS data indicated that the presence of Bi and S with percentages that comparable to those expected in the nominal formula of the $Bi_{1.99}Ni_{0.01}S_3$ sample, and no Ni peak appeared. Additionally, the atomic ratio of Bi and S is about 2:3, which represents the nominal ratio of Bi and S in Bi_2S_3 phase. This result is in good agreement with the XRD analysis which revealed a single phase of Bi_2S_3.

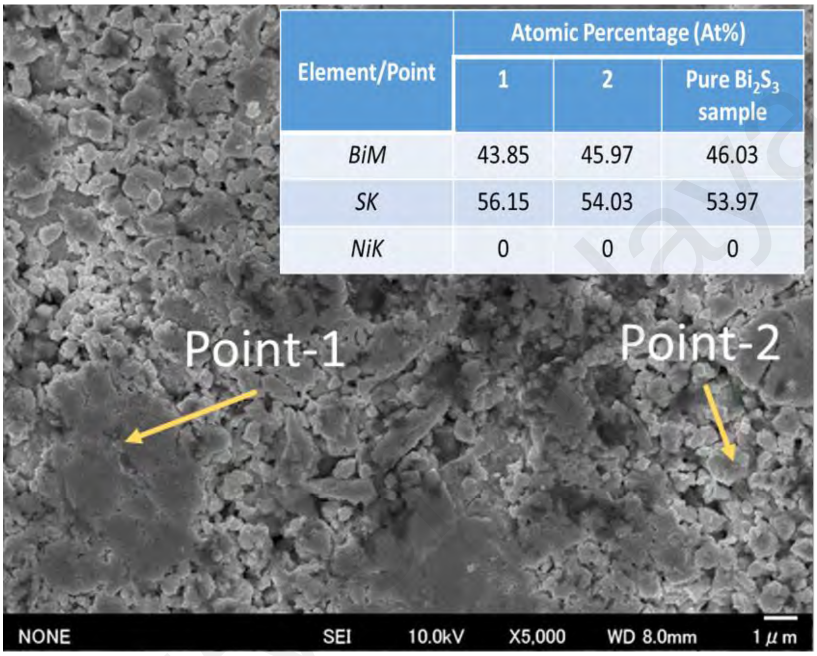

Element/Point	Atomic Percentage (At%)		
	1	2	Pure Bi_2S_3 sample
BiM	43.85	45.97	46.03
SK	56.15	54.03	53.97
NiK	0	0	0

Figure 4.10: Energy dispersive x-ray analysis (EDS) results for $Bi_{1.99}Ni_{0.01}S_3$ cold pressed sample.

4.2.2 Thermoelectric properties

Figure 4.11 displays the temperature dependence of electrical resistivity (ρ) which shows the decreasing electrical resistivity value for all $Bi_{2-x}Ni_xS_3$ samples with increasing temperature, as an indication of semiconductor conducting behavior (Ge *et al.*, 2012a). The presence of Ni atoms into interstices of Bi_2S_3 lattice increased the number of electrons as charge carrier, which can be expressed by the following equation:

$$Ni \xrightarrow{2Bi_2S_3} Ni_i^{\cdot\cdot} + 3S_S + 2Bi_{Bi} + 2\acute{e} \tag{4-1}$$

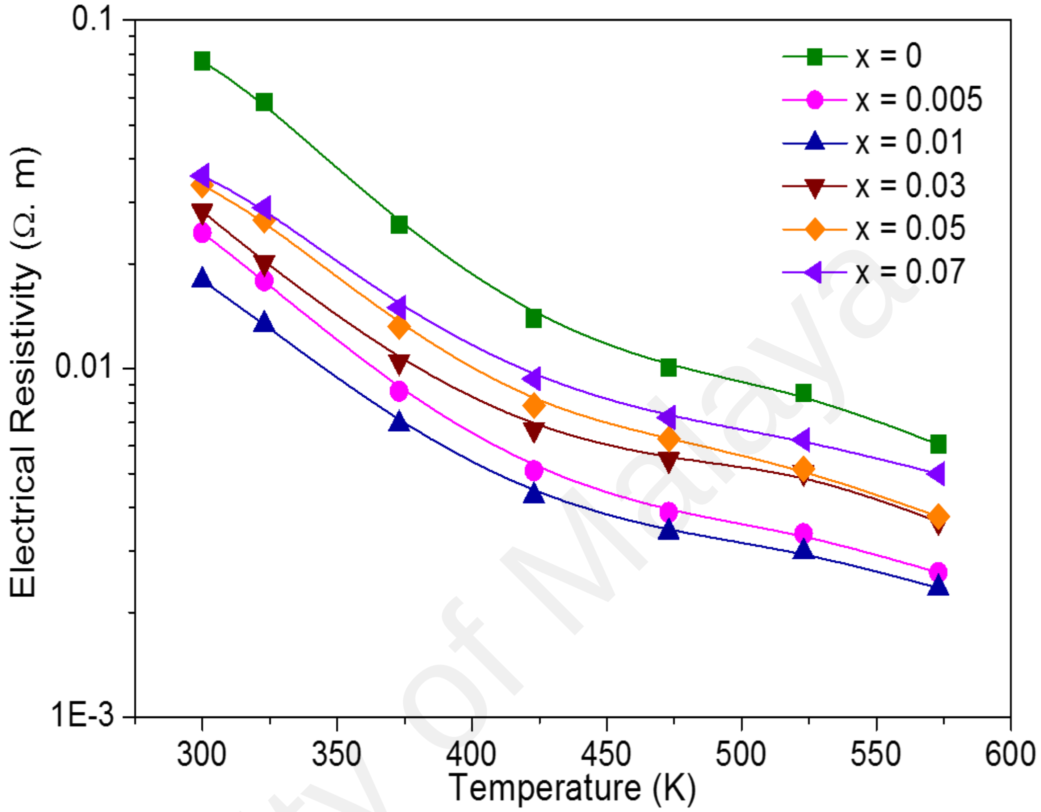

Figure 4.11: Temperature dependence of electrical resistivity ρ for $Bi_{2-x}Ni_xS_3$ cold pressed samples with different Ni contents.

Table 4.4 summarized the results of Hall measurements. As listed, the carrier concentration (n) of Ni doped samples are larger than that of pure Bi_2S_3. This results confirmed the hypothesized that the presence of Ni into Bi_2S_3 interstices increased the number of charge carrier as described in equation (4-1). Generally, the carrier concentration of all compounds are in the order of ~ 10^{18}, which are slightly higher than that of Al added skutterudite compounds reported by Elsheikh *et al.* (2016), -1.2 x 10^{18} cm^{-3}. This results show an appreciable level of charge concentration of the Ni doped Bi_2S_3 formulation.

Table 4.4: Carrier concentration, mobility and average Hall coefficient at room temperature for $Bi_{2-x}Ni_xS_3$ cold pressed samples.

Ni content (x)	Carrier concentration, n (10^{18} cm^3)	Mobility, μ ($cm^2V^{-1}S^{-1}$)	Average Hall coefficient, R_H (cm^2 C^{-1})
0	-2.15	3.95	-2.91
0.005	-3.03	4.98	-2.06
0.01	-2.56	6.03	-2.43
0.03	-3.03	3.80	-2.06
0.05	-2.59	4.33	-2.41
0.07	-4.59	2.44	-1.36

The work of Zhao *et al.* (2008) also showed that the formation of interstitial solid solution will increase electron concentration, which could reduce the electrical resistivity for the Bi_2S_3 material. The electrical resistivity value of Bi_2S_3 sample ranges from $7.64x10^{-2}$ to $6.07x10^{-3}$ Ω.m at room temperature (RT) – 573 K. The addition of Ni has a significant effect of reducing electrical resistivity especially at RT from $7.64x10^{-2}$ Ω.m to $1.79x10^{-2}$ Ω.m for $Bi_{1.99}Ni_{0.01}S_3$ sample implying that 76.6% of the electrical resistivity could be suppressed at this temperature. At room temperature, $Bi_{1.99}Ni_{0.01}S_3$ sample has the lowest electrical resistivity value due to the high mobility of the charge carriers as summarized in Table 4.4. The resistivity still could be decreased as temperature increases but the additional improvement is not significant. A minimum electrical resistivity value of 2.35 $x10^{-3}$ Ω.m at 573 K was achieved for the $Bi_{1.99}Ni_{0.01}S_3$ sample. Comparing with the previous results, which used Cu and Ag atoms as dopant for Bi_2S_3 system with densification method of SPS (Ge *et al.*, 2012a; Yu *et al.*, 2011), the minimum electrical resistivity value for this research is almost an order of magnitude higher than that previous results which was $1.3\text{x}10^{-4}$ Ω.m and $3.6\text{x}10^{-4}$ Ω.m for Cu-doped and Ag-doped Bi_2S_3 system, respectively. It is assumed that the porosity of the samples produced under cold pressing appear to be an important factor influencing electrical resistivity value, as similar results were reported from the experiments on nano-grained SiGe which revealed that porosity caused a significant increase in the resistivity (Lee *et al.*, 2010).

Figure 4.12 presents the temperature dependence of Seebeck coefficient (α) for $Bi_{2-x}Ni_xS_3$ with different Ni contents. It can be clearly seen that the negative values of Seebeck coefficient in the temperature range studied for all samples are indicative of an *n*-type conduction and that the major carriers are electrons. All samples showed the additional increase of Ni resulted in decreasing magnitude of Seebeck coefficient due to extra carrier which is generated by Ni at the interstitial sites (as discussed above). The Seebeck coefficient is sensitive to the electronic band structure and carrier concentration. Thus, the presence of interstitial atoms introduce additional carriers and effectively altered the band structure by lifting the Fermi level as a result of the decrease of the Seebeck coefficient (Du *et al.*, 2012). On the contrary, the presence of porous structure will enhance the Seebeck coefficient due to energy filtering and phonon drag effect (Lee *et al.*, 2010; Valalaki *et al.*, 2016). In this work, the imperfections in the lattice due to Ni interstitial seem to give more contribution on Seebeck values since the samples have approximately the same degree of porosity. Table 4.5 summarized the Seebeck coefficient values of Bi_2S_3 system from the previous reports as comparison to the present work.

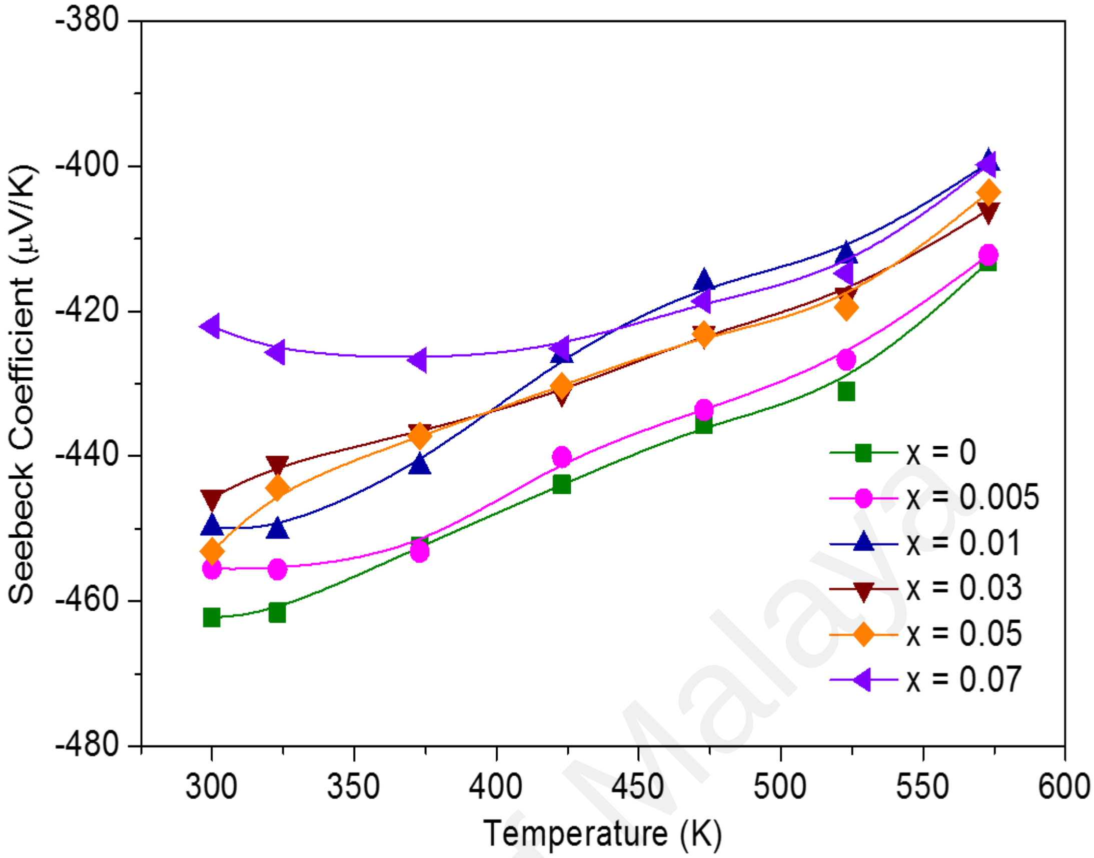

Figure 4.12: Temperature dependence of Seebeck coefficient *α* for $Bi_{2-x}Ni_xS_3$ cold-pressed samples with different Ni contents.

The maximum Seebeck coefficient of $Bi_{2-x}Ni_xS_3$ system is about -462 µV/K, which was attained of Bi_2S_3 sample at 300 K. This Seebeck values is comparable to those previously reported for the Bi_2S_3 system as listed in Table 4.5. The samples with Ni content in the range of $0.005 \leq x < 0.03$ have slightly higher Seebeck value compared to the results with the same composition range for Ag-doped Bi_2S_3 system (Yu *et al.*, 2011), which was in between -400 to -456 µV/K for Ni-doped and in between -250 to -390 µV/K for Ag-doped system, respectively.

Table 4.5: Seebeck coefficient of elementals doped Bi_2S_3 system.

Compound	Maximum Seebeck coefficient of Bi_2S_3 (μV/K)	Range of Seebeck coefficient values for doped samples (μV/K)	References
Bi_2S_{3-x}	-500 @ 323 K	-300 to -400	(Zhao *et al.*, 2008)
$Bi_{2-x}Ag_xS_3$	-500 @ 423 K	-350 to -800	(Yu *et al.*, 2011)
$Bi_{2-x}Cu_xS_3$	- 450 @ 323 K	-220 to -650	(Ge *et al.*, 2012a)
$Bi_{2-x}Ag_{3x}S_3$	-480 @ 323 K	-150 to -300	(Ge *et al.*, 2012b)
$Bi_2S_{3-x}Se_x$	-498 @ 323 K	-390 to -612	(Zhang *et al.*, 2013)
$(Bi_{1-x}Sb_x)_2S$	-180 @ 300 K	-200 to -500	(Kawamoto & Iwasaki, 2014)
ZnO added Bi_2S_3	-370 @ 300 K	-200 to -350	(Du *et al.*, 2015)
$Ce_xBi_2S_3$	-490 @ 323 K	-320 to -440	(Pei *et al.*, 2017)
BiI_3 doped Bi_2S_3	-455@673 K	-225 to -375	(Yang *et al.*, 2017)
Bi/Bi_2S_3 nanocomposite	-500@623 K	-150 to -400	(Ge *et al.*, 2017)
Sn doped Bi_2S_3	-250@673 K	-130 to -280	(Guo *et al.*, 2017)

Figure 4.13 presents the temperature dependence of power factor ($PF = \alpha^2/\rho$) for $Bi_{2-x}Ni_xS_3$ samples with different Ni contents. All samples show a similar positive-temperature dependence, i.e. power factor increases with increasing temperature in the whole measuring temperature ranging from 300 – 573 K. The power factor of Bi_2S_3 sample is 2.80 μW/mK^2 at 300 K and increases to 28.12 μW/mK^2 when raising the temperature to 573 K. It can be seen in Figure 4.13 that the enhancement of power factor is achieved with the presence of Ni into the Bi_2S_3 system. This enhancement is a result of the significant contribution of extra electron carriers, n, by Ni interstitial atoms

dominating the decrease of electrical resistivity than Seebeck coefficient. The higher power factor value of 67.94 μW/mK^2 was achieved for the $Bi_{1.99}Ni_{0.01}S_3$ sample at 573 K. These results suggest that the electrical transport properties of $Bi_{2-x}Ni_xS_3$ can be improved by adjusting of Ni content with the optimal concentration of x = 0.01. Comparing with the previous works on element dopants at Bi site in Bi_2S_3 system, the optimal concentration of dopant (x) were 0.005 and 0.01 for Cu-doped (Ge *et al.*, 2012a) and Ag-doped Bi_2S_3 system (Yu *et al.*, 2011), respectively. From our results, the optimum degree filling of Ni dopant to enhance the electrical transport properties of Bi_2S_3 still could be improved to higher Ni concentration, since through the cold pressing method not all Ni atoms were able to penetrate to Bi_2S_3 crystal as indicated by the JANA results for the actual composition (as listed in Table 4.3).

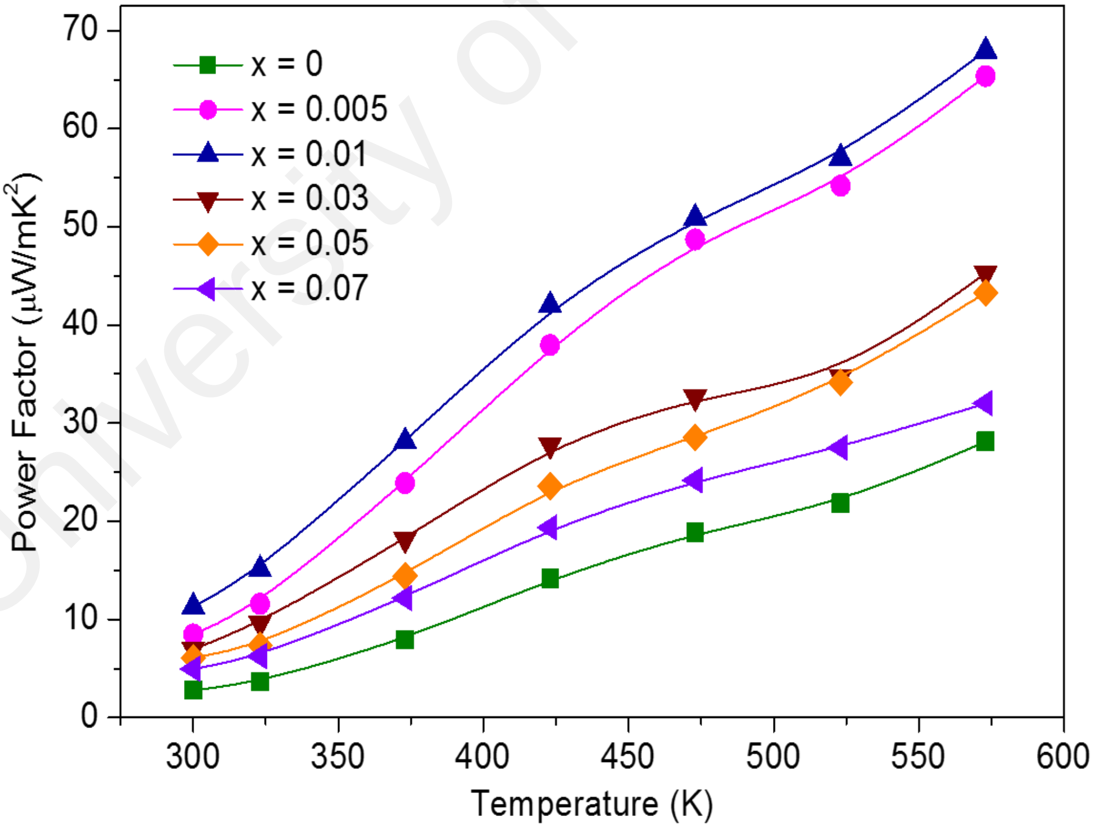

Figure 4.13: Temperature dependence of power factor *PF* for $Bi_{2-x}Ni_xS_3$ cold-pressed samples with different Ni contents.

Figure 4.14 presents thermal diffusivity (D) of $Bi_{2-x}Ni_xS_3$ with different Ni content. Thermal diffusivity was reduced with increasing temperature with the minimum value of 0.25 mm^2/s for Bi_2S_3 sample at 573 K. The thermal diffusivity values of Ni doped samples are slightly larger than pure Bi_2S_3 sample (except for $x = 0.05$ composition) with no significant differences amongst the doped samples, which implies that the effect of Ni on thermal diffusivity parameter is negligible. The range of thermal diffusivity values for this research is lower compared with previous works reported by Yu *et al.* (2011) and Ge *et al.* (2012a) for SPSed Bi_2S_3 system doped with Ag and Cu-, respectively.

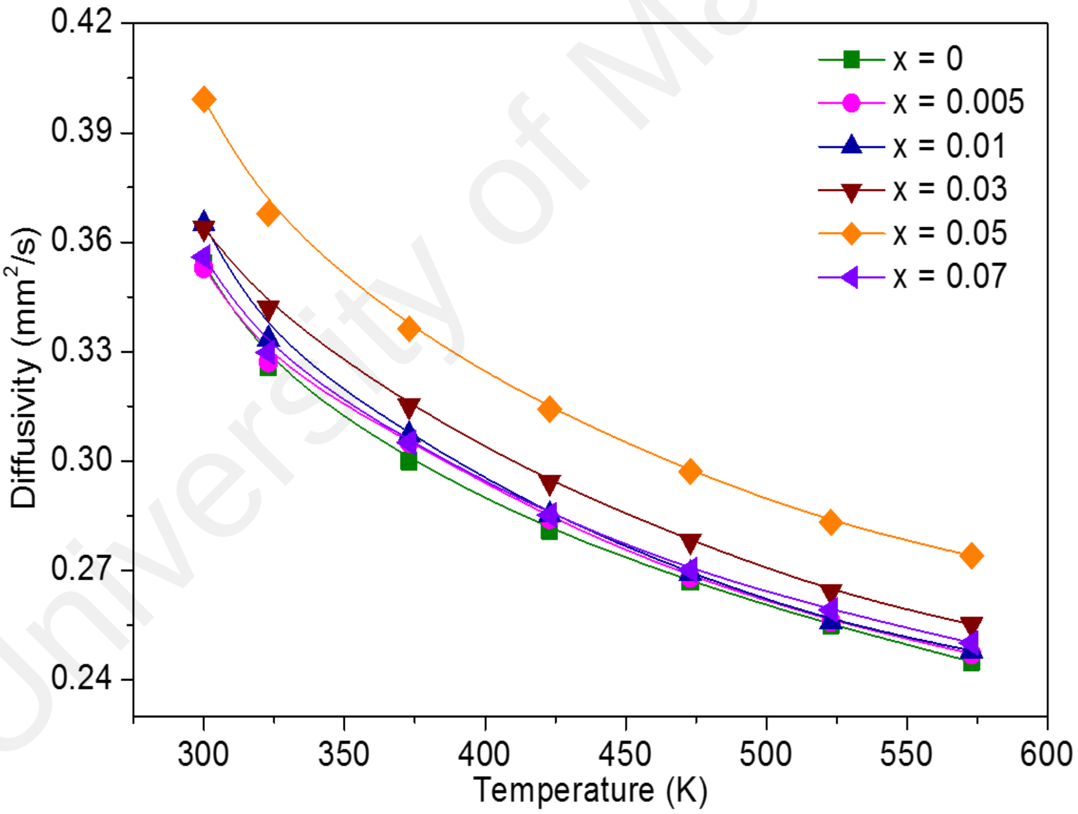

Figure 4.14: Temperature dependence of thermal diffusivity (D) for $Bi_{2-x}Ni_xS_3$ cold-pressed samples with different Ni contents.

Figure 4.15 represent the measured specific heat (*Cp*) values of cold pressed $Bi_{2-x}Ni_xS_3$ samples for measuring temperature of 323-573 K. The *Cp* values were in the narrow range of 0.22 -0.29 $Jg^{-1}K^{-1}$. In addition, the measured *Cp* values were closely match the literature value of Bi_2S_3 under Dulong-Petit law (*Cp* ~ 0.238 $Jg^{-1}K^{-1}$) (Patnaik, 2003).

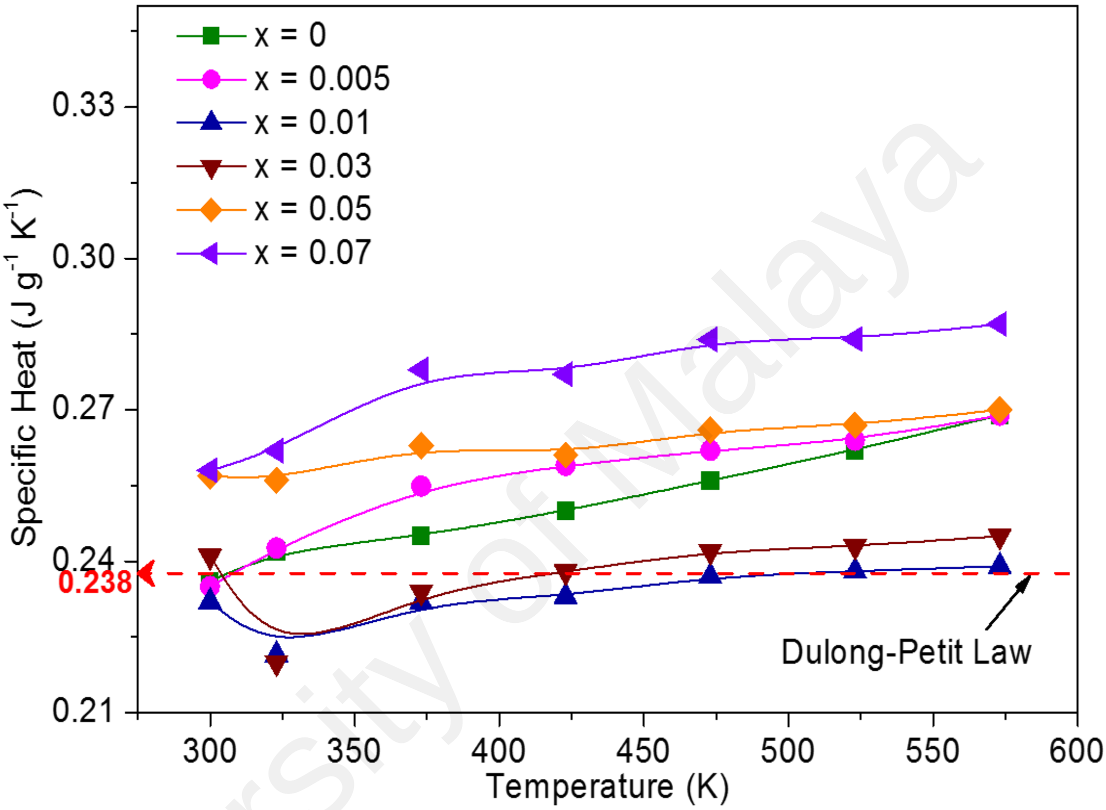

Figure 4.15: Temperature dependence of specific heat (*Cp*) for cold-pressed $Bi_{2-x}Ni_xS_3$ samples with different Ni contents.

Figure 4.16 (a) shows thermal conductivity *κ* for different Ni contents of cold pressed samples calculated from specific heat capacity, thermal diffusivity and bulk density. The trend of thermal conductivity for all samples decrease with increasing temperature, which indicates the dominant mechanism of the phonon scattering inside the material (Cahill *et al.*, 2003). Since there was no significant difference in diffusivity values and measured specific heat in the narrow range of 0.22 -0.29 $Jg^{-1}K^{-1}$, this implies that the thermal conductivity values in this research are strongly affected by the density of samples. The thermal conductivity value of Bi_2S_3 sample in the temperature range of 323 – 573 K decreases from 0.41 to 0.34 W/m.K. These values are lower than 0.84 – 0.86 W/m.K compared to the same composition Bi_2S_3 sample which was previously reported by Zhao *et al.* (2008). Thus, about ~59.6% a reduction in thermal conductivity could be obtained under this study. The presence of porous structures is believed to have a great contribution on the decreasing thermal conductivity value of Bi_2S_3 as clearly seen in Figure 4.16(b), in comparison to thermal conductivity values of high density Bi_2S_3. Amongst the investigated samples, the $Bi_{1.99}Ni_{0.01}S_3$ sample presented the minimum thermal conductivity values in measured temperature range with the lowest value of 0.31 W/m.K at 573 K.

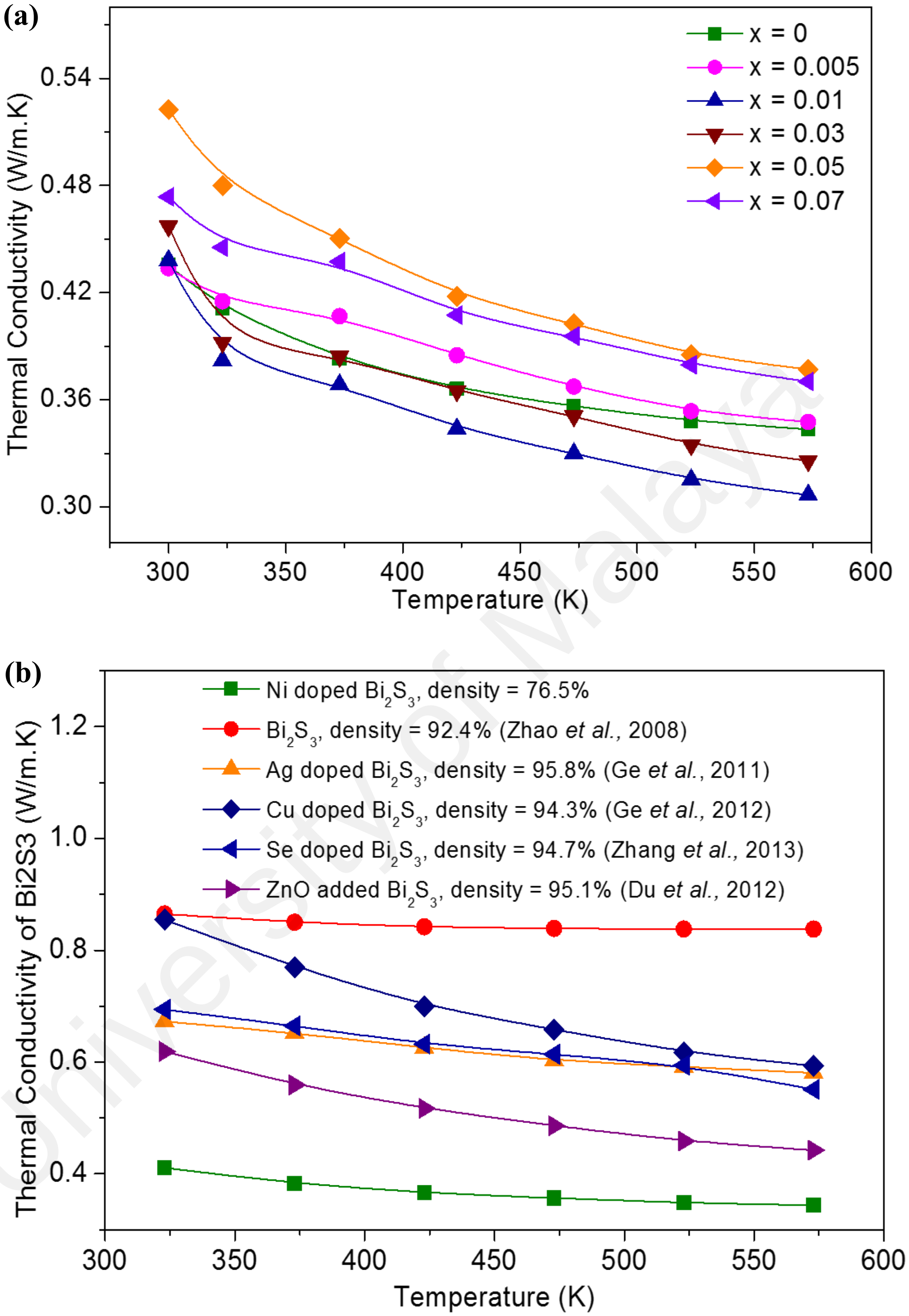

Figure 4.16: (a). Temperature dependence of thermal conductivity κ for $Bi_{2-x}Ni_xS_3$ cold-pressed samples with different Ni contents, (b) Thermal conductivity of Bi_2S_3 at 323 – 573 K. Shown for comparison is the thermal conductivity of Bi_2S_3 from previous studies.

Figure 4.17 illustrates the temperature dependence of the lattice thermal conductivity (κ_{lat}) for different Ni contents of sintered samples. The lattice thermal conductivity can be estimated by subtracting the electronic contribution of the Wiedemann – Franz law,$\kappa_{el} = LT/\rho$ from the total thermal conductivity, where L = 2.45 x 10^{-8} V^2 K^2 is the Lorenz number. The calculated electronic thermal contribution for all samples was found to be smaller than 2% of the total thermal conductivity, which indicates a high degree of decoupling between the charge carrier and thermal conductivity. Thus, the lattice thermal conductivity significantly dominates the decrease in thermal conductivity value. The lattice thermal conductivity for all samples decreases with increasing temperature, which is ascribed to the strong phonon scattering. The lower lattice thermal conductivity value in this work could be related to presence of the porous structure. At 573 K, the lattice thermal conductivity value of Bi_2S_3 sample consolidated by cold pressing followed by sintering is 0.34 W/m.K. In comparison with the value of SPSed Bi_2S_3 sample which was reported by Ge *et al.* (2012a) ($\kappa_{lat} \approx 0.6$ W/m.K at 573 K), under this study lattice thermal conductivity decreased by about 44%, which indicates that the impact of pore structure on the scattering of heat-carrying phonons is significant.

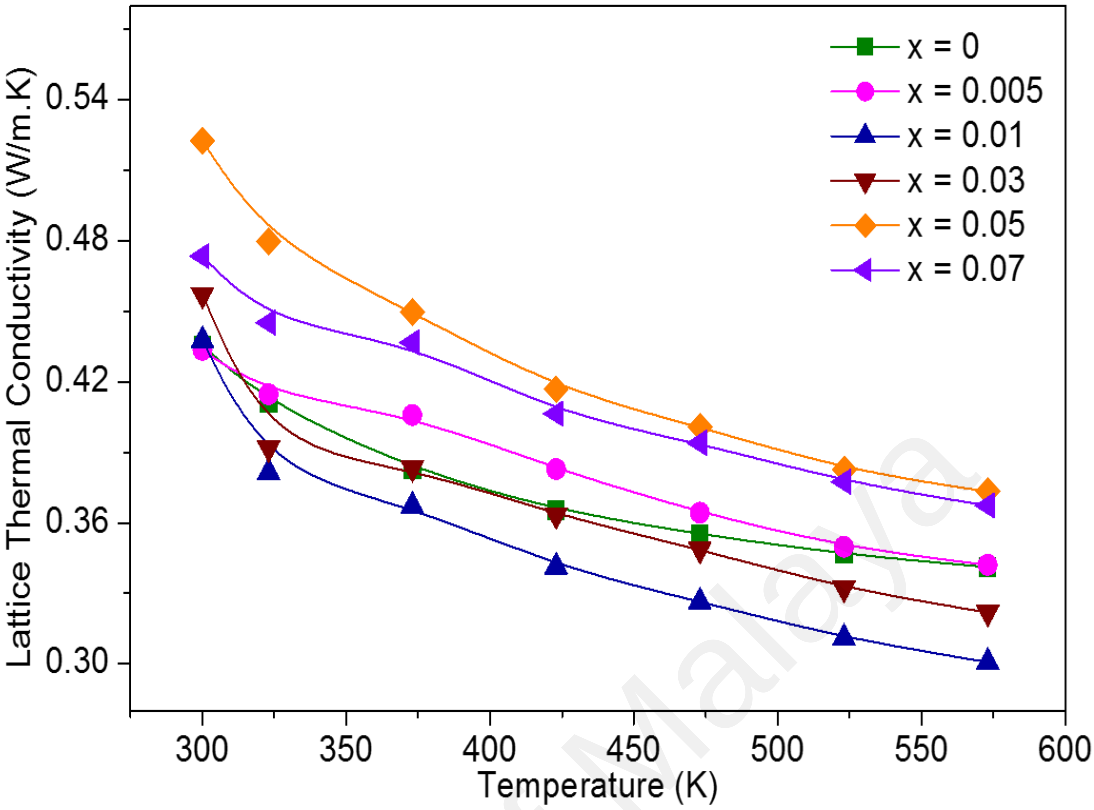

Figure 4.17: Temperature dependence of lattice thermal conductivity κ_{lat} for $Bi_{2-x}Ni_xS_3$ cold-pressed samples with different Ni contents.

4.2.2.1 Thermal conductivity analysis

The presence of pores requires a correction factor for calculation of its actual thermal conductivity. In this case, the corrected thermal conductivity would be given by the effective medium approach (EMA) as (Chen *et al.*, 2012; Nan *et al.*, 1997):

$$\kappa_s = \kappa \left[\frac{2-2f}{2+2f}\right]^{-1} \tag{4-2}$$

where f is the porosity, κ is the measured conductivity of the porous medium, and κ_s is the calculated thermal conductivity with $f = 0$. The corrected thermal conductivity with zero porosity of Bi_2S_3 samples with different Ni contents are shown in Figure 4.18.

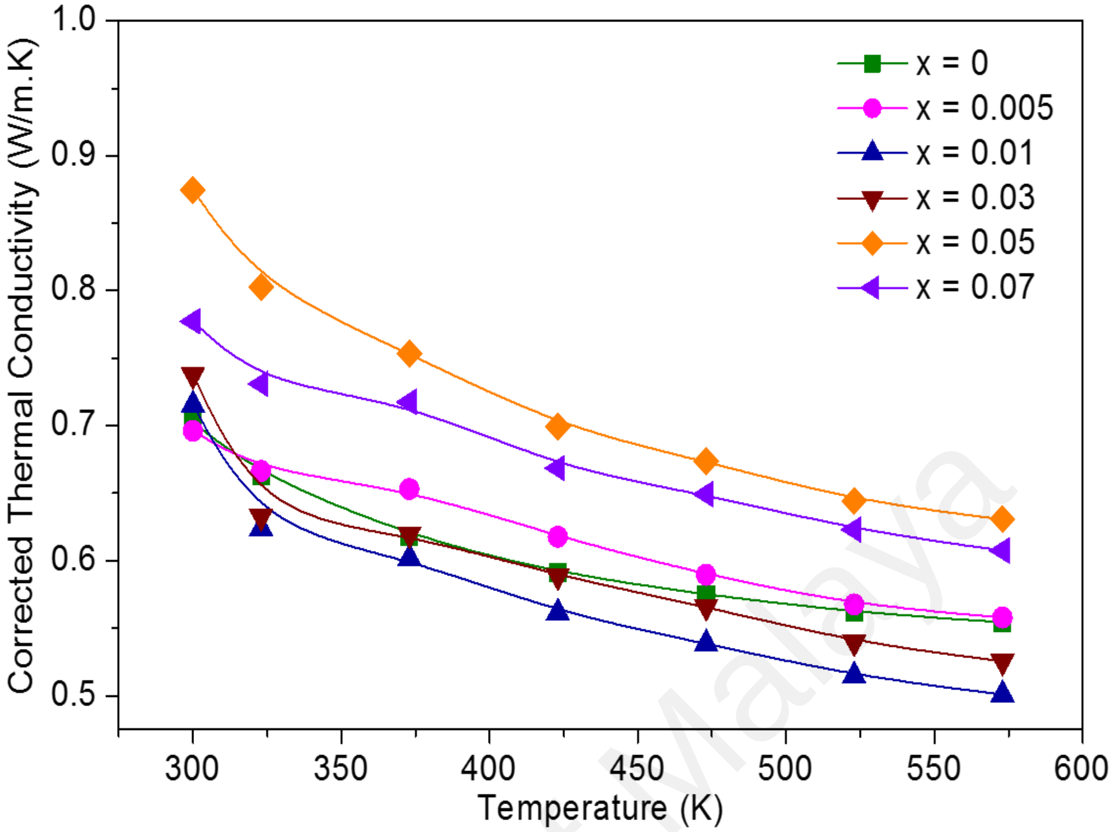

Figure 4.18: Temperature-dependent of corrected thermal conductivity for $Bi_{2-x}Ni_xS_3$ cold-pressed samples with different Ni contents.

The temperature dependence of dimensionless figure of merit *ZT* calculated by the expression, $ZT = \alpha^2 T/\rho\kappa$ is shown in Figure 4.19. The maximum *ZT* value for Bi_2S_3 sample is 0.05 at 573 K, and is further enhanced by adding Ni. A maximum *ZT* value of 0.13 was obtained for $Bi_{1.99}Ni_{0.01}S_3$ sample, which is almost three times larger than that of Ni-free sample, Bi_2S_3. The enhanced *ZT* value is attributed to significant decrease of electrical resistivity by addition of Ni atoms into Bi_2S_3 and effectiveness in suppressing the lattice thermal conductivity values by introducing porosity into the system.

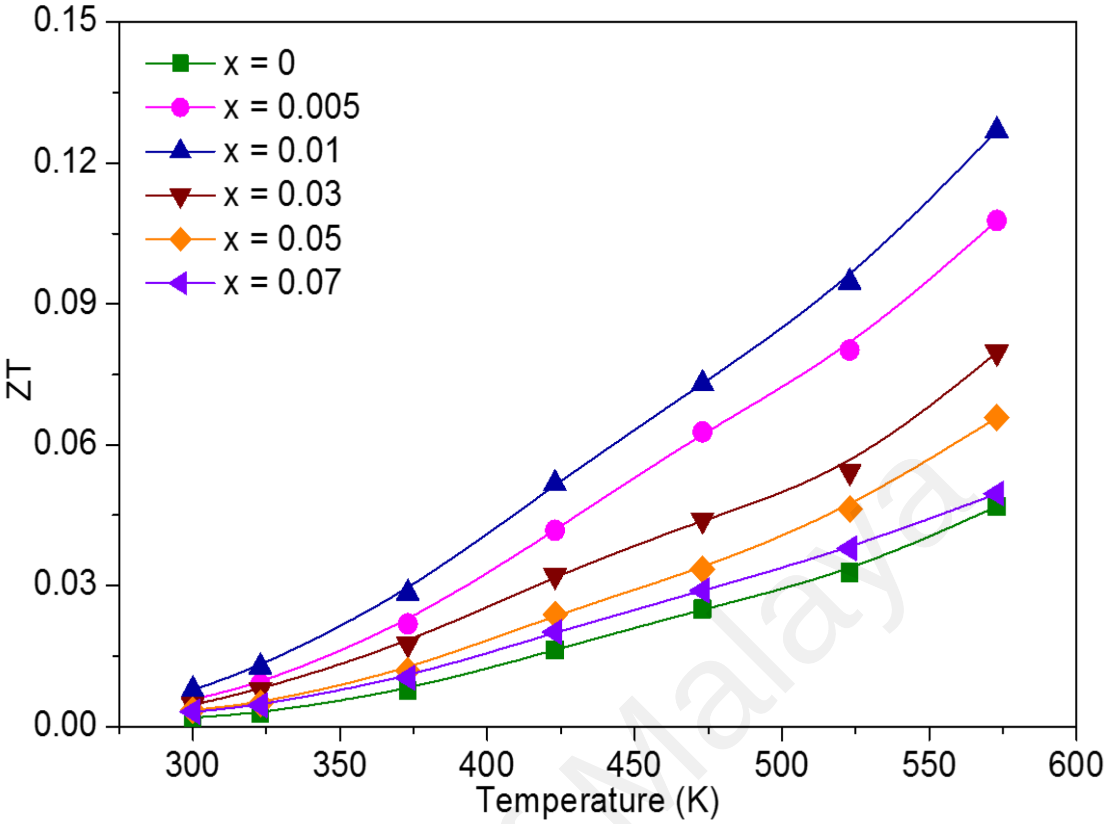

Figure 4.19: Temperature dependence of *ZT* value for $Bi_{2-x}Ni_xS_3$ samples with different Ni contents.

In this sub-section, the concurrent effect of the Ni doping and the use of cold pressing method followed with a sintering process on the thermoelectric performance Bi_2S_3 system had been evaluated. It was found that the cold pressing method impacted the thermoelectric properties in two ways: (1) introduction of Ni dopant atoms in the interstitial sites of the crystal lattice which results in an increase in carrier concentration, and (2) introduction of a porous structure which reduces the thermal conductivity. Moreover, the lower energy of cold pressing method could not able to induce all Ni atoms to penetrate into Bi_2S_3 crystal hence the electrical transport properties of Bi_2S_3 system were not optimum. A maximum *ZT* value of 0.13 was obtained for $Bi_{1.99}Ni_{0.01}S_3$ sample, which is almost three times larger than that of Ni-free sample, Bi_2S_3.

The use of higher energy densification such as SPS method is predicted will improve the electrical transport properties, thus enhance the overall thermoelectric performance of Ni doped Bi_2S_3. Therefore, in the next subsection the evaluation of thermoelectric performance of SPSed Ni doped Bi_2S_3 system will be discussed.

4.3 Group B: SPSed Ni_x added Bi_2S_3 system ($0 \leq x \leq 0.05$)

4.3.1 Microstructural properties

The XRD pattern of milled powders and SPSed bulk samples for $Bi_{2-x}Ni_xS_3$ ($0 \leq x \leq 0.05$) are shown in the Figure 4.20. It has been found that XRD peaks for all samples are identical and matched to the binary orthorhombic Bi_2S_3 phase (PDF 98-015-3946), which implies that a single phase of Bi_2S_3 was successfully formed in all samples for this group under the experimental condition. The intensity peaks obtained were sharp with a narrowed full width at half maximum (FWHM) for SPSed samples, which is a sign of grain growth and a well ordered crystalline phase compared to powder form. The average crystallite size which was calculated by Scherrer's equation showed that the milled powder samples were in the range of 44.83 – 80.92 nm, whilst the SPSed samples were in the range of 64.84 – 106.72 nm with SD of 17.32 nm and 16.1 nm for milled and SPSed samples, respectively (as listed in Table 4.6). The XRD analysis also did not detect any peaks of Ni after doping. This may be due to its low level content in the synthesized samples.

As shown in Fig.4.20(c), compared to Bi_2S_3 ($x = 0$), the addition of Ni ($0.005 \leq x \leq 0.03$) shifted the diffraction peaks toward higher 2θ value which indicated a lattice contraction. The change in the valence state and structure defect as a result of Ni dopant ions have been incorporated into the Bi sub-lattice might be the reasons for contraction in the lattice constant as well as the shift in the 2θ value. As Ni possesses an effective smaller ionic radius (0.69Å) than Bi (1.03Å), it is predicted by VEGARD's law (Pearson & Bardeen, 1949; Vegard, 1921) that the incorporation process takes place by substitution, thus resulting in an appreciable decrease in the lattice parameter of Bi_2S_3. Moreover, the diffraction peak started to shift to slightly lower 2θ value for $x = 0.05$, which indicates that the size of the unit cell become enlarged. This enlargement was predicted to be due to occupation of the interstitial sites by Ni atoms.

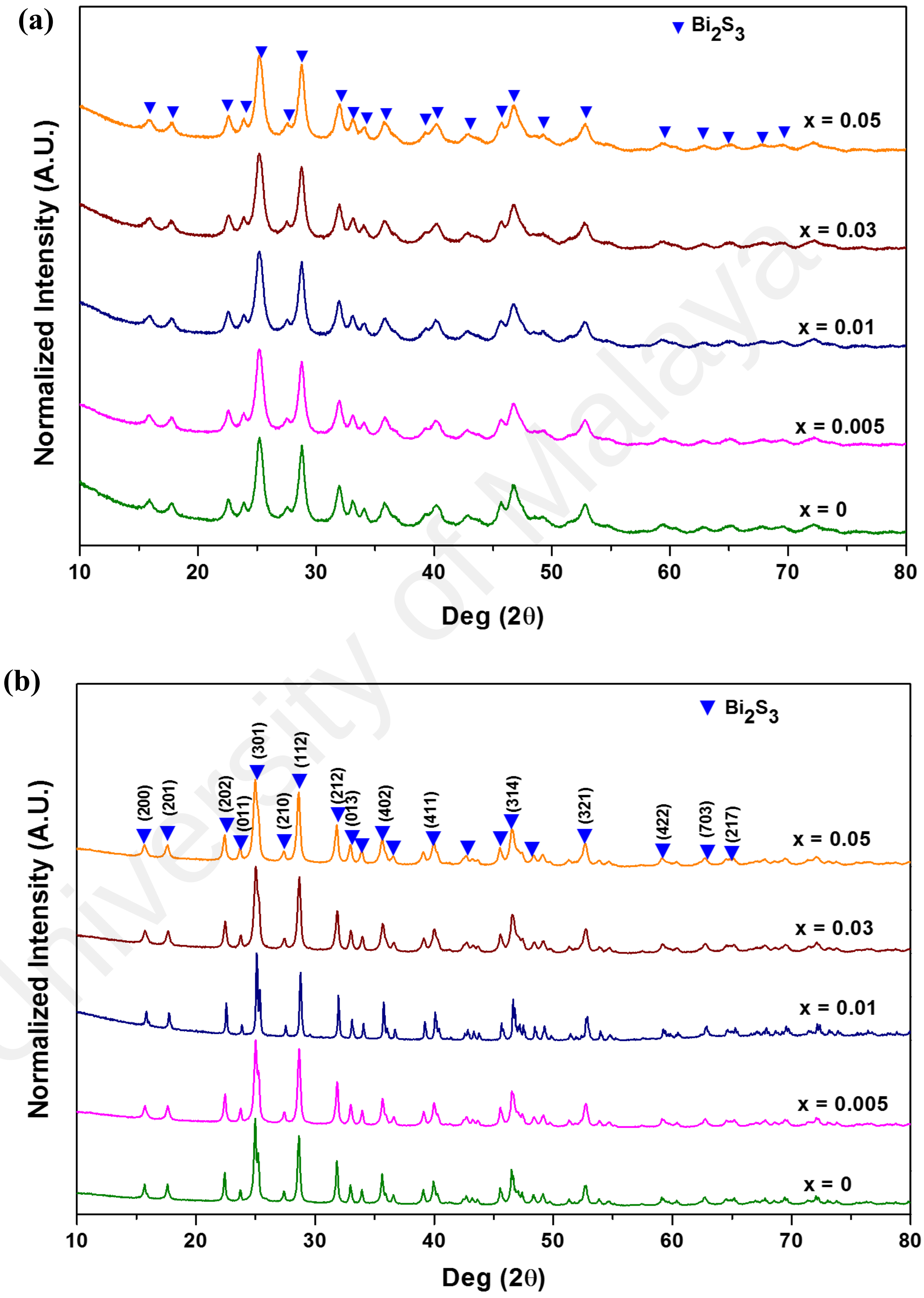

Figure 4.20: XRD patterns of $Bi_{2-x}Ni_xS_3$ samples; (a) after ball milling process, (b) and (c) SPS-treated bulks.

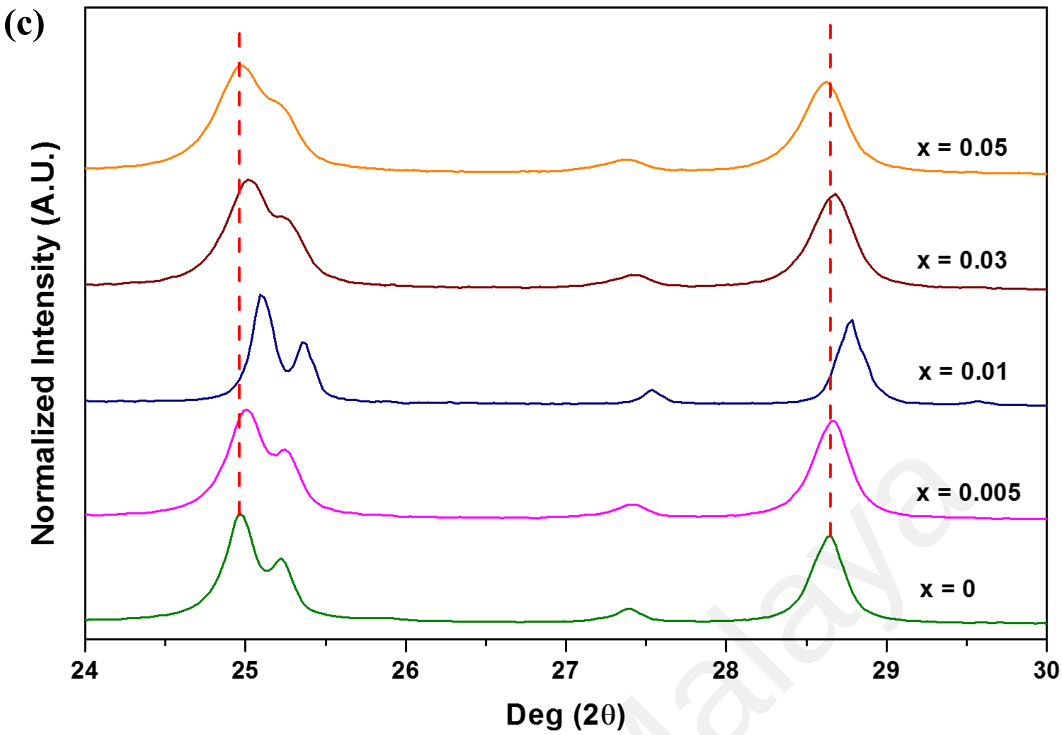

Figure 4.20, continued: XRD patterns of $Bi_{2-x}Ni_xS_3$ samples; (a) after ball milling process, (b) and (c) SPS-treated bulks.

Table 4.6: Average crystallite size and density of $Bi_{2-x}Ni_xS_3$ SPSed samples.

Ni Content (x)	Average Crystallite Size (nm)		Density (g/cm^3)	Relative Density (%)
	Milled powder	SPSed samples		
0	57.65	78.5	6.19	90.95
0.005	44.83	64.84	6.17	90.63
0.01	86.63	106.72	6.33	92.89
0.03	60.19	70.52	6.28	92.28
0.05	80.92	79.38	5.99	87.99

Moreover, the Rietveld refinement analysis of XRD pattern was implemented on all of the bulk samples. The related lattice structures are shown in Figure 4.21 and the room-temperature lattice parameters of SPSed $Bi_{2-x}Ni_xS_3$ bulk system are given in Table 4.7. The lattice parameters of Bi_2S_3 sample (x = 0) are comparable to the standard value with slightly enlargement of unit cell. It was confirmed previously that the enlarged Bi_2S_3 lattice was caused by the sulfur volatilization during MA and SPS processes (Ge *et al.*, 2011a; Ge *et al.*, 2011b). As Ni atom were incorporated into Bi_2S_3 structure, the unit cell became shrinkage and reached a limit at around 494.64Å^3 for the $Bi_{1.99}Ni_{0.01}S_3$ sample. The lattice parameters of $Bi_{1.99}Ni_{0.01}S_3$ sample indicated that *a* and *c* axis are smaller than the standard value, whilst *b* axis is slightly larger than standard value of Bi_2S_3. Furthermore, an increase on nickel content ($0.03 \leq x \leq 0.05$) caused slightly expansion on volume cell. The expansion of volume cell was assumed due to the occupation of interstitial site by a part of Ni atoms as supported by JANA results (Fig. 4.21 (c), (d)). However, the unit cell volume of $Bi_{1.97}Ni_{0.03}S_3$ sample was still smaller than Bi_2S_3 sample.

In comparison with the cold pressed samples of $Bi_{2-x}Ni_xS_3$ system which showed Ni-atoms entered the interstitial sites of Bi_2S_3 lattices for all composition, a higher energy consolidation process of SPS could induce a smaller atomic radius of Ni-atom into Bi site. Thus, lattice parameters shrunk after Ni-doping. However, it should be noted that the lattice parameter can be considered to be a function of not only atomic radius, but also valence state (Ni: 3, 2, 0 and Bi: 5, 3), electron affinity (Ni = 111.5 kJ/mol and Bi = 90.9 kJ/mol) and the increased electrostatic repulsion by Ni. Therefore, it was also could be found that the lattice parameter start to enlarge for higher concentration Ni doping ($0.03 \leq x \leq 0.05$) as a result of the interplay between those parameters.

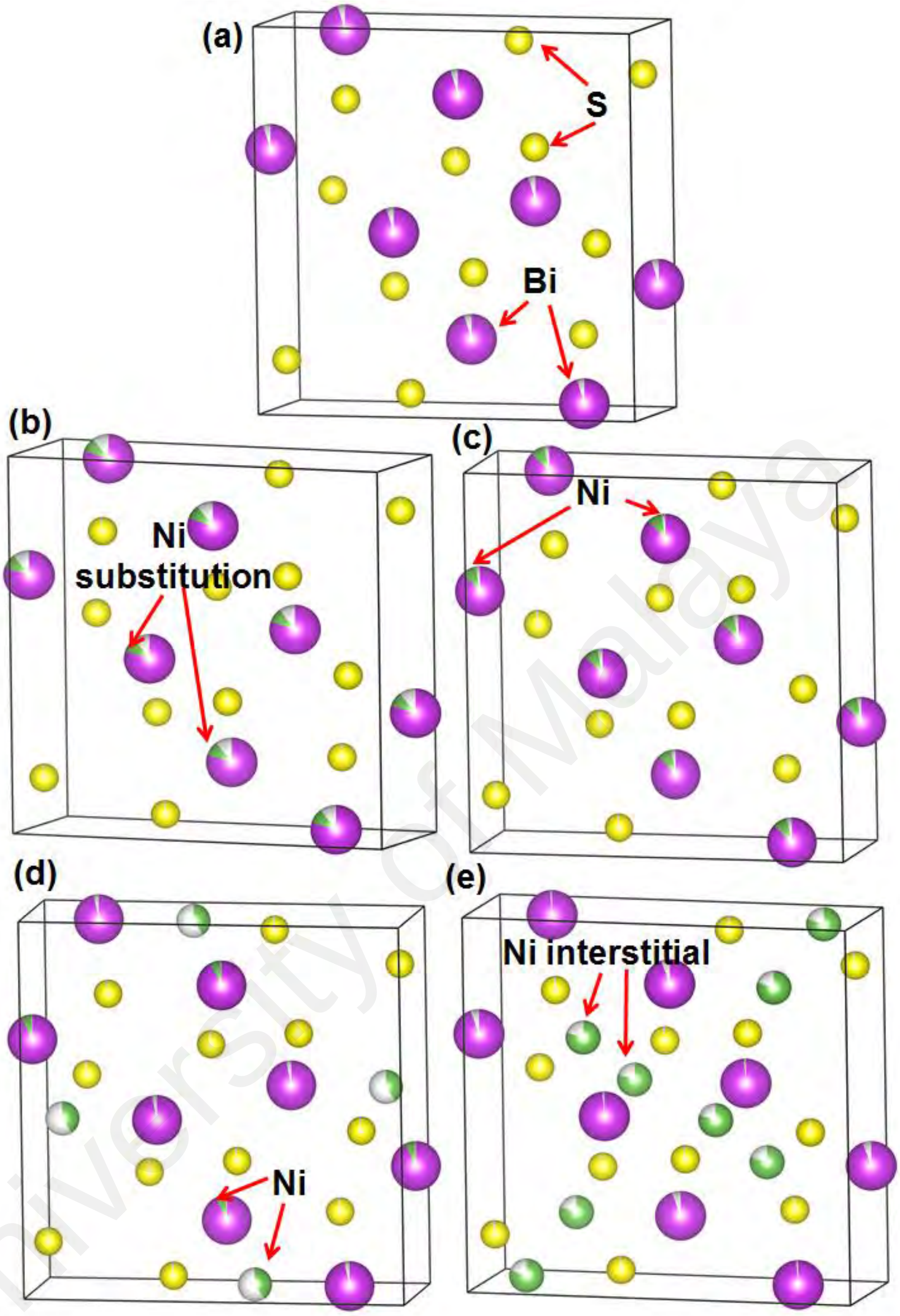

Figure 4.21: JANA 2006 refinement images of $Bi_{2-x}Ni_xS_3$ SPSed samples: (a) x = 0, (b) x = 0.005, (c) x = 0.01, (d) x = 0.03 and (e) x = 0.05.

Table 4.7: Nominal composition, lattice parameters and volume unit cell of SPSed $Bi_{2-x}Ni_xS_3$ samples.

Ni Content (x)	Nominal Composition	Lattice Parameters (Å)			Volume Unit Cell (Å^3)
		a	b	c	
0	Bi_2S_3	11.2923	3.9859	11.1452	501.66
0.005	$Bi_{1.995}Ni_{0.005}S_3$	11.2766	3.9834	11.1301	499.96
0.01	$Bi_{1.99}Ni_{0.01}S_3$	11.2312	3.9728	11.0857	494.64
0.03	$Bi_{1.97}Ni_{0.03}S_3$	11.2693	3.9826	11.1256	499.32
0.05	$Bi_{1.95}Ni_{0.05}S_3$	11.2896	3.9919	11.1386	501.98

The FESEM images of fractured surface for SPSed $Bi_{2-x}Ni_xS_3$ bulks samples are presented in Figure 4.22. All the samples showed lamellar structure with features in the nano-range (~ 55 – 274 nm in length) and no obvious secondary phase could be found on the grain boundaries, which support the XRD data that indicated a single phase of Bi_2S_3. However, the exact number of the grain size was difficult to estimated form FESEM micrographs due to the irregular shapes of the grain and the poor resolution of FESEM. The microstructural analysis confirmed that a small number of porosity appeared in all sample. The measured density as listed in Table 4.6 revealed that in general all samples have density less than 93%.

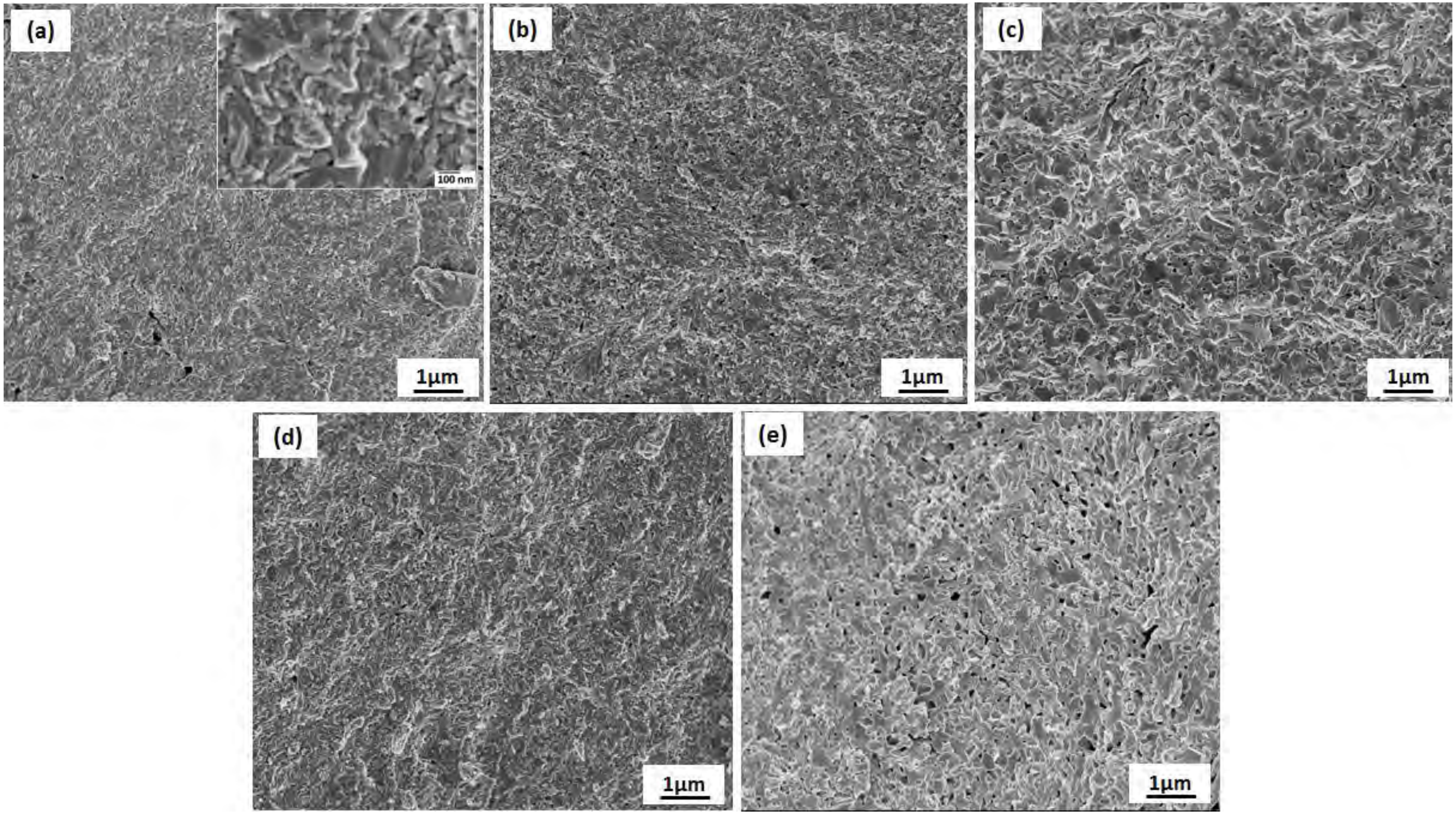

Figure 4.22: FESEM images of fractured surface of SPSed $Bi_{2-x}Ni_xS_3$ samples

a) $x = 0$, (b) $x = 0.005$, (c) $x = 0.01$, (d) $x = 0.03$ and (e) $x = 0.05$.

The energy dispersive x-ray analysis (EDS) result for Bi_2S_3 SPSed sample is shown in Figure 4.23(c). The atomic percentage ratio of Bi and S is ~ 2:3, which is refer to the nominal ratio of Bi and S in Bi_2S_3. In comparison, Figure 4.24 presented the SEM-EDS results for $Bi_{1.97}Ni_{0.03}S_3$ sample. The expected atomic percentage of constituent element would be Bi: 39.4%, Ni: 0.6%, and S: 60%. The recorded EDS spectrum revealed that the presence of Bi and S with percentages comparable to those assumed in the nominal formula of $Bi_{1.97}Ni_{0.03}S_3$ sample, without detection either Ni peak or any impurities. Moreover, the atomic ratio of Bi and S is about 2:3, which is represent the nominal ratio of Bi and S in the Bi_2S_3 phase. This result is in good agreement with the XRD analysis which showed a single phase of Bi_2S_3.

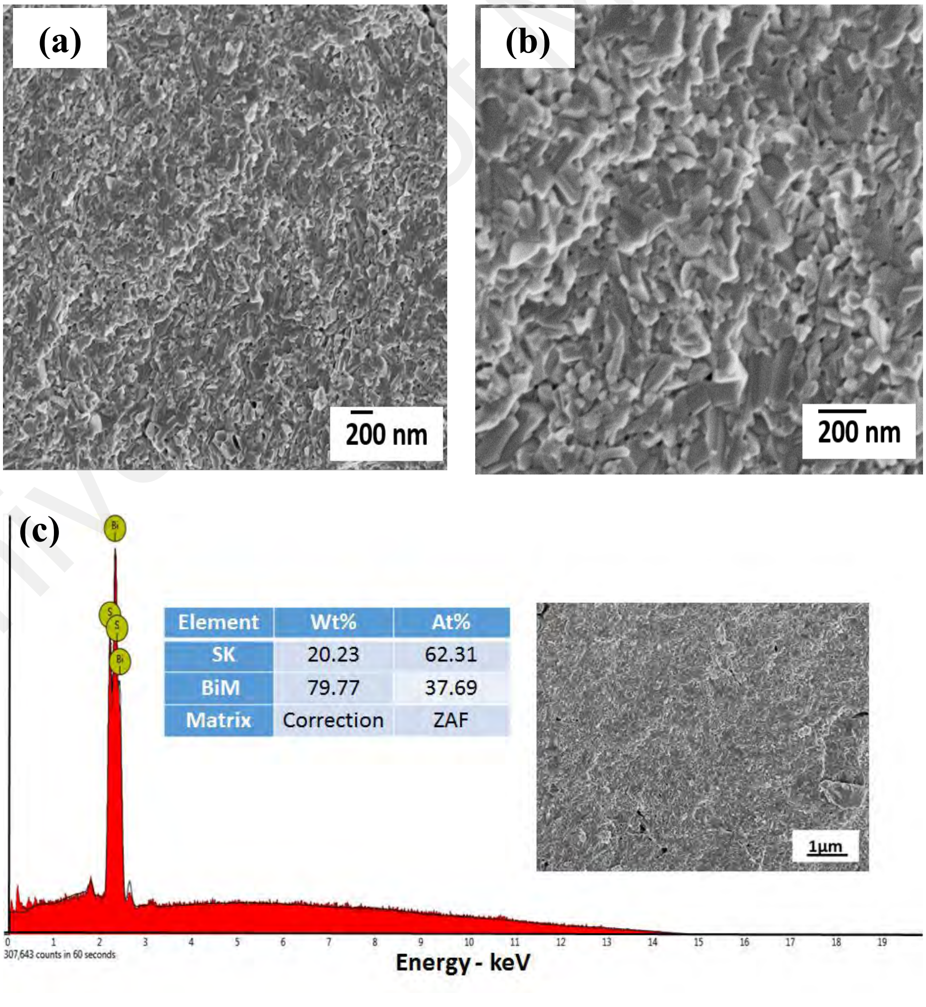

Element	Wt%	At%
SK	20.23	62.31
BiM	79.77	37.69
Matrix	Correction	ZAF

Figure 4.23: FESEM-EDS results for Bi_2S_3 SPSed sample; (a), (b) FESEM images of fractured surface in different magnification, and (c) EDS analysis.

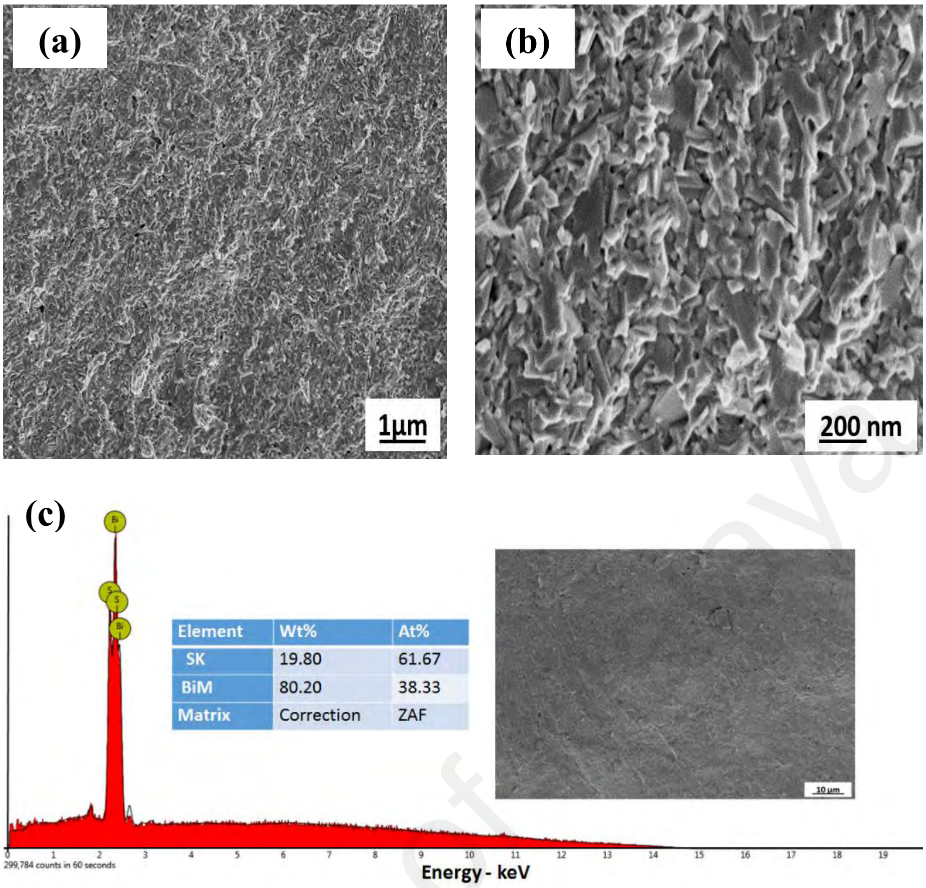

Element	Wt%	At%
SK	19.80	61.67
BiM	80.20	38.33
Matrix	Correction	ZAF

Figure 4.24: FESEM-EDS results for $Bi_{1.97}Ni_{0.03}S_3$ SPSed sample; (a), (b) FESEM images of fractured surface in different magnification, and (c) EDS analysis.

4.3.2 Thermoelectric properties

Figure 4.25 displays the temperature dependence of electrical resistivity of $Bi_{2-x}Ni_xS_3$ SPSed samples ($0 \leq x \leq 0.05$). All the samples show semiconducting behavior in the measured temperature range as the electrical resistivity decreases with increasing temperature (Ge *et al.*, 2012a). The electrical resistivity of Bi_2S_3 SPSed sample ranges from $3.45x10^{-2}$ to $1.6x10^{-3}$ Ω.m at 300 – 623 K which is comparable to the previous works on SPSed Bi_2S_3 system (Ge *et al.*, 2011a; Ge *et al.*, 2012b; Yu *et al.*, 2011). The addition of $x = 0.005$ into the system caused slightly decreasing on resistivity values in the whole measured temperature compared to pure Bi_2S_3. However, the trend of resistivity showed increasing values for an increase of Ni content up to 0.03, then decreased with further increasing Ni content of 0.05. In particular, the reduction of electrical resistivity of Bi_2S_3 already noticed at temperature above 473 K for $Bi_{1.97}Ni_{0.03}S_3$ sample. It is understood that Bi atom is trivalent (Bi^{3+}), whilst the Ni atom is bivalent (Ni^{2+}). Therefore, the replacement of Bi with Ni atom by substitution produce holes as described by the following equation:

$$Ni \xrightarrow{Bi_2S_3} 2Ni_{Bi}^{\cdot} + 3S_S + 2\dot{h} \qquad (4\text{-}3)$$

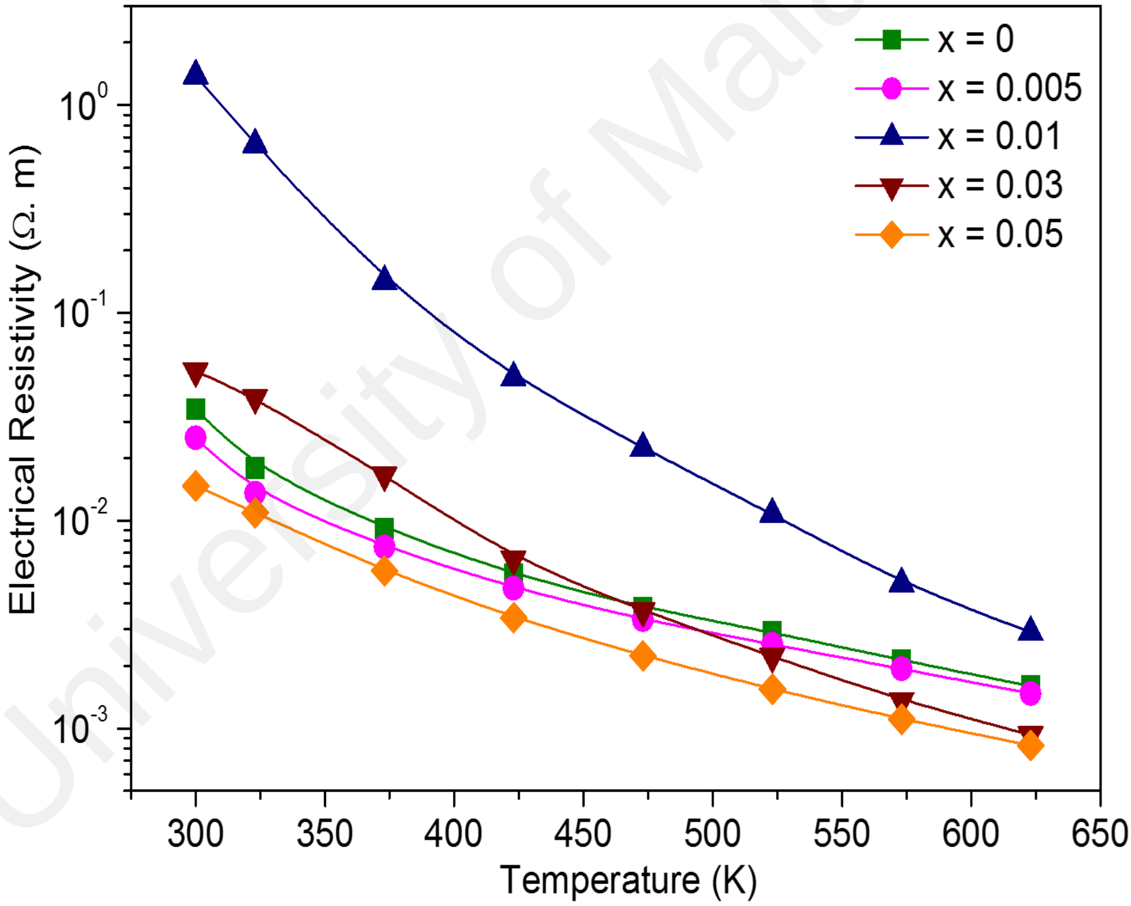

Figure 4.25: Temperature dependence of electrical resistivity ρ of $Bi_{2-x}Ni_xS_3$ SPSed samples ($0 \leq x \leq 0.05$).

The presence of holes caused a decreasing in the numbers of electron via charge neutralization, thus resulting in a corresponding increase in the resistivity value. This was observed for Ni doped samples with $x \leq 0.03$, as Ni atom substituted Bi atom at its sub lattice. Sample with $x = 0.05$ demonstrated the lowest electrical resistivity value due to Ni atoms enter the interstitial site of Bi_2S_3 lattice rather than substitution at the Bi site. This can be supported by the observation in group A (Ni doped porous system), where the interstitial location of Ni increase the numbers of carrier, n as presented in Equation (4-1) hence decrease the electrical resistivity value of Bi_2S_3. $Bi_{1.95}Ni_{0.05}S_3$ sample presented the minimum resistivity values in the whole measured temperature with the lowest value of 8.27 x 10^{-4} Ω.m at 623 K.

In comparison of electrical resistivity values of group A with group B, it was found that the minimum electrical resistivity value of 2.35 x 10^{-3} Ω.m and 8.27 x 10^{-4} Ω.m were achieved for group A and group B, respectively. The use of higher energy consolidation process of SPS lead to more penetration of Ni atom in to Bi_2S_3 system. However, the formation of interstitial solid solution of Ni dopant atoms was found as the effective way to decrease the electrical resistivity of Bi_2S_3 in both group studies, which is conflicting with the expect of Ni substitution at Bi site. Moreover, the optimum concentration of Ni dopant which can reduce electrical resistivity of Bi_2S_3 system to the lowest value by using cold pressing and SPS was shifted from 0.01 to 0.05, respectively. Based on the trend of electrical resistivity values of SPSed Ni doped Bi_2S_3 system, it is assumed that the electrical resistivity still could be reduced by increasing the Ni content.

Figure 4.26 presents the temperature dependence of Seebeck coefficient, α, for $Bi_{2-x}Ni_xS_3$ SPSed samples with different Ni contents (x). It can be clearly seen that all samples showed negative values of Seebeck coefficient in the whole measured temperature which are indicative of an n-type conduction and that the major carriers are electrons. The addition of Ni atoms in the Bi_2S_3 system enhanced the Seebeck coefficient values, which is opposite in trend than that for Ni doped porous Bi_2S_3 system. The Seebeck coefficient values for pure Bi_2S_3 sample range from -402.67 μV/K to -478.92 μV/K (a peak value of Seebeck coefficient at 300 K), whilst the Seebeck coefficient values for $Bi_{2-x}Ni_xS_3$ ($0.005 \leq x \leq 0.05$) samples range from -403.27 μV/K to -766.15 μV/K. The higher values of Seebeck coefficient for Ni doped SPSed samples compared to Bi_2S_3 sample perhaps due to the combination effect of the increase of carrier effective mass (m^*) and the adjustment of carrier concentration, n, as be described by Mott-Boltzmann formalism (Snyder & Toberer, 2008):

$$\alpha = \frac{8\pi^2 k_B^2}{3eh^2} m^* T \left(\frac{\pi}{3n}\right)^{\frac{2}{3}} \qquad (4\text{-}4)$$

where $\kappa_B$is Boltzmann constant, e is electron charge, T is absolute temperature, h is Planck constant, n is the carrier concentration and m^* is the effective mass of the carrier.

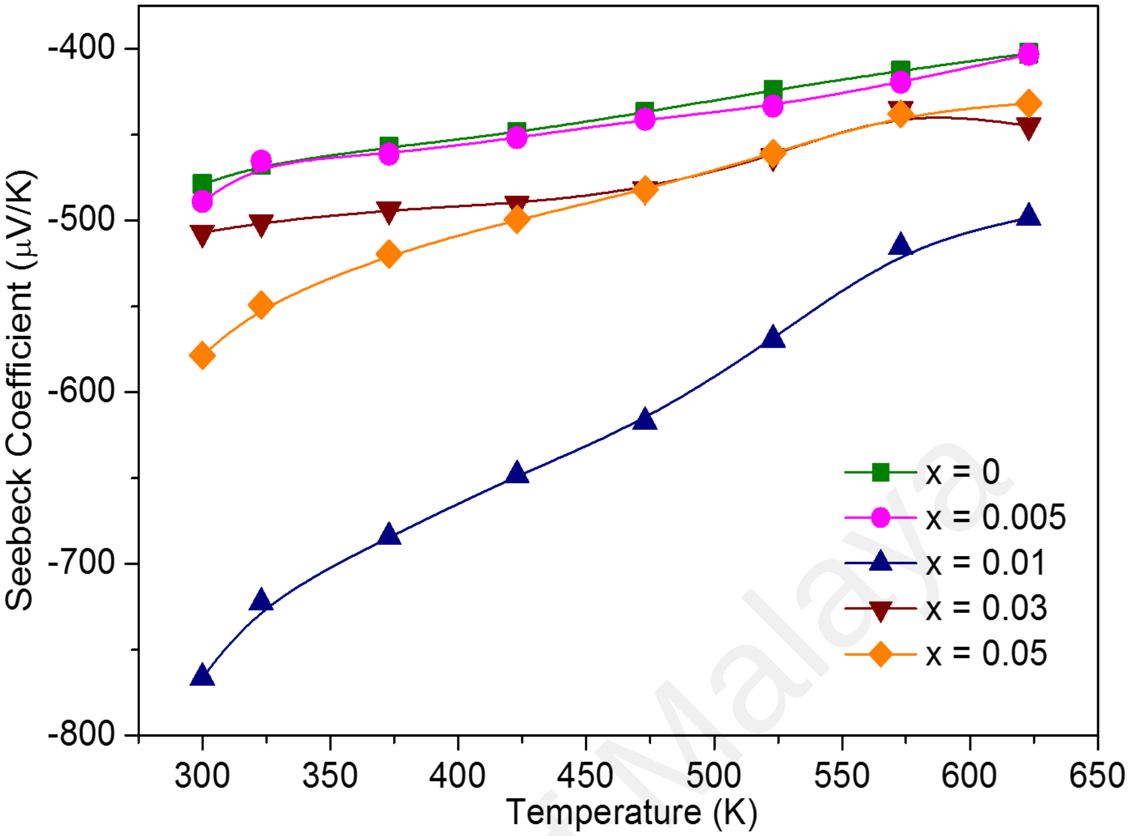

Figure 4.26: Temperature dependence of Seebeck coefficient α of $Bi_{2-x}Ni_xS_3$ SPSed samples ($0\leq x \leq 0.05$).

It can be seen in Figure 4.26 that for doped samples, the magnitude of Seebeck values were enhanced as Ni increase up to x = 0.01, and then decreased upon further Ni doping i.e. the Seebeck value decrease in the case of interstitial Ni doping. As discussed above, the substitution of Ni atoms at Bi-sub lattice will lead to the formation of holes thus decrease the number of electrons, *n*. In concurrent, the lattice shrinkage due to those substitution also lead to a decrease in interatomic distance, and caused an increase in energy gap (E_g). The changes in energy gap will induce the changing of the effective mass, $m*$, according to the Kane band system (Kane, 1957; Ravich *et al.*, 1971):

$$\frac{\hbar k^2}{2m^*} = E\left(1 + \frac{E}{E_g}\right) \tag{4-5}$$

Here *E* is the electron energy and ħ is the reduced Planck constant. Thus, the substitution of Ni atoms at Bi-sub lattice result in an increase on effective mass*,* and lead to enhancement of Seebeck coefficient values. It was also reported from the previous works that the increase of effective mass in PbTe and related materials were induced by either temperature (Tauber *et al.*, 1966; Yu *et al.*, 1970) or chemical substitution (Heremans *et al.*, 2008).

$Bi_{1.99}Ni_{0.01}S_3$ sample which has a smallest unit cell volume, due to substitution of Ni dopant, presented the maximum Seebeck coefficient in the whole measured temperature with the highest magnitude of -766.15 μV/K at 300 K. This value is about 1.6 times higher than that of the Bi_2S_3 sample (-478.92 μV/K). Furthermore, in comparison with other maximum Seebeck values of Bi_2S_3 bulk system found in the literature as presented in Table 4.5 , the obtained Seebeck coefficient in this study higher than reported elemental doped Bi_2S_3 system, except for Ag_x-doped system which showed a comparable value to the results of -800 μV/K for $Bi_{1.93}Ag_{0.07}S_3$ at 323 K (Yu *et al.*, 2011). In conclusion, the role of Ni substitution is significant to enhance the better Seebeck value.

Figure 4.27 displays the temperature dependence of the power factor, *PF*, for $Bi_{2-x}Ni_xS_3$ SPSed samples which is defined from the electrical resistivity and Seebeck coefficient values. The power factor of pure Bi_2S_3 sample is 6.66 $\mu W/m.K^2$ at 300 K and increase to 101.59 $\mu W/m.K^2$ when raising the temperature to 623 K. All samples showed a similar upward trends with temperature. The power factor slightly increased for $Bi_{1.995}Ni_{0.005}S_3$ sample, and further decreases by increasing the Ni content up to $x = 0.03$. Then, the power factor values re-increased by further addition of Ni (x = 0.05). In particular, the power factor for $Bi_{1.97}Ni_{0.03}S_3$ sample showed higher values after 423 K. This trend is similar to the variation of electrical resistivity which indicated that the reduction in electrical resistivity provides more contribution to enhance the power factor than the Seebeck coefficient. Moreover, the highest power factor value of 225.36 µW/m.K^2 at 623 K was achieved for $Bi_{1.95}Ni_{0.05}S_3$ sample. In comparison to the highest power factor value of Ni doped porous Bi_2S_3 system (67.94 µW/mK^2), the SPS method could improve ~3.3 times higher of the power factor value.

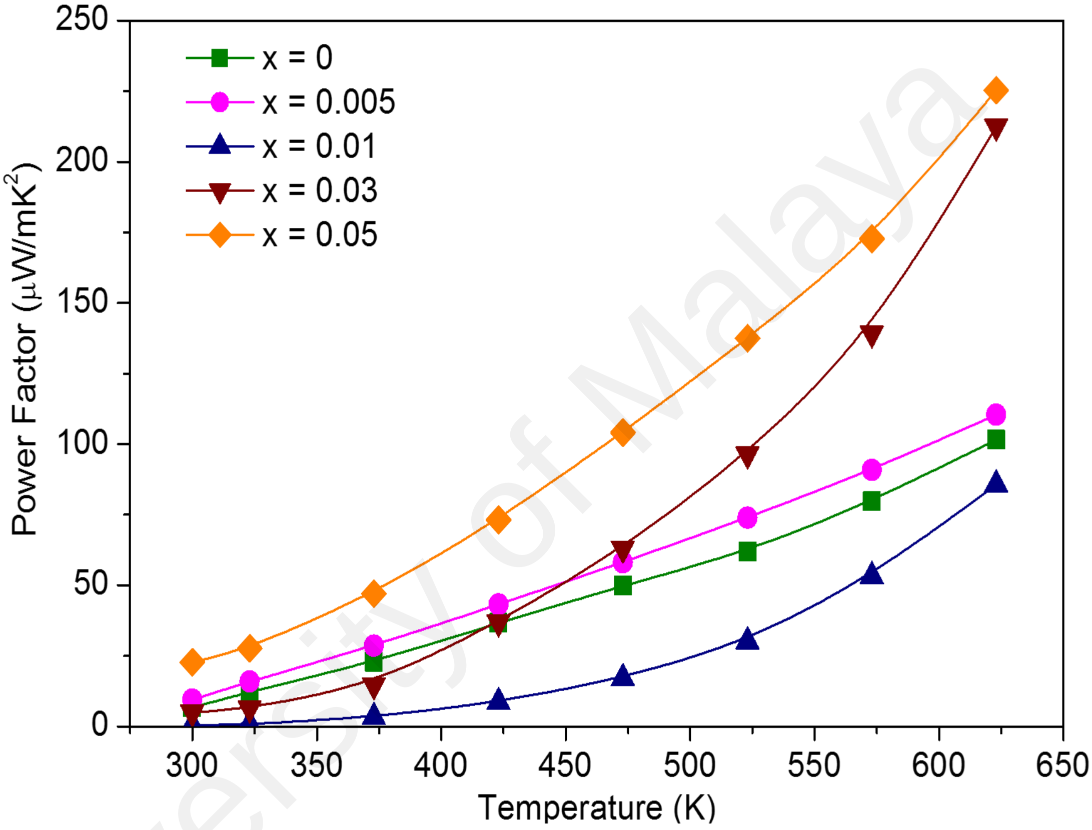

Figure 4.27: Temperature dependence of power factor *PF* of of $Bi_{2-x}Ni_xS_3$ SPSed samples ($0 \leq x \leq 0.05$).

Figure 4.28 presents the variation of thermal conductivity, κ, of $Bi_{2-x}Ni_xS_3$ SPSed samples calculated from thermal diffusivity, specific heat capacity and bulk density. The total thermal conductivity is the sum of electronic thermal contribution (κ_{el}) and lattice thermal contribution (κ_{lat}). As illustrated, almost all of samples showed a downward trend of thermal conductivity as temperature rises which is indicated the dominance of the phonon scattering effect. The calculated electronic thermal contribution ($\kappa_{el} = LT/\rho$

, where $L = 2.45 \times 10^{-8}\ V^2\ K^2$) for all samples was found to be smaller than 5% of the total thermal conductivity (as presented in Fig.4.29), which indicates the lattice thermal conductivity significantly dominates the decreasing in thermal conductivity value.

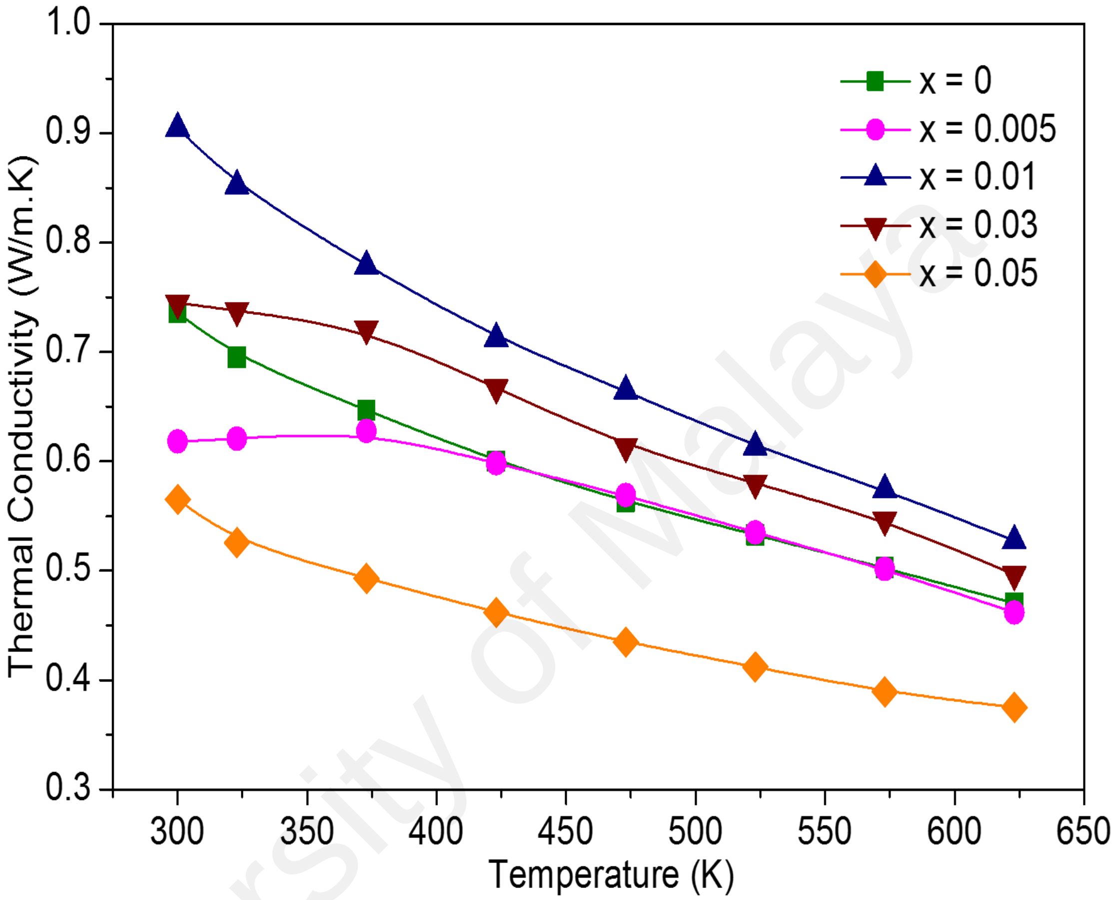

Figure 4.28: Temperature dependence of thermal conductivity of of $Bi_{2-x}Ni_xS_3$ SPSed samples ($0 \leq x \leq 0.05$).

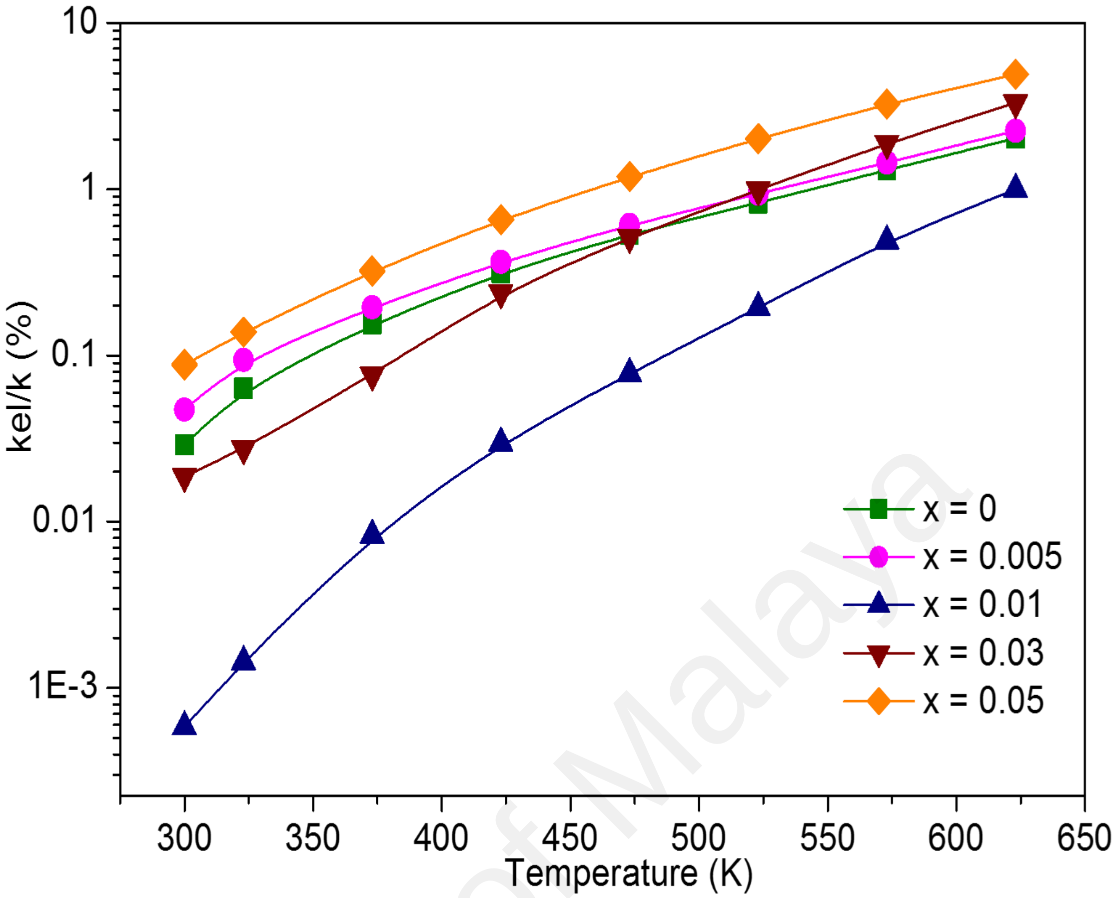

Figure 4.29: Temperature dependence of electronic contribution to total thermal conductivity of $Bi_{2-x}Ni_xS_3$ SPSed samples ($0 \leq x \leq 0.05$).

The thermal conductivity of pure Bi_2S_3 sample decreased from 0.76 W/m.K to 0.47 W/m.K in the temperature ranges from 300 to 623 K, whose values are lower than the same composition of Bi_2S_3 reported by Zhao *et al.* (2008) (0.84-0.88 W/m.K) and Ge *et al.* (2012b) (0.59-0.85 W/m.K). A lower thermal conductivity value of Bi_2S_3 sample in this work could be attributed to its average grain size, which is smaller (~135 nm) than that of 400 nm and 200 nm reported by Zhao *et al.* (2008) and Ge *et al.* (2012b), respectively. The addition of Ni exhibited different effect on thermal conductivity of Bi_2S_3 system. $Bi_{1.995}Ni_{0.005}S_3$ sample presented lower thermal conductivity values than pure Bi_2S_3 sample up to 373 K. Furthermore, its thermal conductivity slightly rise with increasing temperature and tended to decrease above 573 K. The thermal conductivity of

Ni doped samples recorded higher values than Bi_2S_3 sample for $0.005 < x \leq 0.03$, and its values decreasing with an increase in Ni content. Moreover, $Bi_{1.95}Ni_{0.05}S_3$ sample presented the minimum thermal conductivity values in whole measured temperature with the lowest value of 0.38 W/m.K at 623 K, which implies that the thermal conductivity of Bi_2S_3 could be reduced by ~ 20.4%. $Bi_{1.95}Ni_{0.05}S_3$ sample has the lowest bulk density (88%) compared to other samples. Therefore, the presence of porous structure contributed to the decrease on thermal conductivity as the same result appeared in the Ni doped porous Bi_2S_3 system (group A).

Figure 4.30 shows the temperature dependence of lattice thermal conductivity (κ_{lat}) for $Bi_{2-x}Ni_xS_3$ SPSed samples, which was estimated by subtracting the electronic contribution from the total thermal conductivity using Wiedemann–Franz law ($\kappa_{lat} = \kappa - \kappa_{el}$). The lattice thermal conductivity for all samples showed a downward trend with increasing temperature, which is ascribed to the strong phonon scattering (Yu *et al.*, 2011). In the Ni content ranges of $0.005 < x \leq 0.03$, the lattice thermal conductivity presented higher values than that Bi_2S_3 sample. Moreover, there is a reduction on lattice thermal conductivity with further increasing in Ni content. In particular, the $Bi_{1.95}Ni_{0.05}S_3$ sample with interstitial Ni recorded the lowest value of ~ 0.36 W/m.K at 673 K. Those lowest of lattice thermal conductivity is predicted as the results of; (1) higher porosity, which capable of increasing phonon scattering via pores. (2) The presence of Ni atoms in Bi_2S_3 interstices, which strongly scattered the small wavelength of phonons due to the random location of Ni interstitial. Zheng *et al.* (2017) also reported that the introduction of interstitial defects would maximize the mass and strain fluctuation between host and guest atoms and therefore phonon scattering. Compared to the lattice thermal conductivity at room temperature for the recent work of Iodine doped Bi_2S_3 (~0.72 W/m.K) (Yang *et al.*, 2017), the lattice thermal conductivity of $Bi_{1.95}Ni_{0.05}S_3$ sample (0.55 W/m.K) is still lower than that value.

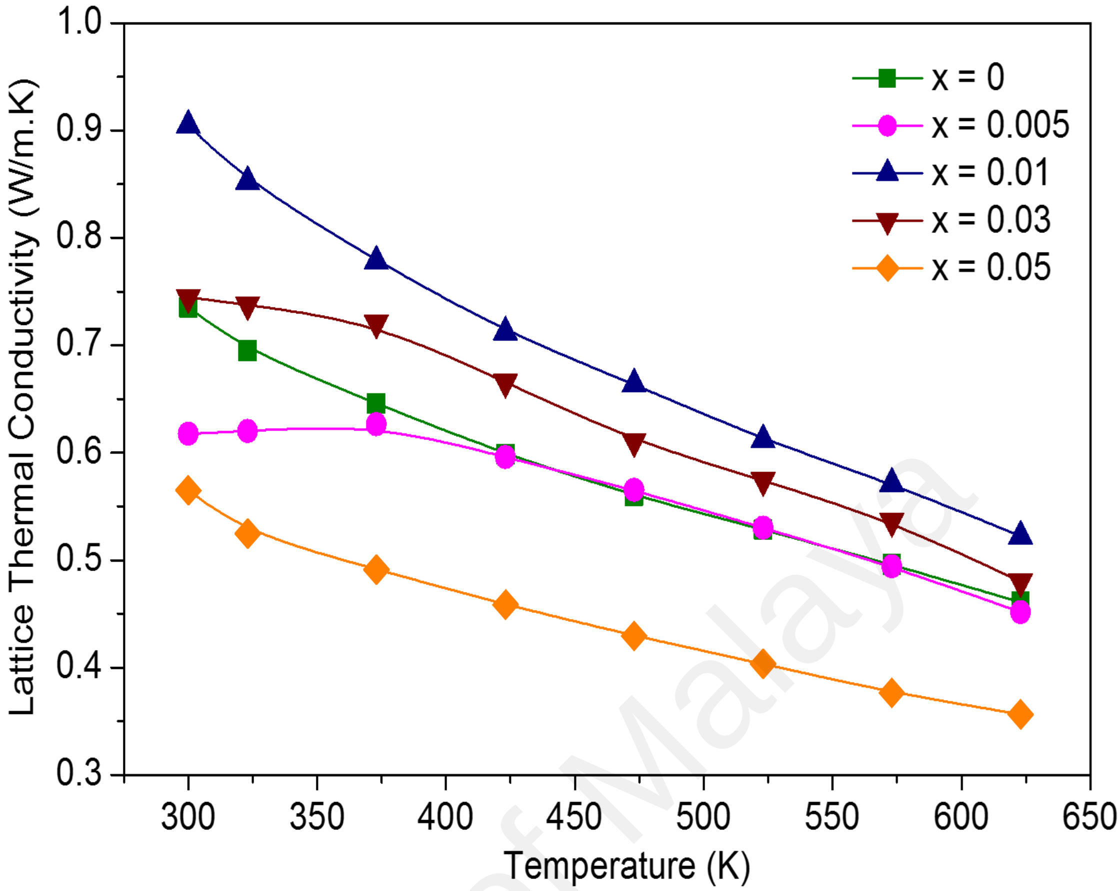

Figure 4.30: Temperature dependence of lattice thermal conductivity of $Bi_{2-x}Ni_xS_3$ SPSed samples ($0 \leq x \leq 0.05$).

Figure 4.31 illustrates the temperature dependence of the thermoelectric dimensionless figure of merit (*ZT*) of $Bi_{2-x}Ni_xS_3$ SPSed samples. The Bi_2S_3 sample has a maximum *ZT* value of 0.13 at 673 K. This value is about 2.6 times higher than that of porous Bi_2S_3 system (ZT_{max} = 0.05). It can be observed that the addition of Ni into the Bi_2S system in the range of Ni contents of $0.005 < x \leq 0.01$ leads to a decrease in the *ZT* values. A considerably enhanced of *ZT* was recorded with increasing Ni more than 0.01. The highest *ZT* value of 0.38 was recorded by $Bi_{1.95}Ni_{0.05}S_3$ sample at 673 K, which is significantly higher than that of Bi_2S_3 sample. Generally, the enhancement of *ZT* values for Ni doped Bi_2S_3 system of SPSed sample is about 2 times higher than that of porous sample (group A) at the same temperature.

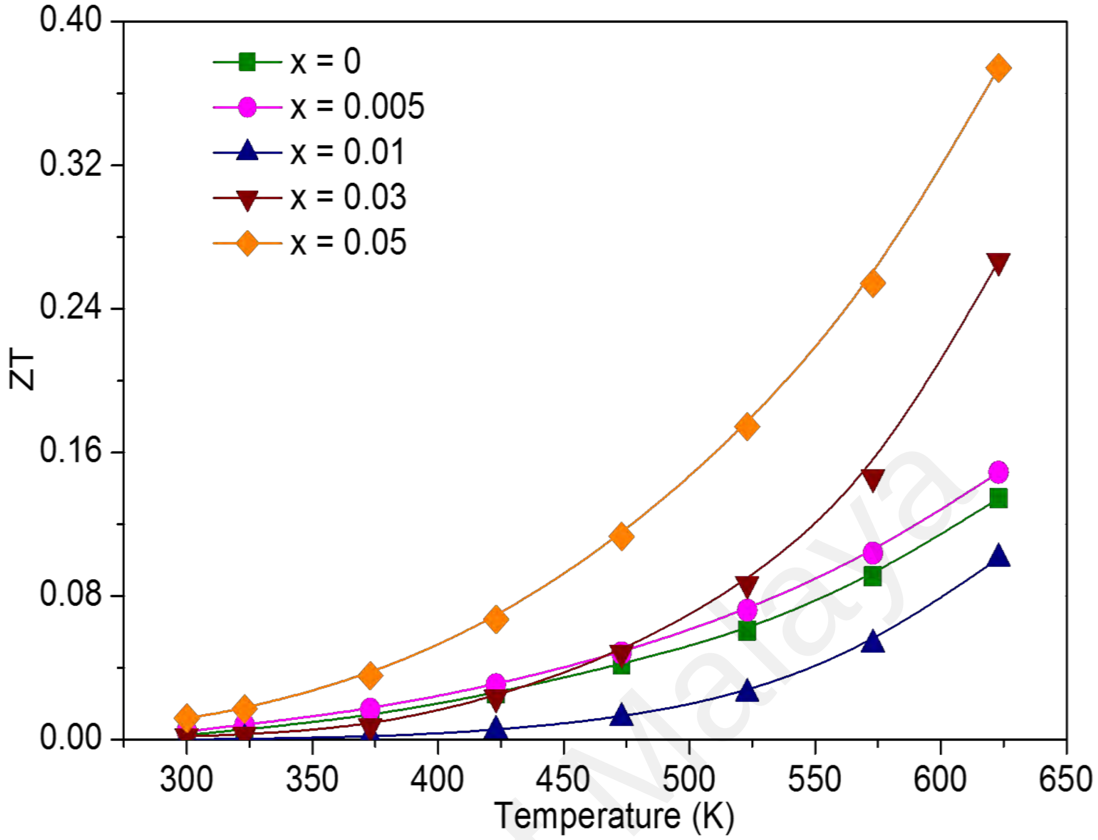

Figure 4.31: Temperature dependence of dimensionless figure of merit, *ZT*, of $Bi_{2-x}Ni_xS_3$ SPSed samples ($0 \leq x \leq 0.05$).

In comparison to the previous reports, the obtained *ZT* value in this study is higher than that attained by $Bi_{1.99}Ag_{0.01}S_3$ in the study of Yu *et al.* (2011) as listed in Table 4.8. It is also comparable to the results for Cu-doped (Ge *et al.*, 2012a), Ce-doped (Pei *et al.*, 2017) and Bi/Bi_2S_3 nano-composite (Ge *et al.*, 2017). The enhancement of *ZT* value for SPSed Ni doped Bi_2S_3 compound is mainly ascribed to; (1) the significant reduction of electrical resistivity, due to the presence of Ni atoms in the Bi_2S_3 interstices, and (2) the decreased on thermal conductivity, due to increase of phonon scattering via pore and interstitial defect structure.

Table 4.8: *ZT* maximum of elementals doped Bi_2S_3 system.

Compound	*ZT* maximum	References
Bi_2S_{3-x}	0.11 @ 523 K	(Zhao *et al.*, 2008)
$Bi_{2-x}Ag_xS_3$	0.25 @ 573 K	(Yu *et al.*, 2011)
$Bi_{2-x}Cu_xS_3$	0.34 @ 573 K	(Ge *et al.*, 2012a)
$Bi_{2-x}Ag_{3x}S_3$	0.23 @ 573 K	(Ge *et al.*, 2012b)
$Bi_2S_{3-x}Se_x$	0.16 @ 573 K	(Zhang *et al.*, 2013)
$(Bi_{1-x}Sb_x)_2S$	0.10 @ 300 K	(Kawamoto & Iwasaki, 2014)
ZnO added Bi_2S_3	0.66 @ 675 K	(Du *et al.*, 2015)
$Ce_xBi_2S_3$	0.33 @ 573 K	(Pei *et al.*, 2017)
BiI_3 doped Bi_2S_3	0.58 @ 773 K	(Yang *et al.*, 2017)
Bi/Bi_2S_3 nanocomposite	0.36 @ 623 K	(Ge *et al.*, 2017)
Sn doped Bi_2S_3	0.67 @ 673 K	(Guo *et al.*, 2017)

As summary for group B, the thermoelectric properties of SPSed Ni doped Bi_2S_3 system are affected by several factors which can be concluded as follows; (1) the formation of interstitial solid solution of Ni dopant atom which lead to the increase of charge carrier, is effectively in reducing the electrical resistivity value of Bi_2S_3 system. Whilst, (2) the formation of substation solid solution of Ni doped Bi_2S_3 was found to give more contribution on the enhancement of Seebeck coefficient, and (3) the concurrent effect of porous structure and interstitial defect significantly scattered the phonons, thus reduced the thermal conductivity values. The highest *ZT* value of 0.38 was attained by $Bi_{1.95}Ni_{0.05}S_3$ sample at 673 K, which is significantly higher than that of Bi_2S_3 sample.

The work of Guo *et al.* (2017) reported that introducing Sn as a dopant into Bi_2S_3 system under solvothermal and microwave sintering method increased the electrical conductivity due to the improvement of carrier concentration, and simultaneously "stabilized" the Seebeck coefficient, which is probably ascribed to the effect of resonant level doping. An enhanced maximum *ZT* value of 0.67 was achieved at 673 K. This prior research motivated our next investigation to study the use of Sn dopant atom on Bi_2S_3 bulk system. Therefore, in the next subsection the evaluation of thermoelectric performance of SPSed Sn doped Bi_2S_3 system will be discussed.

4.4 Group C: SPSed Sn_{3x}-added Bi_2S_3 system ($0 \leq x \leq 0.1$)

4.4.1 Microstructural properties

The XRD pattern of milled powders samples for $Bi_{2-x}Sn_{3x}S_3$ ($0\leq x \leq 0.1$) are shown in Figure 4.32(a). It has been found that the predominant phase is orthorhombic Bi_2S_3 phase (PDF 98-015-3946) with the secondary phase of Bi (PDF 01-085-1330). The XRD analysis did not detect any peaks of Sn after doping. This may due its low level content in the synthesized samples. The Bi peaks are detected at 27.4˚, 38.1˚ and 56.2˚, which 27.4˚ peak showed the highest intensity compare with other peaks. The presence of Bi peaks indicated that there are still sufficient amount of bismuth that not well mechanically alloyed. Further, the introduction of SPS method as consolidation process caused the uniform single phase of crystalline Bi_2S_3 was obtained (Fig. 4.32(b)). A small intensity peak of BiSn phase (PDF 00-027-0896) was showed for SPSed sample with $x = 0.01$. The intensity peaks obtained were sharp with narrowed full width at half maximum (FWHM) for SPSed samples, which is a sign of grain growth and well-ordered crystalline phase compared to powders form. The average crystallite size of milled powder samples calculated by Scherrer's equation showed that the MA powder samples were in the range of 57.65 – 103.33 nm, whilst the SPSed samples were in the range of 73.81 – 92.29 nm with SD of 21.6 nm and 8.33 nm for milled and SPSed samples, respectively (as listed in Table 4.9).

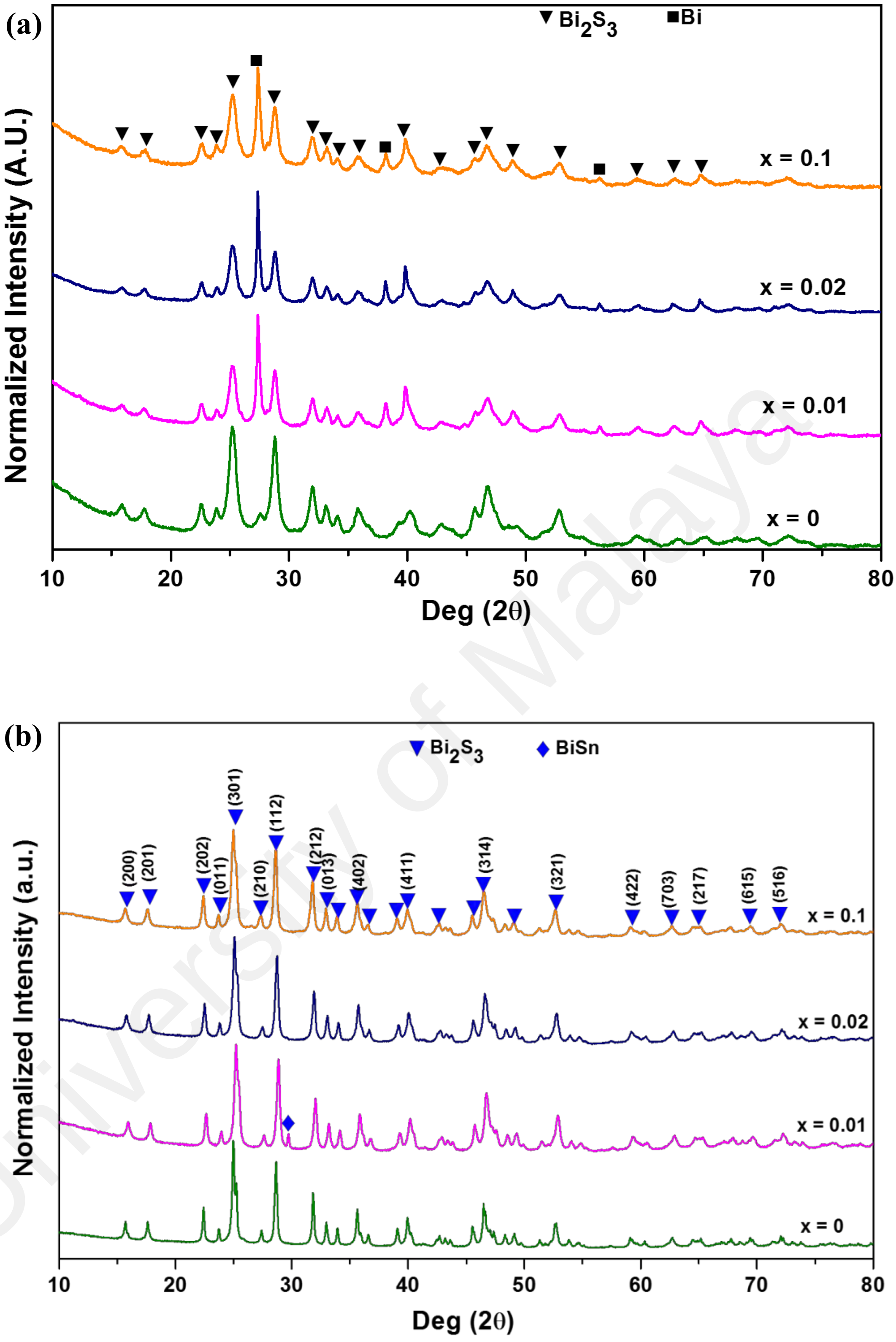

Figure 4.32: XRD patterns of $Bi_{2-x}Sn_{3x}S_3$ samples ($0 \leq x \leq 0.1$); (a) after ball milling process, (b) and (c) SPS-treated bulks.

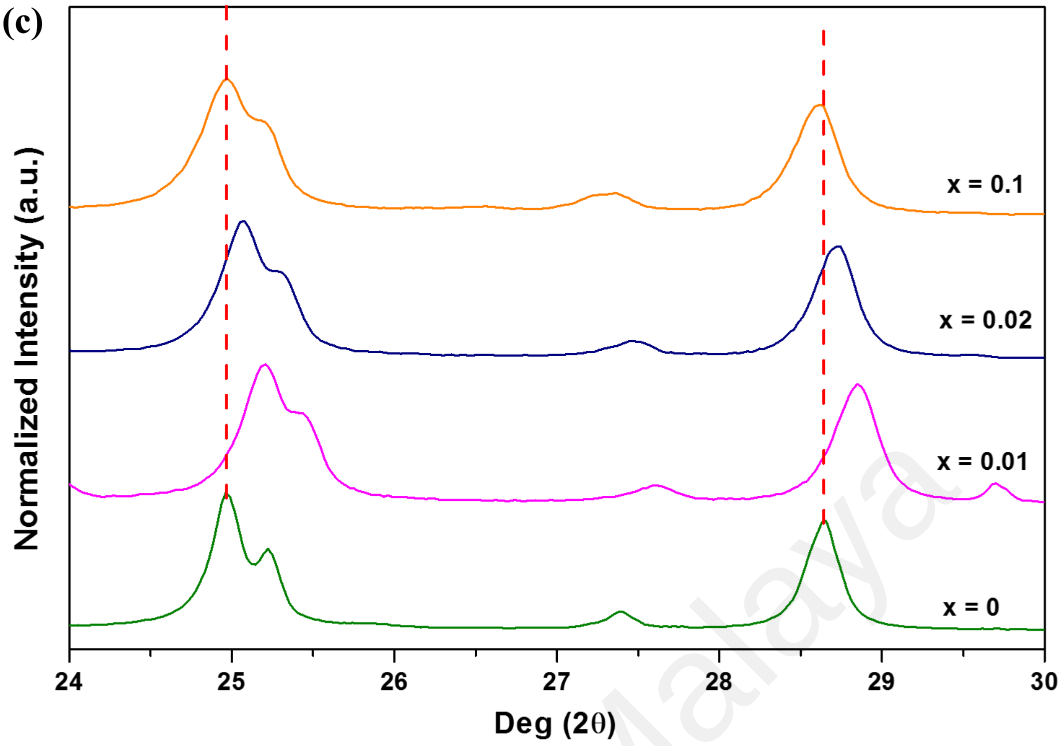

Figure 4.32, continued: XRD patterns of $Bi_{2-x}Sn_{3x}S_3$ samples ($0 \leq x \leq 0.1$); (a) after ball milling process, (b) and (c) SPS-treated bulks.

Table 4.9: Average crystallite size and density of SPSed $Bi_{2-x}Sn_{3x}S_3$ samples.

Sn Content (x)	Average Crystallite Size (nm)		Density (g/cm^3)	Relative Density (%)
	Milled powder	SPSed samples		
0	57.65	78.5	6.19	90.95
0.01	60.20	73.81	6.17	90.62
0.02	84.17	92.29	6.08	89.24
0.1	103.33	87.15	6.29	92.38

As clearly seen in 4.32(c), compared to pure Bi_2S_3 sample, the addition of Sn ($0.01 \leq x \leq 0.02$) produced a shift of diffraction peaks toward higher 2θ value which indicated a lattice contraction. The change in the valence state and structure defect due to strain as a result of Sn dopant ions have been incorporated into the Bi sub-lattice might be the reasons for contraction in the lattice constant as well as the shift in the 2θ value. Furthermore, it is predicted by VEGARD's law (Pearson & Bardeen, 1949; Vegard, 1921) that the incorporation process takes place by substitution due to the fact that the Sn possesses an effective smaller ionic radius (0.69Å) compare to Bi (1.03Å). Thus, resulted in a decreased lattice parameter of Bi_2S_3. For sample with $x = 0.1$, the diffraction peak start to shift to lower 2θ value, which indicating the size of unit cell become enlarged. This enlargement was predicted due to occupation of the interstitial sites of Bi_2S_3 by Sn atoms.

The room-temperature lattice parameters of $Bi_{2-x}Sn_{3x}S_3$ SPSed bulk system which was calculated using the XRD data are given in Table 4.10. The lattice parameters shrunk and reached a limit at around 489.45$Å^3$ of unit volume after Sn-doping, indicating that Sn-atoms have substituted Bi-atoms in the lattice structure. Further addition of Sn_{3x} ($x = 0.02$) caused slightly expansion on volume unit cell compare to sample with $x = 0.01$ but this volume cell still smaller than pure Bi_2S_3 sample. Moreover, increasing of $x > 0.02$ caused an expansion on volume cell and $Bi_{1.9}Sn_{0.3}S_3$ samples exhibited a large volume unit cell than pure Bi_2S_3 sample. The expansion of the lattice parameters as well as the volume unit cell suggest that Sn has occupied the Bi_2S_3 interstices. The proposed structure from Rietveld refinement analysis using JANA2006 of $Bi_{2-x}Sn_{3x}S_3$ compounds are presented in Figure 4.33.

Table 4.10: Nominal composition, lattice parameters and volume unit cell of $Bi_{2-x}Sn_{3x}S_3$ SPSed samples.

Sn Content (x)	Nominal Composition	Lattice Parameters (Å)			Volume Unit Cell (Å^3)
		a	b	c	
0	Bi_2S_3	11.2923	3.9859	11.1452	501.66
0.01	$Bi_{1.99}Sn_{0.03}S_3$	11.1906	3.9617	11.0401	489.45
0.02	$Bi_{1.98}Sn_{0.06}S_3$	11.2502	3.9782	11.1016	496.85
0.1	$Bi_{1.9}Sn_{0.3}S_3$	11.2919	3.9891	11.1466	502.09

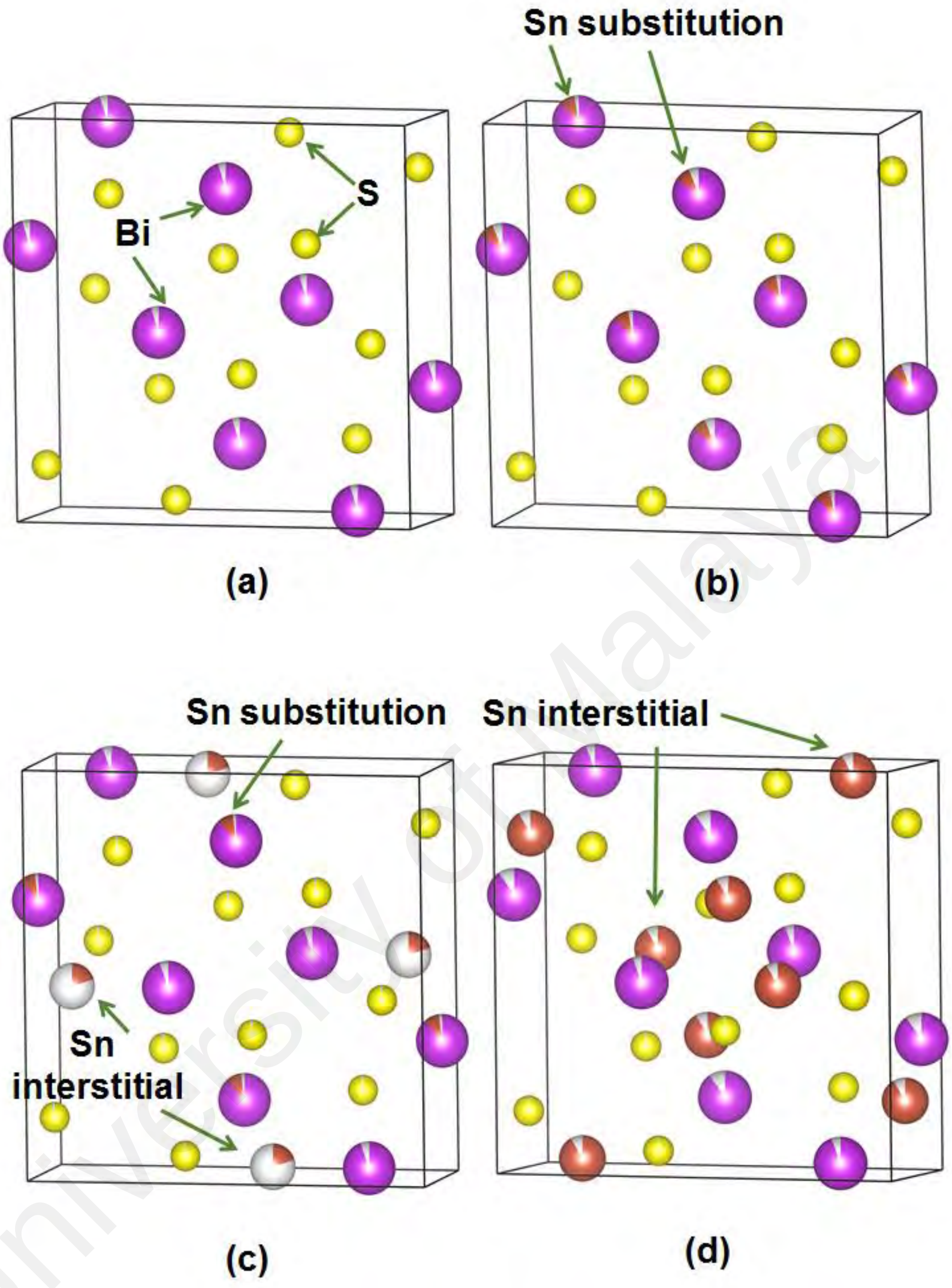

Figure 4.33: JANA 2006 refinement images of $Bi_{2-x}Sn_{3x}S_3$ SPSed samples: (a) x = 0, (b) x = 0.01, (c) x = 0.02, and (d) x = 0.1.

Figure (4.34) – (4.36) display FESEM – EDS results of $Bi_{2-x}Sn_{3x}S_3$ SPSed sample with different Sn content. The results of FESEM images of fracture surface for $Bi_{1.99}Sn_{0.03}S_3$ and $Bi_{1.98}Sn_{0.06}S_3$ sample presented a granular-lamellar structure, whilst a lamellar structures were exhibited for $Bi_{1.9}Sn_{0.3}S_3$ sample. In addition, all the samples have grains of sub-micron size with no obvious large-scale preferred orientation. The microstructural analysis confirmed that all the doped samples are not dense with small porosity appeared. $Bi_{1.98}Sn_{0.06}S_3$ sample has the lowest density i.e. about 89.24% of the theoretical density and smaller grain size compare to other Sn doped samples.

The EDS results of doped samples recorded numerous well-defined peaks were evident concerned to Bi, S and Sn. No other peaks related to impurities detected in the spectrum, which further confirmed that the synthesized compounds are Sn doped Bi_2S_3. According to EDS, the ration of Bi to S is ~ 2: 3, which represent the nominal ratio of Bi and S in Bi_2S_3 phase. This result is in good agreement with the XRD analysis which revealed the dominate phase of the Bi_2S_3. Although a small peak of BiSn was observed in XRD patterns of $Bi_{1.99}Sn_{0.03}S_3$ sample (Figure 4.32(b)), such impurity phase was not clearly observed from SEM and EDS analysis.

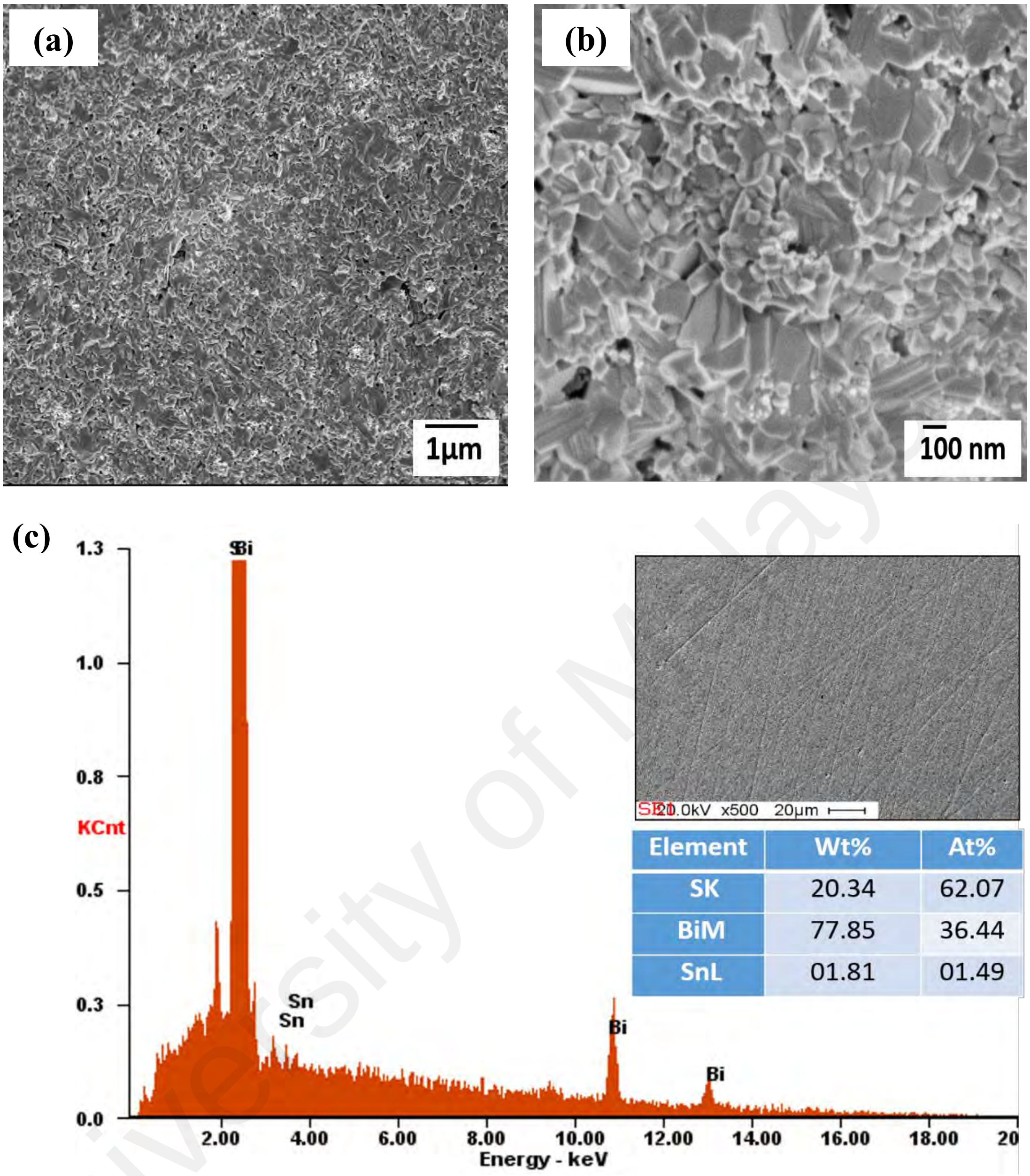

Element	Wt%	At%
SK	20.34	62.07
BiM	77.85	36.44
SnL	01.81	01.49

Figure 4.34: SEM-EDS results of $Bi_{1.99}Sn_{0.03}S_3$ SPSed sample; (a), (b) SEM images of fractured surface in different magnification, and (c) EDS analysis.

.

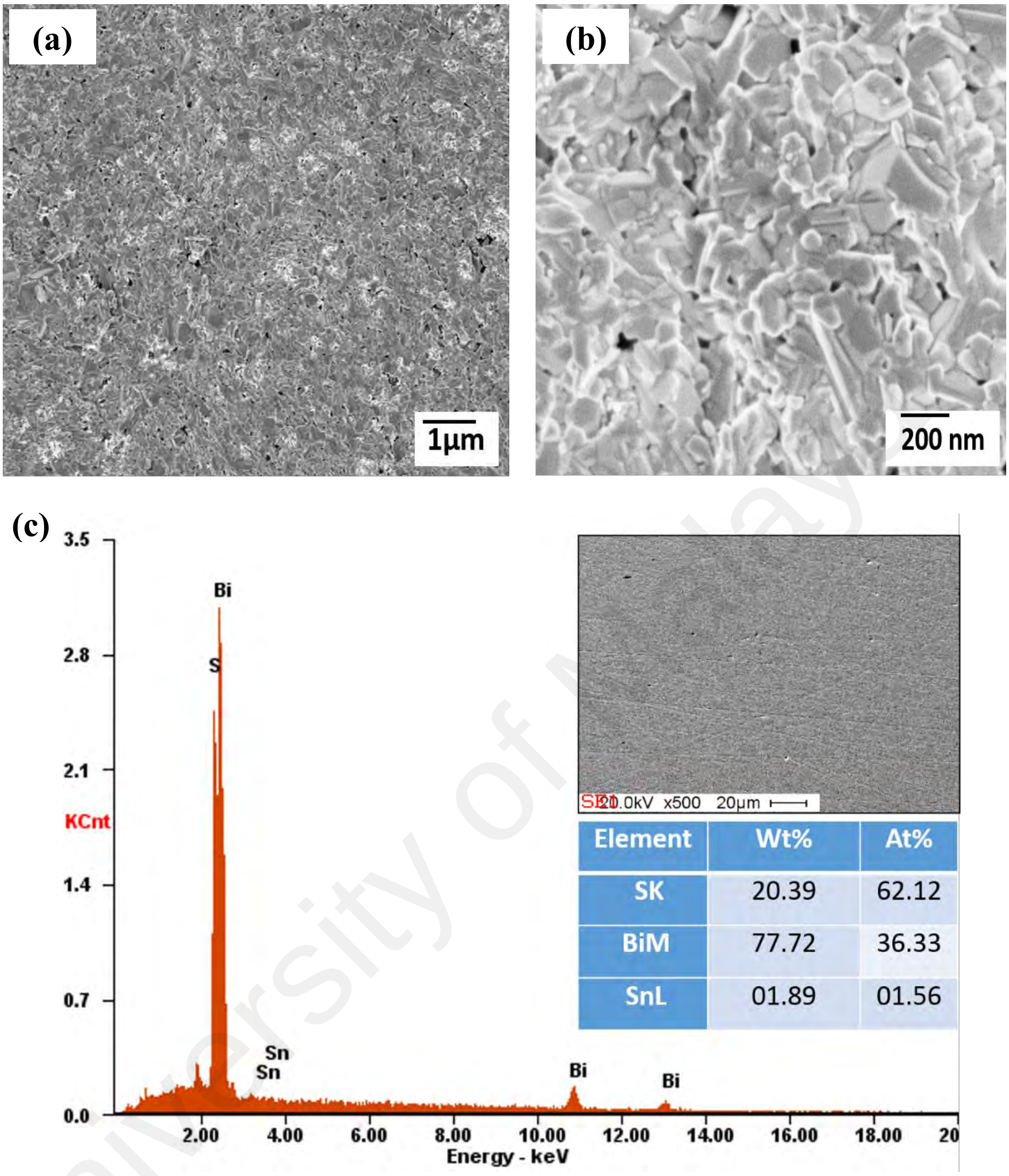

Element	Wt%	At%
SK	20.39	62.12
BiM	77.72	36.33
SnL	01.89	01.56

Figure 4.35: SEM-EDS results of $Bi_{1.98}Sn_{0.06}S_3$ SPSed sample; (a), (b) SEM images of fractured surface in different magnification, and (c) EDS analysis.

.

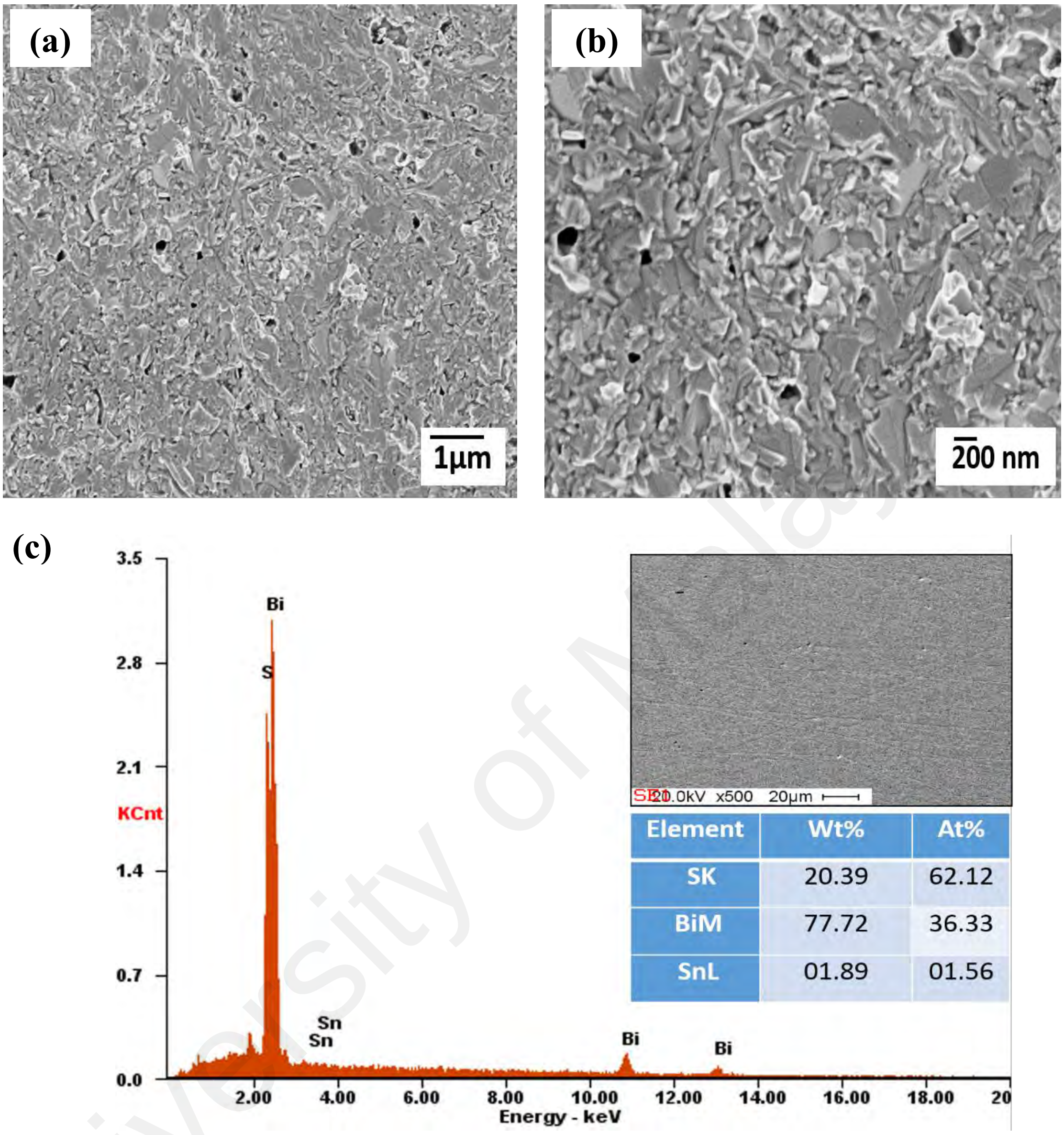

Element	Wt%	At%
SK	20.39	62.12
BiM	77.72	36.33
SnL	01.89	01.56

Figure 4.36: SEM-EDS results of $Bi_{1.9}Sn_{0.3}S_3$ SPSed sample; (a), (b) SEM images of fractured surface in different magnification, and (c) EDS analysis.

.

4.4.2 Thermoelectric properties

The temperature dependence of electrical resistivity, ρ, for $Bi_{2-x}Sn_{3x}S_3$ SPSed bulk samples with different Sn contents are shown in Figure.4.37. All samples show semiconducting behavior in the measured temperature range as the electrical resistivity decreases with increasing temperature (Ge *et al.*, 2012a). The addition of Sn into Bi_2S_3 system resulted in increasing the electrical resistivity values. These results indicated that the acceptor will be introduced as Sn^{2+} is substituted for Bi^{3+}. The electron concentration will decrease due to compensation effect, resulted in a rise of electrical resistivity value. It was noticed from the Figure.4.37 that the electrical resistivity of doped samples reduced with increasing the Sn content. The electrical resistivity values of heavily doped compound ($x = 0.1$) are smaller than that of lightly doped compound ($x = 0.01, 0.02$). This phenomenon arises in consequence of Sn atoms start to entering the interstitial site of Bi_2S_3 lattice and formed an interstitial solid solution, and resulted in an increase in the number of carrier. The minimum resistivity value of 1.26 x 10^{-3} Ω.m at 623 K was achieved for $Bi_{1.9}Sn_{0.3}S_3$ sample. It is predicted that further increase in Sn content ($x > 0.1$) will result in a decrease of electrical resistivity values lower than that of pure Bi_2S_3 sample. The microwave-sintered Sn doped Bi_2S_3 recorded an electrical resistivity value of 1.33 x 10^{-4} Ω.m at 623 K (Guo *et al.*, 2017), which was an order of magnitude lower than result herein. It is assumed that the difference of results are comes from that fact that the work of microwave-sintered Sn doped Bi_2S_3 by Guo *et al.* (2017) has successfully introduced Sn dopant atom in the form of Sn^{4+} which lead to increase the carrier concentration, hence decreased the electrical resistivity values. Whilst, Sn^{2+} was introduced under this work.

In comparison to Ni doped Bi_2S_3 system results in group B, the minimum electrical resistivity value of Sn doped Bi_2S_3 system under this investigation is about 1.5 times higher at the same temperature. Moreover, there is a different in minimum dopant concentration to improve the carrier concentrations and reduce electrical resistivity. The minimum dopant concentration (x) was 0.05 and 0.1 for Ni and Sn, respectively. Sn is more resistive than Ni due the fact that the electrical resistivity of 1.09 x 10^{-7} Ω.m and 6.99 x 10^{-8} Ω.m at 300 K for Sn and Ni, respectively.

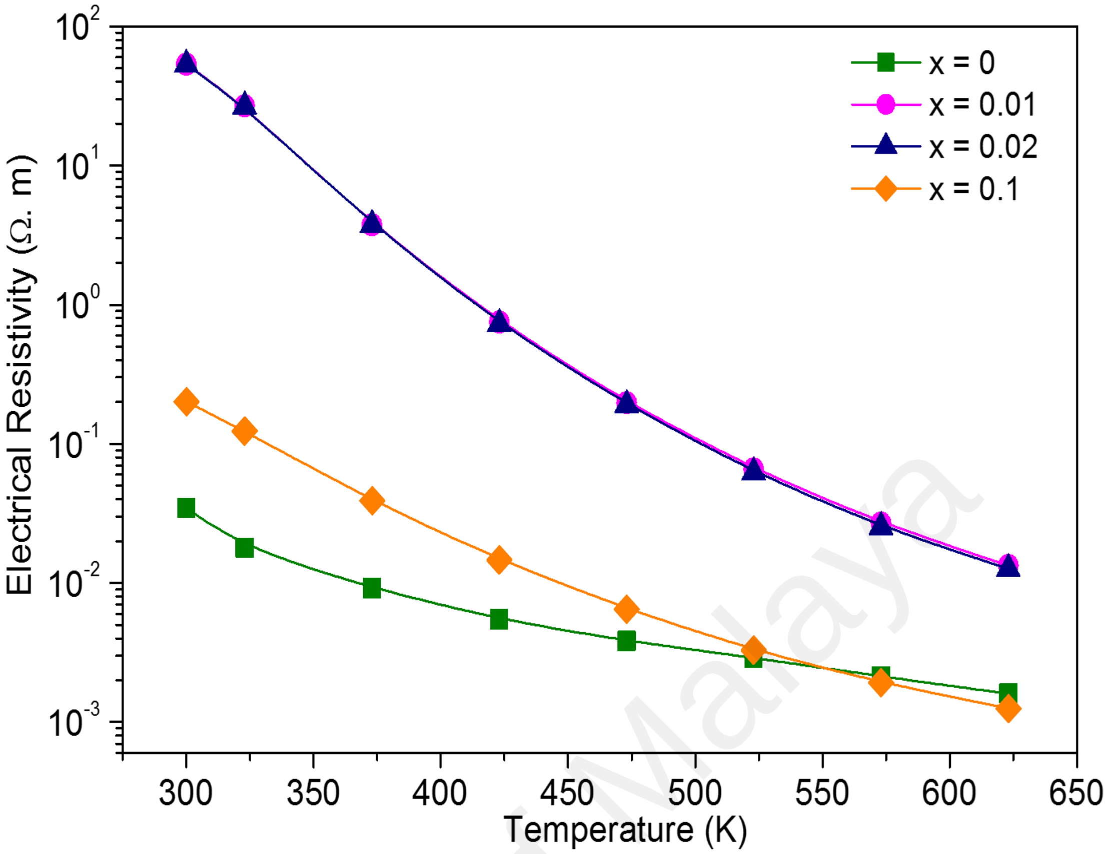

Figure 4.37: Temperature dependence of electrical resistivity ρ of $Bi_{2-x}Sn_{3x}S_3$ SPSed samples ($0 \leq x \leq 0.1$).

The variation of the Seebeck coefficient (α) for $Bi_{2-x}Sn_{3x}S_3$ with temperature are shown in Figure. 4.38. The negative values of Seebeck coefficient found for all of samples over entire temperature range showed that an *n*-type conduction, and that the major charge carriers are electrons. The Seebeck coefficient values of Sn doped samples ($x > 0$) is larger than that of pure Bi_2S_3. At 300 K, the magnitude of Seebeck coefficient increased from -478.92 µV/K to -1168.05 µV/K as x increased from 0 to 0.01, which is about 2.4 times higher than that (-478.92 µV/K) of Bi_2S_3. The Seebeck coefficient values for $Bi_{2-x}Sn_{3x}S_3$ ($0.01 \leq x \leq 0.1$) samples ranges from -407.80 µV/K to -1170.25 µV/K. The trend of Seebeck coefficient for Sn doped samples are found to decrease with increasing Sn content. A higher values of Seebeck coefficient for Sn doped samples perhaps due to the combination effect of the increase of carrier effective mass (m^*) and the adjustment of carrier concentration, *n*, in consequence of the formation substitution or interstitial solution as discussed in the previous sub section 4.3.2 for Seeebeck coefficient of Ni doped Bi_2S_3 system (group B). $Bi_{1.99}Sn_{0.03}S_3$ sample which has the smallest unit cell volume presented the largest Seebeck coefficient in the whole measured temperature with the highest magnitude of -1170.25 μV/K at 50˚C, which is about 2.5 times higher than that of the pure Bi_2S_3 sample (-467.24 μV/K). Furthermore, in comparison with other Seebeck values of Bi_2S_3 bulk system found in the literature as listed in Table 4.5 and Ni doped Bi_2S_3 in the group B, $Bi_{1.9}Sn_{0.01}S_3$ presented the largest Seebeck value so far.

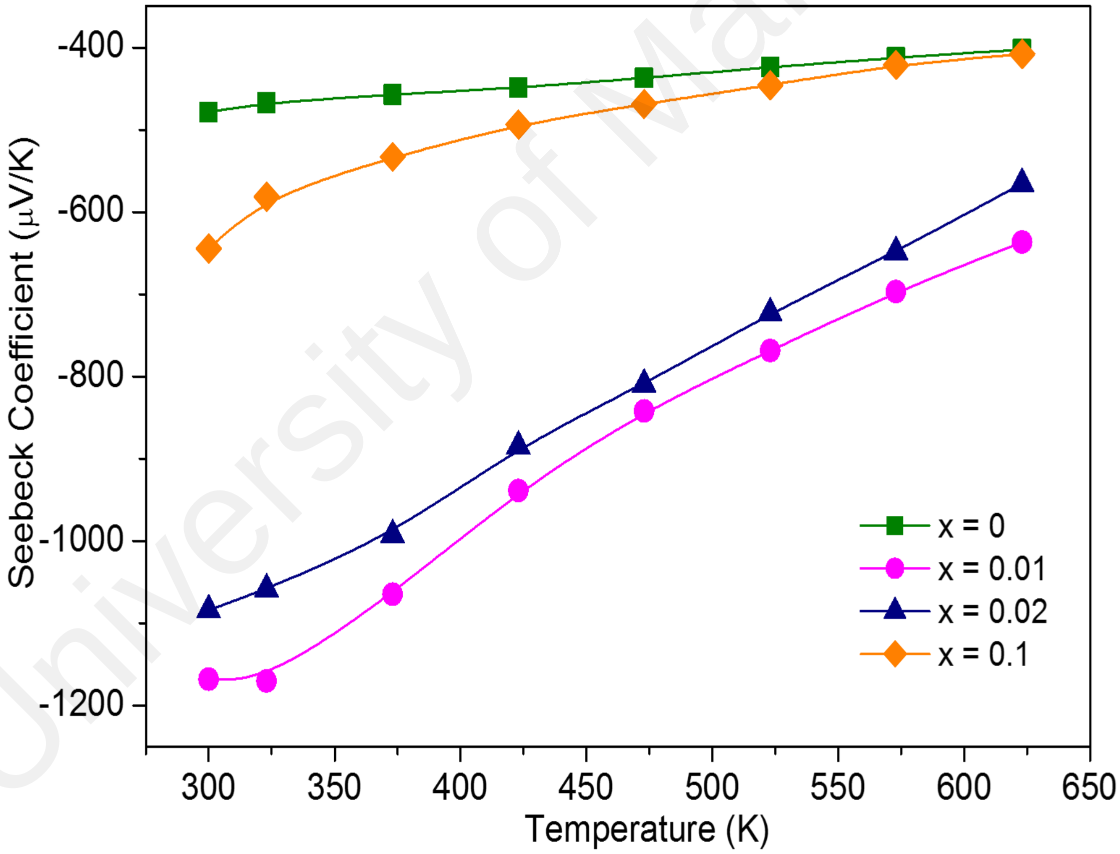

Figure 4.38: Temperature dependence of Seebeck coefficient *α* of $Bi_{2-x}Sn_{3x}S_3$ SPSed samples ($0 \leq x \leq 0.1$).

The temperature behaviour of Seebeck coefficient for all of samples is similar, which found to decrease continuously with increasing temperature in the whole temperature range investigated. At the temperature above 323 K, the Seebeck coefficient for $Bi_{2-x}Sn_{3x}S_3$ system has approximately linear to temperature, which represented the diffusive part of Seebeck coefficient and can be described by equation (Li *et al.*, 2004):

$$\alpha = \frac{\pi^2 k_B^2 T}{e E_F} \qquad (4\text{-}6)$$

where k_B and e are Boltzmann constant and electron charge, respectively. This formula indicates that the slope of the Seebeck coefficient versus T graph is inversely proportional to Fermi Level. The increase of Seebeck coefficient values for the doped compounds as compared to that of pure Bi_2S_3 would reflect decrease in Fermi level, E_F (or decrease in electron concentration) due to Sn substitutional doping. Best fit of the data to Equation (4-6) yield estimation of the Fermi level E_F for all compounds, as listed in Table 4.11.

Table 4.11: The slope of the plot α versus T and calculated E_F for $Bi_{2-x}Sn_{3x}S_3$ SPSed samples.

x	0	0.01	0.02	0.1
Slope (μV/K)	0.228	1.766	1.639	0.673
E_F (eV)	0.321	0.042	0.045	0.109

The E_F decreased from 0.321 eV for $x = 0$ to 0.0042 eV for $x = 0.0$, respectively. Nevertheless, as x increased further E_F show a tendency of increase. The significant increase in E_F for $x = 0.1$, could be ascribed to increase in electron concentration owing to interstitial doping of Sn atoms.

The temperature dependence of power factors for $Bi_{2-x}Sn_{3x}S_3$ SPSed samples are depicted in Figure 4.39, in which the power factors were calculated from the Seebeck coefficients and electrical resistivity values. All the samples have similar positive temperature dependence of power factor. It was found that the power factor of lightly doped compound ($x \leq 0.02$) is smaller than that of pure Bi_2S_3 due to the considerable increase in electrical resistivity. The heavily doped compound, $Bi_{1.9}Sn_{0.3}S_3$, presented the higher power factor values than Bi_2S_3 for temperature above 523 K and reached the maximum value of 132.38 µW/m.K^2 at 623 K. The above results indicated that the electrical properties of $Bi_{2-x}Sn_{3x}S_3$ can be increased by doping Sn, and have an optimal doping concentration at $x = 0.1$. In comparison, the power factor of the optimum Sn-doped sample is slightly higher than that reported by Zhang *et al.* (2013), i.e. ~ 124 µW/m.K^2 for $Bi_2S_{2.85}Se_{0.15}$ compound at 573 K. However, the optimum power factor of Sn-doped SPSed sample remains lower than Sn-doped microwave-sintered sample that recorded a maximum value of 230 µW/m.K^2 at 523K and Ni-doped SPSed sample i.e. 225.36 µW/m.K^2.

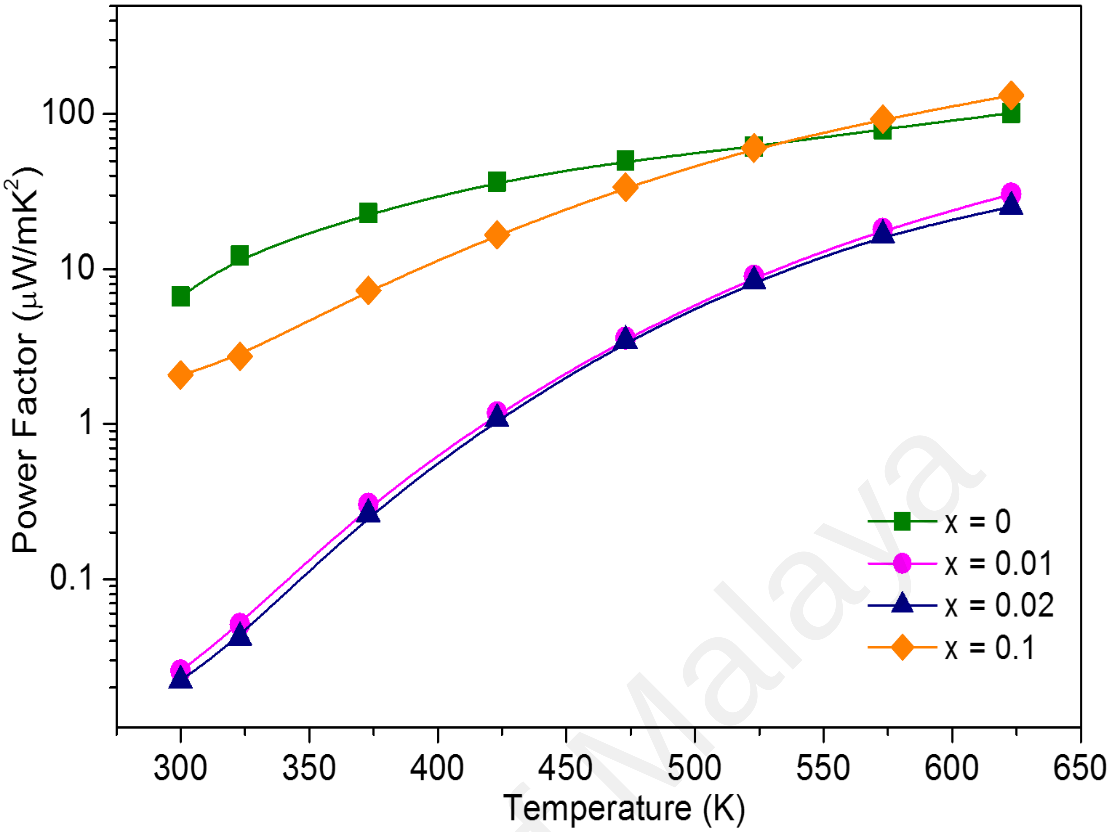

Figure 4.39: Temperature dependence of power factor, *PF*, of $Bi_{2-x}Sn_{3x}S_3$ SPSed samples (0≤ x ≤0.1).

The variation of total thermal conductivity κ as a function of temperature for $Bi_{2-x}Sn_{3x}S_3$ compositions is presented in Figure 4.40. The thermal conductivity of Bi_2S_3 system was remarkably suppressed with addition of Sn in which continuously decrease by increasing temperature, except for $Bi_{1.9}Sn_{0.3}S_3$ sample at temperature above 573K. The lattice disharmony due to the formation of either substitution or interstitial solid solution of Sn dopant atoms lead to strongly scattered the phonons. As a result, the phonon transport is suppressed and hence thermal conductivity of doped samples was significantly reduced compare to that of pure Bi_2S_3. The thermal conductivity values in this work are in range of 0.45 - 0.74 W/m.K, whilst for Sn-doped microwave sintered sample are in the range of 0.21 – 0.65 W/m.K.

$Bi_{1.98}Sn_{0.06}S_3$ sample has the lowest value of thermal conductivity in the range temperature of 300 K – 573 K. Beside due to the substitution of Sn at Bi sub-lattice, the lowest thermal conductivity value of $Bi_{1.98}Sn_{0.06}S_3$ sample is also presumably attributed to in a concurrent presence of BiSn secondary phase and pore structure. The presence of nano-sized secondary phase has been proven to be an efficient approach to suppress the thermal conduction in thermoelectric materials (Girard *et al.*, 2011; Johnsen *et al.*, 2011; Li *et al.*, 2015; Liu *et al.*, 2013). On the other hand, $Bi_{1.99}Sn_{0.03}S_3$ sample recorded the lowest thermal conductivity of 0.45 W/m.K at 623 K.

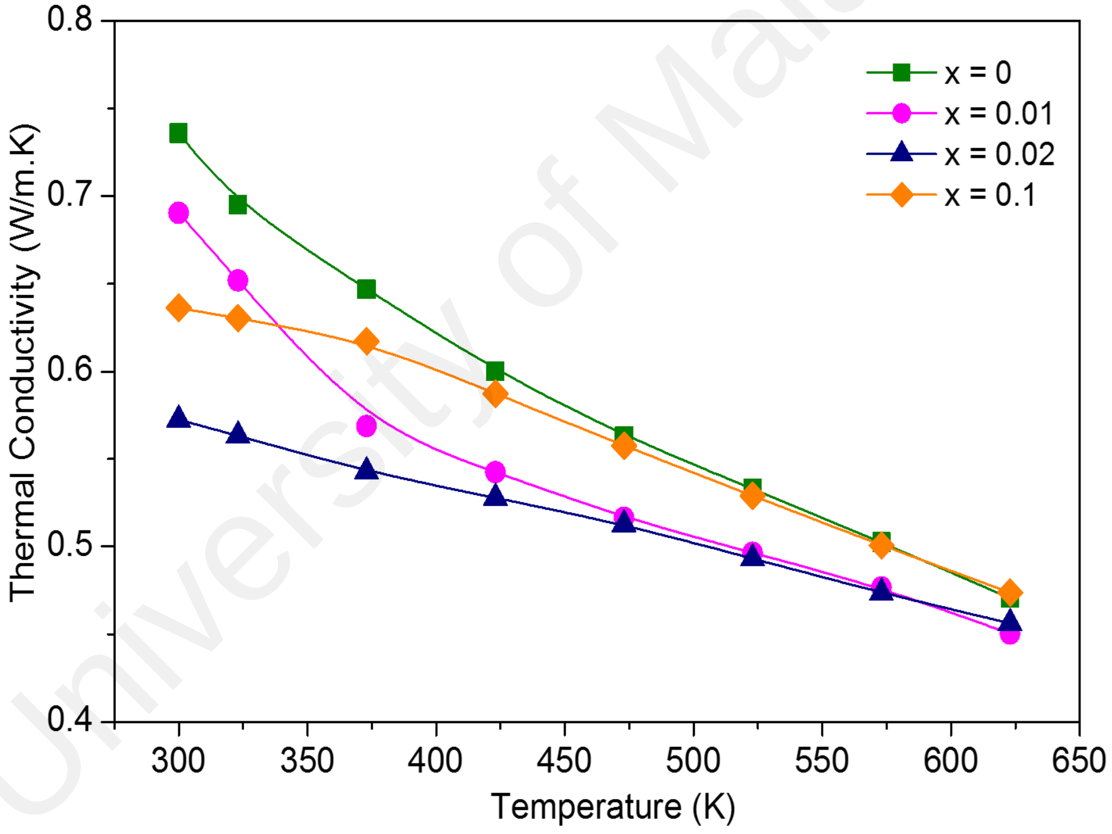

Figure 4.40: Temperature dependence of thermal conductivity, κ, of $Bi_{2-x}Sn_{3x}S_3$ SPSed samples ($0 \leq x \leq 0.1$).

The lattice thermal conductivity,κ_{lat} was roughly estimated by subtracting $\kappa_{el} = LT/\rho$, ($L = 2.45 \times 10^{-8}$ V^2K^2 is the Lorenz number) from the measured thermal conductivity, κ, as presented in Figure 4.41. The calculated κ_{el} contribution for all samples was found to be smaller than 3% of the total κ, thus the lattice thermal conductivity values, κ_{lat}, significantly affect the total thermal conductivity value. The lattice thermal conductivity values of Sn doped samples are lower than that of pure Bi_2S_3 due to the strengthening of phonon scattering by the formation of either substitution or interstitial solid solution. Moreover, the presence of nano-sized BiSn secondary phase and pore structure on the scattering of heat-carrying phonons will also contribute in reducing lattice thermal conductivity. The lowest values of lattice thermal conductivity were presented by $Bi_{1.98}Sn_{0.06}S_3$ and $Bi_{1.99}Sn_{0.03}S_3$ samples for temperature ranges of 300 K – 573 K and 623 K, respectively.

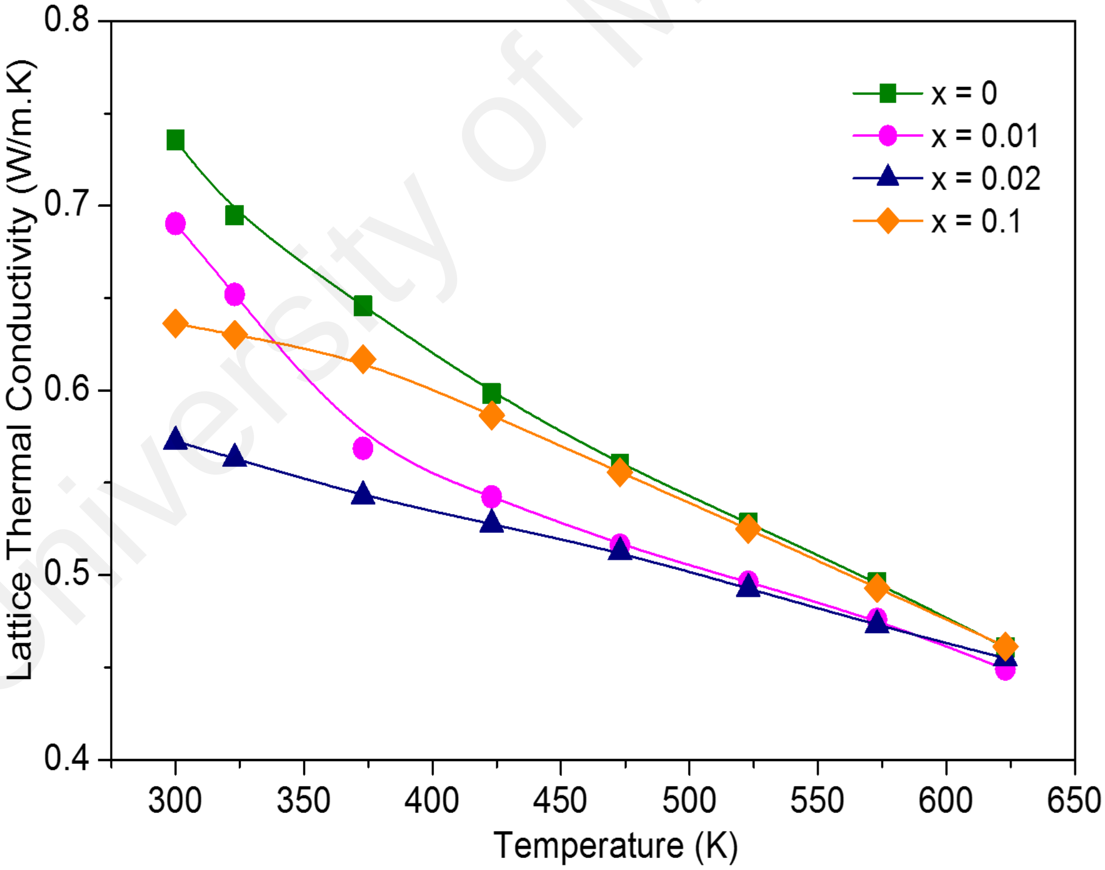

Figure 4.41: Temperature dependence of lattice thermal conductivity of $Bi_{2-x}Sn_{3x}S_3$ SPSed samples ($0\leq x \leq 0.1$).

Figure 4.42 demonstrates the temperature dependence of dimensionless figure of merit, *ZT*, for $Bi_{2-x}Sn_{3x}S_3$ SPSed samples. The *ZT* values of Sn doped samples appeared to be on monotonically increasing trend with increasing temperature. Moreover, the trend of *ZT* values are increasing with an increase of Sn content. $Bi_{1.9}Sn_{0.3}S_3$ sample recorded a *ZT* value of $9.75x10^{-4}$ at 300 K, which is lower than that of pure Bi_2S_3. However, it showed an enhancement on *ZT* and achieved the highest value of 0.17 for this system when the temperature raised to 623 K. The addition of Sn_{3x} ($0.01\leq x \leq 0.1$) into Bi_2S_3 system significantly enhance the Seebeck coefficient values and suppressed the thermal conductivity values, but it still insufficient to reduce the electrical resistivity of Bi_2S_3 which leads to inadequate *ZT*s values. It is predicted that *ZT* could be enhanced by carefully controlling the carrier concentration in sample with the presence of Sn in the interstitials site.

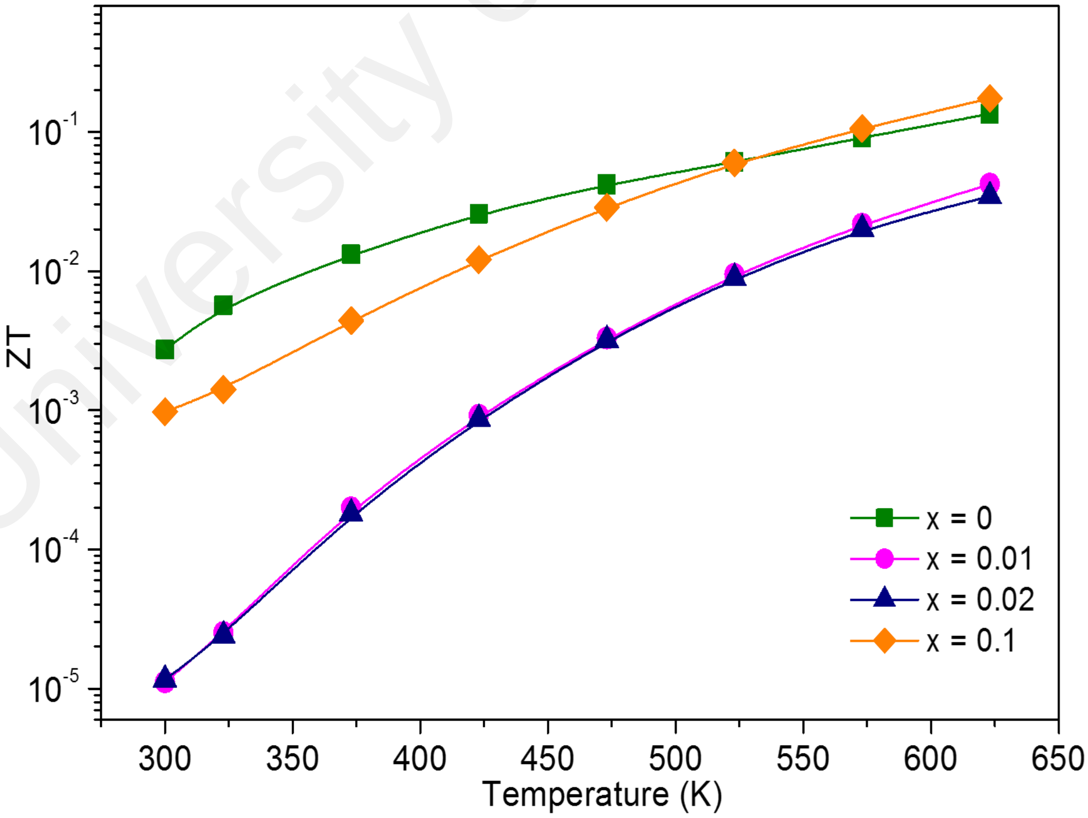

Figure 4.42: Temperature dependence of dimensionless figure of merit, *ZT*, of $Bi_{2x}Sn_{3x}S_3$ SPSed samples ($0 \leq x \leq 0.1$).

In summary, Sn atom has successfully applied as a dopant atom into Bi_2S_3 system which was synthesized under the combination processes of MA and SPS. It was found that depending on the concentration of dopant atom, either the substitution solid solution or interstitial solid solution could be obtained. The light doped compound ($x \leq 0.02$) showed a higher electrical resistivity than Bi_2S_3 due to the bivalent Sn ion (Sn^{2+}) partially substituted the trivalent Bi ion (Bi^{3+}). However, a significant enhancement on Seebek coefficient was reported for those compounds. Whilst, for heavily doped compound ($x = 0.1$) performed a better results for electrical resistivity at temperature above 573K. Moreover, the thermal conductivity of Bi_2S_3 system was remarkably suppressed with addition of Sn in which continuously decrease by increasing temperature, due to the lattice defects caused by the formation of substitution and interstitial solid solution. $Bi_{1.9}Sn_{0.3}S_3$ sample recorded a maximum *ZT* value of 0.17 at 623 K.

Group B and Group C had performed the thermoelectric properties of elemental doped Bi_2S_3 bulk system. The results showed that Ni doped samples presented an appreciable level of thermoelectric properties than Sn doped samples. Moreover, a research on Bi_2S_3 as a thermoelectric material had also applied an oxide element i.e ZnO to tune electrical and thermal properties of Bi_2S_3 system. It was reported by Du *et al.* (2015) that the maximum *ZT* value of 0.66 at 675 K for Bi_2S_3 doped with 1.0 mol% ZnO . This previous result on the use of oxide element and in combination with current results of Ni doped sample have motivated to extend the investigation of NiO added Bi_2S_3 system. The details of results will be discussed in the next sub section.

4.5 Group D: SPSed xNiO added Bi_2S_3 system ($0 \leq x \leq 1.5$)

4.5.1 Microstructural properties

Figure 4.43 presents the XRD patterns for the synthesized powders with different NiO content, x. It can be clearly seen that most of peaks on the XRD patterns well matched with those for Bi_2S_3, indicating that the main phase is Bi_2S_3 (PDF 98-015-3946) with orthorhombic structure. Furthermore, all of the NiO added compounds exhibited the secondary phase of Bi (PDF 01-085-1330). The Bi peaks are detected at 27.4˚ and 38.1˚, in which 27.4˚ peak showed the highest intensity compare to other Bi peak. The XRD analysis for milled powder samples also did not detect any peaks of Ni or NiO after doping.

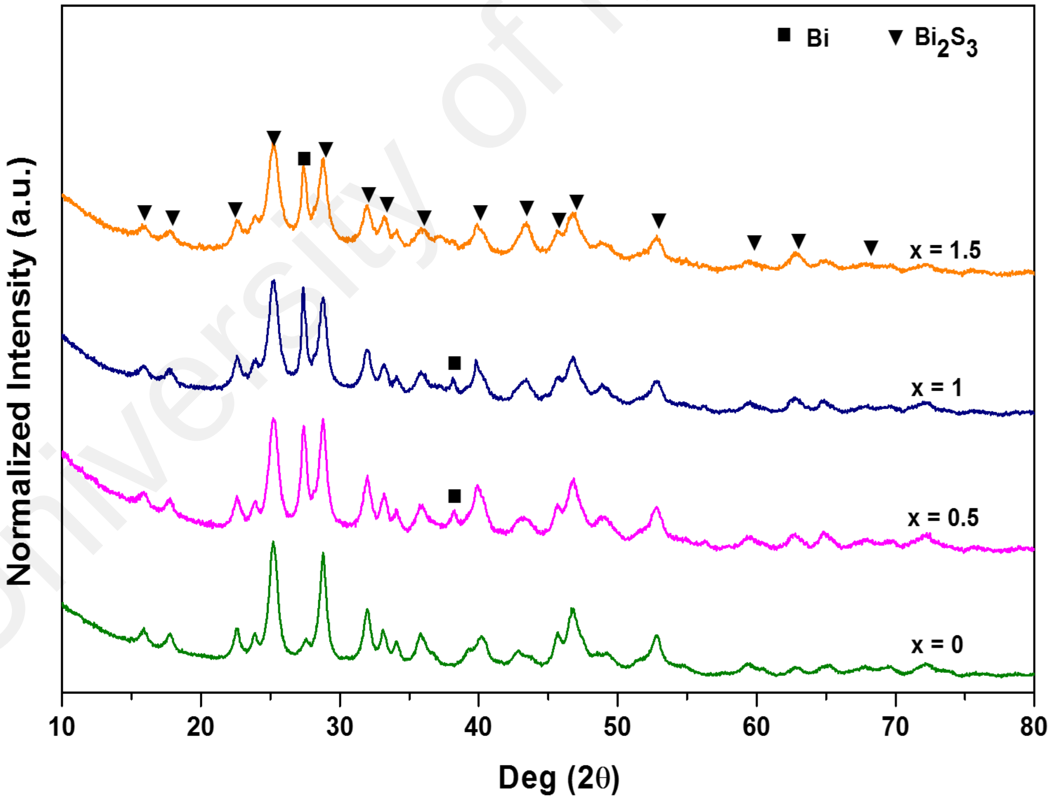

Figure 4.43: XRD patterns of $Bi_2S_3 + x$NiO samples ($0.5 \leq x \leq 1.5$). After ball milling process, a small peak of Bi appeared.

The XRD patterns for NiO added SPSed samples were displayed in Figure 4.44. All of Bi_2S_3 + xNiO ($0.5 \leq x \leq 1.5$) compounds exhibited predominant phase of Bi_2S_3 with secondary phase of NiS_2 (PDF 00-003-0734) and minor SO_2 phase (PDF 00-005-0428). The obtained intensity peaks were sharp with narrowed full width at half maximum (FWHM) for SPSed samples which is a sign of grain growth and a good crystallization compare to powders form. The average crystallite size of milled powder samples which was calculated by Scherrer's equation were in the range of 57.65 – 73.11 nm, whilst for SPSed samples were in the range of 46.75 – 78.50 nm with SD of 7.1 nm and 12.9 nm for milled and SPSed samples, respectively (as listed in Table 4.12).

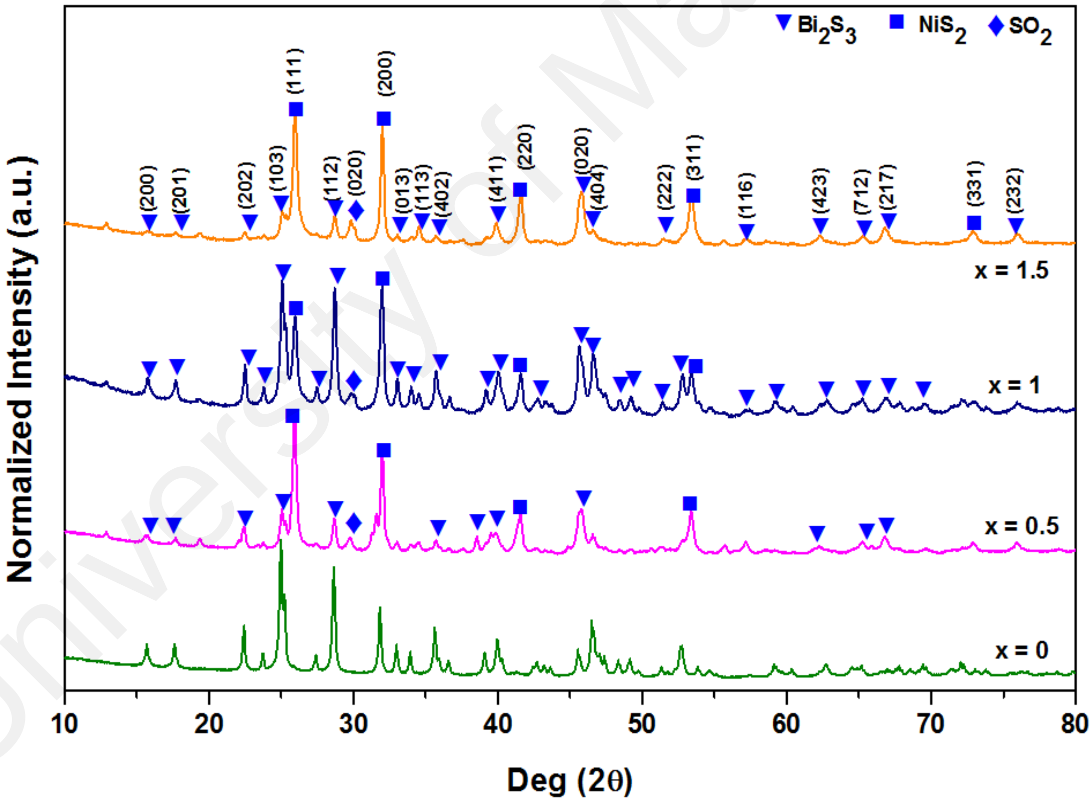

Figure 4.44: XRD patterns of Bi_2S_3 + xNiO SPSed samples ($0.5 \leq x \leq 1.50$). The main phase of Bi_2S_3 with secondary phases of NiS_2 were observed.

Table 4.12: Average crystallite size and density of SPSed $Bi_2S_3 + x$NiO samples.

NiO Content (x)	Average Crystallite Size (nm)		Density (g/cm^3)	Relative Density (%)
	Milled powder	SPSed samples		
0	57.65	78.5	6.19	90.95
0.5	71.81	60.84	6.51	90.27
1.0	73.11	61.75	6.13	90.00
1.5	69.26	46.75	5.89	86.49

Table 4.13 presented the room temperature lattice parameters of Bi_2S_3 phase and NiS_2 phase for different NiO content (x) which was calculated using the XRD data. The standard values of lattice parameters for each phases were cited from PDF 98-015-3946 and PDF 00-003-0734 for Bi_2S_3 and NiS_2, respectively. In general, the addition of NiO caused the shrinkage of unit cell volume of Bi_2S_3 phase which may due the deficiency of sulfur content in the Bi_2S_3 host phase because of the formation of NiS_2 secondary phase as the following equation:

$$2\mathrm{NiO} + 5\mathrm{S} \leftrightarrow 2\mathrm{NiS}_2 + \mathrm{SO}_2 \uparrow \qquad (4\text{-}7)$$

Moreover, the chemical reaction can activate the sintering process and the products act as secondary phases, which inhibits the grain growth. However, the gas production (SO_2) will decrease the density of sintered sample (Du *et al.*, 2015; Wood, 1988). Therefore, an increase in NiO content (x) will reduce the density of samples, which is consistent with densities results for NiO added samples as listed in Table 4.12.

Table 4.13: Lattice parameters of Bi_2S_3 phase and NiS_2 phase.

Compound/Lattice Parameters	Bi_2S_3 phase, orthorhombic				NiS_2 phase, cubic			
	a (Å)	b (Å)	c (Å)	Volume unit cell (Å^3)	a (Å)	b (Å)	c (Å)	Volume unit cell (Å^3)
Reference	11.2690	3.9720	11.1290	498.14	5.6680	5.6680	5.6680	182.09
SPS-ed Bi_2S_3	11.2963	3.9860	11.1452	501.66	-	-	-	-
Bi_2S_3 + 0.5 NiO	11.0699	3.9636	11.2612	494.11	5.6861	5.6861	5.6861	183.84
Bi_2S_3 + 1.0 NiO	11.0261	3.9617	11.2593	491.84	5.6887	5.6887	5.6887	184.09
Bi_2S_3 + 1.5 NiO	11.0712	3.9782	11.1728	492.09	5.6972	5.6972	5.6972	184.92

Figure (4.45) – (4.47) display FESEM – EDS results of Bi_2S_3 + *x*NiO SPSed sample with different NiO content. The results of FESEM images of fracture surface for Bi_2S_3+0.5 NiO sample presented a granular-lamellar structure, whilst a lamellar structures were exhibited for samples with NiO content of 1 and 1.5 mol%. In addition, all the samples possess grains with sub-micron size and no obvious large-scale preferred orientation. The microstructural analysis confirmed that all the doped samples have a porous structure. Those porous structures in all doped samples may be attributed to sulphur deficiency due to the SO_2 gas formation as described in Equation (4-7). Along with the decreased density from 90.27% to 86.49%, lots of pores appeared in the Bi_2S_3 + 1.5NiO sample as shown in Fig 4.47 (a).

The EDS analysis of all samples have confirmed the dominate phase of the Bi_2S_3 with NiS_2 being detected as secondary phase, which is in good agreement with XRD results. The atomic ratio of Bi and S in the matrix for all observed point indicated that S content lower than the nominal ratio of 2:3. This may be explained as the NiS_2 second phase is S-rich, an increase of NiS_2 phase will reduce the S content in Bi_2S_3 matrix and form non stoichiometric Bi_2S_3. Additionally, NiS_2 phase is clearly seen in Bi_2S_3+1.5NiO sample with rectangular like area. This may related to the fact that NiS_2 phase has a cubic crystal structure.

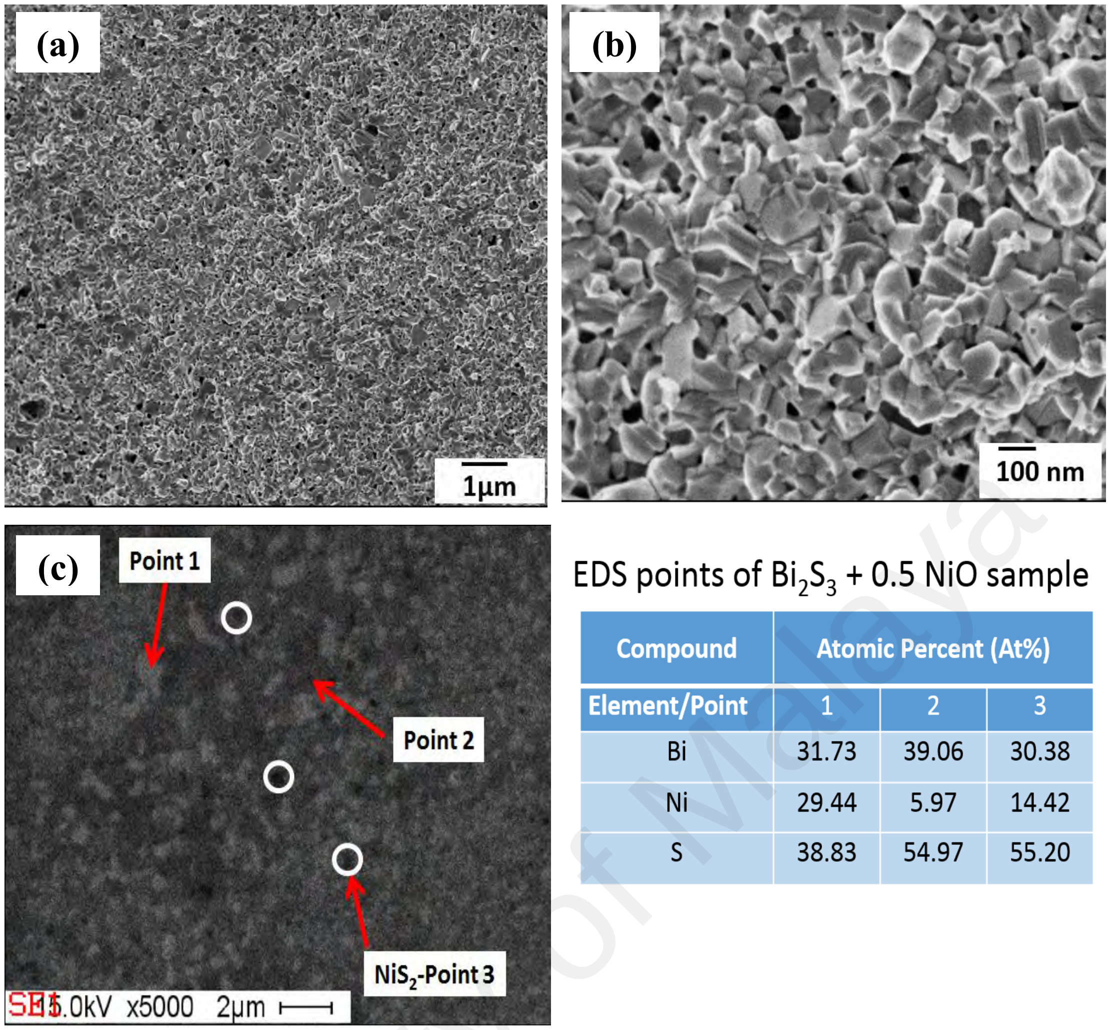

EDS points of Bi_2S_3 + 0.5 NiO sample

Compound	Atomic Percent (At%)		
Element/Point	1	2	3
Bi	31.73	39.06	30.38
Ni	29.44	5.97	14.42
S	38.83	54.97	55.20

Figure 4.45: SEM – EDS results for Bi_2S_3 + 0.5 NiO sample; (a), (b) SEM images of fractured surface in different magnification, and (c) EDS analysis. The white circles indicated the NiS_2 phase.

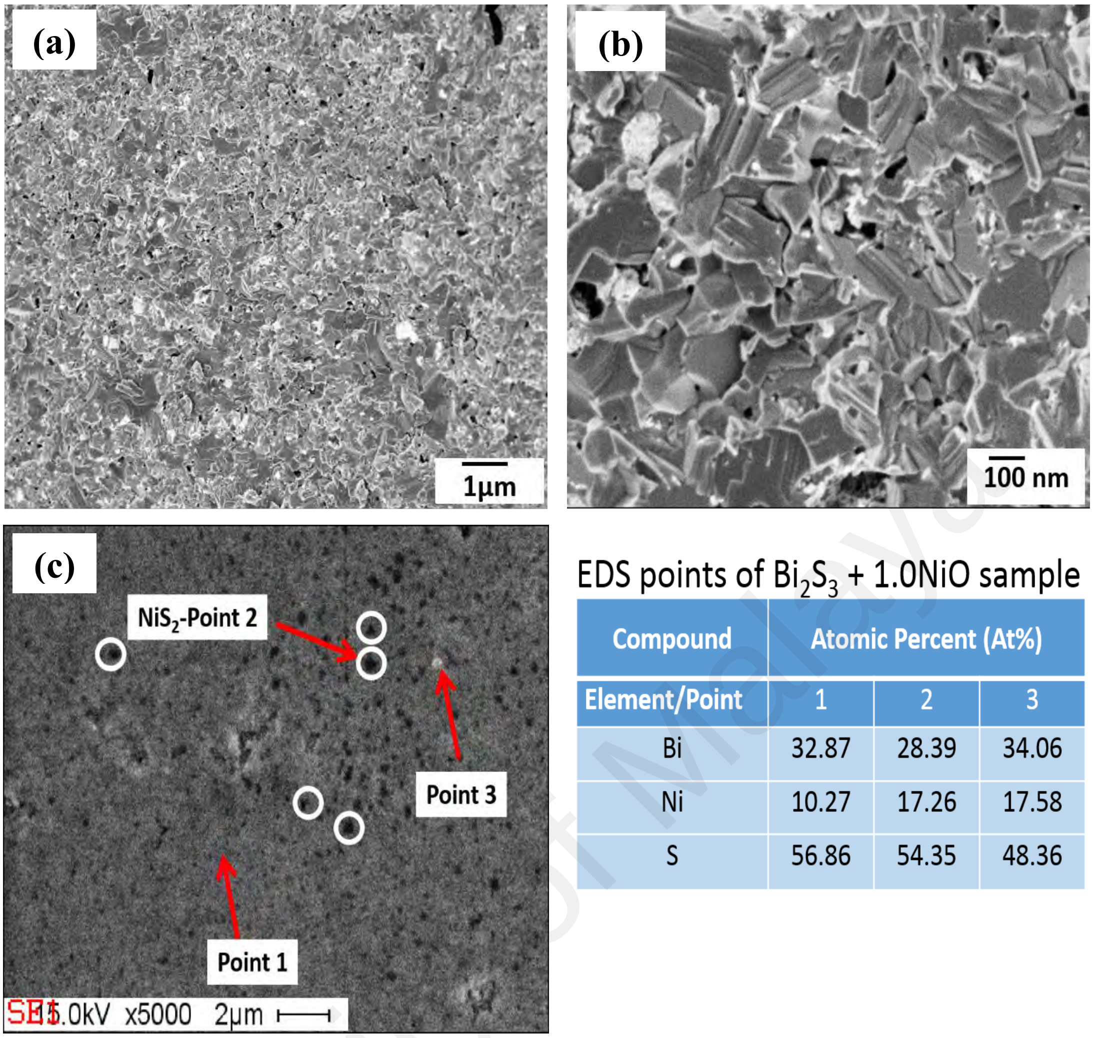

EDS points of Bi_2S_3 + 1.0NiO sample

Compound	Atomic Percent (At%)		
Element/Point	1	2	3
Bi	32.87	28.39	34.06
Ni	10.27	17.26	17.58
S	56.86	54.35	48.36

Figure 4.46: SEM – EDS results for Bi_2S_3 + 1.0NiO sample; (a), (b) SEM images of fractured surface in different magnification, and (c) EDS analysis. The white circles indicated the NiS_2 phase.

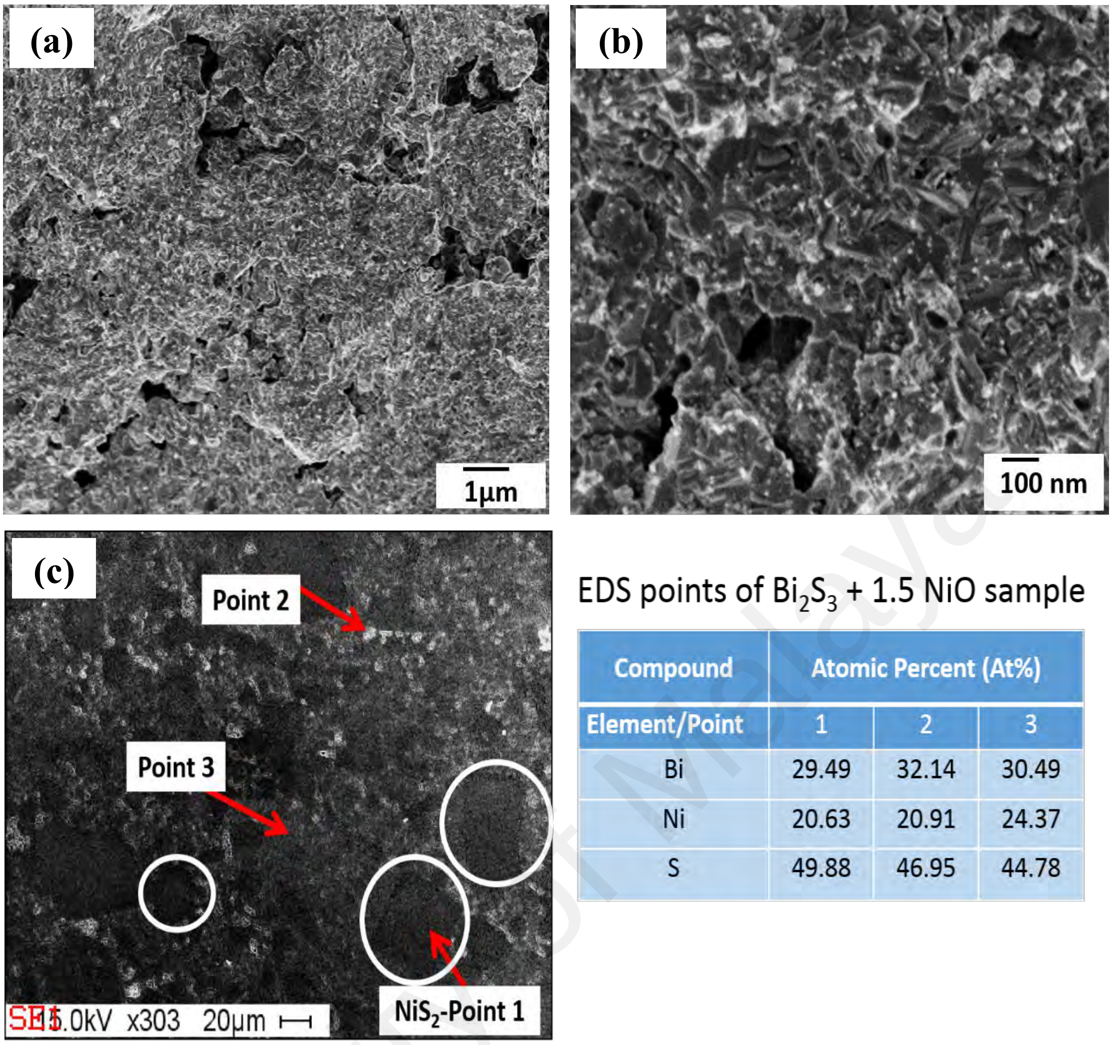

EDS points of Bi_2S_3 + 1.5 NiO sample

Compound	Atomic Percent (At%)		
Element/Point	1	2	3
Bi	29.49	32.14	30.49
Ni	20.63	20.91	24.37
S	49.88	46.95	44.78

Figure 4.47: SEM – EDS results for Bi_2S_3 + 1.5 NiO sample; (a), (b) SEM images of fractured surface in different magnification, and (c) EDS analysis. The white circles indicated the NiS_2 phase.

4.5.2 Thermoelectric properties

Figure 4.48 presents the temperature dependence of electrical resistivity for NiO added Bi_2S_3 SPSed samples. The addition of NiO is expected to tune the electrical and thermal properties of Bi_2S_3.The resistivity value of pure Bi_2S_3 sample decreases with increasing temperature over the measured temperature range, indicating a semiconducting behavior. However, the electrical resistivity of Bi_2S_3 +0.5NiO and Bi_2S_3 +1.5NiO samples showed a slight increment with increasing temperature, which indicate a semi-metallic conducting behavior of samples. This phenomenon can be mainly caused by the shift of Fermi level due to the increased second phase of NiS_2, which is a similar result was found in previous study carried out by Ge *et al.* (2012b) on $Bi_{2-x}Ag_{3x}S_3$ samples. Moreover, Bi_2S_3+1.0NiO sample showed a slightly reducing trend of electrical resistivity with increasing temperature, which is a typical phenomenon for standard semiconductor. Furthermore, the difference of electrical resistivity values with increasing temperature was very small for all NiO added samples, thus it can be assumed that those samples are temperature independent of electrical resistivity. This property indicating the potentially of NiO added Bi_2S_3 materials to use in widespread applications of electronic area, as no significant changing on electrical resistivity to the temperature.

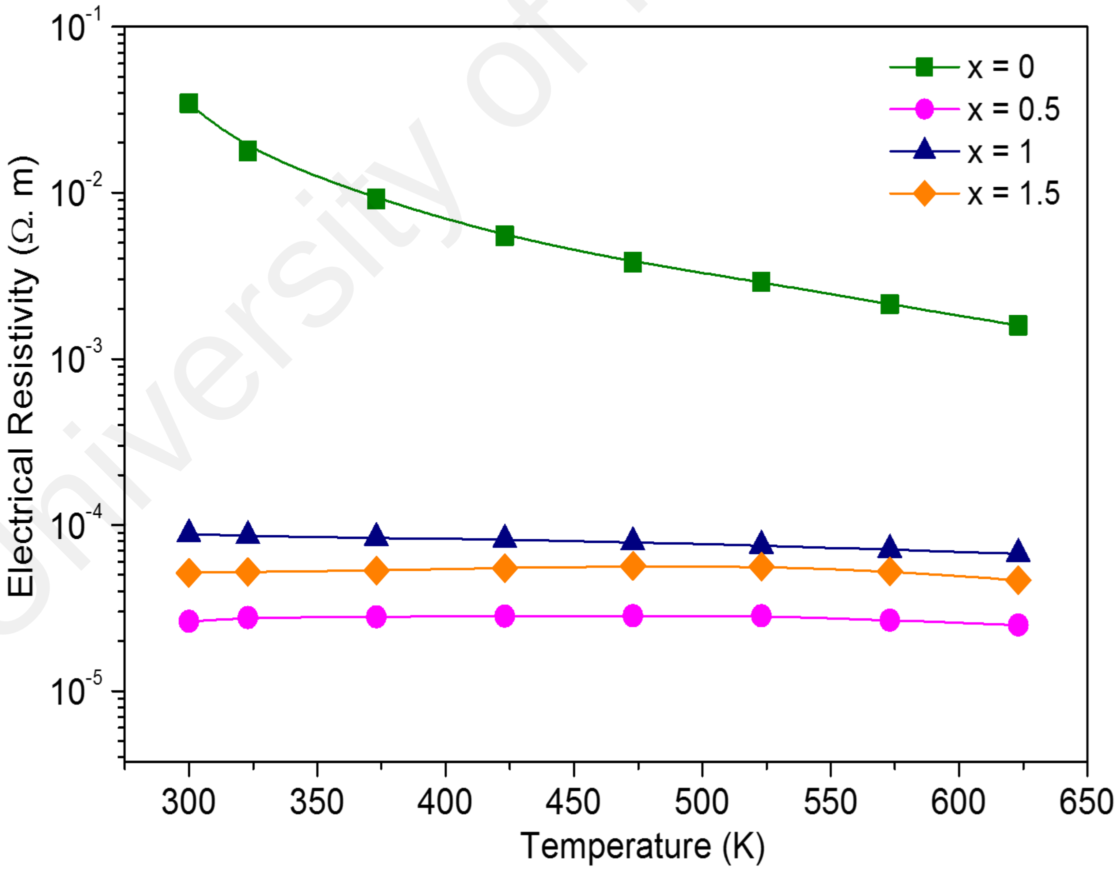

Figure 4.48: Temperature dependence of electrical resistivity ρ for $Bi_2S_3 + x$NiO SPSed samples ($0 \leq x \leq 1.5$).

It can be clearly see in Figure 4.48 that the addition of NiO into the system could significantly reduce the resistivity of Bi_2S_3 which can be attributed to the increased generation of charge carrier. During the MA and SPS process, NiO will be reacted with elementary sulfur and produced NiS_2 (Kosmac *et al.*, 1993) which reduced the sulfur stoichiometric ratio in Bi_2S_3 and resulted in sulfur vacancies ($\ddot{V_s}$) and free electron ($\acute{e}$). The process can be described by the following equation:

$$x\mathrm{NiO} + 2\mathrm{Bi} + 3\mathrm{S} \rightarrow x\mathrm{NiS_2} + \mathrm{Bi_2S}_{\left(3-\frac{5}{2}x\right)} + \frac{1}{2}x\mathrm{SO_2}\uparrow + \frac{5}{2}x\ddot{V_s} + 5x\acute{e} \qquad (4\text{-}8)$$

From Equation (4-8), it can be explained the significant reduction in electrical resistivity through the following parameters which have increased after the reaction: (i) sulfur deficiency, (ii) sulfur vacancies ($\ddot{V_s}$), and (iii) additional number of electron ($\acute{e}$). The same phenomena were also reported from previous works on Bi_2S_3 system (Ge *et al.*, 2012a; Ge *et al.*, 2011a; Mizoguchi *et al.*, 1995; Zhao *et al.*, 2008). Thus, the electrical resistivity of $Bi_2S_3 + x$NiO samples are lower than pure Bi_2S_3.

Table 4.14 summarized the Hall measurement results, which support the hypotheses that the charge carrier of the NiO added Bi_2S_3 system have significant increased. As listed, the carrier concentration (*n*) of NiO added samples are larger than that of pure Bi_2S_3. Those results confirmed that the additional number of charge carriers (electron) were gained by addition NiO into Bi_2S_3 system as described in Equation (4-8).

Table 4.14: Carrier concentration, mobility and average Hall coefficient at room temperature for $Bi_2S_3 + x$ NiO SPSed samples.

NiO content (x)	Carrier concentration, *n* (10^{18} cm^3)	Mobility, μ ($cm^2V^{-1}S^{-1}$)	Average Hall coefficient, *RH* (10^{-2} cm^2 C^{-1})
0	-2.72	6.08	-253
0.5	-185	17.09	-3.37
1.0	-154	11.07	-4.06
1.5	-149	13.41	-4.20

At 300 K, the resistivity of Bi_2S_3 could be reduced from $3.44x10^{-2}$ Ω.m to $2.63x10^{-5}$ Ω.m by addition of 0.5 mol% NiO. It means that the electrical resistivity of Bi_2S_3 could be suppressed up to ~ 98%. Bi_2S_3+0.5NiO sample presented the highest values of carrier concentration and mobility (as listed in Table 4.14), hence resulted in the lower electrical resistivity value. Further, the electrical resistivity values are slightly increase with an increase of NiO content, *x*, which attributes to the lattice and/or microstructure defects scattering the electron (Du *et al.*, 2015). Amongst the samples, Bi_2S_3+0.5NiO sample recorded the lowest electrical resistivity of 2.49 x 10^{-5} Ω.m at 623 K, which is a significant reduction value from than that of pure Bi_2S_3 sample (1.6 x 10^{-3} Ω.m) at the same temperature.

In comparison with the previous research outcomes, Du *et al.* (2015) reported an electrical resistivity of 2.27 x 10^{-4} Ω.m for Bi_2S_3+ZnO sample at 300 K, which is higher one order than the result herein. A recent research study on Bi_2Te_3 compound which were prepared by mechanical alloying and SPS process reported the electrical resistivity of 9.61 x 10^{-6} Ω.m at 300 K was achieved for Bi_2Te_3 SPSed bulk sample (Ge *et al.*, 2018).

The result of NiO added Bi_2S_3 has improved the electrical resistivity of Bi_2S_3 which is become competitive value to recent Bi_2Te_3 bulk sample.

The temperature dependence of Seebeck coefficients for $Bi_2S_3 + x$NiO SPSed samples ($0 \leq x \leq 1.5$) is shown in Figure 4.49. The results of all NiO added samples exhibited a negative sign (*n* - type) of the Seebeck coefficients over the entire range of temperature range, indicating the majority of charge carriers in the samples are electron and NiO dopant has acted as electron donor (acceptor). The NiO added samples showed a lower Seebeck coefficient values than pure Bi_2S_3 sample over the entire range of temperature range. In general, the magnitude of Seebeck coefficients decrease with increasing carrier concentration (*n*) according Mott expression (Snyder & Toberer, 2008) as mentioned in Equation (4-4). Therefore, the absolute Seebeck coefficient of Bi_2S_3 system become decreased whereas the electrical resistivity decreased by addition of NiO. The same trend of reduction on Seebeck coefficient was also found in the study of ZnO added Bi_2S_3 system which was reported by Du *et al.* (2015). Furthermore, NiO added samples presented monotonously increasing trend of Seebeck coefficients with increasing temperature (except for Bi_2S_3+NiO sample at temperature above 573 K). Moreover, it is understood that semi-metallic behavior materials have a lower Seebeck coefficient values than semiconductor materials, therefore amongst NiO added samples, the highest Seebeck coefficient of -98.32 μV/K was recorded at 573 K for Bi_2S_3+1.0NiO sample.

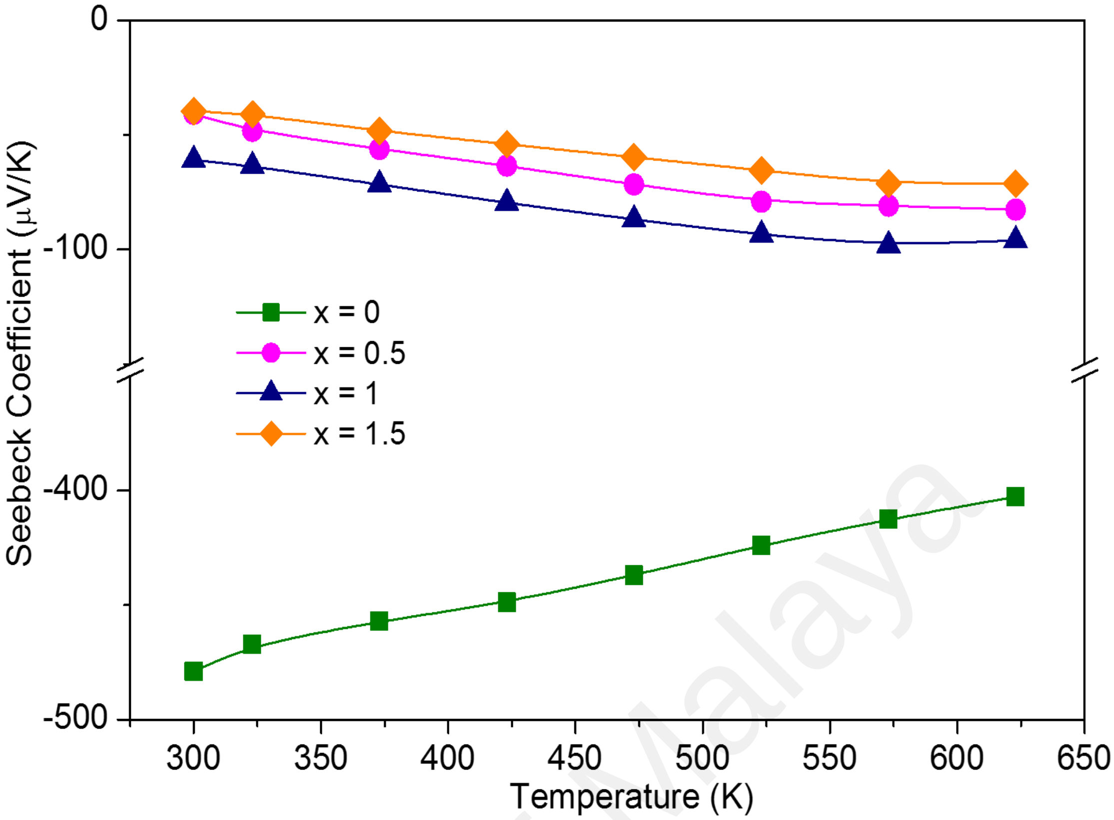

Figure 4.49: Temperature dependence of Seebeck coefficient *α* for $Bi_2S_3 + x$NiO SPSed samples ($0 \leq x \leq 1.5$).

In Figure 4.50, the power factors for $Bi_2S_3 + x$NiO compositions of ($0 \leq x \leq 1.5$) are highlighted, in which the power factors were calculated from the Seebeck coefficients and electrical resistivity values. All samples show a similar positive-temperature dependence, i.e. power factor increases with increasing temperature in the whole measuring temperature ranging from 300 – 623 K. It can be seen in Figure 4.50, the enhancement of power factor is achieved with the presence of NiO into the Bi_2S_3 system. At 300 K, the Bi_2S_3+0.5NiO sample recorded a power factor value of 63.25 $\mu W/m.K^2$, which was improved ~9.5 times than that of pure Bi_2S_3 sample (6.67 $\mu W/m.K^2$). The power factor for NiO added samples showed a declining trend with increasing NiO content (*x*). Bi_2S_3+0.5NiO sample presented the higher power factor than other samples over entire measured temperature and has a maximum value of 273.67 $\mu W/m.K^2$ at 623

K. These results suggest that the electrical properties of Bi_2S_3 + xNiO can be enhanced by subtle tailoring the NiO content with an optimal concentration of $x = 0.5$. The Seebeck coefficients observed herein lower than that of Bi_2S_3 + xZnO system reported by Du *et al.* (2015), therefore the maximum power factor value of Bi_2S_3+0.5NiO lower than that of Bi_2S_3+ZnO sample which achieved ~ 600 µW/mK^2 at the same temperature.

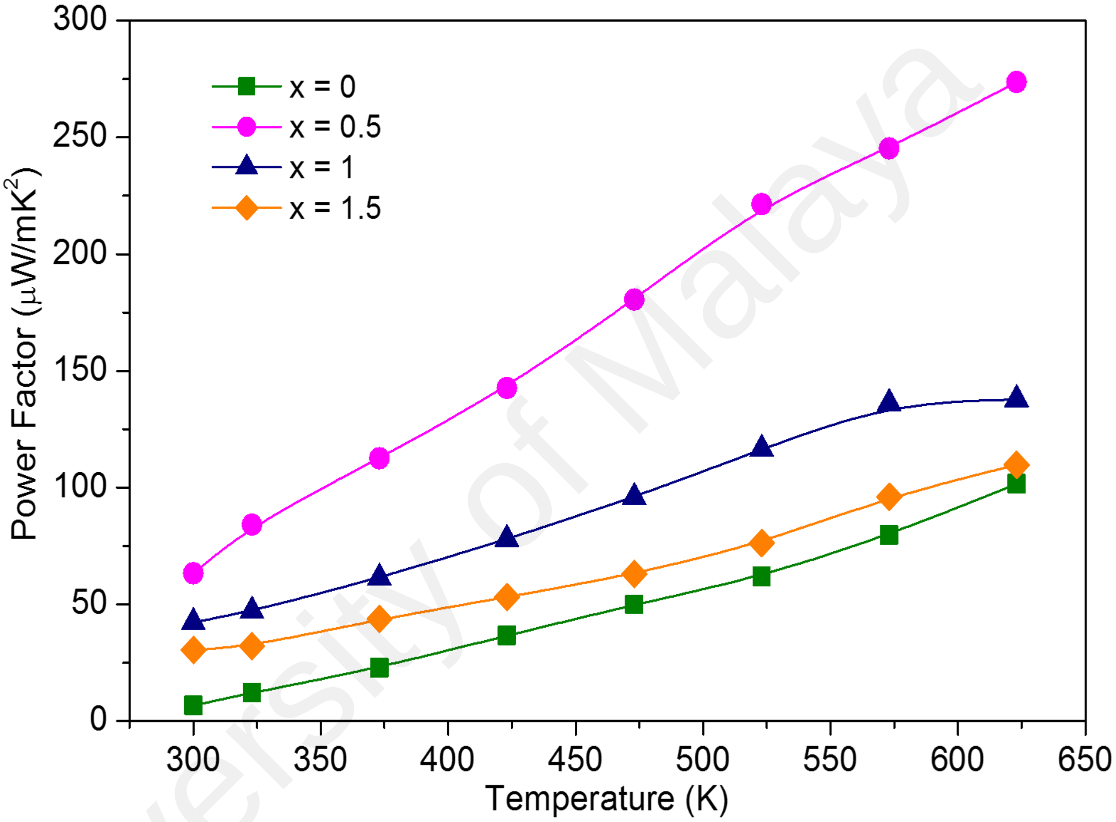

Figure 4.50: Temperature dependence of power factor *PF* for Bi_2S_3 + xNiO SPSed samples ($0 \leq x \leq 1.5$).

The temperature dependence of thermal conductivity, κ, for Bi_2S_3 + xNiO SPSed samples ($0 \leq x \leq 1.5$) is demonstrated in Figure 4.51. The pure Bi_2S_3 sample showed a decreased of thermal conductivity values by increasing the temperature. It was found that the thermal conductivity of the sample was noticeably increased after NiO addition. The same upward trend of thermal conductivity was also found for ZnO added samples (Du *et al.*, 2015). Moreover, parabolic like behavior of thermal conductivity curves were recorded for all NiO added samples. As illustrated, thermal conductivity first increased with an increase of temperature up to 373 K, which presumably due to the increasing of ambipolar thermal contributions arising from the diffusion of electron-hole pairs with the onset intrinsic contribution (Ge *et al.*, 2018; Han *et al.*, 2017; Imamuddin & Dupre, 1972). Further, the thermal conductivity of doped samples decreased with an increase of temperature, indicating the dominant mechanism of phonon scattering.

Thermal conductivity values of NiO added samples also showed decreases values with an increase of NiO content (x). Amongst doped samples, Bi_2S_3+NiO presented the lowest thermal conductivity of 0.89 W/m.K at 300 K. This result is higher than that obtained for Bi_2S_3+xZnO sample (Du *et al.*, 2015) i.e. ~ 0.4 W/m.K at 675 K.

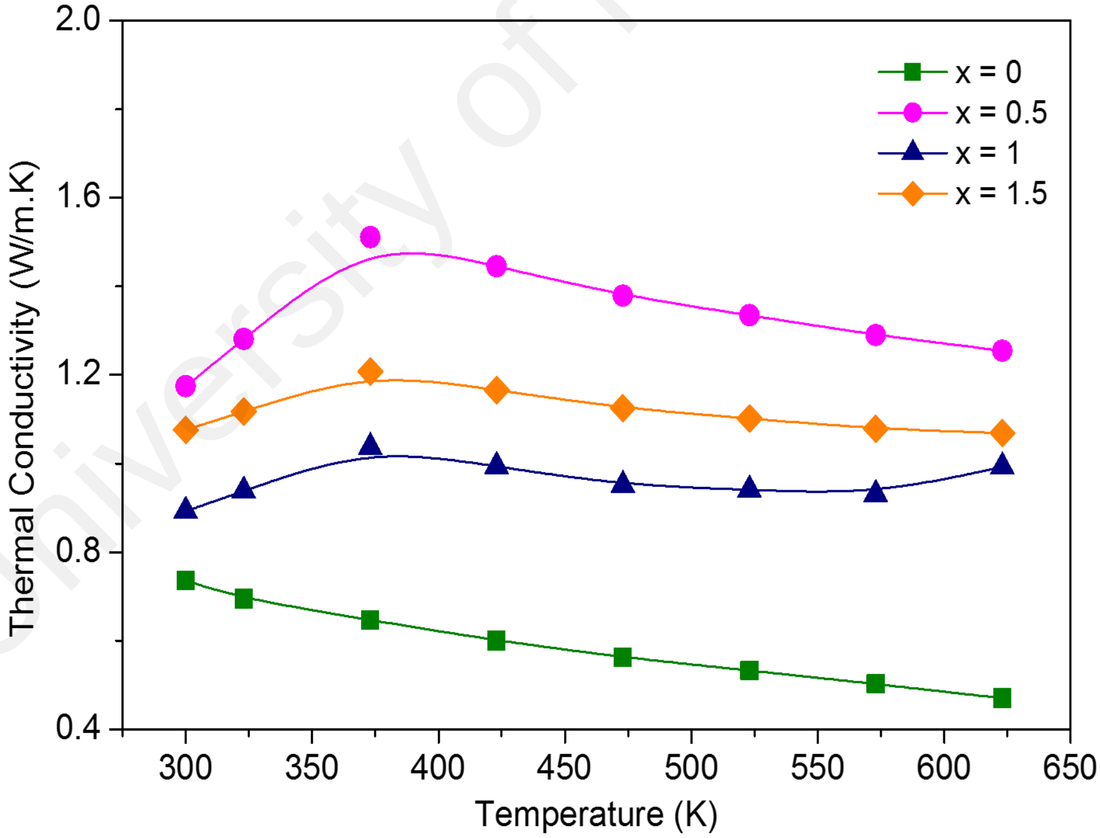

Figure 4.51: Temperature dependence of thermal conductivity κ for $Bi_2S_3 + x$ NiO ($0 \leq x \leq 1.5$) SPSed samples.

The lattice thermal conductivity,κ_{lat} can be estimated by subtracting the electronic contribution, κ_{el}= LT/ρ, from the total thermal conductivity, where $L = 2.45 \times 10^{-8}$ V^2K^2 is the Lorenz number as presented in Figure 4.52. The electronic contribution to the total thermal conductivity has increased to as high as ~ 48.8 % for Bi_2S_3 + 0.5NiO sample at a temperature of 623 K. The lattice thermal conductivity results of NiO added samples demonstrated that its values reduced with increasing NiO content over entire measured temperature. The lowest lattice thermal conductivity of 0.46 W/mK and 0.64 W/mK was achieved for pure Bi_2S_3 and Bi_2S_3+0.5NiO doped sample at 627 K, respectively. For NiO added samples, the lowest value lattice thermal conductivity is assumed to the phonon scattering from the interfacial phase of secondary phase NiS_2. Vineis *et al*., (2010) reported that a significant reduction in lattice thermal conductivity can be achieved by the additional scattering of mid- and long-wavelength phonons by the nanoparticles or secondary phase. Moreover, the presence of pore structure in all NiO added samples also contributed to the scattering of heat-carrying phonons.

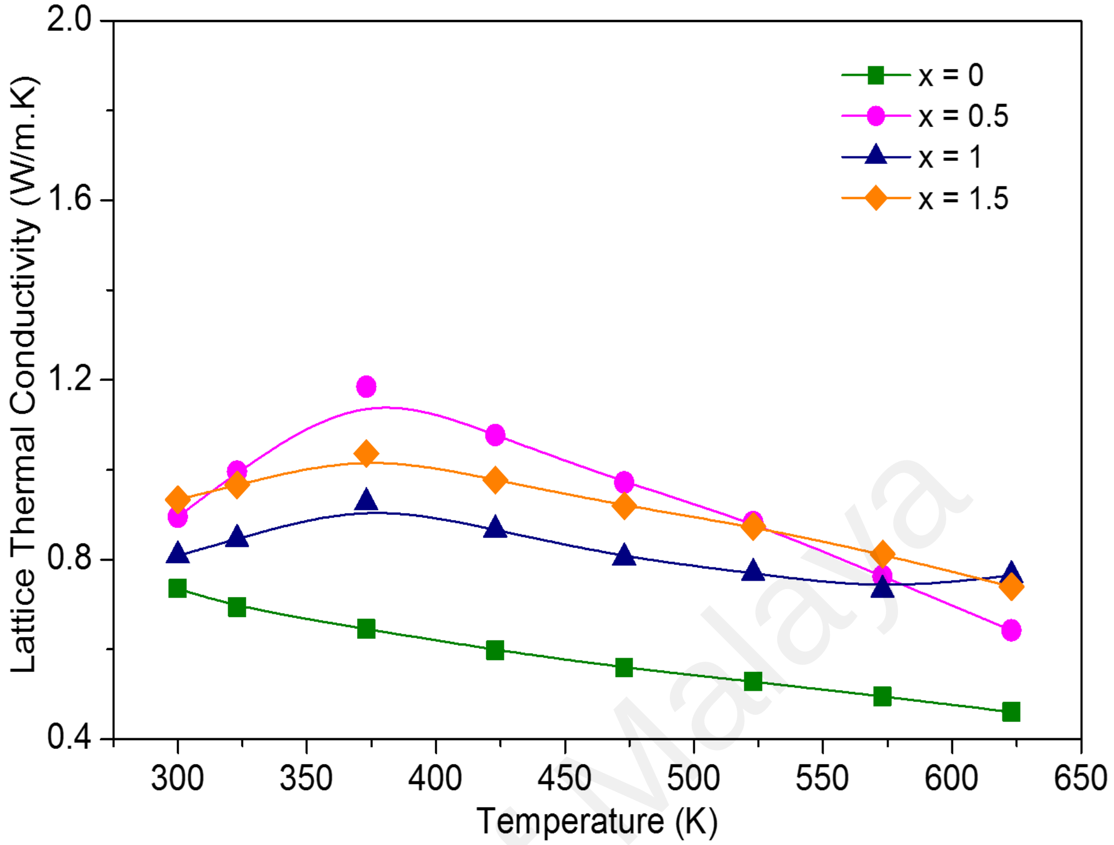

Figure 4.52: Temperature dependence of lattice thermal conductivity κ_{lat} for Bi_2S_3 + xNiO ($0 \leq x \leq 1.5$) SPSed samples.

The dimensionless figure of merit, *ZT* for Bi_2S_3 + xNiO SPSed samples is displayed in Figure 4.53 as a function of temperature. It can be seen that the *ZT* values improved via addition of NiO for temperature and/below 373 K. A small NiO content (x) sample presented a higher *ZT* value at the temperature higher than 373K. A maximum *ZT* of ~ 0.14 was attained by Bi_2S_3 + 0.5NiO sample at 623 K. A moderate *ZT* values for NiO added samples were found as a result of high thermal conductivity, although the power factor was improved.

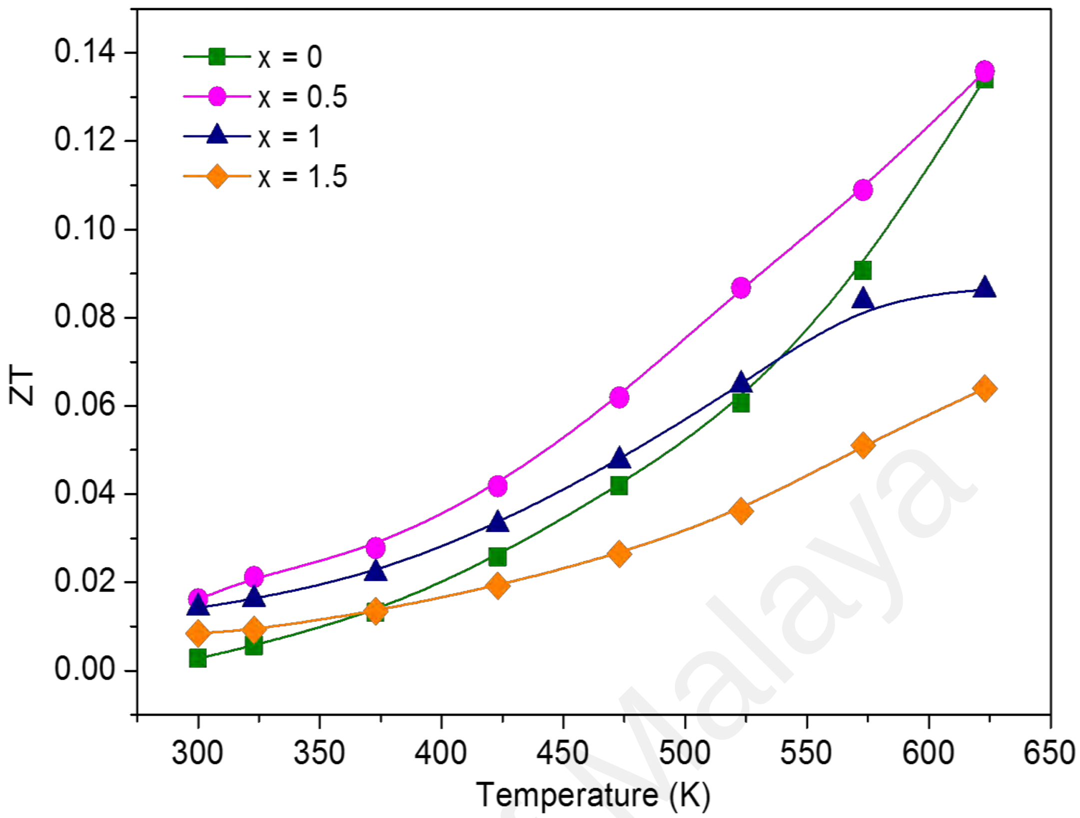

Figure 4.53: Temperature dependence of dimensionless figure of merit *ZT* for Bi_2S_3+ xNiO SPSed samples ($0 \leq x \leq 1.5$).

In summary for group D, a lower concentration of NiO is a promising candidate to improve thermoelectric properties of Bi_2S_3 system for low temperature application. The electrical resistivity of Bi_2S_3 was found to significantly decrease by addition of NiO due to the improvement of the charge carrier. However, due to the semi-metallic behavior of the doped samples, the Seebeck coefficient and thermal conductivity properties shown a lower performances than that of Bi_2S_3. Hence, a moderate *ZT* value of ~ 0.14 was attained by Bi_2S_3 + 0.5NiO sample at 623 K.

The use of single dopant atoms in Bi_2S_3 bulk system already evaluated in the following groups: B, C and D. The results shown a variation of composition that could improve the thermoelectric properties of Bi_2S_3. In the next sub section, the thermoelectric properties of double doped Bi_2S_3 system will be discussed. Beside the properties are in well agreement with the Hume Rothery rules, Sb was chosen as one of dopant due to the fact that addition of Sb in Bi_2Te_3 resulted a higher *ZT* material. It was reported by Xie *et al.* (2010) that nanostructured $Bi_{0.48}Sb_{1.52}Te_3$ exhibited a maximum *ZT* of ~ 1.56 at 300 K.

4.6 Group E: SPSed Sb-X added Bi_2S_3 system (X = Ni, Hf, Zn and Sn)

4.6.1 Microstructural properties

Figure 4.54(a) shows the XRD patterns of $Bi_{0.95}SbX_{0.05}S_3$ milled powders samples (X = Ni, Hf, Zn and Sn). Most of diffraction peaks can be indexed to the standard diffraction pattern of orthorhombic Bi_2S_3 structure (PDF 98-015-3946). Meanwhile, a trace of secondary phase Bi (PDF 01-085-1330) and Sb (PDF 00-002-0587) were also observed. The characteristic peaks of SPSed bulk samples for double doped samples indicated a dominate Bi_2S_3 phase with secondary phase of Sb_2S_3 (PDF 00-006-0474), and minor phases of Sb and Bi as presented in Figure 4.54(b). Most of diffraction peaks for SPSed samples become much narrow than the milled powder samples, which indicates a substantial increase of the grain size. The average crystallite size of SPSed sample, which was calculated by Scherrer's equation is ~ 82.79 nm, while for a milled powders samples is ~ 76.17 nm.

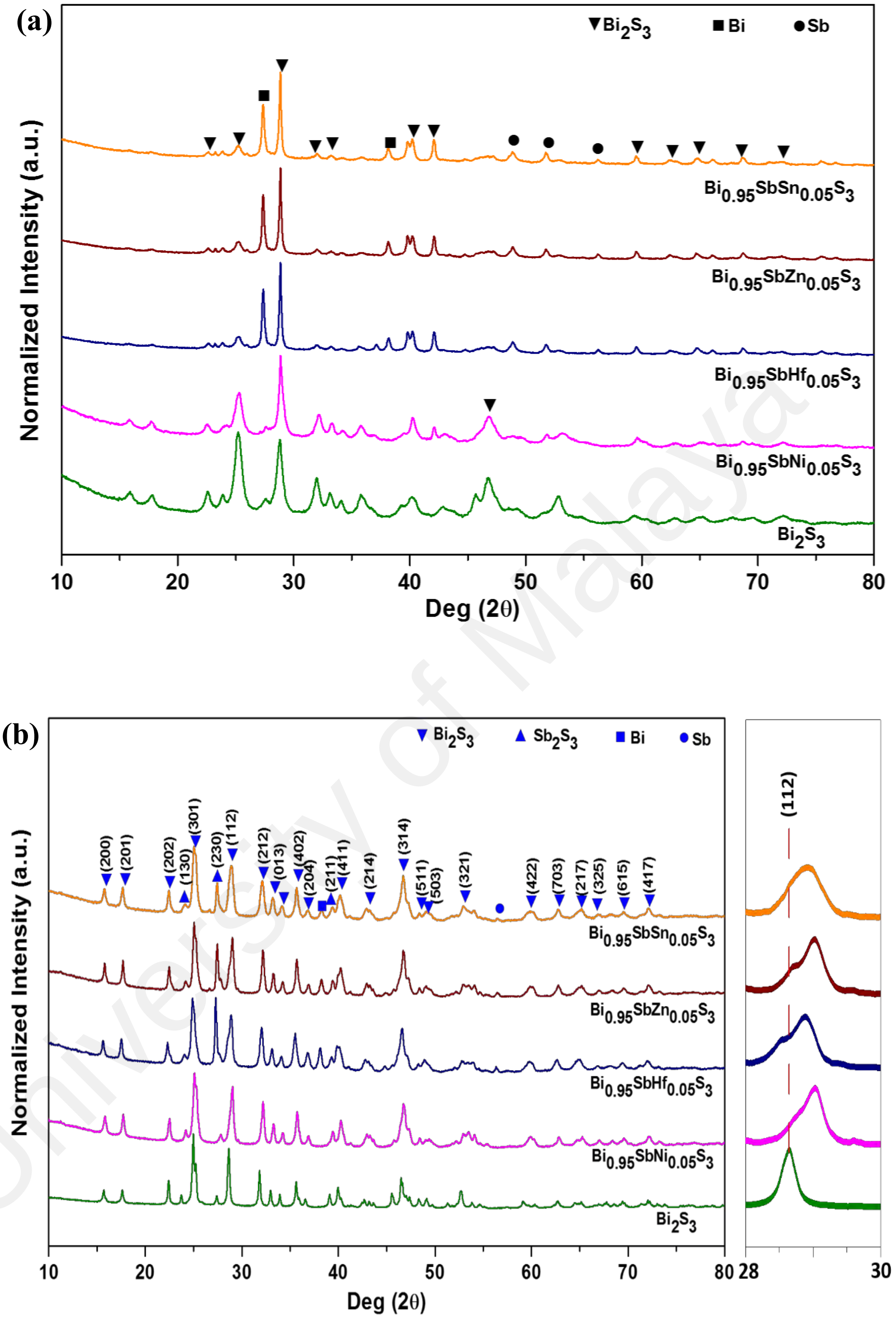

Figure 4.54: XRD patterns of $Bi_{0.95}SbX_{0.05}S_3$ samples; (a) after ball milling process, and (b) SPS-treated bulks. The dominate phase is Bi_2S_3 with secondary phases of Sb_2S_3, Bi and Sb appeared.

Table 4.15: Average crystallite size and density of $Bi_{0.95}SbX_{0.05}S_3$ SPSed samples.

Nominal Composition	Average Crystallite Size (nm)		Density (g/cm^3)	Relative Density (%)
	Milled powder	SPS-ed samples		
Bi_2S_3	57.65	78.5	6.19	90.95
$Bi_{0.95}SbNi_{0.05}S_3$	66.38	94.79	5.30	77.83
$Bi_{0.95}SbHf_{0.05}S_3$	76.51	83.55	4.86	71.32
$Bi_{0.95}SbZn_{0.05}S_3$	87.69	94.78	4.92	72.20
$Bi_{0.95}SbSn_{0.05}S_3$	74.12	58.04	5.07	74.43

Nevertheless, it can clearly be seen in Figure 4.54(b) that the peak position of the (112) diffraction peak gradually shifts to the higher 2θ value with the present of dopant elements (Sb-X), suggesting mild lattice Bi_2S_3 become shrinkage. This is probably because of more substitution of the Bi sites by the Sb or/and dopant atoms as the effective ionic radius of Sb (0.76 Å), Ni (0.96 Å), Hf (0.71 Å), Zn (0.74 Å), and Sn (0.96 Å) are smaller than that of Bi (1.03 Å). To further confirm this, the calculation of room temperature lattice parameters of Bi_2S_3 phase for all samples using XRD data are presented in Table 4.16. As comparison, the lattice parameter for standard Bi_2S_3 references and $Bi_{1.95}Ni_{0.05}S_3$ SPSed sample are also included. It is clearly seen that the volume of unit cell for Sb-X doped samples are smaller than that of pure Bi_2S_3 sample, i.e. shrunken unit cell, which is attributed the entering the Sb or/and dopant atoms into Bi site, as supported from the crystal structure plotted after refinement using JANA2006 (in Figure 4.55)

Table 4.16: Lattice parameters of Bi_2S_3 phase and Sb_2S_3 phase.

Compound/Lattice Parameters	Bi_2S_3 phase, orthorhombic				Sb_2S_3 phase, orthorhombic			
	a (Å)	b (Å)	c (Å)	Volume unit cell (Å^3)	a (Å)	b (Å)	c (Å)	Volume unit cell (Å^3)
Reference	11.2690	3.9720	11.1290	498.14	11.2290	11.3100	3.8390	487.55
SPSed Bi_2S_3	11.2963	3.9860	11.1452	501.66	-	-	-	-
SPSed $Bi_{1.95}Ni_{0.05}S_3$	11.2896	3.9919	11.1386	501.98	-	-	-	-
$Bi_{0.95}SbNi_{0.05}S_3$	11.2313	3.8984	11.1936	490.10	11.3517	11.0374	3.2045	401.50
$Bi_{0.95}SbHf_{0.05}S_3$	11.2272	3.9433	11.1550	493.86	12.0460	11.6729	3.7862	532.38
$Bi_{0.95}SbZn_{0.05}S_3$	11.2473	3.8984	11.2151	491.74	11.3121	11.0559	3.8867	486.10
$Bi_{0.95}SbSn_{0.05}S_3$	11.2701	3.9115	11.1722	492.50	11.8651	11.6622	3.7838	523.58

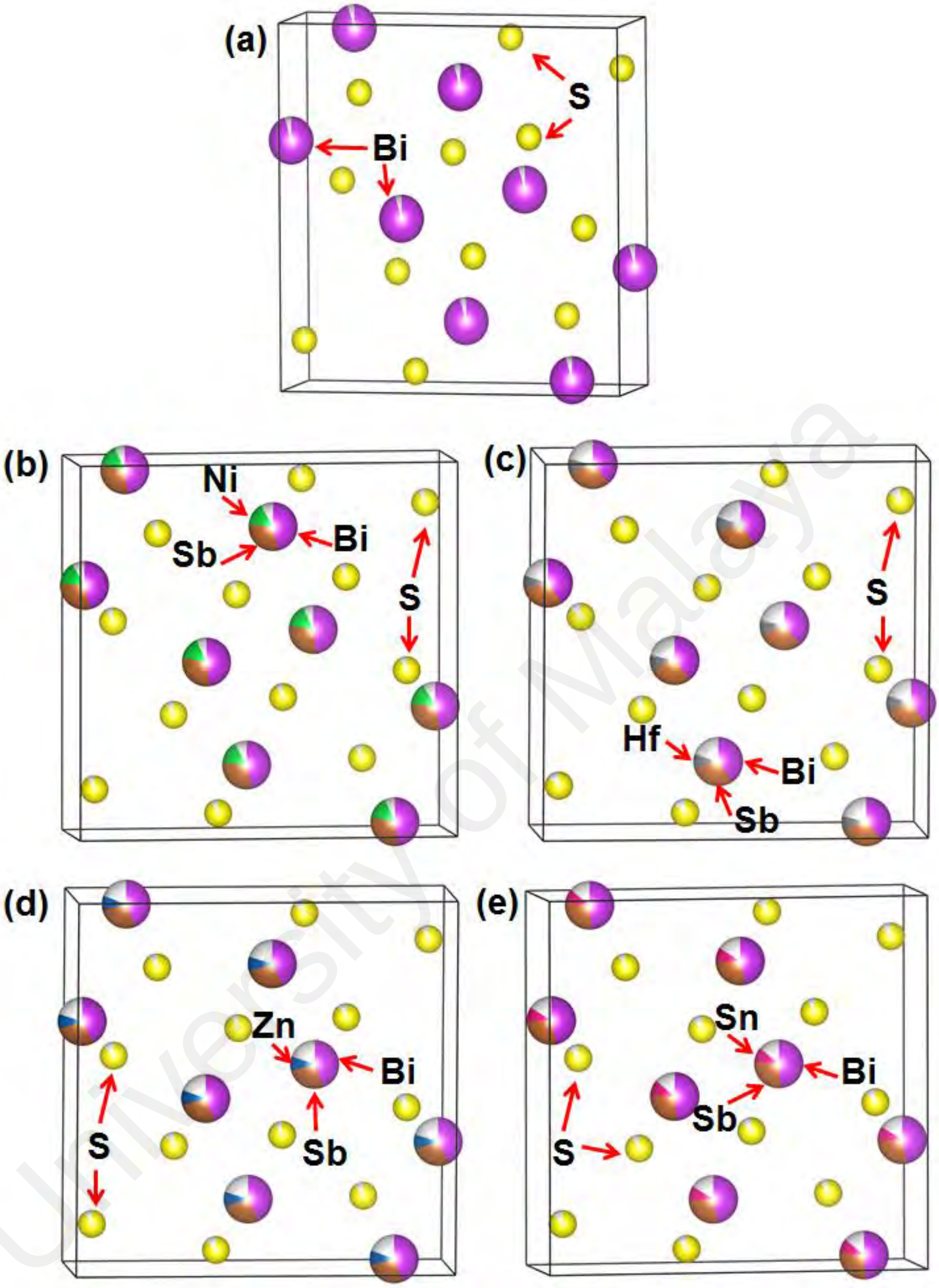

Figure 4.55: The crystal structure of sintered $Bi_{2-x}Ni_xS_3$ samples after refinement using JANA 2006; (a) Bi_2S_3, (b) $Bi_{0.95}SbNi_{0.05}S_3$, (c) $Bi_{0.95}SbHf_{0.05}S_3$, (d) $Bi_{0.95}SbZn_{0.05}S_3$, and (e) $Bi_{0.95}SbSn_{0.05}S_3$. The Sb and dopant atoms substituted the Bi site.

Figure (4.56) – (4.59) display FESEM – EDS results of $Bi_{0.95}SbX_{0.05}S_3$ SPSed samples with different dopant atoms (X). The results of FESEM images of fracture surface for $Bi_{1.95}Ni_{0.05}S_3$ sample showed lamellar structures (Fig. 4.56(a)). However, after addition of Sb ($Bi_{0.95}SbNi_{0.05}S_3$ sample), all the lamellar structures turned into granular square structures (Fig. 4.56(b)). A similar granular square structure was also found for $Bi_{0.95}SbHf_{0.05}S_3$ and $Bi_{0.95}SbZn_{0.05}S_3$ samples, whilst for $Bi_{0.95}SbSn_{0.05}S_3$ sample showed sheet shaped structures. The observed grains have dimension less than 1 μm with no obvious large-scale preferred orientation. For all samples, there are some tiny grains among the larger one, which shows an obvious non-uniformity. Those kinds of microstructure may scatter phonons effectively but do not scatter carriers much (Poudel *et al.*, 2008; Xie *et al.*, 2010). The microstructural analysis of fracture surfaces also presented a porous structure for all of doped samples (Fig. 4.56(b), 4.57(b), 4.58(b) and 4.59(b)), which indicated the samples are not dense. As listed in Table 4.15, the density of all doped samples are less than 80%. The decreased on density for doped samples may be due to the presence of the Sb_2S_3 secondary phase which has a lower density (4.63 g/cm^3) compared to that of the Bi_2S_3 matrix (6.81 g/cm^3).

The EDS analysis for all doped samples confirmed that the dominate phases of Bi_2S_3 and Sb_2S_3 with a small amount of Bi excess (EDS point 1 for $Bi_{0.95}SbHf_{0.05}S_3$ sample in Fig.4.57(c), EDS point 1 and 2 for $Bi_{0.95}SbSn_{0.05}S_3$ in Fig.4.59(c)) and Sb excess (EDS point 3 for $Bi_{0.95}SbHf_{0.05}S_3$ in Fig. 4.57(c)), which is in good agreement with the XRD results. The secondary phase of Sb_2S_3 appears to be distributed homogeneously along with the Bi_2S_3 phase in the samples. This might be due to the same orthorhombic structure for Bi_2S_3 and Sb_2S_3 phase.

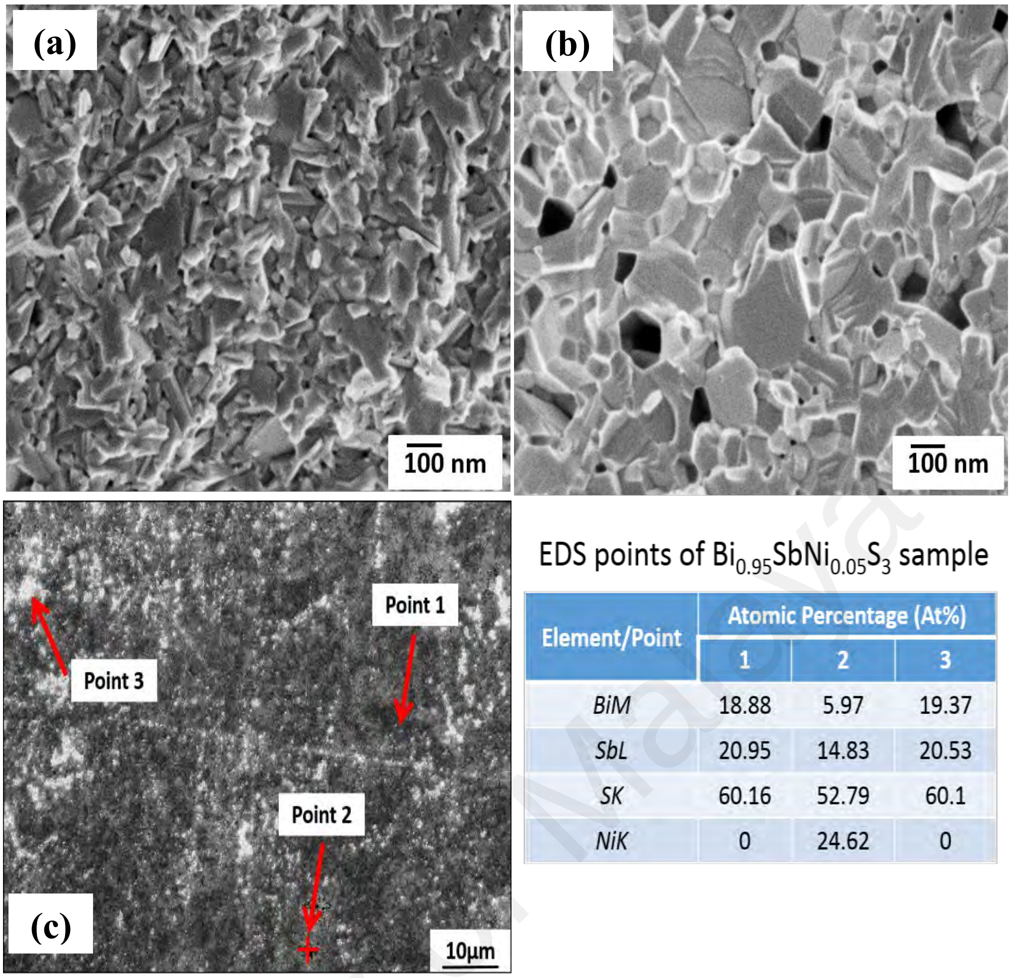

EDS points of $Bi_{0.95}SbNi_{0.05}S_3$ sample

Element/Point	Atomic Percentage (At%)		
	1	2	3
BiM	18.88	5.97	19.37
SbL	20.95	14.83	20.53
SK	60.16	52.79	60.1
NiK	0	24.62	0

Figure 4.56: SEM images of the fractured surface; (a) $Bi_{1.95}Ni_{0.05}S_3$, (b) $Bi_{0.95}SbNi_{0.05}S_3$, and (c) EDS analysis of $Bi_{0.95}SbNi_{0.05}S_3$ sample.

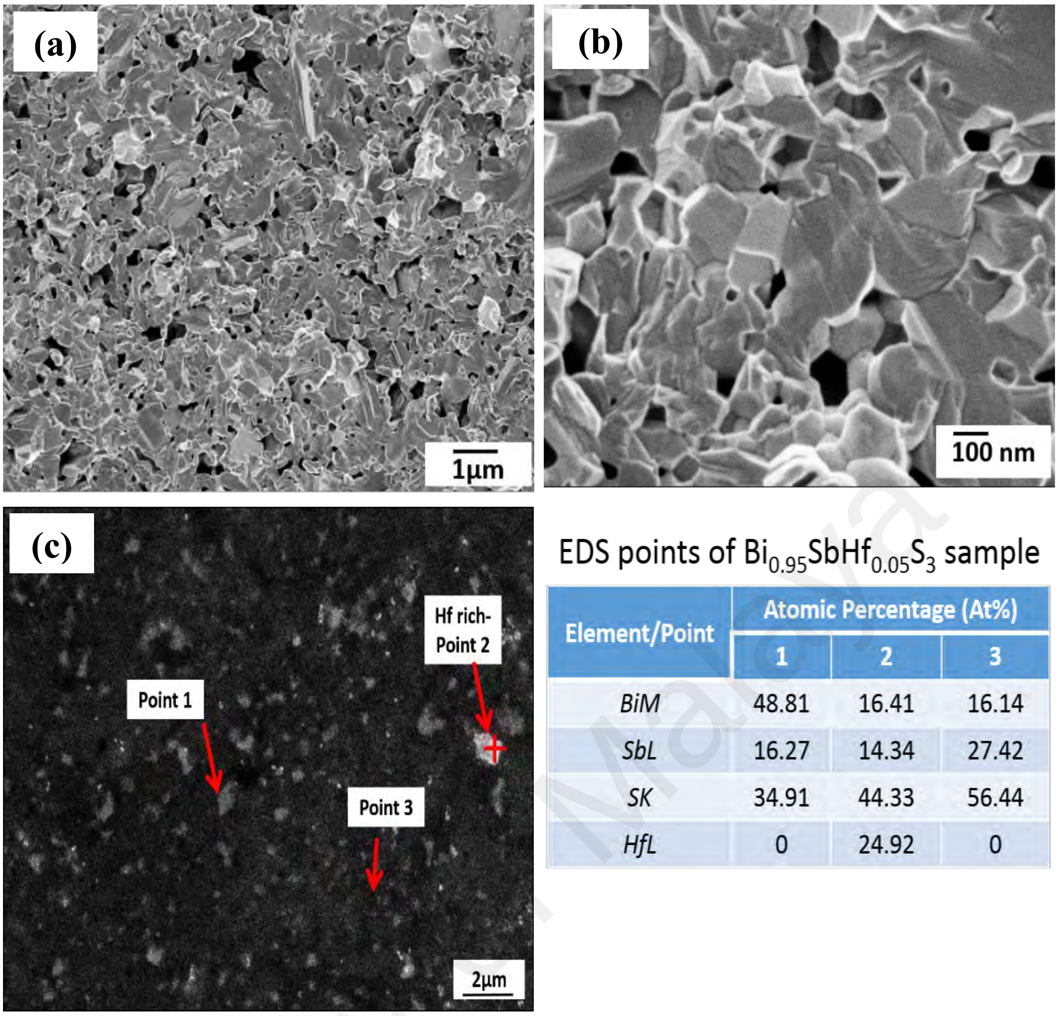

EDS points of $Bi_{0.95}SbHf_{0.05}S_3$ sample

Element/Point	Atomic Percentage (At%)		
	1	2	3
BiM	48.81	16.41	16.14
SbL	16.27	14.34	27.42
SK	34.91	44.33	56.44
HfL	0	24.92	0

Figure 4.57: SEM – EDS results for $Bi_{0.95}SbHf_{0.05}S_3$ sample; (a), (b) SEM images of fractured surface in different magnification, and (c) EDS analysis.

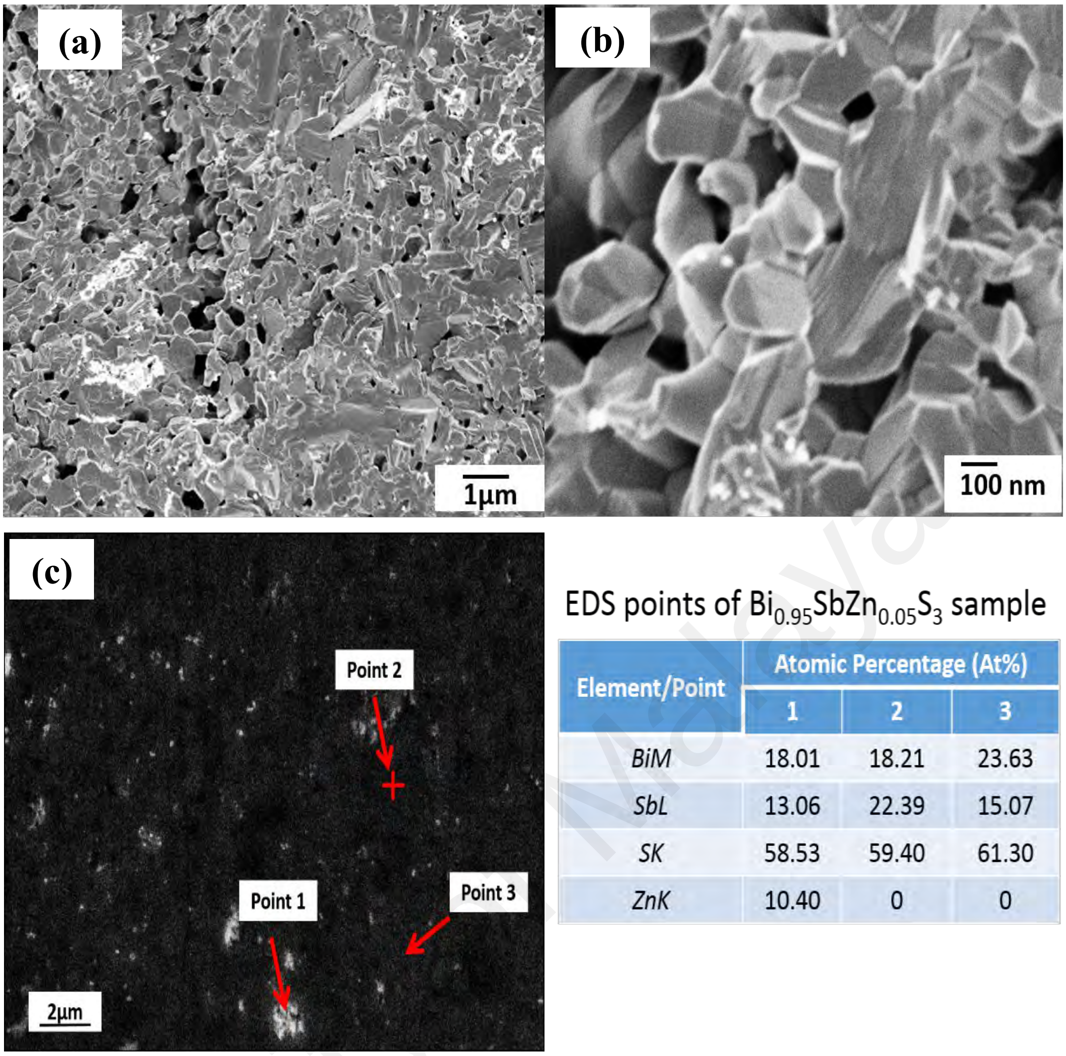

EDS points of $Bi_{0.95}SbZn_{0.05}S_3$ sample

Element/Point	Atomic Percentage (At%)		
	1	2	3
BiM	18.01	18.21	23.63
SbL	13.06	22.39	15.07
SK	58.53	59.40	61.30
ZnK	10.40	0	0

Figure 4.58: SEM – EDS results for $Bi_{0.95}SbZn_{0.05}S_3$ sample; (a), (b) SEM images of fractured surface in different magnification, and (c) EDS analysis.

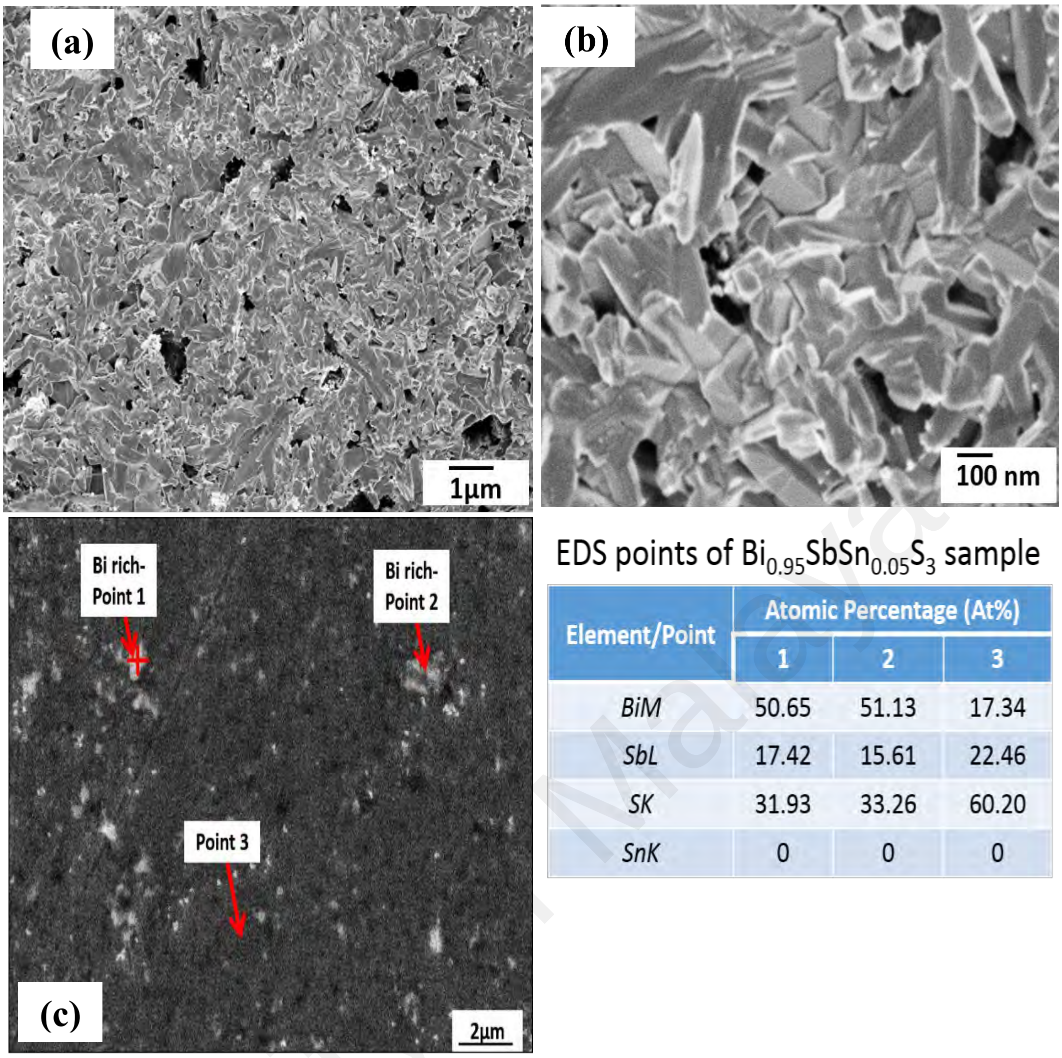

EDS points of $Bi_{0.95}SbSn_{0.05}S_3$ sample

Element/Point	Atomic Percentage (At%)		
	1	2	3
BiM	50.65	51.13	17.34
SbL	17.42	15.61	22.46
SK	31.93	33.26	60.20
SnK	0	0	0

Figure 4.59: SEM – EDS results for $Bi_{0.95}SbSn_{0.05}S_3$ sample; (a), (b) SEM images of fractured surface in different magnification, and (c) EDS analysis.

4.6.2 Thermoelectric properties

Figure 4.60 displays the temperature dependence of electrical resistivity for double doped, $Bi_{0.95}SbX_{0.05}S_3$ (X = Ni, Hf, Zn and Sn) SPSed samples. All the samples showed a trend of decreasing in electrical resistivity with increasing the temperature, which indicated a semiconducting like behavior (Ge *et al.*, 2012a). The addition of double dopant atoms (Sb-*X*) shifted the electrical resistivity of Bi_2S_3 into a higher values in the whole measured range temperature. At 300 K, Bi_2S_3 recorded an electrical resistivity value of 3.45 x 10^{-2} Ω.m. Further, addition 0.05 of Ni into Bi_2S_3 reduced the electrical resistivity to become 1.473 x 10^{-2} Ω.m (group B results). However, the electrical resistivity of Ni doped Bi_2S_3 showed an increase after Sb addition, $Bi_{0.95}SbNi_{0.05}S_3$, (387.63 Ω.m at the same temperature). An increase on electrical resistivity of Bi_2S_3 system was also reported by Kawamoto and Iwasaki (2014) from the study of $(Bi_{1-x}Sb_x)_2S_3$ compound in which resistivity increased from 8 mΩ.cm to ~ 1x10^5 mΩ.cm for $(Bi_{0.2}Sb_{0.8})_2S_3$ sample at 300 K. The higher electrical resistivity values of doped samples may also be related with the appearance of Sb_2S_3 phase which is highly resistive i.e. 3.03 x 10^5 Ω.m at 300 K (Ibuki & Yoshimatsu, 1955).

Amongst the used dopants, hafnium doped sample, $Bi_{0.95}SbHf_{0.05}S_3$, presented the lowest electrical resistivity in the whole measured range temperature. Such behavior was expected as a result of the substitution doping of Hf^{4+} at the Bi^{3+} site created one extra free carrier in the process. Whilst for other dopants (X = Ni, Zn and Sn), as X^{2+} is substituted for Bi^{3+}, acceptor (X^{2+}) will be introduced. Then, the electron concentration will decrease if compensation takes place. In correlation with the previous report, the 4+ valence electron elements (e.g. group IV) are potential dopants for Bi substitution with Sn could lead to low carrier concentrations, whereas Hf could lead to a small improvement of the carrier concentration (Chmielowski *et al.*, 2015). Therefore, the electrical resistivity tendency of $Bi_{0.95}SbHf_{0.05}S_3$ and $Bi_{0.95}SbSn_{0.05}S_3$ in this study could be well understood.

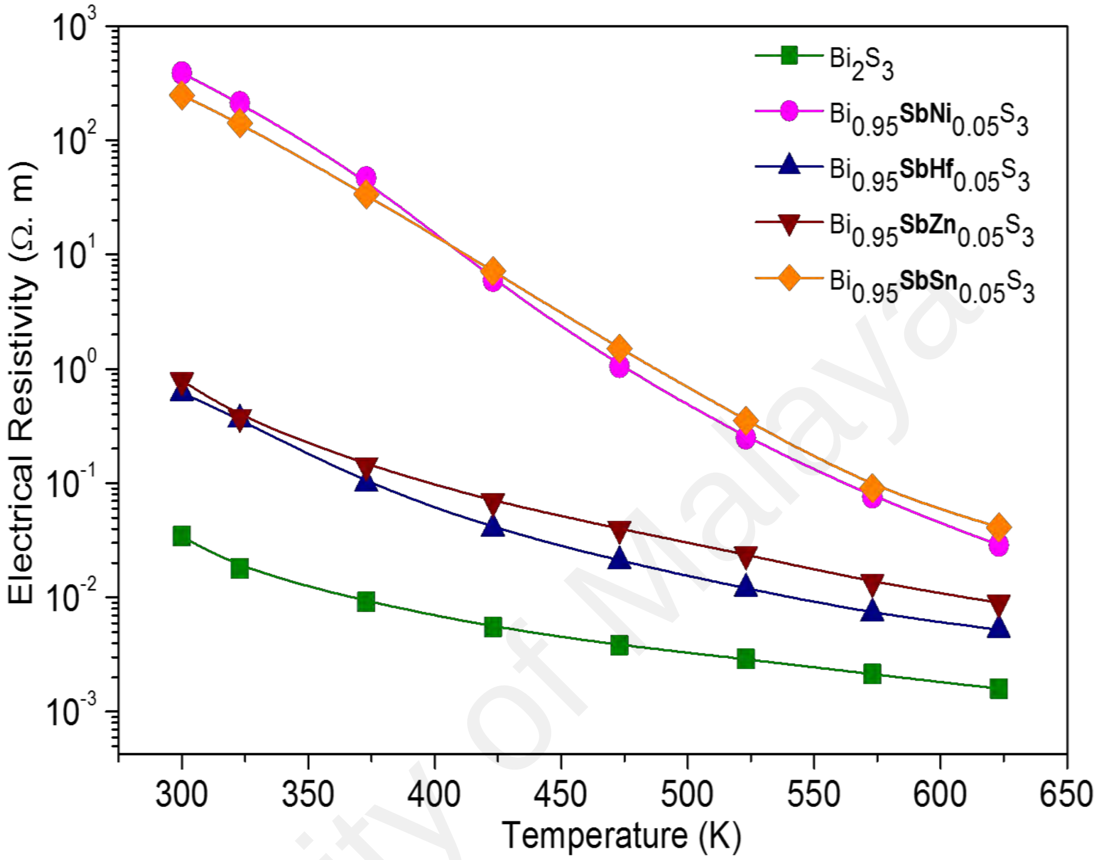

Figure 4.60: Temperature dependence of electrical resistivity ρ for $Bi_{0.95}SbX_{0.05}S_3$ (X = Ni, Hf, Zn and Sn) SPSed samples.

The negative values of the Seebeck coefficient for double doped, $Bi_{0.95}SbX_{0.05}S_3$ (X = Ni, Hf, Zn and Sn) SPSed samples were evaluated over the temperatures ranging from 300 K to 623 K, as shown in Figure 4.61. Those results implied that the major charge carriers in all the samples are electron. The Seebeck coefficient for $Bi_{0.95}SbX_{0.05}S_3$ samples was observed to decrease with increasing temperature, except for $Bi_{0.95}SbZn_{0.05}S_3$ and $Bi_{0.95}SbSn_{0.05}S_3$ at a certain temperature (373 K), which showed a slight increased with an increase in temperature. A similar behavior has been also reported previously on $Bi_xSb_{2-x}Te_3$ nanoplates (Hong *et al.*, 2016), Sn-doped Bi–Sb (Hor & Cava,

2009) and (Bi,Sb)$_2$Te$_3$ compound (Son *et al.*, 2013) which may be due to the excitation of carrier at a high temperature. The highest Seebeck coefficient value was attained by Bi$_{0.95}$SbNi$_{0.05}$S$_3$ sample in whole measured range temperature. It should be noted that Bi$_{0.95}$SbNi$_{0.05}$S$_3$ sample has the smallest unit cell volume as presented in Table 4.16. Thus, a higher values of Seebeck coefficient for Bi$_{0.95}$SbNi$_{0.05}$S$_3$ sample perhaps due to the combination effect of the increase of carrier effective mass (m^*) and the adjustment of carrier concentration, n, in consequence of the formation substitution solution as previously discussed in Ni- and Sn- doped system. At 323K, the magnitude of Seebeck coefficient for Bi$_2$S$_3$ improved from about 467 to 1002 μV/K by addition of Sb and Ni (Bi$_{0.95}$SbNi$_{0.05}$S$_3$ sample).

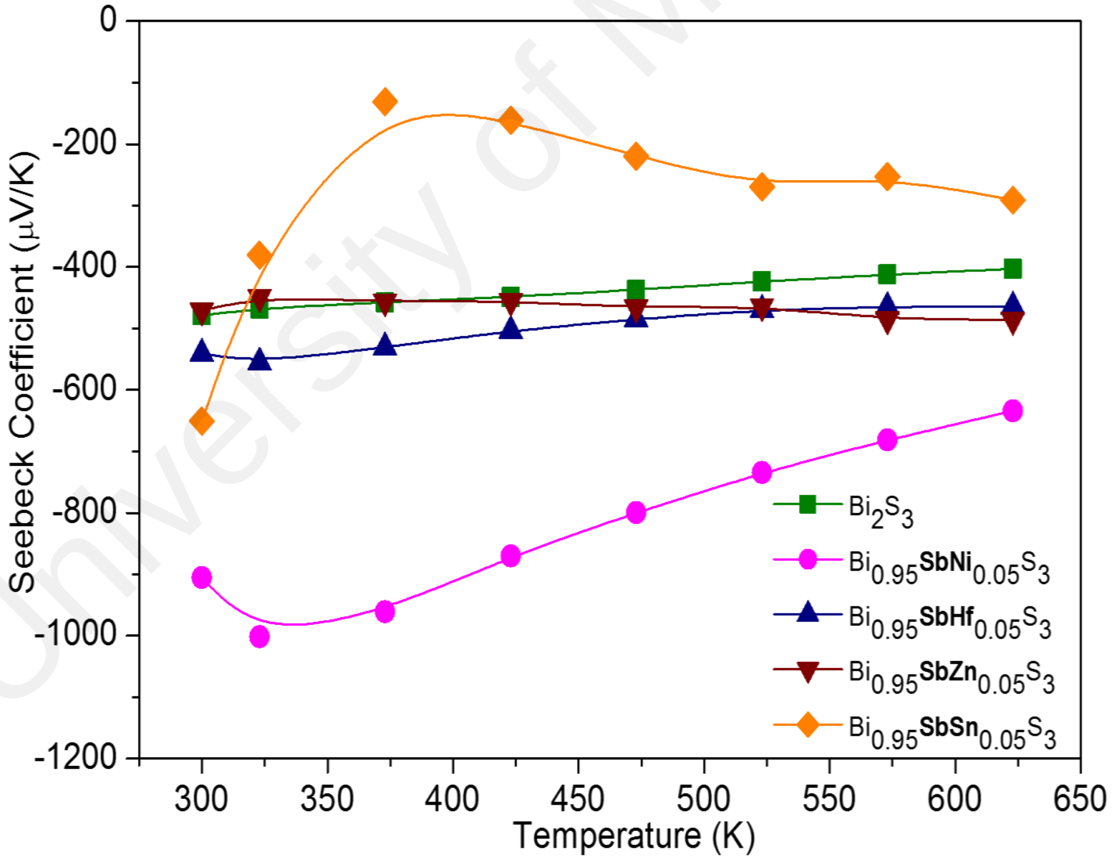

Figure 4.61: Temperature dependence of Seebeck coefficient α for Bi$_{0.95}$SbX$_{0.05}$S$_3$ (X = Ni, Hf, Zn and Sn) SPSed samples.

In comparison with previous reports on Seebeck coefficient values as listed in Table 4.5, the largest Seebeck coefficient of ~ -500 μV/K was attained by $(Bi_{0.2}Sb_{0.8})_2S_3$ compound at 300 K (Kawamoto & Iwasaki, 2014). Which means, the addition of Ni, Hf and Sn into Sb doped Bi_2S_3 under this study successful improved the Seebeck coefficient.

The temperature dependence of power factor *PF* (= α^2/ρ) for double doped system, $Bi_{0.95}SbX_{0.05}S_3$ (X = Ni, Hf, Zn and Sn) SPSed samples is performed in Figure 4.62. It can be seen that the power factor of all the samples increased with increasing temperature. The power factor for doped samples are much lower than that of pure Bi_2S_3. This trend is inverse to the Seebeck coefficient values, which reveals that the electrical resistivity gives more contribution to power factor than that of Seebeck coefficient. Amongst the doped samples, $Bi_{0.95}SbHf_{0.05}S_3$ presented the higher power factor value in the whole temperature range investigated due to its lower electrical resistivity values.

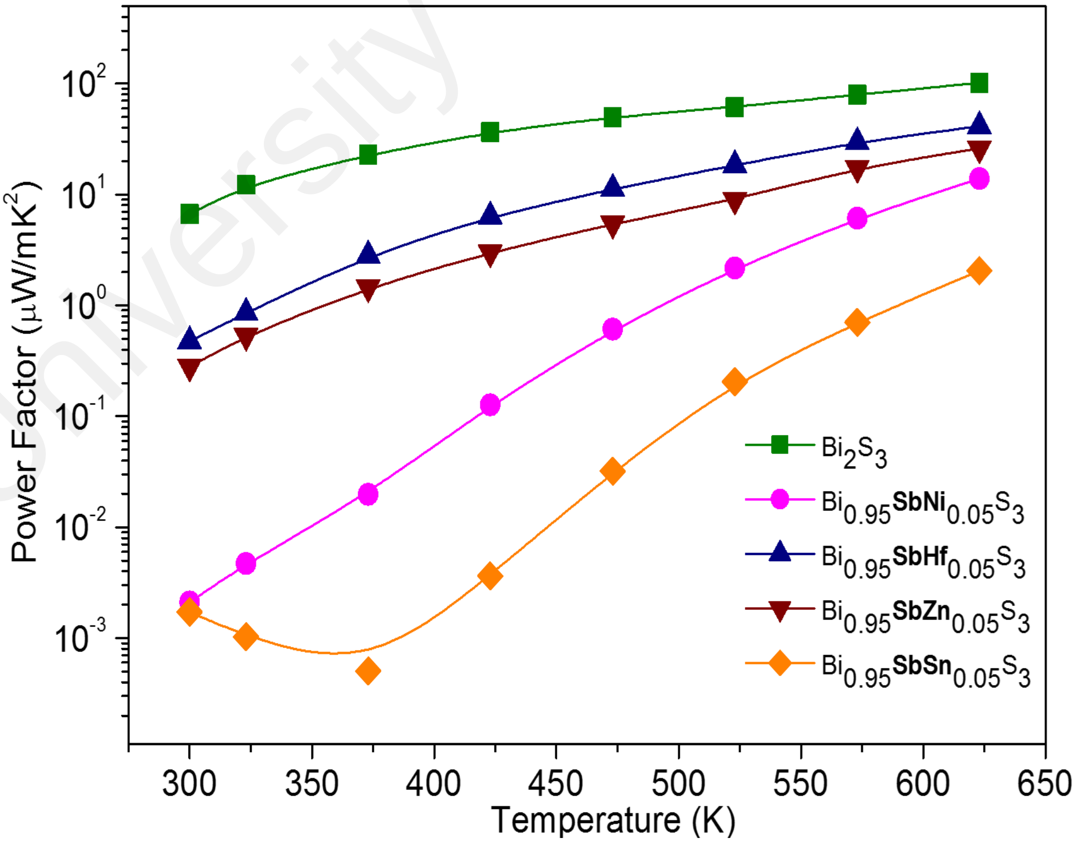

Figure 4.62: Temperature dependence of power factor *PF* for $Bi_{0.95}SbX_{0.05}S_3$ (X = Ni, Hf, Zn and Sn) SPSed samples.

Figure 4.63 presented the temperature dependence of thermal conductivity of double doped, $Bi_{0.95}SbX_{0.05}S_3$ (X = Ni, Hf, Zn and Sn) SPSed samples. All the doped samples showed a lower thermal conductivity value than pure Bi_2S_3 at room temperature. Increasing the measured temperature, the doped samples still recorded a lower thermal conductivity values than that of Bi_2S_3 except for $Bi_{0.95}SbZn_{0.05}S_3$ sample at temperature above 523 K. Recently materials that exhibit intrinsically low thermal conductivity have attracted a lot of attention within the thermoelectric community (Zhao *et al.*, 2014). Thus, $Bi_{0.95}SbX_{0.05}S_3$ indicates their great potentials to satisfy one of the key requirements for a useful thermoelectric material at least from the perspective of thermal transport.

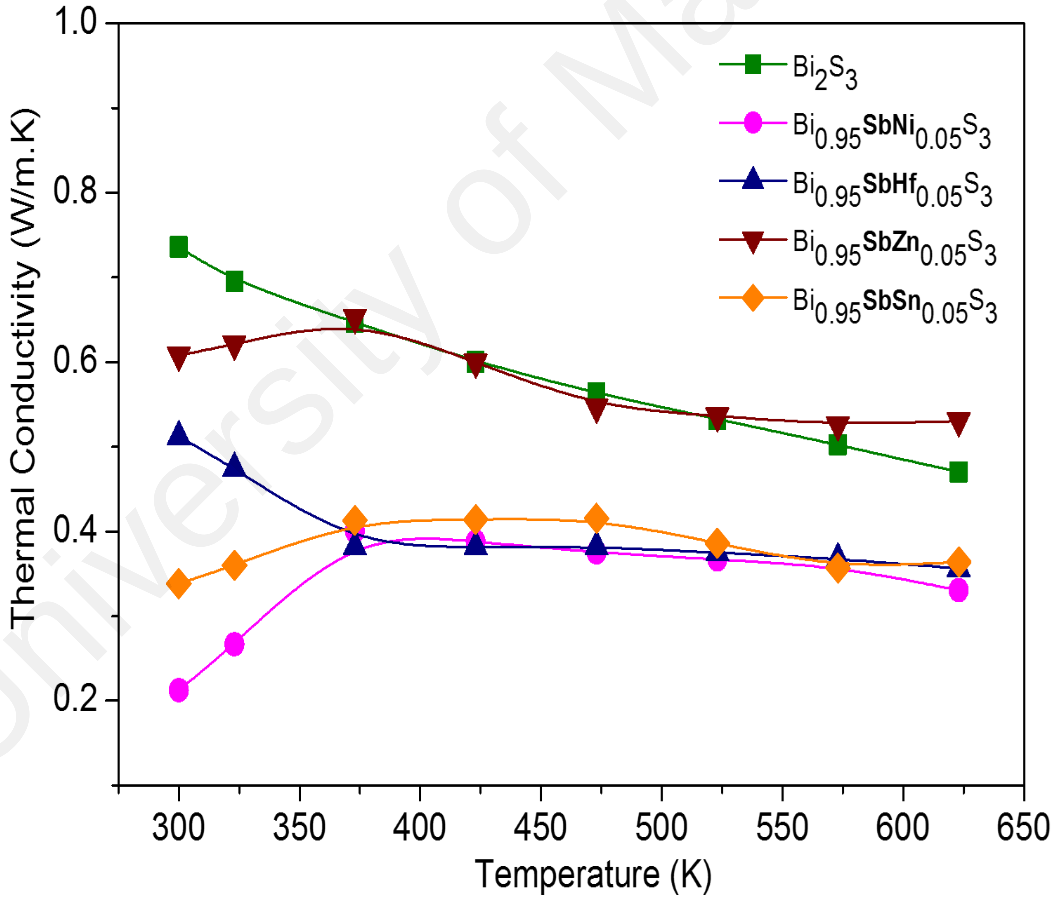

Figure 4.63: Temperature dependence of thermal conductivity κ for $Bi_{0.95}SbX_{0.05}S_3$ (X = Ni, Hf, Zn and Sn) SPSed samples.

$Bi_{1.95}Ni_{0.05}S_3$ sample recorded a thermal conductivity value of 0.57 W/mK at 300 K (Group B results). Addition of Sb into that sample has successfully reduce the thermal conductivity to 0.21 W/mK at the same temperature, which showed a significant lower thermal conductivity at room temperature. As clearly seen in Figure 4.63, $Bi_{0.95}SbNi_{0.05}S_3$ showed an increase in thermal conductivity with increasing the temperature up to 373 K then slightly decreased with further increasing temperature. Whilst, the trend of thermal conductivity for $Bi_{0.95}SbHf_{0.05}S_3$ showed a decrease with increasing temperature in the whole measured range temperature which indicates the dominant mechanism of the phonon scattering inside the material (Cahill *et al.*, 2003). Moreover, $Bi_{0.95}SbZn_{0.05}S_3$ and $Bi_{0.95}SbSn_{0.05}S_3$ samples showed a same thermal conductivity trend to $Bi_{0.95}SbNi_{0.05}S_3$ except the thermal conductivity value start to slightly re-increase above 573 K. $Bi_{0.95}SbNi_{0.05}S_3$ recorded a minimum thermal conductivity of 0.21 W/m.K and 0.33 W/m.K at 300 K and 623 K, respectively. It should be stressed that the thermal conductivity of 0.21 W/m.K for $Bi_{0.95}SbNi_{0.05}S_3$ sample is the lowest value reported for Bi_2S_3-based system, even lower than ~ 0.31 W/m.K of $Bi_{1.99}Ni_{0.01}S_3$ porous system in this study (as discussed in group A – sub section 4.2). The presence of Sb_2S_3 secondary phase is assumed has contributed to those lowest thermal conductivity values.

Generally, the thermal conductivity consists of two parts, including the lattice thermal conductivity (κ_{lat}) and the electronic thermal conductivity (κ_{el}). The electrical resistivity of double doped, $Bi_{0.95}SbX_{0.05}S_3$ samples are notably higher than that of the pure Bi_2S_3 sample (Figure 4.60), which has a meaning that the electronic thermal conductivity of double doped, $Bi_{0.95}SbX_{0.05}S_3$ are lower than that of pure Bi_2S_3 sample. The highest value of electronic thermal conductivity contribution is not excess than 2.04% at 623 K, which is calculated through the Wiedemann–Franz relationship, $\kappa_{el} = LT/\rho$, ($L = 2.45 \times 10^{-8}$ V^2K^2 is the Lorenz number). Therefore, it can be conclude that the total thermal conductivity should be strongly relative to the variation of lattice thermal conductivity.

Figure 4.64 displays the temperature dependence of lattice thermal conductivity of double doped, $Bi_{0.95}SbX_{0.05}S_3$ (X = Ni, Hf, Zn and Sn) SPSed samples. The lattice thermal conductivity can be obtained by directly subtracting the electronic thermal conductivity from total thermal conductivity. All the doped samples showed a lower lattice thermal conductivity value than pure Bi_2S_3 except for $Bi_{0.95}SbZn_{0.05}S_3$ sample at temperature above 523 K. A lower values for $Bi_{0.95}SbX_{0.05}S_3$ samples presumably related with the presence of secondary phase, Sb_2S_3, and porous structure, as well as a lattice imperfection due to substitution dopants. The nanoparticle Sb_2S_3 and micro-porous are effective at scattering intermediate-to-long-wavelength phonons to further reduce lattice thermal conductivity by scattering a wide phonon spectrum (Khan *et al.*, 2017; Vineis *et al.*, 2010). Whilst, the lattice imperfection due to substitution dopants can intensify phonon scattering and make the phonon propagation slowly (Cahill *et al.*, 1992; Callaway & von Baeyer, 1960). The minimum lattice thermal conductivity was achieved by $Bi_{0.95}SbNi_{0.05}S_3$ sample (~ 0.21 W/m.K and ~ 0.33 W/m.K at 300 K and 623 K, respectively).

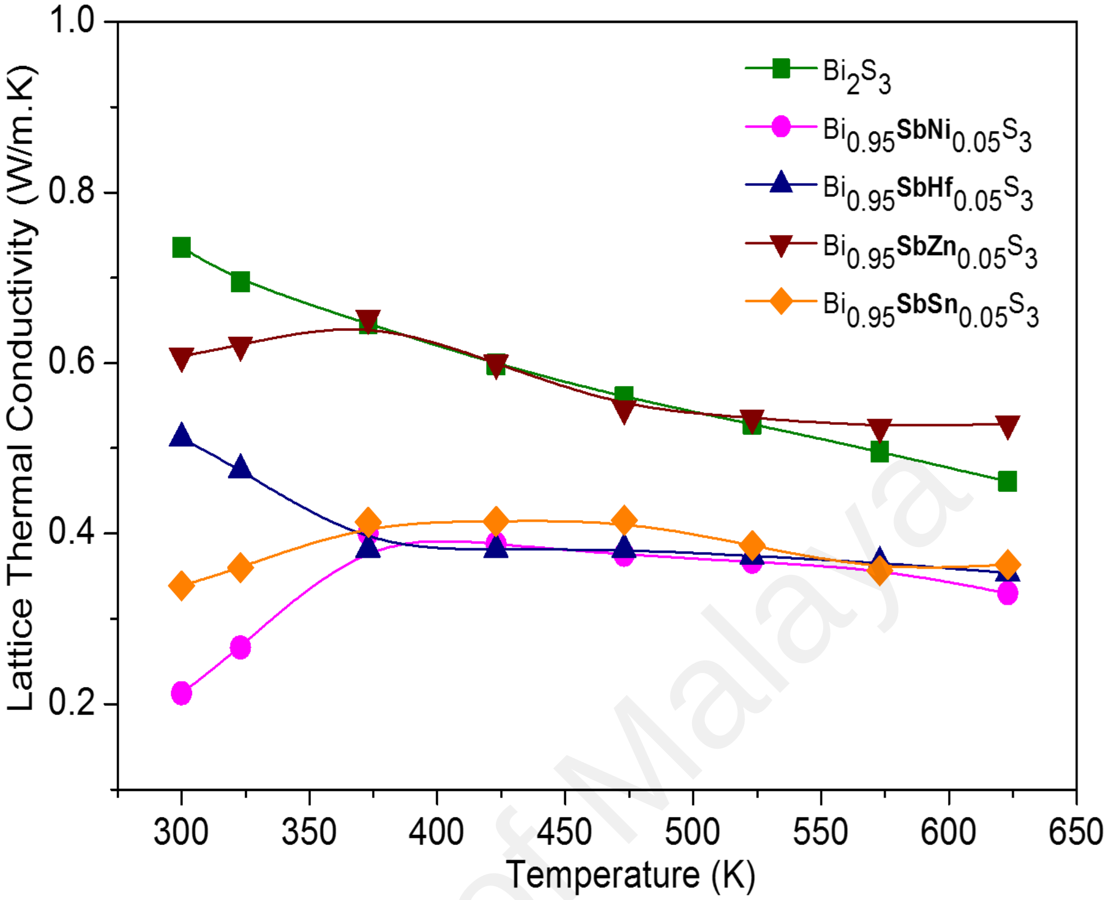

Figure 4.64: Temperature dependence of lattice thermal conductivity κ_{lat} for $Bi_{0.95}SbX_{0.05}S_3$ (X = Ni, Hf, Zn and Sn) SPSed samples.

Combining the electrical and thermal properties of double doped, $Bi_{0.95}SbX_{0.05}S_3$ (X = Ni, Hf, Zn and Sn) SPSed samples, the corresponding *ZT* values are shown in Figure 4.65. All the samples presented an upward trend of *ZT* with increasing the temperature. A moderate figures of merit (ZTs < 0.1) for double doped samples were presented due to a relatively high electrical resistivity values. It is expected that *ZT* could be enhanced by controlling the carrier density in samples with small amounts of antimony substitution.

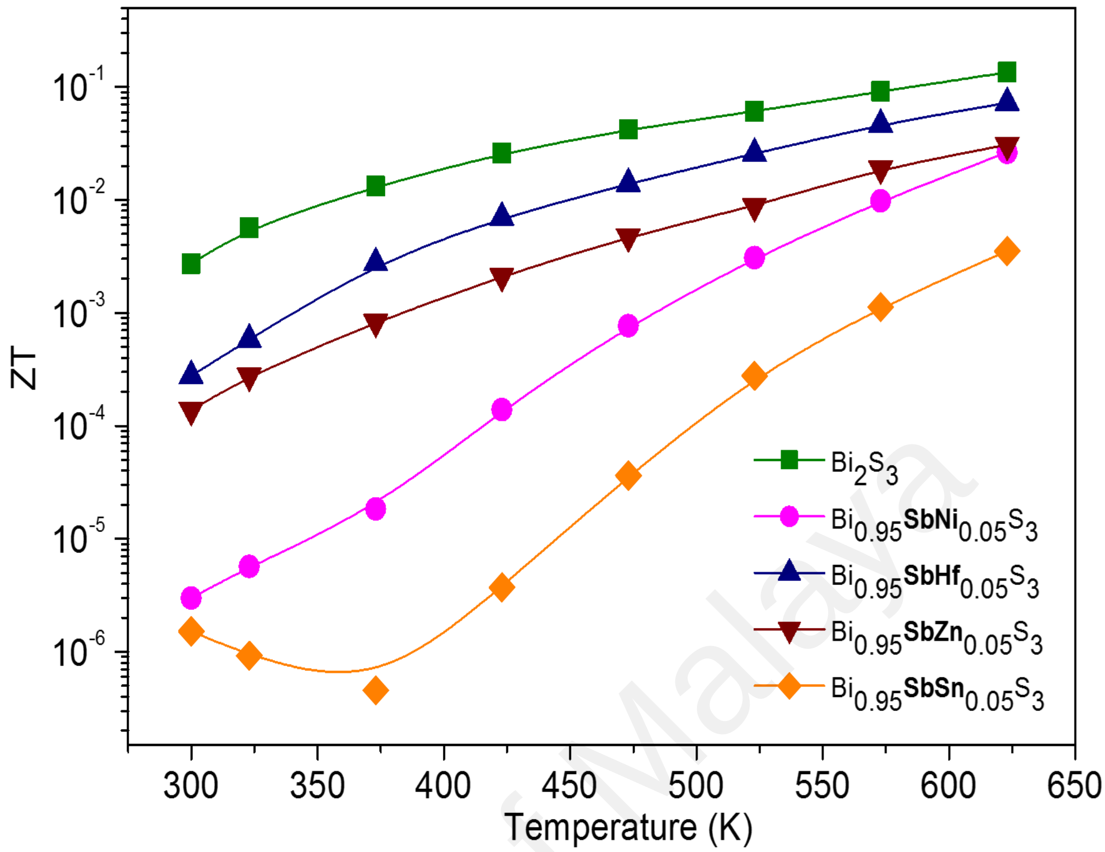

Figure 4.65: Temperature dependence of dimensionless figure of merit *ZT* for $Bi_{0.95}SbX_{0.05}S_3$ (X = Ni, Hf, Zn and Sn) SPSed samples.

In summary, the double doped samples, $Bi_{0.95}SbX_{0.05}S_3$ system (X = Ni, Hf, Zn and Sn) have been evaluated. It was found that all investigated samples have a higher electrical resistivity values than that un-doped Bi_2S_3. This occurrence could be related to the presence of Sb_2S_3 secondary phase in all doped bulk samples. However, the presence of Sb_2S_3 phase has a positive contribution on enhancement of phonon scattering hence resulted in the reduction on thermal conductivity. $Bi_{0.95}SbNi_{0.05}S_3$ sample presented the lowest thermal conductivity value which is 0.21 W/mK at room temperature.

CHAPTER 5: CONCLUSION AND RECOMMENDATION

5.1 Conclusion

In conclusion of this thesis, the elemental doping approach was selected to improve the carrier concentration and reduce the electrical resistivity of Bi_2S_3. Either the single doped system of $Bi_{2-x}Ni_xS_3$, $Bi_{2-x}Sn_{3x}S_3$ and Bi_2S_3+xNiO or double doped system of $Bi_{0.95}SbX_{0.05}S_3$ (X = Ni, Hf, Zn and Sn) were investigated. Nanostructure and nano-microporous structure methods were chosen to improve thermoelectric performance through reduction of thermal conductivity. Mechanical alloying (MA) method by using high energy ball milling (BM) was applied to produce the nanoparticle size powders, which will then be consolidated into bulk thermoelectric materials either through cold pressing or spark plasma sintering (SPS) process. XRD and SEM-EDS analysis of all samples have successfully identified the predominant phase of orthorhombic Bi_2S_3. The results of thermoelectric properties obtained are summarized as follows:

1. The cold pressing method was found to impact the thermoelectric properties in two ways: (1) introduction of the dopant atom in the interstitial sites of the crystal lattice which results in an increase in carrier concentration, and (2) introduction of a porous structure which reduces the thermal conductivity. The electrical resistivity of Bi_2S_3 was decreased by adding Ni atoms, which showed a minimum value of 2.35×10^{-3} Ω.m at 573 K for $Bi_{1.99}Ni_{0.01}S_3$ sample. The presence of porous structures contributed a significant effect on reduction of thermal conductivity, by a reduction of ~59.6% compared to a high density Bi_2S_3. The maximum *ZT* value of 0.13 for Ni doped Bi_2S_3 sample ($Bi_{1.99}Ni_{0.01}S_3$) was found almost three times higher than that pure Bi_2S_3 sample.

2. It was proved that samples with Ni or Sn addition and consolidated with spark plasma sintering (SPS) process demonstrated a predominant phase of orthorhombic Bi_2S_3. The enlargement or shrunken of volume cell of samples indicated that Ni and Sn atoms which were initially expected to replace Bi sites entered the Bi_2S_3 lattice in different atomic position i.e. substitutional or interstitial sites. It was found that interstitial doping significantly affect the reduction of electrical resistivity. The presence of Ni or Sn atoms into interstices of Bi_2S_3 lattice increased the number of electrons as charge carrier, hence decreased the electrical resistivity of Bi_2S_3. The lowest resistivity of 8.27×10^{-4} Ω.m and 1.26×10^{-3} Ω.m were achieved for $Bi_{1.95}Ni_{0.05}S_3$ and $Bi_{1.9}Sn_{0.3}S_3$ samples, respectively, at 623 K. The changing of lattice constant due to substitution or inclusion of Ni or Sn into Bi_2S_3 lattice also affected the Seebeck coefficient of Bi_2S_3 system. The lattice shrinkage due to atomic substitution will lead to increase the effective mass, m^*, thus increase the Seebeck coefficient. $Bi_{1.99}Ni_{0.01}S_3$ and $Bi_{1.99}Sn_{0.03}S_3$ which have the smallest volume cell in its system presented the highest Seebeck coefficient values in the whole measuring temperature. The highest Seebeck coefficient of -766.15 μV/K at 300 K and -1170.25 μV/K at 323 K were exhibited by $Bi_{1.99}Ni_{0.01}S_3$ and $Bi_{1.99}Sn_{0.03}S_3$, respectively. Moreover, either substitutional or interstitial of dopant atoms create the structural disorder and then increase the phonon scattering, hence reduce the lattice thermal conductivity. In conclusion, $Bi_{1.95}Ni_{0.05}S_3$ and $Bi_{1.9}Sn_{0.3}S_3$ presented the highest *ZT* values of 0.38 and 0.17, respectively.
3. The addition of NiO had significant effect on electrical resistivity of Bi_2S_3 system, which was suppressed up to ~ 98% by the addition of 0.5 mol% NiO at room temperature. Furthermore, all NiO added samples showed a very small difference of electrical resistivity values with increasing temperature. Evaluation on all three parameters of transport properties which was represented by dimensionless figure

of merit (*ZT*) results, the addition of NiO significantly enhanced the *ZTs* of Bi_2S_3 system for temperature under 373 K. This implies that NiO added Bi_2S_3 system is suitable for low temperature thermoelectric application. Moreover, the concentration of Ni as dopant element into Bi_2S_3 system should not be higher than 0.5 mol% since increasing the concentration will degenerate its thermoelectric properties. A maximum *ZT* of ~ 0.14 was attained by Bi_2S_3 + 0.5NiO sample at 623 K.

4. It was also demonstrated that the double doped samples, $Bi_{0.95}SbX_{0.05}S_3$ (X = Ni, Hf, Zn and Sn), showed higher electrical resistivity values compare to un-doped Bi_2S_3. This occurrence could be related to the presence of Sb_2S_3 phase in all bulk samples. However, the presence of Sb_2S_3 phase contributed the positive effect on enhancement of phonon scattering hence resulted in the reduction on thermal conductivity. $Bi_{0.95}SbNi_{0.05}S_3$ sample presented the lowest thermal conductivity value which is 0.21 W/mK at room temperature. A moderate figures of merit (*ZTs* < 0.1) were presented due to a relatively high electrical resistivity of samples. It is expected that *ZT* could be enhanced by controlling the carrier density in samples with small amounts of antimony substitution.

The use of dopant atom with lower valence than host atom which can lead to the formation of interstitial solution is an effective strategy to increase the carrier concentration hence decrease the electrical resistivity of Bi_2S_3. Careful examination on dopant concentration range will provide the optimum condition for enhancing the power factor of Bi_2S_3 system, since the formation of substitution solution also give positive impact on improving the Seebeck coefficient of system. Whilst, the presence of secondary phase which has lower density than the main Bi_2S_3 phase which act as nano-inclusion will effectively reduce the lattice thermal conductivity and resulted in lower thermal conductivity of system.

5.2 Recommendations

Several investigation can be performed in the future for further improve the thermoelectric properties of Bi_2S_3 system. It was demonstrated that introducing the porosity effectively in reducing the thermal conductivity of materials. However, the electrical transport properties not showed its optimum performance. Further studies could be done to control the porosity in Bi_2S_3 system (e.g. optimization of the conditions of the spark plasma sintering process) that may reduce the thermal conductivity more, and may improve the electrical transport properties at the same time, and hence improving *ZT*. It is also worth to study the relevance of mechanical strength for porous materials on service-induced stress states to obtain useful information on the robustness of high-performance Bi_2S_3 thermoelectric systems.

It was shown that the single doped of Sn_{3x} could suppressed the electrical resistivity of Bi_2S_3 system for the dopant content (x) more than 0.1. Continuous study to tuning the dopant concentration and measure the corresponding change in the electrical resistivity and other the physical parameters needed for a good estimate of *ZT*. Moreover, the effectiveness of hafnium (Hf) as single doped in Bi_2S_3 system could also be investigated to insure improvement of the overall parameters. It would be also motivating to further discover the effect of antimony (Sb) incorporating in Bi_2S_3 system since the addition of Sb in Bi_2Te_3 system resulted in a high ZT (~1.5).

REFERENCES

Amatya, R., & Ram, R. J. (2012). Trend for thermoelectric materials and their earth abundance. *Journal of Electronic Materials, 41*(6), 1011-1019.

Anselmi-Tamburini, U., Garay, J., Munir, Z., Tacca, A., Maglia, F., Chiodelli, G.*, et al.* (2004a). Spark plasma sintering and characterization of bulk nanostructured fully stabilized zirconia: Part II. Characterization studies. *Journal of Materials Research, 19*(11), 3263-3269.

Anselmi-Tamburini, U., Garay, J., Munir, Z., Tacca, A., Maglia, F., & Spinolo, G. (2004b). Spark plasma sintering and characterization of bulk nanostructured fully stabilized zirconia: Part I. Densification studies. *Journal of Materials Research, 19*(11), 3255-3262.

Barma, M. C. (2016). *Estimation of TE power generations from thermal oil heater and TE material synthesis.* Jabatan Kejuruteraan Mekanik, Fakulti Kejuruteraan, Universiti Malaya.

Biswas, K., He, J., Zhang, Q., Wang, G., Uher, C., Dravid, V. P.*, et al.* (2011). Strained endotaxial nanostructures with high thermoelectric figure of merit. *Nature chemistry, 3*(2), 160-166.

Biswas, K., Zhao, L. D., & Kanatzidis, M. G. (2012). Tellurium-free thermoelectric: The anisotropic n-type semiconductor Bi_2S_3. *Advanced Energy Materials, 2*(6), 634-638.

Bux, S. K., Blair, R. G., Gogna, P. K., Lee, H., Chen, G., Dresselhaus, M. S.*, et al.* (2009). Nanostructured bulk silicon as an effective thermoelectric material. *Advanced Functional Materials, 19*(15), 2445-2452.

Cadavid, D., & Rodriguez, J. (2005). Thermoelectric properties of Bi-Sb samples grown by mechanical alloy. *physica status solidi (c), 2*(10), 3677-3680.

Cahill, D. G., Ford, W. K., Goodson, K. E., Mahan, G. D., Majumdar, A., Maris, H. J.*, et al.* (2003). Nanoscale thermal transport. *Journal of Applied Physics, 93*(2), 793-818.

Cahill, D. G., Watson, S. K., & Pohl, R. O. (1992). Lower limit to the thermal conductivity of disordered crystals. *Physical Review B, 46*(10), 6131.

Caillat, T., Firdosy, S., Li, B., Chi, S., Paik, J., Huang, C.*, et al.* (2009). Advanced high-temperature thermoelectric devices. *Nimbus, 100*, 210C.

Callaway, J., & von Baeyer, H. C. (1960). Effect of point imperfections on lattice thermal conductivity. *Physical Review, 120*(4), 1149.

Cao, Y. Q., Zhao, X. B., Zhu, T. J., Zhang, X. B., & Tu, J. P. (2008). Syntheses and thermoelectric properties of Bi_2Te_3/Sb_2Te3 bulk nanocomposites with laminated nanostructure. *Applied Physics Letters, 92*(14), 143106.

Case, T. W. (1917). Notes on the change of resistance of certain substances in light. *Physical Review, 9*(4), 305.

Champier, D. (2017). Thermoelectric generators: A review of applications. *Energy Conversion and Management, 140*, 167-181.

Chang, Y. W., Chang, C. C., Ke, M. T., & Chen, S. L. (2009). Thermoelectric air-cooling module for electronic devices. *Applied Thermal Engineering, 29*(13), 2731-2737.

Chein, R., & Huang, G. (2004). Thermoelectric cooler application in electronic cooling. *Applied Thermal Engineering, 24*(14), 2207-2217.

Chen, B., Uher, C., Iordanidis, L., & Kanatzidis, M. G. (1997). Transport properties of Bi_2S_3 and the ternary bismuth sulfides $KBi_{6.33}S_{10}$ and $K_2Bi_8S_{13}$. *Chemistry of Materials, 9*(7), 1655-1658.

Chen, K. (2016). *Synthesis and thermoelectric properties of Cu-Sb-S compounds.* (Doctoral Thesis), Queen Mary University of London, United Kingdom.

Chen, X., Weathers, A., Moore, A., Zhou, J., & Shi, L. (2012). Thermoelectric properties of cold-pressed higher manganese silicides for waste heat recovery. *Journal of Electronic Materials, 41*(6), 1564-1572.

Cheng, T. C., Cheng, C. H., Huang, Z. Z., & Liao, G. C. (2011). Development of an energy-saving module via combination of solar cells and thermoelectric coolers for green building applications. *Energy, 36*(1), 133-140.

Chmielowski, R., Péré, D., Bera, C., Opahle, I., Xie, W., Jacob, S., *et al.* (2015). Theoretical and experimental investigations of the thermoelectric properties of Bi_2S_3. *Journal of Applied Physics, 117*(12), 125103.

Choi, H. S., Yun, S., & Whang, K. I. (2007). Development of a temperature-controlled car-seat system utilizing thermoelectric device. *Applied Thermal Engineering, 27*(17), 2841-2849.

Choi, J., Lee, J. Y., Lee, H., Park, C. R., & Kim, H. (2014). Enhanced thermoelectric properties of the flexible tellurium nanowire film hybridized with single-walled carbon nanotube. *Synthetic Metals, 198*, 340-344.

Dai, D., Zhou, Y. X., & Liu, J. (2011). Liquid metal based thermoelectric generation system for waste heat recovery. *Renewable Energy, 36*(12), 3530-3536.

David, B., Ramousse, J., & Luo, L. (2012). Optimization of thermoelectric heat pumps by operating condition management and heat exchanger design. *Energy Conversion and Management, 60*, 125-133.

Dou, Y., Qin, X., Li, D., Li, L., Zou, T., & Wang, Q. (2013). Enhanced thermopower and thermoelectric performance through energy filtering of carriers in $(Bi_2Te_3)_{0.2}(Sb_2Te_3)_{0.8}$ bulk alloy embedded with amorphous SiO_2 nanoparticles. *Journal of Applied Physics, 114*(4), 044906.

Du, X., Cai, F., & Wang, X. (2014a). Enhanced thermoelectric performance of chloride doped bismuth sulfide prepared by mechanical alloying and spark plasma sintering. *Journal of Alloys and Compounds, 587*, 6-9.

Du, X., Shi, R., Ma, Y., Cai, F., Wang, X., & Yuan, Z. (2015). Enhanced thermoelectric performance of n-type Bi_2S_3 with added ZnO for power generation. *RSC Advances, 5*(39), 31004-31009.

Du, Y., Cai, K., Chen, S., Cizek, P., & Lin, T. (2014b). Facile preparation and thermoelectric properties of Bi_2Te_3 based alloy nanosheet/PEDOT: PSS composite films. *ACS Applied Materials & Interfaces, 6*(8), 5735-5743.

Du, Z., Zhu, T., Chen, Y., He, J., Gao, H., Jiang, G.*, et al.* (2012). Roles of interstitial Mg in improving thermoelectric properties of Sb-doped $Mg_2Si_{0.4}Sn_{0.6}$ solid solutions. *Journal of Materials Chemistry, 22*(14), 6838-6844.

El-Asfoury, M. S., Nasr, M. N., Nakamura, K., & Abdel-Moneim, A. (2018a). Structural and thermoelectric properties of $Bi_{85}Sb_{15}$ prepared by non-equal channel angular extrusion. *Journal of Electronic Materials, 47*(1), 242-250.

El-Asfoury, M. S., Nasr, M. N. A., Nakamura, K., & Abdel-Moneim, A. (2018b). Enhanced thermoelectric performance of $Bi_{85}Sb_{15}$-graphene composite by modulation carrier transport and density of state effective mass. *Journal of Alloys and Compounds, 745*, 331-340.

El-Genk, M. S., & Saber, H. H. (2005). Performance analysis of cascaded thermoelectric converters for advanced radioisotope power systems. *Energy Conversion and Management, 46*(7-8), 1083-1105.

El-Genk, M. S., & Saber, H. H. (2006). Thermal and performance analyses of efficient radioisotope power systems. *Energy Conversion and Management, 47*(15-16), 2290-2307.

El-Genk, M. S., Saber, H. H., & Caillat, T. (2003). Efficient segmented thermoelectric unicouples for space power applications. *Energy Conversion and Management, 44*(11), 1755-1772.

El-Genk, M. S., Saber, H. H., Caillat, T., & Sakamoto, J. (2006). Tests results and performance comparisons of coated and un-coated skutterudite based segmented unicouples. *Energy Conversion and Management, 47*(2), 174-200.

Elsheikh, M. H., Sabri, M. F. M., Said, S. M., Miyazaki, Y., Masjuki, H., Shnawah, D. A.*, et al.* (2016). Microstructural Modification of Co4Sb12 Skutterudite Thermoelectric Material Through Al Exceed Doping. *Science of Advanced Materials, 8*(11), 2121-2127.

Enescu D, & Virjoghe EO. (2014). A review on thermoelectric cooling parameters and performance. *Renewable and Sustainable Energy Reviews, 38*, 903-916. doi:

Fitriani, Ovik, R., Long, B. D., Barma, M. C., Riaz, M., Sabri, M. F. M.*, et al.* (2016). A review on nanostructures of high-temperature thermoelectric materials for waste heat recovery. *Renewable and Sustainable Energy Reviews, 64*, 635-659.

Fthenakis, V., & Kim, H. C. (2010). Life-cycle uses of water in U.S. electricity generation. *Renewable and Sustainable Energy Reviews, 14*(7), 2039-2048.

Ge, Z. H., Ji, Y. H., Qiu, Y., Chong, X., Feng, J., & He, J. (2018). Enhanced thermoelectric properties of bismuth telluride bulk achieved by telluride-spilling during the spark plasma sintering process. *Scripta Materialia, 143*, 90-93.

Ge, Z. H., Qin, P., He, D. S., Chong, X., Feng, D., Ji, Y. H., *et al.* (2017). Highly enhanced thermoelectric properties of Bi/Bi_2S_3 nanocomposites. *ACS Applied Materials & Interfaces, 9*(5), 4828-4834.

Ge, Z. H., Zhang, B. P., Liu, Y., & Li, J. F. (2012a). Nanostructured $Bi_{2-x}Cu_xS_3$ bulk materials with enhanced thermoelectric performance. *Physical Chemistry Chemical Physics, 14*(13), 4475-4481.

Ge, Z. H., Zhang, B. P., Shang, P. P., Yu, Y. Q., Chen, C., & Li, J. F. (2011a). Enhancing thermoelectric properties of polycrystalline Bi_2S_3 by optimizing a ball milling process. *Journal of Electronic Materials, 40*(5), 1087-1094.

Ge, Z. H., Zhang, B. P., Yu, Y. Q., & Shang, P. P. (2012b). Fabrication and properties of $Bi_{2-x}Ag_{3x}S_3$ thermoelectric polycrystals. *Journal of Alloys and Compounds, 514*, 205-209.

Ge, Z. H., Zhang, B. P., Yu, Z. X., & Li, J. F. (2011b). Effect of spark plasma sintering temperature on thermoelectric properties of Bi_2S_3 polycrystal. *Journal of Materials Research, 26*(21), 2711-2718.

German, R. (2013). History of sintering: empirical phase. *Powder Metallurgy, 56*(2), 117-123.

Gilfrich, J. (1993). From the Editor. *X-Ray Spectrometry, 22*(5), 341-341.

Gillott, M., Jiang, L., & Riffat, S. (2010). An investigation of thermoelectric cooling devices for small-scale space conditioning applications in buildings. *International Journal of Energy Research, 34*(9), 776-786.

Girard, S. N., He, J., Zhou, X., Shoemaker, D., Jaworski, C. M., Uher, C., *et al.* (2011). High performance Na-doped PbTe–PbS thermoelectric materials: electronic density of states modification and shape-controlled nanostructures. *Journal of the American Chemical Society, 133*(41), 16588-16597.

Goldsmid, H., & Douglas, R. (1954). The use of semiconductors in thermoelectric refrigeration. *British Journal of Applied Physics, 5*(11), 386.

Goldsmid, H. J. (2016). The improvement of a specific material—Bismuth telluride *Introduction to Thermoelectricity* (pp. 85-107): Springer.

Goldstein, J. I., Newbury, D. E., Echlin, P., Joy, D. C., Fiori, C., & Lifshin, E. (1981). *Scanning electron microscopy and X-ray microanalysis. A text for biologists, materials scientists, and geologists*: Plenum Publishing Corporation.

Guo, Y., Du, X., Wang, Y., & Yuan, Z. (2017). Simultaneous enhanced performance of electrical conductivity and Seebeck coefficient in $Bi_{2-x}Sn_xS_3$ by solvothermal and microwave sintering. *Journal of Alloys and Compounds, 717*, 177-182.

Hamid Elsheikh M, Shnawah DA, Sabri MFM, Said SM, Haji Hassan M, Ali Bashir MB, *et al.* (2014). A review on thermoelectric renewable energy: Principle parameters that affect their performance. *Renewable and Sustainable Energy Reviews, 30*, 337-355.

Han, M. K., Jin, Y., Lee, D. H., & Kim, S. J. (2017). Thermoelectric properties of Bi_2Te_3: CuI and the Effect of its doping with Pb atoms. *Materials, 10*(11), 1235.

Harman, T., Taylor, P., Walsh, M., & LaForge, B. (2002). Quantum dot superlattice thermoelectric materials and devices. *Science, 297*(5590), 2229-2232.

He, W., Zhang, G., Zhang, X., Ji, J., Li, G., & Zhao, X. (2015). Recent development and application of thermoelectric generator and cooler. *Applied Energy, 143*, 1-25.

Henry, A. S., & Chen, G. (2008). Spectral phonon transport properties of silicon based on molecular dynamics simulations and lattice dynamics. *Journal of Computational and Theoretical Nanoscience, 5*(2), 141-152.

Heremans, J. P., Jovovic, V., Toberer, E. S., Saramat, A., Kurosaki, K., Charoenphakdee, A., *et al.* (2008). Enhancement of thermoelectric efficiency in PbTe by distortion of the electronic density of states. *Science, 321*(5888), 554-557.

Heremans, J. P., Wiendlocha, B., & Chamoire, A. M. (2012). Resonant levels in bulk thermoelectric semiconductors. *Energy & Environmental Science, 5*(2), 5510-5530.

Hong, M., Chen, Z. G., Yang, L., & Zou, J. (2016). $Bi_xSb_{2-x}Te_3$ nanoplates with enhanced thermoelectric performance due to sufficiently decoupled electronic transport properties and strong wide-frequency phonon scatterings. *Nano Energy, 20*, 144-155.

Hor, Y. S., & Cava, R. J. (2009). Thermoelectric properties of Sn-doped Bi–Sb. *Journal of Alloys and Compounds, 479*(1–2), 368-371.

Hossain, M. A. (2015). *Fabrication and characterization of bulk nanostructured cobalt antimonide based skutterudites materials for thermoelectric applications.* (Thesis Master), KTH - Royal Institute of Technology.

Houghton, J. (2001). Intergovernmental panel on climate change (2001) climate change 2001: Synthesis report summary for policymakers: Cambridge University Press, Cambridge, London.

Hsiao, Y., Chang, W., & Chen, S. (2010). A mathematic model of thermoelectric module with applications on waste heat recovery from automobile engine. *Energy, 35*(3), 1447-1454.

Hsu, K. F., Loo, S., Guo, F., Chen, W., Dyck, J. S., Uher, C.*, et al.* (2004). Cubic AgPbmSbTe$_{2+m}$: bulk thermoelectric materials with high figure of merit. *Science, 303*(5659), 818-821.

Huang, J. (2009). Aerospace and Aircraft Thermoelectric Applications, The Boeing Company, Thermoelectrics Applications Workshop. San Diego, CA.

Ibrahim, A., & Thompson, D. (1985). Thermoelectric properties of BiSb alloys. *Materials Chemistry and Physics, 12*(1), 29-36.

Ibuki, S., & Yoshimatsu, S. (1955). Photoconductivity of stibnite (Sb_2S_3). *Journal of the Physical Society of Japan, 10*(7), 549-554.

Imamuddin, M., & Dupre, A. (1972). Thermoelectric properties of p-type Bi_2Te_3–Sb_2Te_3–Sb_2Se_3 alloys and n-type Bi_2Te_3–Bi_2Se_3 alloys in the temperature range 300 to 600 K. *physica status solidi (a), 10*(2), 415-424.

Jaworski, C. M., Wiendlocha, B., Jovovic, V., & Heremans, J. P. (2011). Combining alloy scattering of phonons and resonant electronic levels to reach a high thermoelectric figure of merit in PbTeSe and PbTeS alloys. *Energy & Environmental Science, 4*(10), 4155-4162.

Johnsen, S., He, J., Androulakis, J., Dravid, V. P., Todorov, I., Chung, D. Y.*, et al.* (2011). Nanostructures boost the thermoelectric performance of PbS. *Journal of the American Chemical Society, 133*(10), 3460-3470.

Joshi, G., Yan, X., Wang, H., Liu, W., Chen, G., & Ren, Z. (2011). Enhancement in thermoelectric figure-of-merit of an *n*-type Half-Heusler compound by the nanocomposite approach. *Advanced Energy Materials, 1*(4), 643-647.

Jung, S. J., Kim, J. H., Kim, D. I., Kim, S. K., Park, H. H., Kim, J. S.*, et al.* (2014). Strain-assisted, low-temperature synthesis of high-performance thermoelectric materials. *Physical Chemistry Chemical Physics, 16*(8), 3529-3533.

Kahn, B. (2017). We just breached the 410 ppm threshold for CO_2. from https://www.scientificamerican.com/article/we-just-breached-the-410-ppm-threshold-for-co2/

Kane, E. O. (1957). Band structure of indium antimonide. *Journal of Physics and Chemistry of Solids, 1*(4), 249-261.

Karri, M., Thacher, E., & Helenbrook, B. (2011). Exhaust energy conversion by thermoelectric generator: Two case studies. *Energy Conversion and Management, 52*(3), 1596-1611.

Kawamoto, Y., & Iwasaki, H. (2014). Thermoelectric properties of $(Bi_{1-x}Sb_x)_2S_3$ with orthorhombics structure. *Journal of Electronic Materials, 43*(6), 1475-1479.

Khan, A. U., Kobayashi, K., Tang, D. M., Yamauchi, Y., Hasegawa, K., Mitome, M.*, et al.* (2017). Nano-micro-porous skutterudites with 100% enhancement in ZT for high performance thermoelectricity. *Nano Energy, 31*, 152-159.

Killedar, V. V., Katore, S. N., & Bhosale, C. H. (2000). Preparation and characterization of electrodeposited Bi_2S_3 thin films prepared from non-aqueous media. *Materials Chemistry and Physics, 64*(2), 166-169.

Kim, D. (2013). *Thermoelectric properties of InSb-and $CoSb_3$-based compounds.* (Doctoral dissertation), Osaka University.

Kim, S. I., Lee, K. H., Mun, H. A., Kim, H. S., Hwang, S. W., Roh, J. W., *et al.* (2015). Dense dislocation arrays embedded in grain boundaries for high-performance bulk thermoelectrics. *Science, 348*(6230), 109-114.

Kim, S. L., Choi, K., Tazebay, A., & Yu, C. (2014). Flexible power fabrics made of carbon nanotubes for harvesting thermoelectricity. *ACS nano, 8*(3), 2377-2386.

Kim, W., Zide, J., Gossard, A., Klenov, D., Stemmer, S., Shakouri, A., *et al.* (2006). Thermal conductivity reduction and thermoelectric figure of merit increase by embedding nanoparticles in crystalline semiconductors. *Physical Review Letters, 96*(4), 045901.

Ko, D.-K., Kang, Y., & Murray, C. B. (2011). Enhanced thermopower via carrier energy filtering in solution-processable Pt–Sb_2Te_3 nanocomposites. *Nano Letters, 11*(7), 2841-2844.

Kosmac, T., Maurice, D., & Courtney, T. H. (1993). Synthesis of nickel sulfides by mechanical alloying. *Journal of the American Ceramic Society, 76*(9), 2345-2352.

Koumoto, K., & Mori, T. (2015). *Thermoelectric nanomaterials*: Springer.

Kousksou, T., Bedecarrats, J. P., Champier, D., Pignolet, P., & Brillet, C. (2011). Numerical study of thermoelectric power generation for an helicopter conical nozzle. *Journal of Power Sources, 196*(8), 4026-4032.

Kurlov, A., & Gusev, A. (2007). Effect of ball milling parameters on the particle size in nanocrystalline powders. *Technical Physics Letters, 33*(10), 828-832.

Lee, H., Vashaee, D., Wang, D. Z., Dresselhaus, M. S., Ren, Z. F., & Chen, G. (2010). Effects of nanoscale porosity on thermoelectric properties of SiGe. *Journal of Applied Physics, 107*(9), 094308.

Leonov, V., Torfs, T., Vullers, R. J., & Van Hoof, C. (2010). Hybrid thermoelectric–photovoltaic generators in wireless electroencephalography diadem and electrocardiography shirt. *Journal of Electronic Materials, 39*(9), 1674-1680.

Lewis, N. S., & Nocera, D. G. (2006). Powering the planet: Chemical challenges in solar energy utilization. *Proceedings of the National Academy of Sciences, 103*(43), 15729-15735.

Li, D., Qin, X., Liu, J., & Yang, H. (2004). Electrical resistivity and thermopower of intercalation compounds Bi_xTiS_2. *Physics Letters A, 328*(6), 493-499.

Li, L., Liu, Y., Dai, J., Zhu, H., Hong, A., Zhou, X., *et al.* (2015). Thermoelectric property studies on $Cu_xBi_2SeS_2$ with nano-scale precipitates Bi_2S_3. *Nano Energy, 12*, 447-456.

Lineykin, S., & Ben-Yaakov, S. (2007). Modeling and analysis of thermoelectric modules. *Industry Applications, IEEE Transactions on, 43*(2), 505-512.

Liu, D., Zhao, F. Y., & Tang, G. F. (2010). Active low-grade energy recovery potential for building energy conservation. *Renewable & Sustainable Energy Reviews, 14*(9), 2736-2747.

Liu, W., Ren, Z., & Chen, G. (2013). Nanostructured thermoelectric materials *Thermoelectric Nanomaterials* (pp. 255-285): Springer.

Liu, W., Yan, X., Chen, G., & Ren, Z. (2012). Recent advances in thermoelectric nanocomposites. *Nano Energy, 1*(1), 42-56.

Liu, W. S., Zhang, Q., Lan, Y., Chen, S., Yan, X., Zhang, Q., *et al.* (2011). Thermoelectric property studies on Cu-doped *n*-type $Cu_xBi_2Te_{2.7}Se_{0.3}$ nanocomposites. *Advanced Energy Materials, 1*(4), 577-587.

Liu, Z., Pei, Y., Geng, H., Zhou, J., Meng, X., Cai, W., *et al.* (2015). Enhanced thermoelectric performance of Bi_2S_3 by synergistical action of bromine substitution and copper nanoparticles. *Nano Energy, 13*, 554-562.

Luo, Q., Wang, Y., & Zhang, P. (2010). *A novel thermoelectric air-conditioner for a truck cab.* Paper presented at the Advances in Energy Engineering (ICAEE), 2010 International Conference.

Mansour, K., Qiu, Y., Hill, C. J., Soibel, A., & Yang, R. Q. (2006). Mid-infrared interband cascade lasers at thermoelectric cooler temperatures. *Electronics Letters, 42*(18), 1034-1036.

Manzano, C. V., Abad, B., Rojo, M. M., Koh, Y. R., Hodson, S. L., Martinez, A. M. L., *et al.* (2016). Anisotropic effects on the thermoelectric properties of highly oriented electrodeposited Bi_2Te_3 films. *Scientific reports, 6*, 19129.

Martín-González, M., Caballero-Calero, O., & Díaz-Chao, P. (2013). Nanoengineering thermoelectrics for 21st century: Energy harvesting and other trends in the field. *Renewable and Sustainable Energy Reviews, 24*, 288-305.

Min, G., & Rowe, D. M. (2006). Experimental evaluation of prototype thermoelectric domestic-refrigerators. *Applied Energy, 83*(2), 133-152.

Minnich AJ, Dresselhaus MS, Ren ZF, & Chen G. (2009). Bulk nanostructured thermoelectric materials: Current research and future prospects. *Energy & Environmental Science, 2*(5), 466-479.

Miranda, A. G., Chen, T. S., & Hong, C. W. (2013). Feasibility study of a green energy powered thermoelectric chip based air conditioner for electric vehicles. *Energy, 59*, 633-641.

Mizoguchi, H., Hosono, H., Ueda, N., & Kawazoe, H. (1995). Preparation and electrical properties of Bi_2S_3 whiskers. *Journal of Applied Physics, 78*(2), 1376-1378.

Mizutani, U. (2016). *Hume-Rothery rules for structurally complex alloy phases*: CRC Press.

Mori, T. (2017). Novel principles and nanostructuring methods for enhanced thermoelectrics. *Small*.

Munir, Z., Anselmi-Tamburini, U., & Ohyanagi, M. (2006). The effect of electric field and pressure on the synthesis and consolidation of materials: A review of the spark plasma sintering method. *Journal of materials science, 41*(3), 763-777.

Nan, C. W., Birringer, R., Clarke, D. R., & Gleiter, H. (1997). Effective thermal conductivity of particulate composites with interfacial thermal resistance. *Journal of Applied Physics, 81*(10), 6692-6699.

Nguyen, P., Lee, K., Moon, J., Kim, S., Ahn, K., Chen, L., *et al.* (2012). Spark erosion: A high production rate method for producing $Bi_{0.5}Sb_{1.5}Te_3$ nanoparticles with enhanced thermoelectric performance. *Nanotechnology, 23*(41), 415604.

Nolas, G. S., Sharp, J., & Goldsmid, J. (2013). *Thermoelectrics: Basic principles and new materials developments* (Vol. 45): Springer Science & Business Media.

Pandey, T., & Singh, A. K. (2016). Simultaneous enhancement of electrical conductivity and thermopower in Bi_2S_3 under hydrostatic pressure. *Journal of Materials Chemistry C, 4*(10), 1979-1987.

Parker, W., Jenkins, R., Butler, C., & Abbott, G. (1961). Flash method of determining thermal diffusivity, heat capacity, and thermal conductivity. *Journal of Applied Physics, 32*(9), 1679-1684.

Patnaik, P. (2003). *Handbook of inorganic chemicals* (Vol. 529): McGraw-Hill New York.

Pearson, G. L., & Bardeen, J. (1949). Electrical properties of pure silicon and silicon alloys containing boron and phosphorus. *Physical Review, 75*(5), 865.

Pei, J., Zhang, L.-J., Zhang, B.-P., Shang, P.-P., & Liu, Y.-C. (2017). Enhancing the thermoelectric performance of $Ce_xBi_2S_3$ by optimizing the carrier concentration combined with band engineering. *Journal of Materials Chemistry C, 5*(47), 12492-12499.

Pei, Y., Shi, X., LaLonde, A., Wang, H., Chen, L., & Snyder, G. J. (2011). Convergence of electronic bands for high performance bulk thermoelectrics. *Nature, 473*(7345), 66.

Petit, J. R., Jouzel, J., Raynaud, D., Barkov, N. I., Barnola, J. M., Basile, I., *et al.* (1999). Climate and atmospheric history of the past 420,000 years from the Vostok ice core, Antarctica. *Nature, 399*(6735), 429.

Petříček, V., Dušek, M., & Palatinus, L. (2014). Crystallographic Computing System JANA2006: General features *Zeitschrift für Kristallographie - Crystalline Materials* (Vol. 229, pp. 345).

Poudel, B., Hao, Q., Ma, Y., Lan, Y., Minnich, A., Yu, B.*, et al.* (2008). High-thermoelectric performance of nanostructured bismuth antimony telluride bulk alloys. *Science, 320*(5876), 634-638.

Puneet, P., Podila, R., Karakaya, M., Zhu, S., He, J., Tritt, T. M.*, et al.* (2013). Preferential scattering by interfacial charged defects for enhanced thermoelectric performance in few-layered n-type Bi_2Te_3. *Scientific reports, 3*, 3212.

Putra, N., Sukyono, W., Johansen, D., & Iskandar, F. (2010). The characterization of a cascade thermoelectric cooler in a cryosurgery device. *Cryogenics, 50*(11), 759-764.

Ravich, Y. I., Efimova, B., & Tamarchenko, V. (1971). Scattering of current carriers and transport phenomena in lead chalcogenides. *physica status solidi (b), 43*(1), 11-33.

Riffat, S. B., & Ma, X. L. (2003). Thermoelectrics: a review of present and potential applications. *Applied Thermal Engineering, 23*(8), 913-935.

Riffat, S. B., & Qiu, G. (2004). Comparative investigation of thermoelectric air-conditioners versus vapour compression and absorption air-conditioners. *Applied Thermal Engineering, 24*(14), 1979-1993.

Rowe, D. M. (1995). *CRC Handbook of thermoelectrics*: CRC press.

Rowe, D. M., & Bhandari, C. M. (1983). *Modern thermoelectrics*: Prentice Hall.

Saidur, R., Rezaei, M., Muzammil, W. K., Hassan, M. H., Paria, S., & Hasanuzzaman, M. (2012). Technologies to recover exhaust heat from internal combustion engines. *Renewable & Sustainable Energy Reviews, 16*(8), 5649-5659.

Shakouri, A. (2011). Recent developments in semiconductor thermoelectric physics and materials. *Annual Review of Materials Research, 41*(1), 399-431.

Shu, G. Q., Liang, Y. C., Wei, H. Q., Tian, H., Zhao, J., & Liu, L. N. (2013). A review of waste heat recovery on two-stroke IC engine aboard ships. *Renewable & Sustainable Energy Reviews, 19*, 385-401.

Siegenthaler, U., Stocker, T. F., Monnin, E., Lüthi, D., Schwander, J., Stauffer, B.*, et al.* (2005). Stable carbon cycle–climate relationship during the late Pleistocene. *Science, 310*(5752), 1313-1317.

Snyder, G. J., & Toberer, E. S. (2008). Complex thermoelectric materials. *Nature materials, 7*(2), 105-114.

Son, J. H., Oh, M. W., Kim, B. S., Park, S. D., Min, B. K., Kim, M. H.*, et al.* (2013). Effect of ball milling time on the thermoelectric properties of p-type $(Bi,Sb)_2Te_3$. *Journal of Alloys and Compounds, 566*, 168-174.

Sterzel, H. J. (2006). Patent number: WO2006/089938 A1.

Suryanarayana, C. (2001). Mechanical alloying and milling. *Progress in Materials Science, 46*(1), 1-184.

Tang, C., Wang, C., Su, F., Zang, C., Yang, Y., Zong, Z.*, et al.* (2010). Controlled synthesis of urchin-like Bi_2S_3 via hydrothermal method. *Solid State Sciences, 12*(8), 1352-1356.

Tang, C. J., Su, J. F., Hu, Q. B., Yang, Y. X., Wang, C. Q., Zhao, C. H.*, et al.* (2011). Facile synthesis of Bi_2S_3 network nanostructure. *Solid State Sciences, 13*(5), 1152-1156.

Tang, X., Xie, W., Li, H., Zhao, W., Zhang, Q., & Niino, M. (2007). Preparation and thermoelectric transport properties of high-performance p-type Bi_2Te_3 with layered nanostructure. *Applied Physics Letters, 90*(1), 012102.

Tarachand, Sharma, V., Bhatt, R., Ganesan, V., & Okram, G. S. (2016). A catalyst-free new polyol method synthesized hot-pressed Cu-doped Bi_2S_3 nanorods and their thermoelectric properties. *Nano Research, 9*(11), 3291-3304.

Tarkhanyan, R. H., & Niarchos, D. G. (2013). Reduction in lattice thermal conductivity of porous materials due to inhomogeneous porosity. *International Journal of Thermal Sciences, 67*, 107-112.

Tauber, R., Machonis, A., & Cadoff, I. (1966). Thermal and optical energy gaps in PbTe. *Journal of Applied Physics, 37*(13), 4855-4860.

Tie, S. F., & Tan, C. W. (2013). A review of energy sources and energy management system in electric vehicles. *Renewable & Sustainable Energy Reviews, 20*, 82-102.

Ubale, A. U., Daryapurkar, A. S., Mankar, R. B., Raut, R. R., Sangawar, V. S., & Bhosale, C. H. (2008). Electrical and optical properties of Bi_2S_3 thin films deposited by successive ionic layer adsorption and reaction (SILAR) method. *Materials Chemistry and Physics, 110*(1), 180-185.

Ullah, K. R., Saidur, R., Ping, H. W., Akikur, R. K., & Shuvo, N. H. (2013). A review of solar thermal refrigeration and cooling methods. *Renewable & Sustainable Energy Reviews, 24*, 499-513.

Valalaki, K., Benech, P., & Nassiopoulou, A. G. (2016). High Seebeck coefficient of porous silicon: study of the porosity dependence. *Nanoscale research letters, 11*(1), 201.

Van der Pauw, L. (1958). A method of measuring specific resistivity and Hall effect of discs of arbitrary shape. *Philips research reports, 13*, 1-9.

Vegard, L. (1921). Die konstitution der mischkristalle und die raumfüllung der atome. *Zeitschrift für Physik, 5*(1), 17-26.

Vélez, F., Segovia, J. J., Martín, M. C., Antolín, G., Chejne, F., & Quijano, A. (2012). A technical, economical and market review of organic Rankine cycles for the conversion of low-grade heat for power generation. *Renewable and Sustainable Energy Reviews, 16*(6), 4175-4189.

Venkatasubramanian, R., Siivola, E., Colpitts, T., & O'quinn, B. (2001). Thin-film thermoelectric devices with high room-temperature figures of merit. *Nature, 413*(6856), 597-602.

Vineis, C. J., Shakouri, A., Majumdar, A., & Kanatzidis, M. G. (2010). Nanostructured thermoelectrics: big efficiency gains from small features. *Advanced Materials, 22*(36), 3970-3980.

Voyager, the interstellar mission n.d. (2015). from <http://voyager.jpl.nasa.gov/spacecraft/index.html>

W. Hofmann, Z. (1935). *Kristallogr* (Vol. 86).

Wang, T. Y., Zhang, Y. J., Peng, Z. J., & Shu, G. Q. (2011). A review of researches on thermal exhaust heat recovery with Rankine cycle. *Renewable & Sustainable Energy Reviews, 15*(6), 2862-2871.

Wang, Z., Leonov, V., Fiorini, P., & Van Hoof, C. (2009). Realization of a wearable miniaturized thermoelectric generator for human body applications. *Sensors and Actuators A: Physical, 156*(1), 95-102.

Weber, J., Potje-Kamloth, K., Haase, F., Detemple, P., Völklein, F., & Doll, T. (2006). Coin-size coiled-up polymer foil thermoelectric power generator for wearable electronics. *Sensors and Actuators A: Physical, 132*(1), 325-330.

Wood, C. (1988). Materials for thermoelectric energy conversion. *Reports on progress in physics, 51*(4), 459.

Wu, F., Song, H., Jia, J., & Hu, X. (2014). Thermoelectric properties of rare earth-doped *n*-type $Bi_2Se_{0.3}Te_{2.7}$ nanocomposites. *Bulletin of Materials Science, 37*(5), 1007-1012.

Xie, W., He, J., Kang, H. J., Tang, X., Zhu, S., Laver, M., *et al.* (2010). Identifying the specific nanostructures responsible for the high thermoelectric performance of $(Bi, Sb)_2Te_3$ nanocomposites. *Nano Letters, 10*(9), 3283-3289.

Yang, J., Liu, G., Yan, J., Zhang, X., Shi, Z., & Qiao, G. (2017). Enhanced the thermoelectric properties of *n*-type Bi_2S_3 polycrystalline by iodine doping. *Journal of Alloys and Compounds, 728*, 351-356.

Yang, J., & Stabler, F. R. (2009). Automotive applications of thermoelectric materials. *Journal of Electronic Materials, 38*(7), 1245-1251.

Yang, Q., Hu, C., Wang, S., Xi, Y., & Zhang, K. (2013). Tunable synthesis and thermoelectric property of Bi_2S_3 nanowires. *The Journal of Physical Chemistry C, 117*(11), 5515-5520.

Yoon, S., Kwon, O.-J., Ahn, S., Kim, J.-Y., Koo, H., Bae, S.-H., *et al.* (2013). The effect of grain size and density on the thermoelectric properties of Bi_2Te_3-PbTe compounds. *Journal of Electronic Materials, 42*(12), 3390-3396.

Yu, C., & Chau, K. T. (2009). Thermoelectric automotive waste heat energy recovery using maximum power point tracking. *Energy Conversion and Management, 50*(6), 1506-1512.

Yu, H., Li, Y., Shang, Y., & Su, B. (2008). *Design and investigation of photovoltaic and thermoelectric hybrid power source for wireless sensor networks.* Paper presented at the Nano/Micro Engineered and Molecular Systems, 2008. NEMS 2008. 3rd IEEE International Conference on.

Yu, I., Ravich, B., & Smirnov, I. (1970). Semiconducting lead chalcogenides: Plenum Press: New York.

Yu, Y. Q., Zhang, B. P., Ge, Z. H., Shang, P. P., & Chen, Y. X. (2011). Thermoelectric properties of Ag-doped bismuth sulfide polycrystals prepared by mechanical alloying and spark plasma sintering. *Materials Chemistry and Physics, 131*(1), 216-222.

Zhang, J., Song, L., Pedersen, S. H., Yin, H., Hung, L. T., & Iversen, B. B. (2017). Discovery of high performance low cost *n*-type Mg_3Sb_2-based thermoelectric materials with multi valley conduction bands. *Nature Communications, 8*, 13901.

Zhang, L. J., Zhang, B. P., Ge, Z. H., & Han, C. G. (2013). Fabrication and properties of $Bi_2S_{3-x}Se_x$ thermoelectric polycrystals. *Solid State Communications, 162*, 48-52.

Zhang, Q., Zhang, Q., Chen, S., Liu, W., Lukas, K., Yan, X., *et al.* (2012). Suppression of grain growth by additive in nanostructured p-type bismuth antimony tellurides. *Nano Energy, 1*(1), 183-189.

Zhao, D., & Tan, G. (2014). A review of thermoelectric cooling: Materials, modeling and applications. *Applied Thermal Engineering, 66*(1–2), 15-24.

Zhao, L. D., Lo, S. H., Zhang, Y., Sun, H., Tan, G., Uher, C., *et al.* (2014). Ultralow thermal conductivity and high thermoelectric figure of merit in SnSe crystals. *Nature, 508*(7496), 373.

Zhao, L. D., Zhang, B. P., Liu, W. S., Zhang, H. L., & Li, J. F. (2008). Enhanced thermoelectric properties of bismuth sulfide polycrystals prepared by mechanical alloying and spark plasma sintering. *Journal of Solid State Chemistry, 181*(12), 3278-3282.

Zheng, L., Li, W., Lin, S., Li, J., Chen, Z., & Pei, Y. (2017). Interstitial defects improving thermoelectric SnTe in addition to band convergence. *ACS Energy Letters, 2*(3), 563-568.

Zheng, X., Liu, C., Boukhanouf, R., Yan, Y., & Li, W. (2014). Experimental study of a domestic thermoelectric cogeneration system. *Applied Thermal Engineering, 62*(1), 69-79.

Zheng, X., Yan, Y., & Simpson, K. (2013). A potential candidate for the sustainable and reliable domestic energy generation–Thermoelectric cogeneration system. *Applied Thermal Engineering, 53*(2), 305-311.

Zhu, L., Tan, H., & Yu, J. (2013). Analysis on optimal heat exchanger size of thermoelectric cooler for electronic cooling applications. *Energy Conversion and Management, 76*, 685-690.

LIST OF PUBLICATIONS AND PAPERS PRESENTED

List of publications:

1. **Fitriani**, Ovik, R., Long, B. D., Barma, M. C., Riaz, M., Sabri, M. F. M.*,* Said, S. M. Saidur, R. (2016). A review on nanostructures of high-temperature thermoelectric materials for waste heat recovery. *Renewable and Sustainable Energy Reviews, 64*, 635-659.
2. **Fitriani Fitriani,** Suhana Mohd Said, Shaifulazuar Bin Rozali, Mohd Faiz Bin Mohd Salleh, Mohd Faizul Mohd Sabri, Bui Duc Long, Tadachika Nakayama, Ovik Raihan, Megat Muhammad Ikhsan Megat Hasnan, Mohamed Bashir Ali Bashir, Farhan Kamal. Enhancement of Thermoelectric Properties in Cold Pressed Nickel Doped Bismuth Sulfide Compound. Electron. Mater. Lett. (2018). https://doi.org/10.1007/s13391-018-0072-8

List of conference:

1. **Fitriani**, B.D.Long, S.M. Said, S. Rozali, M.F.M. Sabri: "Thermoelectric performance of Nickel doped Bismuth Sulfide (Bi_2S_3)", oral presentation at International Technical Postgraduate Conference, Kuala Lumpur, Malaysia, April 5th-6th 2017.